THE INFLUENCE OF SEMI-RIGID CONNECTIONS ON THE BEHAVIOUR OF SLENDER STRUCTURES

XIU FENG

A thesis submitted to

Oxford Brookes University for

the degree of Doctor of Philosophy

October 1994

THE INFLUENCE OF SEMI-RIGID CONNECTIONS ON THE BEHAVIOUR OF SLENDER STRUCTURES

By Xiu Feng

ABSTRACT

In the classical analysis and design of slender frame structures, it is normally assumed that the connections of the structures are either rigidly fixed or perfectly pinned. However, the real situation is that most connections often exhibit semi-rigid characteristics. This no doubt has a significant influence on the overall behaviour of the structures such as buckling capacity and deformation.

With the aim of evaluating the influence of semi-rigid connections and baseplates on the overall behaviour of slender structures, this thesis is devoted to investigating the properties of semi-rigid connections, particularly the semi-rigid baseplates in pallet racks which are usually used in the storage and materials handling industry, and then evaluating their effects on the buckling and deformation response of the structures. The investigations are carried out with the combination of theory and experiment, and with the utilization of a computer approach and engineering simplification.

The rotational stiffness of baseplates is investigated theoretically and experimentally aiming at estimating the principal factors that influence the behaviour of baseplates. A beam-compression spring model is proposed to calculate the rotational stiffness of baseplates. The compression springs are characterised by the equivalent modulus of subgrade reaction and are used to model the combined action of concrete floor and soil foundation. The initial rotational stiffness of baseplates is determined analytically and the subsequent nonlinear rotational stiffness is determined numerically using an associated computer program. The investigation showed that the rotational stiffness of baseplates is not only dependent on the applied axial loads but also on the subgrade which supports the baseplate. The experiments, which were conducted in the present work using concrete and timber as subgrade materials to model the effects of different subgrades, support this conclusion.

A structural model for buckling analysis is presented which considers the beam-column and column-baseplate semi-rigid connections. The governing equations are derived by the exact analysis of column elements.

They can be reduced to a transcendental function in terms of buckling load factor. The fundamental critical load of the structure is found from an engineering point of view rather than a purely mathematical point. The domain of the critical load is determined firstly and then a computer iterative approach is developed. The investigation showed that the dependence of buckling loads on the rotational stiffness of semi-rigid connections is significant. A comparison between the predicted results and those of other methods is made.

Also proposed is a simplified model for deformation analysis when the structure is subjected to both axial and lateral loads. The second-order analysis is carried out where the P-Δ effect is considered. The initial imperfection of the structure is taken into account. The Gauss elimination procedure is used to find deformation and ultimate load. The calculated results are compared with those obtained from a finite element analysis computer program LUSAS.

As one aspect of the investigation, adjustable telescopic steel props with semi-rigid baseplates are analyzed. The analysis is formulated and programmed in accordance with the new Euro-Norm and the German Standards. The computed results were compared with those of LUSAS and good agreement was achieved.

Based on the results obtained, discussion is made on the design of slender frame structures with semi-rigid connections. Also discussed is the procedure for the load capacity check of a slender structure with a given configuration.

In addition to the results obtained in the present research about the rotational stiffness of baseplates and about its influence on structural behaviour, the investigation also demonstrated how to evaluate the rotational properties of connections and their effects on buckling and deformation of structures.

DECLARATION

I wish to declare that, except for commonly understood and accepted ideas, or where specific reference is made to the research of other authors, the contents of this thesis are my own original work. The work has not been previously submitted, in part or in whole, to any University for any degree, Diploma, or other qualification. The work was carried out in the School of Construction & Earth Sciences, Oxford Brookes University, between September 1990 to September 1993.

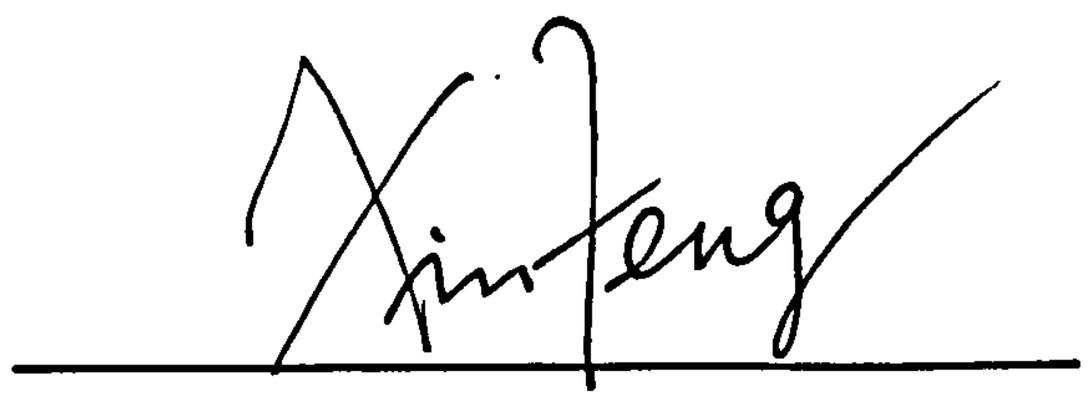

Candidate

ACKNOWLEDGEMENTS

First and foremost , I would like to thank my supervisor Dr. M.H.R. Godley and my second supervisor Mr. R. Beale for their guidance and encouragement provided throughout this research work. Thanks are also due to Prof. J.M. Davies for acting as my second supervisor, and also for many stimulating discussions on the theoretical models.

I am very grateful to the School of Construction & Earth Sciences, Oxford Brookes University, for giving me the opportunity to undertake the present work.

The materials used for the test were kindly provided by DEXION Ltd., and I thank them for their generosity. Thanks are due to Mr D. Dunning of DEXION Ltd.

I would also like to thank the technical staff of the Structures laboratory for their assistance with the experiments. I express my gratitude to R.T. Salter, I. Wesson, M. Baskerville and many others for their help.

NOTATION

Symbols are defined when they appear for the first time in the thesis. Each one is redefined when its meaning changes. Some symbols are used throughout the thesis with the following meaning.

a_0,a_{0j}	Maximum initial lateral deflection
a	Distance between centres of holes, half the distance between flange centroid of column
b	Half length of baseplate
c	Width of flange of column
d	Diameter of a hole
f(P)	Function of axial load *P*
i,i_{ij}	Flexural rigidity EI/l and EI_j/l_j, respectively
i,j,k	Nodal numbering
k	End rotational stiffness factor, constant elastic stiffness
k_{b0},k_b^1,k_b^2	Initial rotational stiffness of baseplate
k_e	Equivalent stiffness of compression spring
k_i	Rotational stiffness of beam-column connection
k'_i	Modified rotational stiffness of k_i
k_{li},k_{ri}	Rotational stiffness of left and right end of beam
k_s	Modulus of subgrade reaction
k_{sc}	Modulus of subgrade reaction of concrete block

k_{se}	Equivalent modulus of subgrade reaction
k_{st}	Modulus of subgrade reaction of timber block
l	Span, length
l_i	Height of storey, distance
l_j,l_k	Length of elements *j* and *k*
n	Number of storey
q	Uniformly distributed load
q'	Uniform reaction force on concrete floor
q_x,q_y	Distributed load per unit length
r	Inner radius
t_1	Thickness of baseplate
t_2	Thickness of concrete floor
w	Deflection of baseplate
w_0	Average deflection of baseplate
x,y,z	Orthogonal cartesian coordinates
y	Deflection curve
y_0	Initial imperfection curve
A_1,B_1,C_1,D_1	Constants
A	Area of baseplate
A_{gr}	Area of gross cross-section
A_n	Area of net cross-section
D	Flexural rigidity of concrete floor
E	Equivalent modulus of elasticity of compression column
E_c,E_{c1},E_{c2}	Modulus of elasticity of concrete block
E_s	Modulus of elasticity of baseplate
E_t	Modulus of elasticity of timber block
EA_B	Axial tensile rigidity of beam in Fig 3.5

EI_B	Flexural rigidity of beam in Fig 3.5
EA_i	Axial rigidity of compression column
EI_i	Flexural rigidity of compression column
E_iI_i	Flexural rigidity of simplified model
EA_i^c	Axial compression rigidity of compression column
EA_i^t	Axial tensile rigidity of compression column
H,H_j	Constants
I_{gr}	Moment of inertia of gross cross-section
I_i	Equivalent moment of inertia of cross-section
J_B	Second moment of area of compression column
L	Span, length, height
L	Total length of the prop
L_1	Length of top prop
L_2	Length of bottom prop
L_1,S_1	Length and width of column cross-section
L_2,S_2	Length and width of baseplate
L_n	Distance between two neighbouring compression springs or columns, span
M	Bending moment
M_0	Bifurcation bending moment
M_{AB},M_{BA}	End bending moment at end *A* and *B*
M_{jk},M_{ji}	Bending moment at node *j*
M_p	Maximum bending moment
O	Origin of axes
P,P_1,P_2	Concentrated load, axial force
P'	Fundamental critical load
P_i	Axial forces
P_{cr}	Critical axial load

P_m	Antisymmetric concentrated load
P_{maxcr}	Upper limit of P_{cr}
Q_A, Q_{AB}	Shear forces at end A
Q_B, Q_{BA}	Shear forces at end B
Q_i	Horizontal force
R	Outer diameter of a tube
R_0	Constant
U	Complementary energy per unit volume

Matrices, Vectors and Elements

[C]	Overall stiffness matrix of structure
c_{ij}	Elements of [C]
c'_{ij}	Elements of [C] after Gauss Elimination
det[D]	Value of determinant of [C]
{D}	Rotation and deflection vector
{F}	Load vector

Greek Symbols

α, β	Parameter, coefficient
β_1 to β_4	Components of buckling mode
$\theta_1, \theta_2, \theta_A, \theta_B, \theta_i, \theta_j, \theta_k$	Angle, angle of rotation
$\{\theta\}$	Nodal rotation vector
θ_{gap}	Initial gap of baseplate
γ	Coefficient

Δ_j^e	Initial deflection of global structure
Δ,Δ_i	Deflection
Δ_1,Δ_2	Initial eccentricity
$\Delta\psi_0$	Angle of inclination
$\delta,\delta_0,\delta_M,\delta_i$	Nodal deflections
φ_1 to φ_4, η_2 and η_3	Stability functions
Δ_1,Δ_2	Initial eccentricities of prop
ν	Poisson's ratio
ν,ν_{ij}	Load parameter
π	3.14159
Σ	Summation
Ψ_R,Ψ_r	Angle
σ_y	Yield stress of baseplate

CONTENTS

APPENDICES

CHAPTER 1 INTRODUCTION

1.1 General outline

Many structures can be regarded as slender structures which normally deform in the form of sway when subjected to external loading. Examples of these include pallet racks which are widely used in the storage and material handling industry and in scaffolds in the construction industry [1,2].

The classical analysis and design of slender structures is often based on the assumption that the beam-column and column-baseplate connections are either perfectly pinned or rigidly fixed. Pinned connections have no moment transfer and fixed connections have complete rotational continuity. These are two simplified extremes. The real situation is that pinned connections often exhibit some rotational stiffness, whilst rigid connections possess some degree of flexibility [3-6]. These properties are referred to as semi-rigidity of connections.

It has long been realised that the semi-rigidity of connections has a significant influence on the behaviour of slender structures. This includes buckling capacity, load-deformation relationships and elastic-plastic behaviour of the structures. The pallet rack systems, for example, have semi-rigidity in their connections because their beam-column connections

are often designed with the facility of easy removal when required. Their buckling behaviour, load-defection response and load capacity, which are the major concern of industry, are obviously dependent upon the rotational stiffness of semi-rigid connections.

The realisation of the existence of semi-rigidity of connections in structures, including slender structures, is one thing. The consideration of them in structural analysis and design is another. As it involves significant calculations to consider semi-rigid properties of connections in structural design, it was not until the advent and application of computer technology that involvement of semi-rigid connections in design became possible.

In order to evaluate the influence of semi-rigid connections and baseplates on the overall behaviour of structures, two phases of work need to be done. First is to investigate how semi-rigid connections and baseplates perform and secondly, to estimate how they influence the behaviour of structures. Some theoretical and experimental studies on the properties of semi-rigid beam-column joints can be found, as reviewed in Chapter 2. But those involving semi-rigid baseplates are very limited, especially those for the baseplates used in pallet racking systems. Consequently, on the investigations into the structural behaviour and the behaviour of structural members with semi-rigid connections, there is still significant work to be done to improve the understanding of the effects of semi-rigid beam-column connections and semi-rigid baseplates on the overall behaviour of the structures. In this area, slender structures are particularly interesting since buckling failure and nonlinear load-deflection behaviour are predominant.

From these points of view, this thesis is devoted to investigating and evaluating, first of all, the properties of semi-rigid connections and then their effects on the overall behaviour of slender structures. The investigations are carried out with the combination of theory and experiment and with the utilization of computer approach and engineering simplification, so as to identify the deformation mechanisms of semi-rigid baseplate and to evaluate stability and deformation response of the structures. The following sections and chapters are set for these purposes.

1.2 Objectives of the research

The following objectives are set in the present research:

(1) To propose a theoretical method to evaluate the rotational stiffness of a baseplate, to conduct appropriate experiments to estimate the range of applicability of the method and to find out the factors that are dominant in determining the behaviour of the baseplate.

(2) To investigate the influence of the semi-rigid connections, including semi-rigid baseplates, on the buckling behaviour of slender frame structures.

(3) To present a simplified computational method for second-order analyses of slender frame structures in which semi-rigid behaviour of connections is considered.

(4) To analyze a specific slender structure ---- telescopic steel prop which has an initial gap between its inner and outer tubes, an initial gap between baseplate and subgrade, and semi-rigid characteristics on the baseplate.

(5) To discuss the necessary attention to be paid in the design of slender structures when considering semi-rigid behaviour of connections and to present a general procedure for the load capacity predictions of a slender structure of a given configuration. The discussions are based on the results obtained from the present research.

(6) To develop the associated computer programs on the above subjects for research and industrial use.

These objectives are achieved respectively in the subsequent chapters.

1.3 The methods used in the research

The classical analysis and design of a slender frame structure is based on the assumption of rigid or pinned joints including baseplates. It can be seen that the assumption has the effects of either overestimating (for rigid joints) or underestimating (for pinned joints) the ultimate load capacity of the structures. In the present research, this assumption was dropped and semi-rigid connections were assumed so as to investigate their influence on the behaviour of the structures.

The research was focused on slender structures. Significant considerations were given to the buckling behaviour and the load-deflection interaction of the structures. The influence of semi-rigid connections, including semi-rigid baseplates, was taken into account. The slenderness of the structures was considered in the simplification of structural model.

A simplification of the real problem has been made so that the computational models of the problems are acceptable in design. However, the major features of the problem have been retained in spite of the simplification by replacing the interaction between some factors with an equivalent quantity. For example, the equivalent modulus of subgrade reactions was used to model the combined action of a concrete floor and a soil foundation, and the equivalent rotational stiffness of beam-column joints was adopted to incorporate the effects of the beam flexural stiffness and the beam-column semi-rigid joints.

Appropriate experiments were conducted independently to confirm the predicted results and the applicability of the theoretical models. Meanwhile, they served as a general guide for the development and modification of the theoretical models. In order to investigate the effects of different materials of subgrade, concrete and timber blocks were used in the experiments.

The formulation of the basic governing equations made use of conventional plate and beam theories. The superposition approach was employed to determine the initial rotational stiffness of baseplate which was modeled as a uniform beam resting on an elastic foundation with constant elastic stiffness. The nonlinear part of the moment-rotation curve of

baseplate was determined numerically using a beam-compression column model and a previously developed computer program. The compression column was only able to be subjected to compression. Tension was not allowed. An exact analysis was used to derive the bending equilibrium equations at the joints, and the differential equations were solved to obtain the slope-deflection relations.

The fundamental critical load of the structure was found from an engineering point of view rather than purely mathematical point. The domain of the fundamental critical load was found out firstly and then an efficient computer iterative approach was developed to find the fundamental critical load.

The solutions of the matrix equations governing the equilibrium of the overall structure were found by means of specifically developed computer programs and were compared with those of experiments and those obtained from the finite element analysis computer program LUSAS, wherever possible.

In all, the methods used follow the ideas of a combination of theory and experiment, utilization of a computer approach and engineering simplification, to achieve the objectives outlined in the proceeding section.

1.4 Outline of the thesis

A brief description of the contents of the subsequent chapters in this

thesis is made below.

The work previously done in the area of semi-rigid framed structures is reviewed in Chapter 2. · In particular, semi-rigid characteristics of connections and baseplates, their effects on buckling behaviour and deformation of the overall structure, some specific types of slender structures, and the application of research in design are emphasized.

Chapters 3, 4 and 5 are devoted to the theoretical and experimental investigations into the semi-rigid behaviour of baseplates. Chapter 3 presents a theoretical method for the calculation of rotational stiffness of baseplates, in which the interaction between the baseplate, the subgrade and the applied loads is taken into account. The effects of subgrade are described using its equivalent modulus, and the effects of applied loads are characterised using the ratio of bending moment to axial force. The initial rotational stiffness of a baseplate is determined analytically using a model of a uniform beam on an elastic foundation by means of a superposition approach, whilst the subsequent nonlinear rotational stiffness is determined numerically using a model of beam-compression columns and the associated computer program.

Chapter 4 deals with the experimental aspects of the rotational stiffness of baseplates with the aim of determining the factors which influence the behaviour of baseplates. A test rig was designed to apply both an axial force and a bending moment to a baseplate. The rig consisted of a servo-controlled hydraulic jack and a hand-controlled hydraulic jack in a reaction frame. The test panel was located between pinned spherical bearings at either end of the rig. Concrete and timber

were used in the experiments to investigate the effects of different subgrades on the rotational stiffness of baseplates. Different combinations of axial forces and bending moments were tested to investigate the overturning resistance of baseplates.

Chapter 5 gives the comparison between the theoretical predictions and the experimental results of the rotational stiffness of baseplates, and it also illustrates the use of the theoretical model presented in Chapter 3. It explains how the subgrade and the applied axial loads influence the rotational stiffness of baseplates. A bifurcation bending moment for the moment-rotation curve of baseplate is defined in this chapter. This moment is used to identify the limit of the model with a constant initial rotational stiffness of baseplate.

The buckling behaviour and the load-deflection response of slender frame structures are stiffness-dependent, and consequently they directly depend on the stiffness of semi-rigid joints and baseplates. Chapters 6 and 7 are devoted, respectively, to investigating the influence of the semi-rigid joints and baseplates on the buckling behaviour and the deformation analysis of these structures.

A structural model for buckling analysis is proposed in Chapter 6 where the equivalent rotational stiffness of beam-column joints is formulated using continuous beam theory. The rotational stiffness of a baseplate is provided by the previous chapters. The buckling equations are derived by the exact analysis of the column elements. For the proposed model with unbraced sway, a symmetric tri-diagonal stiffness matrix can be obtained, from which a transcendental function for the determination of the

fundamental critical load is formulated by the conditions of non-trivial solutions of the buckling problem. Then, an efficient algorithm is proposed from an engineering point of view to find the fundamental critical load and the corresponding buckling mode. The application of the methods to a multi-bay slender frame structure with variable number of storeys, semi-rigid baseplates and semi-rigid beam-column joints is presented. A comparison between the computed results and those of other methods is made.

Chapter 7 uses a simplified second-order analysis to determine the final deflection and bending moment of semi-rigid slender frame structures subjected to both lateral and vertical loads. Based on the structural model for buckling analysis, a simplified model for second-order analysis is proposed. The governing bending equilibrium equations are derived using the exact analysis. The initial imperfection of the structure is considered. The Gauss elimination procedure is used to find the solution of the equations. The numerical examples are given and wherever possible, compared with those obtained from the finite element analysis computer program LUSAS.

Chapter 8 is devoted to analysing adjustable telescopic steel props. Models were developed based on the new Euro-Norm (CEN/TC53-WG8-No36E) and the German Standards (DIN4422). The basic bending equilibrium equations were formulated and a computerized approach was presented to determine the ultimate load capacity and to calculate the deflections and internal forces of props under various loading and boundary conditions. Two practical computer programs, based on the two Standards, were written for industrial use.

Chapter 9 discusses the necessary attention to be paid in the design of slender structures when considering semi-rigid behaviour of connections. The discussion is based on the results and conclusions of the present research. Also discussed are the procedures for the load capacity check of a slender framed structure with a given configuration. A flow diagram is given to illustrate the procedures and to develop computer automated predictions of load capacity. The incremental load approach is used to find the ultimate load of the structure.

Finally, the conclusions on the present research are drawn in Chapter 10 and suggestions for further research are discussed.

CHAPTER 2 REVIEW OF THE PREVIOUS WORK

2.1 General outline

Over the last half century, research in framed structures has been concentrated into the behaviour of structural members and the performance of overall structures. Significantly less attention has been directed to the study of the behaviour of connections in the structures due to the complexity of the problem. Modern methods of analyses coupled with computer technology have enabled more detailed analysis to be carried out and have encouraged more rigorous study of design approaches.

As has been stated in the opening chapter, the overall behaviour of slender frame structures depends not only on the behaviour of individual members, but also on how the members interact through their connections which include beam-column connections and baseplates. At the early stage of analysis and design, the members of framed structures are assumed to be connected either by frictionless pins or by fully rigid connections. However, extensive experimental and analytical research [3-6] has shown that most connections generally fall between the two extremes of perfectly pinned and fully rigid. In addition, the moment-rotation behaviour of the connections is usually nonlinear. These effects will alter the force distribution in the members of the structure and have a significant influence

on its overall behaviour such as buckling and moment-rotation characteristics. Following these points, some of the work previously done is reviewed in this chapter.

2.2 Semi-rigid characteristics of connections and baseplates

Beam-column connections and column baseplates in a framed structure join beams or columns together and transfer the applied loads from one part of the structure to another. The semi-rigidity of connections and baseplates stems from the construction and fabrication of practical cold-formed steel structures. For example, the beam-column connections in pallet racking systems are of a mechanical nature with the facility of easy removal when required [7]. They therefore possess semi-rigid characteristics.

Similarly, baseplates (referring to steel baseplates throughout the thesis) in cold-formed steel structures are used to distribute loads from a steel column over a subgrade, normally a concrete foundation. There is always an initial gap beneath the baseplate because the surface of the subgrade is not absolutely smooth, and because the baseplate may not be fully bolted to the foundation. This will cause baseplates to behave loosely and therefore they possess semi-rigid spring characteristics [8]. On the other hand, the baseplate is subjected to a combination of axial loads and moment because the action of the column load is often eccentric. When the moment is large there will be a tendency for the baseplate to lift and the

elevated side of the baseplate will no longer be able to transmit forces over the subgrade. Anchor bolts in this case, together with the unlifted side of the baseplate, are necessary to maintain the equilibrium of column-baseplate-subgrade system.

Research into the behaviour of connections and their moment-rotation characteristics started as early as 1917 when Wilson and Moores [9] conducted experiments to determine the stiffness of riveted joints in steel structures. Since then changes in the design of connections have continued and many investigations have been published offering various design methods [10].

Parsanejad and Anderson [11] presented the experimental data of some beam-column specimens tested to study the behaviour of connection assemblies commonly used in drive-through or drive-in pallet racking systems. The research tried to establish the behaviour of a standard connection and to investigate means of improving its behaviour. From the structural and economical points of view, one way of improving the behaviour of the standard connection is to elongate the end plate assembly and provide additional connecting studs. Aggarwal [12] investigated experimentally the behaviour and moment-rotation characteristics of beam-column connections. It was concluded from his investigation that the non-linearity of moment-rotation relationship exists over the complete range of loading, and that the deviation from linearity in the elastic regime is small but becomes large in the post-elastic regime.

The investigations into the behaviour of semi-rigid beam-column connections are vast, as reviewed by Jones et al [3-6]. However, work on

the behaviour of semi-rigid baseplates is relatively limited. Though some theoretical and experimental studies have been done on the behaviour of column baseplates, most of them are to do with axial loads on the columns to determine ultimate load [13], or to do with the load distribution of baseplate itself to improve the design of baseplate [14]. Baseplates under the action of eccentric loads have not received much attention and no work has been found on the rotational stiffness of baseplates, particularly those in pallet racks. For example, De Wolf and Sarisley [13] conducted tests on baseplates subjected to eccentric loads and tried to determine failure loads. But rotational stiffness of the baseplates was not one of the factors considered. Thambiratnam [14] investigated both experimentally and analytically the behaviour of baseplates under the action of eccentric loads using the finite element method. The investigation revealed that baseplates deform when loaded eccentrically and the pressure distribution under baseplates is nonlinear. However, this investigation was focused purely into the behaviour of a baseplate subjected to eccentric column loads but not into the moment-resistance of baseplate to column. The present concern is to investigate the influence of the rotational stiffness of semi-rigid baseplates, together with beam-column semi-rigid connections, on the overall behaviour of the structure, not only the baseplate itself.

2.3 Effects of semi-rigid connections on buckling behaviour

The buckling behaviour of structures has been the subject of many experimental and analytical investigations [15].

As is well known, one of the decisive factors for the column strength at a given length is the end support condition. For example, the elastic buckling loads for the two extreme cases of end support conditions, perfectly pinned and fully rigid fixed on both ends, are (π^2EI/l^2) and ($4\pi^2EI/l^2$), respectively, where EI represents the flexural rigidity of column, and l the length. Obviously, the fully rigid case on both ends has a higher resistance to buckling than the case of perfectly pinned on both ends when they have the same length and cross-section area.

It can be seen that the buckling load for the case of neither perfectly pinned nor fully rigid fixed but elastically restrained falls between these two extremes. Rasmussen and Hancock [16] studied the effects of end support conditions on the flexural behaviour of thin-walled singly symmetric columns. The relationship between the restraining bending moment, M, caused by adjoining members, and the end rotation, θ, is defined as $M=k(EI/L)\theta$, where (EI/L) is the stiffness of the column and k is a factor of end rotational stiffness (M/θ) varying from zero (perfectly pinned) to infinity (rigidly fixed). It is interesting to look at the variation of the elastic ultimate load P_u as a function of k, which is shown schematically in Fig 2.1. Three combinations of end support conditions were considered in the figure. They were a) elastically restrained at one end and fixed at the opposite end ($k=\infty$), b) elastically restrained at both ends and assuming the same value of k at both ends ($0<k<\infty$), and c) elastically restrained at one end and pinned at the opposite end ($k=0$). The extreme case of a) and b) is shown in d) where the elastically restrained end becomes fixed ($k=\infty$), whilst e) is the extreme case of c) when $k=\infty$. For all three combinations of end supports, the strength increases rapidly with increasing k.

Many beams and columns form part of integrated framed structures. They are likely in many practical situations to be neither perfectly pinned nor rigidly fixed but elastically restrained at the ends by adjoining members, which is the so-called semi-rigid end support condition. As a result semi-rigid connections in a framed structure will inevitably influence not only the buckling behaviour of columns and beams of the structure (local buckling), but also the overall buckling of the structure.

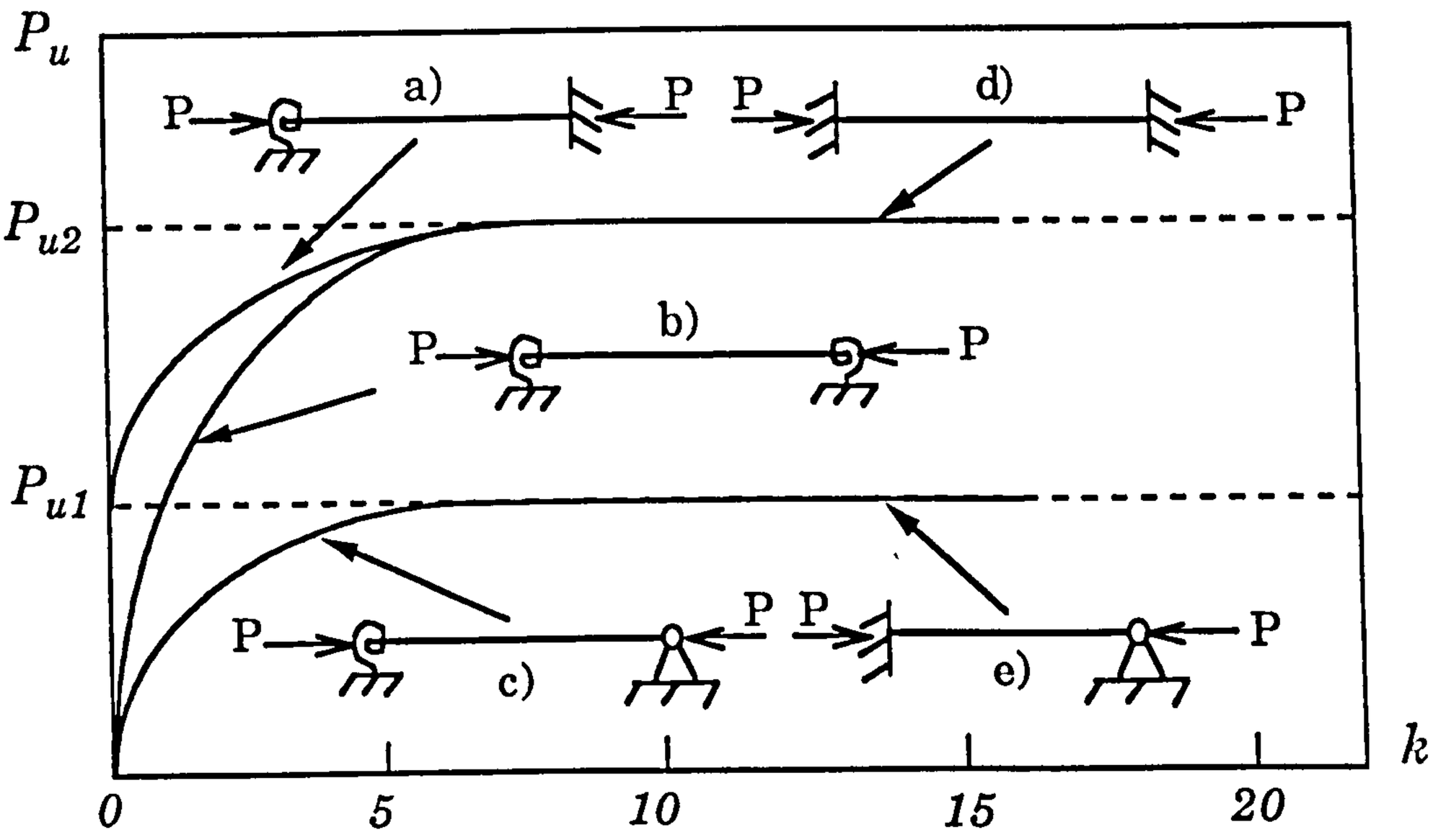

Fig 2.1 Schematic representation of the effects of end rotational stiffness factor (k) on buckling loads (P_u)

A lot of research has been devoted to investigating the influence of semi-rigid connections on the buckling behaviour of steel framed structures.

A comprehensive state-of-the-art report by Jones et al [17] summarised the extensive analytical and experimental work on the behaviour of steel beam-column connections and on the behaviour of overall structures carried out over the past 50 years. Romstad and Subamaniam [18] investigated the effects of semi-rigid connections on the buckling behaviour of simple plane frames in 1970. The effects of semi-rigidity on stability of single-bay double-storey plane frames was studied by Yu and Shanmugan [19].

In another investigation [20], Yu and Shanmugan studied the effects of partial rigidity of the joints in semi-rigid framed structures using the modified stiffness matrix method to predict the elastic buckling loads, which concluded that the buckling capacity (overall stability) of the structure could significantly be increased by allowing for a marginal increase in the rotational stiffness of joints.

The work on the buckling behaviour of semi-rigid framed structures has been helpful in improving the understanding and the design methods of this type of structure. However, since most of the work was based on the precondition that the rotational stiffness of connections had been known, and the computational models were normally based on full three-dimensional or two-dimensional finite element analyses, this would no doubt put a limitation on their engineering use. From this point of view, it is necessary to make some simplifications into the construction of a structural model and to develop an efficient algorithm to find the solutions of the problem.

2.4 Deformation behaviour of semi-rigid framed structures

The deformation behaviour of a framed structure subjected to combined horizontal and vertical loads is linear if the loads are small, but it becomes nonlinear for slender structures in the case of large applied loads. This is due to the so-called 'P-Δ' effects which are produced by the vertical forces acting through the laterally deflected position of the structure and cannot be ignored. Thus a second-order analysis needs to be made to look into the nonlinear behaviour of the structure to external loading.

The determination of deformation behaviour of slender semi-rigid structures should consider the effects of semi-rigid connections, linear or nonlinear wherever possible. A generalized method of treating partially rigid connections using the matrix analysis procedure was presented by Monforton and Wu [21]. In their analysis, the moment-rotation behaviour of connections was assumed to be linear. For the cases of considering nonlinear behaviour of connections, improved representation was implemented into the analysis procedures by Ang and Morris [4], Ackroyd and Gerstle [22], and Lui and Chen [23,24].

Tan and Rhodes [25] used a systematic analytical approach to study the behaviour of symmetrical single and double storey frameworks constructed from cold-formed thin-walled plain channel members and semi-rigid connections. In their studies, for a given moment-rotation curve of a connection, the stiffness was determined by curve fitting techniques.

A common point of these investigations on deformation analysis of frame structures considering semi-rigid properties is that most of them

assumed a given moment-rotation curve of a connection, and they commonly used the matrix analysis procedure based on a full scale model. Little was done on the effects of baseplates and on the consideration of the applied axial load dependence and the subgrade dependence of rotational stiffness of baseplate.

2.5 Specific type of slender structures

An application of cold-formed steel slender structures is industrial steel storage rack systems used in the storage and material handling industry. The beams in these structures are braced into upright (column) frames by connecting inclined or horizontal bracing using either welded or bolted connections, and often, these connections have a mechanical nature with the facility of easy removal when required. Consequently the integrity and stability of the structures are heavily dependent upon the behaviour of the beam-to-upright connections and upon the rotation-resistant ability of the baseplates. Due to the complexity of the behaviour of the semi-rigid connections, there is, as yet, no universally accepted procedure for analysis and design.

The investigation into stability of rack structures has recently been made by some authors. Davies [26,27] analyzed the down-aisle stability of racking structures where a single internal upright model carrying both vertical and horizontal loads was used. The model took into account the semi-rigid beam-to-upright joints and the rotational stiffness at the steel

bases of the uprights which rested on a floor. An improved approach was presented to exploit the design expressions of some current Codes of Practice. However, this model only allowed for column flexibility below the level of the first beam, the rest of the columns being treated as rigid. As indicated in [27], this assumption becomes increasingly unsafe as the number of storey levels increases, and it is particularly inappropriate when the first beam is near the ground.

A simple design approach was proposed by Lewis [28] to investigate the stability of pallet rack structures. Semi-rigid behaviour was assumed at beam ends, and all uprights were assumed pinned at the floor. Further, the loads at each level were assumed to be the same, the heights between beam levels to be equal, and the bending distortion of the upright to be small and therefore negligible. These assumptions lead to a simple model for design practice on one hand, but, on the other hand, they pose many restrictions on the application of the model. It seems to be appropriate to adopt a more flexible and realistic approach in design since computers are readily available.

Another type of slender structure is the steel telescopic prop that is mainly used on construction sites for supporting formwork. These are usually composed of cylindrical tubes with a coarse adjustment via a pin and a fine adjustment via a screwed connection. The Standards [29,30] stipulate in some of the specifications that props may be extended up to 6 metres. Relative to their small diameters, steel telescopic props may therefore fall into the category of 'slender' structures.

Research into the behaviour of props has been very limited. For

industrial use it is necessary to produce a practical approach to predict their buckling and deformation behaviour.

2.6 Application of semi-rigid characteristics of connections in design

The design of connections, based on semi-rigid analysis, was introduced in 1936 [31], but it did not gain much popularity at that time because of the large computational work involved in assuming semi-rigid behaviour. So for a long time steel framed structures have been designed based on the assumption that the beam-column joints are either pinned or fully rigid.

The insistence on assumption of 'pinned' or 'fully rigid' joints ignores the inherent stiffness which exists in most practical joints. In reality, all steel framed structures are semi-rigid in nature because all connections exhibit a certain degree of flexibility under loads. So an additional rotation within the members of the connections is created and thereby the sway displacement is increased in unbraced frames under the combined action of vertical and lateral loads. These facts have been the subjects of intensive research during the last decade, which, together with the advance of computer technology, makes it possible to incorporate the true behaviour of connections in design.

Modelling joint behaviour can be made by means of moment-rotation curves expressed in an appropriate mathematical representation. Such a representation which is very effective for design purposes is based on

available experimental data and curve fitting techniques. Maquoi [34] made a review of mathematical formulae developed to predict the moment-rotation response of a joint under different types of joint loading. Sources of joint flexibility were described to fall within flexibility due to connection means, or flexibility due to load introduction effect, or flexibility due to shear of column web panel. From these points of view, the modelling of moment-rotation relationship of a specified joint was discussed. It was demonstrated that a bi-linear moment-rotation response seemed appropriate for design. This format was based on the initial stiffness, the strain-hardening stiffness and pseudo-plastic moment of the connection.

It would be helpful if an appropriate mathematical formula could be constructed to represent the semi-rigid behaviour of a connection. But it was not always possible due to the complexity of the semi-rigid behaviour. For example, the rotational stiffness of a baseplate is dependant on the applied axial loads and the subgrade. So, a practical method should be developed to represent these features.

2.7 Concluding remarks

The prediction of the real structural behaviour such as ultimate load capacity and moment-rotation relationship under various loading conditions requires knowledge of the response of the connections employed in the steel framed structures. There has been extensive research into beam-column connections and the structural behaviour by considering semi-rigid connections. But little was about the rotational stiffness of column-

baseplate connections, particularly the baseplate in pallet rack system, and their effects on structural stability and deformation.

In addition, most of the work conducted on semi-rigid effects on structural behaviour assumed a given moment-rotation curve of connection, and normally a full scale model was used by means of a matrix analysis procedure. It has been helpful in improving the understanding and the design method of semi-rigid structures. But it is not enough from an engineering point of view. A model in a more practical way is needed to evaluate the ultimate load capacity which should, wherever possible, consider the factors such as semi-rigid beam-column connections and the rotational stiffness of baseplates. This thesis will be devoted to achieve these objectives.

CHAPTER 3: THEORETICAL ANALYSIS OF SEMI-RIGID BASEPLATES

3.1 General outline

Theoretical investigations into the rotational stiffness of column baseplates in cold-formed steel structures are carried out in this chapter. The interaction between the baseplate, the subgrade, and the applied column load is taken into account. The equivalent modulus of subgrade is derived from the theory of elasticity. It is indicated that this modulus is related to the thickness and the flexural rigidity of the concrete floor and related to the modulus of subgrade reaction of the soil foundation.

The nonlinear semi-rigid characteristic of the baseplates is obtained from a model in which the subgrade is divided into a number of special compression spring elements and the baseplate is treated as a continuous beam supported on these spring elements.

3.2 Introduction

Slender structures such as pallet racks and scaffolds are widely used in the storage, materials handling and construction industries [1]. Such

structures are usually beam-column systems with columns supported on the subgrade through column baseplates. The beam-column pallet rack structure shown in Fig 3.1 gives an example where the square blocks represent the applied loading.

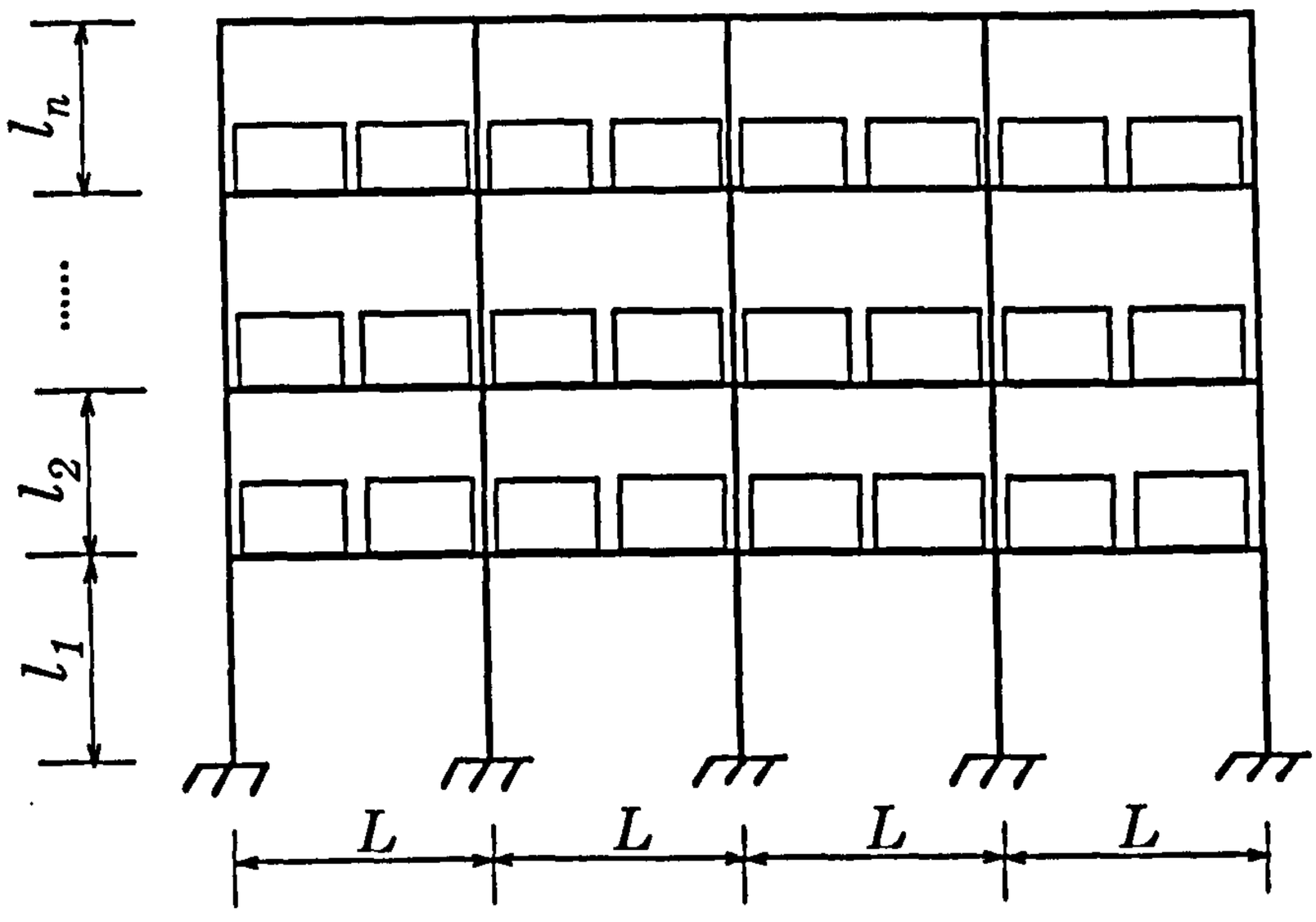

Fig 3.1 Beam-column pallet rack structure

One of the main concerns in the design of slender structures is how to design column baseplates to ensure that applied column loads are transmitted safely from the column to the foundation floor. Another is how to predict the structural characteristics of beam-column connections and

column baseplate connections for use in the analysis of the whole structure. Since the baseplate may be bolted to the foundation floor, sometimes unbolted or lightly bolted, the joint possesses semi-rigid spring characteristics which have very significant effect on column buckling and the behaviour of overall structures.

The classical analysis and design of a steel column baseplate is based on the assumption that the baseplate is rigidly fixed to its subgrade [2]. However, experimental studies have shown that steel column baseplates have non-rigid characteristics, especially when loaded at higher eccentricities [35~39].

A modification of the rigid baseplate assumption is to assume a trilinear moment-rotation relationship in the baseplate, which has been used for the design of prop baseplates in the German Code [29]. However, with the rapid application of slender structures in industry, further investigation into the actual non-linear behaviour of the baseplates is desirable, not only because of the lack of an appropriate design specification, but also because of the absence of an adequate way of predicting the influence of baseplates on column buckling and the behaviour of the whole structures.

In recent years, attempts have been made to investigate analytically and experimentally the behaviour of semi-rigid beam-columns and column-subgrade connections in steel structures [40~43]. But fewer investigations into the rotational stiffness of column baseplates in cold-formed steel structures have been found. No effective and practical method has been developed to determine the rotational stiffness of column baseplates and to estimate its effects on the stability of the overall structure.

Theoretical studies are therefore made in this chapter to predict the rotational stiffness of a column baseplate in a steel structure, taking into account the interaction between the baseplate, the subgrade and the applied loads. The equivalent modulus of subgrade reaction is firstly derived from the theory of elasticity. The derivation shows that the equivalent modulus of subgrade reaction is related to the thickness and the flexural rigidity of the concrete floor on which the baseplate is supported, and it is also related to the modulus of subgrade reaction of the soil foundation. Based on the equivalent modulus of subgrade, a theoretical model has been created to describe the nonlinear semi-rigid characteristics of baseplates. It gives the nonlinear rotational stiffness of the baseplate.

3.3 Analysis of semi-rigid baseplate

3.3.1 Compression spring model of baseplate

Fig 3.2 shows the column baseplate system, where the baseplate is fully bolted or partially bolted to a concrete floor. The concrete floor is constructed on a soil foundation. The applied column loads on the baseplate, an axial load P_c and a bending moment M, are statically simplified as an equivalent uniform distributed load q and two concentrated loads P_1 and P_2, as shown in Fig 3.3. They are defined as

$$q=\frac{P_c}{(2S_1+L_1)}$$

$$P_1 = qS_1 - \frac{M}{L_1} \qquad (3.1)$$

$$P_2 = qS_1 + \frac{M}{L_1}$$

where L_1 and S_1 are the length and width of the column cross section, respectively.

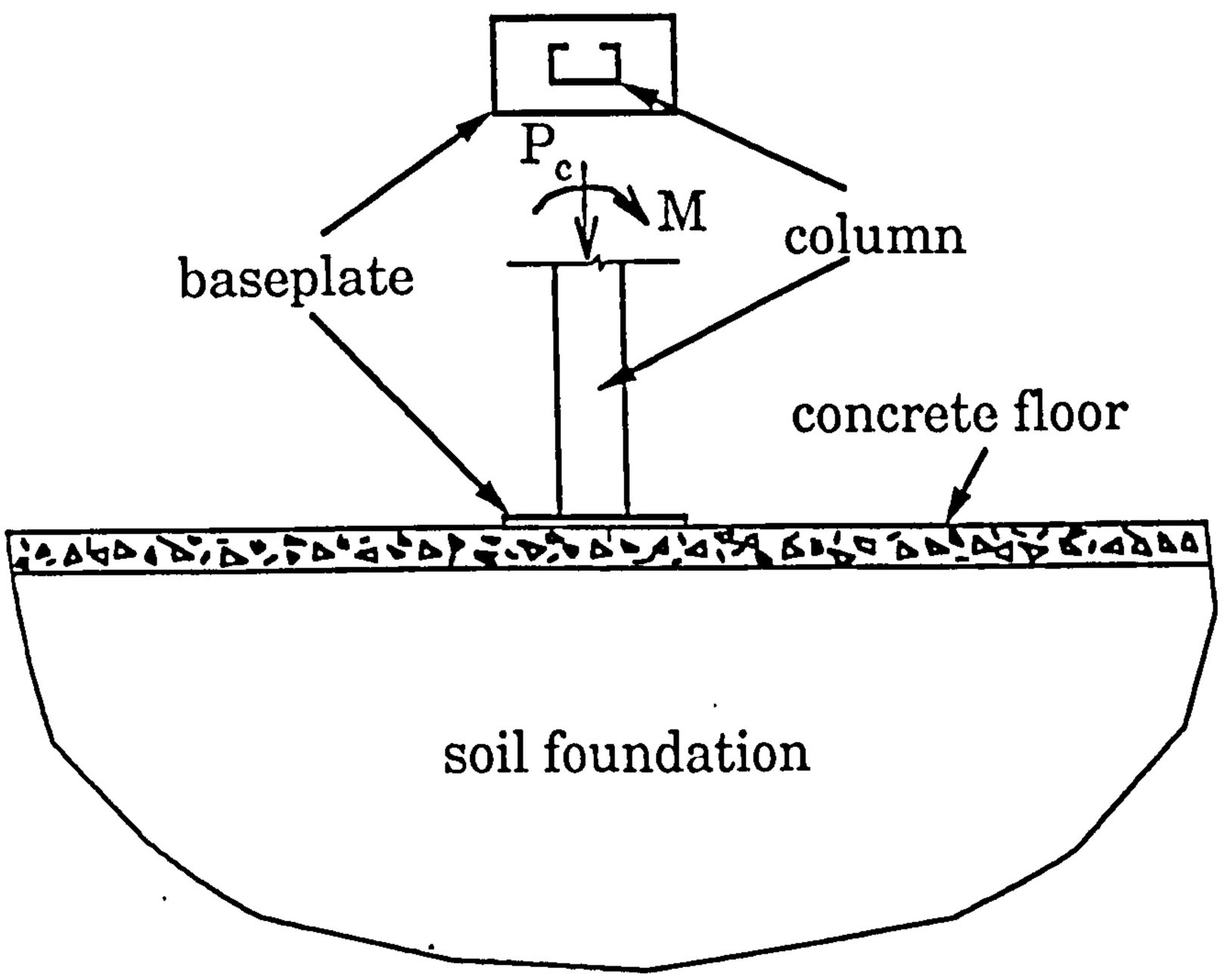

Fig 3.2 Column baseplate system

Also shown in Fig 3.3 are the sizes of the baseplate and concrete floor where L_2 and S_2 are the length and width of baseplate, and t_1 and t_2 are the thickness of baseplate and concrete floor, respectively.

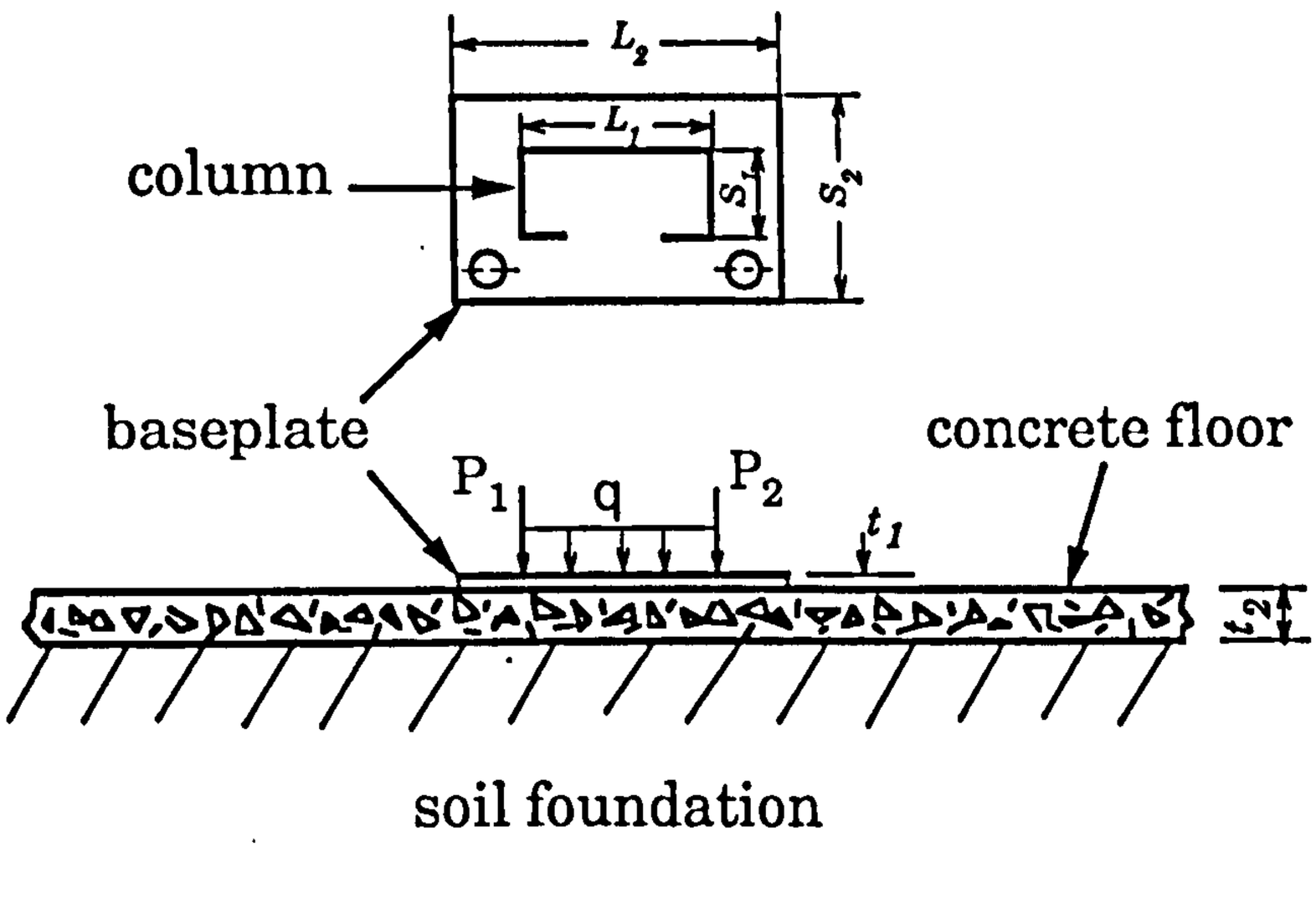

Fig 3.3 Baseplate considered and the loading condition

When subjected to external loads, some part of the baseplate shown in Fig 3.3 can be uplifted whilst the rest of the baseplate remains compressed towards the subgrade in order to retain equilibrium. As the lifted part of the baseplate is detached from subgrade, no reaction will be exerted by subgrade to that part of the baseplate. This phenomenon can be modelled using a *compression spring*, as shown in Fig 3.4, which is only able to be subjected to compression. When in tension, the spring

gives no forces to the baseplate.

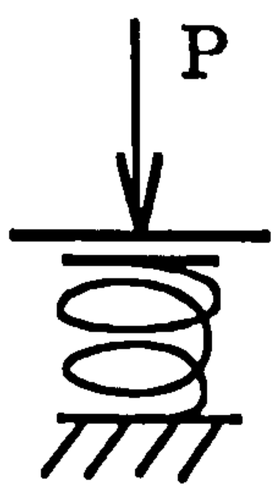

Fig 3.4 Compression spring element

Fig 3.5 is the computational model of the baseplate using compression spring elements. The stiffness of spring elements comes from the equivalent modulus of the subgrade, k_e, which is a description of the combined action of the concrete floor and soil foundation. The distance between spring elements is L_n. The choice of L_n depends on the accuracy required.

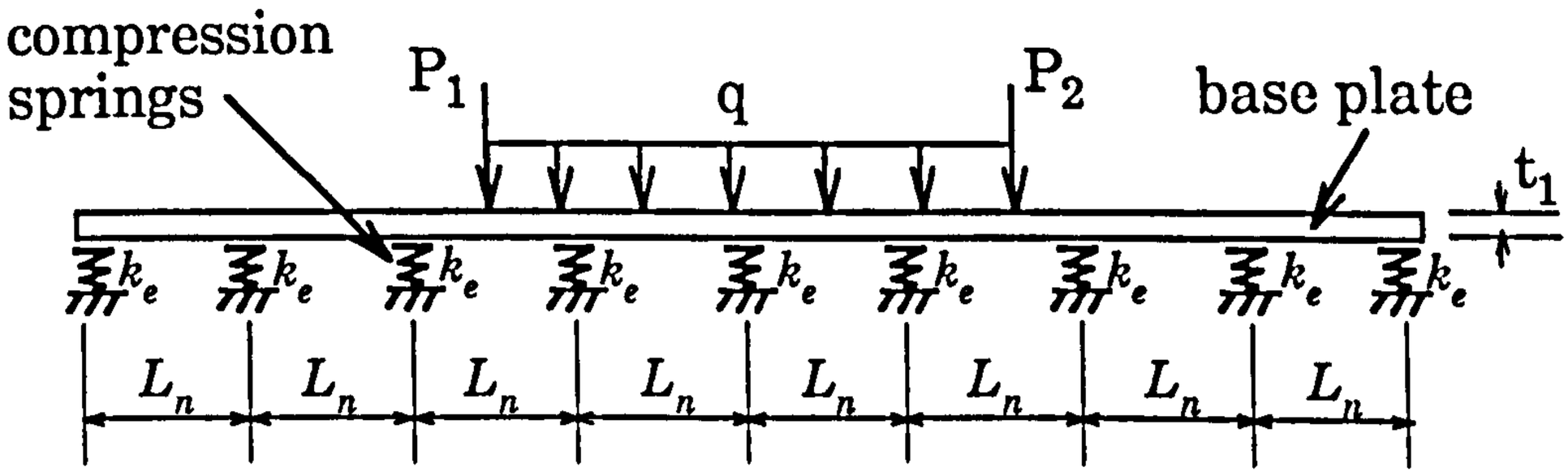

Fig 3.5 Compression spring model of baseplate

3.3.2 Determination of the equivalent modulus of subgrade reactions

In engineering practice, a concrete floor is built on a foundation such as soil foundation. When the baseplate is bolted to the concrete floor, the concrete floor and soil foundation will exert reactions directly and indirectly on the baseplate. One way to predict the behaviour and response of baseplate is to use equivalent modulus of subgrade reaction, defined as the equivalent action of the subgrade.

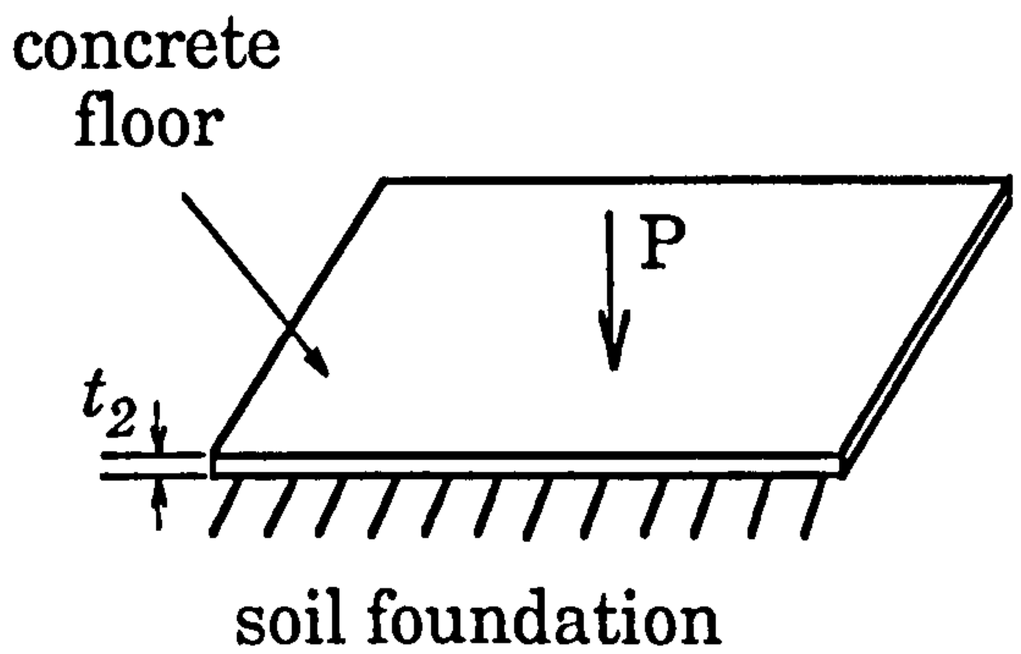

Fig 3.6 Subgrade for supporting the baseplate

Fig 3.6 shows a subgrade that supports the baseplate. It consists of a semi-infinite soil foundation and an infinite concrete floor with the

thickness t_2. The concrete floor is subjected to a concentrated load P. The equivalent modulus of subgrade reaction will be derived from this model.

The deflection at the position where the concentrated load P is applied can be found from the theory of elasticity [44], as follows:

$$w=\frac{P}{8\sqrt{k_s D}} \qquad (3.2)$$

where k_s is the modulus of subgrade reaction of the soil foundation and D is the flexural rigidity of the concrete floor.

The modulus of soil foundation depends on the conditions that form the soil. For example, it is about 0.008N/mm^3 for loose wet sand and 0.3N/mm^3 for dense sand [45]. The flexural rigidity of the concrete floor D is calculated from

$$D=\frac{E_c t_2^3}{12(1-\nu^2)} \qquad (3.3)$$

where E_c is the Young's modulus of the concrete floor, ν is the Poisson's ratio and t_2 is the thickness.

When the baseplate is subjected to a concentrated load, its reaction forces on the concrete floor can be regarded as uniform, denoted as q′. This assumption is based on the fact that the ratio of the sizes of the baseplate to those of the infinite concrete floor is very small.

The average deflection under the baseplate is obtained by substituting

P=q′A into Eq(3.2), denoted as w_0

$$w_0=\frac{q'A}{8\sqrt{k_sD}} \qquad (3.4)$$

where A is the area of the baseplate.

By definition, the modulus of subgrade reaction is the force required to produce a unit vertical deflection in a unit area on the subgrade. Therefore, the equivalent modulus of subgrade reaction k_{se} is the force required to produce a unit vertical deflection in a unit area on the concrete floor, with soil foundation underneath. Thus, k_{se} can be written, from Eq(3.4), as

$$k_{se}=\frac{q'}{w_0} \qquad (3.5a)$$

or

$$k_{se}=\frac{8}{A}\sqrt{k_sD} \qquad (3.5b)$$

Eq(3.5b) indicates that the equivalent modulus of subgrade reaction is related to the flexural rigidity of the concrete floor, the modulus of subgrade reaction of the soil foundation, and the area of the baseplate.

For a baseplate with a width of S_2, see Fig 3.3, the equivalent spring constant is given by

$$k_e=(L_nS_2)k_{se} \qquad (3.6)$$

where L_n is the distance between the two neighbouring compression springs,

shown in Fig 3.5.

Note from Fig 3.3 that the area of the baseplate is $A=L_2S_2$, substituting Eq(3.5b) into Eq(3.6) gives

$$k_e=\frac{L_n}{L_2}8\sqrt{k_sD} \qquad (3.7)$$

Assuming $n=L_2/L_n$, Eq(3.7) can be rewritten as

$$k_e=\frac{8\sqrt{k_sD}}{n} \qquad (3.8)$$

Eq(3.8) indicates that the equivalent spring stiffness of compression spring model of baseplate in Fig 3.5 is dependent on the modulus of soil foundation, the flexural rigidity of the concrete floor and the ratio of L_n/L_2.

3.3.3 Beam-column modelling of baseplate

As described in the previous section, the baseplate is modelled as a beam supported on the special compression springs and subjected to the equivalent applied column loads q, P_1 and P_2, see Fig 3.5. Alternatively, the structural analysis of Fig 3.5 can be made by an existing Frame Analysis Computer Program [46]. The compression springs in this case are regarded as compression columns having the same characteristics as the compression springs, as shown in Fig 3.7. By comparison with the compression spring model of Fig 3.5, the beam-column model of Fig 3.7

replaces compression springs using n compression columns with length of L.

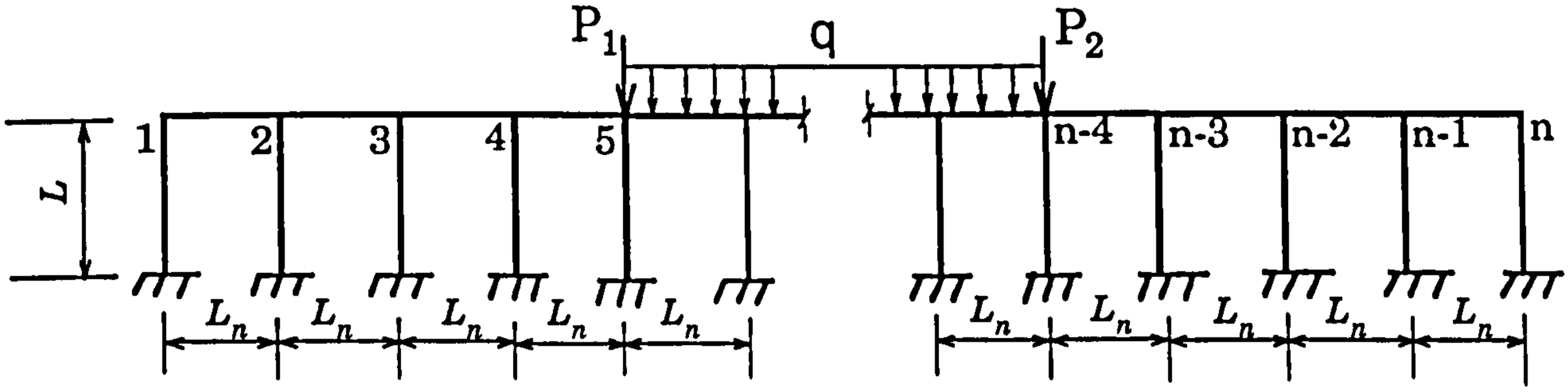

Fig 3.7 Beam-column modelling of baseplate

Let EA_i and EI_i be the axial and flexural rigidity of the i-th compression column, respectively. Since the compression spring has no flexural rigidity, nor does the compression column. This gives,

$$EI_i=0 \qquad (3.9)$$

The axial compression rigidity can be written, by definition, as

$$EA_i^c=k_{se}(L_nS_2)L \qquad (3.10a)$$

where L is the length of the compression column, k_{sc} is the equivalent modulus of subgrade reaction and given by Eq(3.5b), L_n is the distance between the two neighbouring compression columns, S_2 is the width of the

baseplate, and the superscript "c" denotes compression.

The compression column is not able to be subjected to tension. So, the axial tension rigidity is given as

$$EA_i^t=0 \qquad (3.10b)$$

with the superscript "t" denoting tension.

The beam in Fig 3.7 is the same as the beam in Fig 3.5. It is the substitution of the baseplates. Its axial and flexural rigidity can be expressed as

$$EA_B=E_s(S_2t_1) \qquad (3.11)$$

and

$$EJ_B=E_s(\frac{S_2t_1^3}{12}) \qquad (3.12)$$

where E_s is the Young's modulus of the baseplate, S_2 is the width, and t_1 is the thickness of the baseplate.

Thus, the baseplate of Fig 3.2, supported on subgrade and subjected to an axial load P_c and a bending moment on column M, can be analyzed according to its equivalent beam-column model of Fig 3.7, subjected to the equivalent loading conditions of a uniformly distributed load q and two concentrated loads P_1 and P_2. This procedure can be developed into a computer program and solved numerically. This will give the moment-rotation relationship of the baseplate. The rotation is defined as

$$\theta=\frac{\Delta_c}{L_1} \qquad (3.13)$$

where Δ_c indicates the difference of the deflections across the column cross-section and L_1 is the length of column cross section. For example, $\Delta_c=|\Delta_{n-4} - \Delta_5|$ indicates the difference of deflection between the node (n-4) and the node 5 in Fig 3.7. The rotation defined in Eq(3.13) actually denotes the average rotation across the column cross-section.

The rotational stiffness of the baseplate is thus defined as

$$k_b=\frac{M}{\theta} \qquad (3.14)$$

which is the secant stiffness of the moment-rotation curve, as shown in the line *OB* in Fig 3.8.

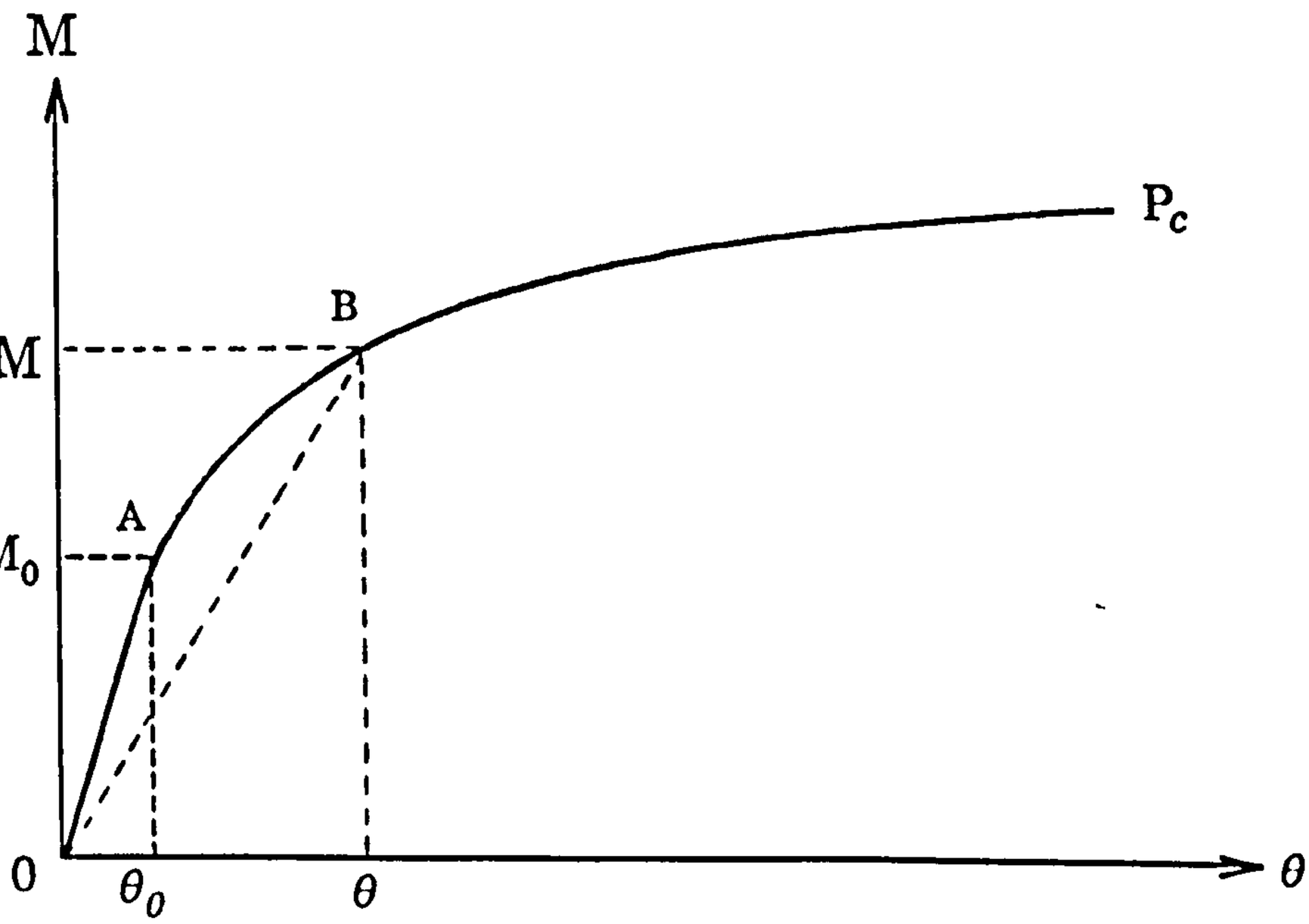

Fig 3.8 The moment-rotation curve of a baseplate

The moment-rotation curve in Fig 3.8 corresponds to a given axial load P_c. The curve consists of two regions, one is linear when the bending moment is below a critical moment M_0 and the other is nonlinear when the bending moment goes beyond M_0.

Note that the stiffness matrix in the analysis of the frame structure in Fig 3.7 has to be modified if any of the compression columns are in tension because there is no axial tension in the columns. The modification is made automatically by the computer program [46].

3.4 Initial rotational stiffness of baseplate

As indicated in Fig 3.8, the initial region of the moment-rotation curve of a baseplate, corresponding to a given axial load P_c, is linear when the bending moment is below the critical moment M_0. It implies that the rotational stiffness of the baseplate within the region is linear and thus independent of bending moment. This rotational stiffness is defined as initial rotational stiffness of the baseplate. Normally, any point at the moment-rotation curve can be determined by the procedures described in the previous section and then the corresponding rotational stiffness is obtained by Eq(3.14). The initial rotational stiffness can also be determined in this way. Alternatively, it can be derived analytically using a superimposition approach, according to the implication of the critical moment M_0, which is more helpful in practice and described in this section.

3.4.1 Application of superimposition approach

Assume that the baseplate is placed on the subgrade and not fixed by bolts or other means, as shown in Fig 3.9, where the column is welded to the baseplate and thus applies an axial force P_c and a bending moment M to the baseplate. Under the action of the axial load, the baseplate deflects towards the direction that compresses the subgrade. The addition of the bending moment will not change this trend if the moment is small enough. However, the increase of the bending moment will finally reach such a stage that one end of the baseplate will uplift whilst the other is still in compression. The moment at this state is the critical moment M_0. The rotational stiffness is defined as the initial rotational stiffness when the applied bending moment is below the critical moment M_0.

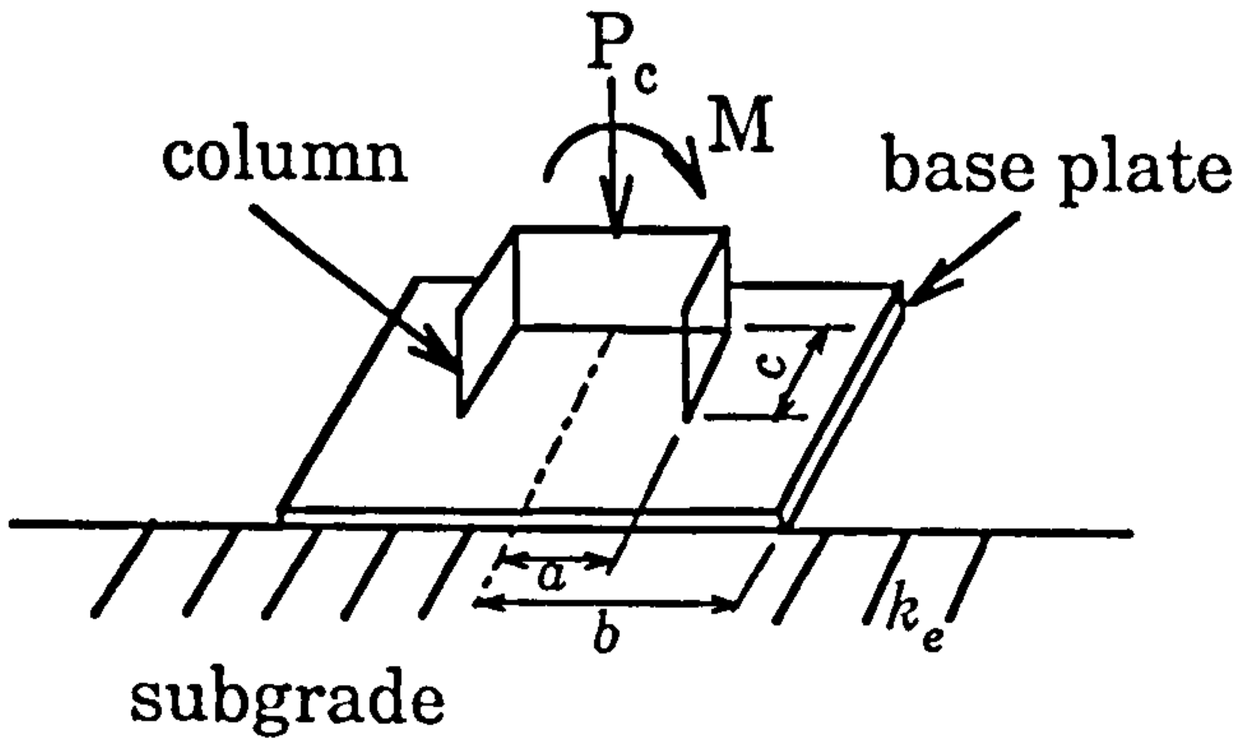

Fig 3.9 Baseplate subjected to an axial force and a bending moment

In order to determine the initial rotational stiffness of the baseplate in an efficient and convenient way, the action of the column and subgrade on the baseplate will be simplified. As demonstrated in Section 3.3, the axial force of the column is modelled by using a uniformly distributed force and two concentrated forces, and the bending moment of the column is equivalently replaced by a pair of antisymmetrical concentrated loads. They are again shown in Fig 3.10 and Fig 3.11, respectively. The dimensions *a and b* represent the half width of column and baseplate. P and q in Fig 3.10 are equivalent to the axial load P_c, whilst P_m in Fig 3.11 is equivalent to the applied bending moment M in the way shown in Eq(3.1). Then, the baseplate is modelled as a uniform beam resting on a elastic foundation with constant elastic stiffness k_{se} (taken as k during derivation for simplicity). The superimposition of Fig 3.10 and Fig 3.11 produces Fig 3.12 which is used to model the behaviour of the baseplate in Fig 3.9. The statically equivalent relations between Fig 3.10, Fig 3.11 and Fig 3.12 are

$$P_1 = P - P_m \ , \qquad P_2 = P + P_m \tag{3.15}$$

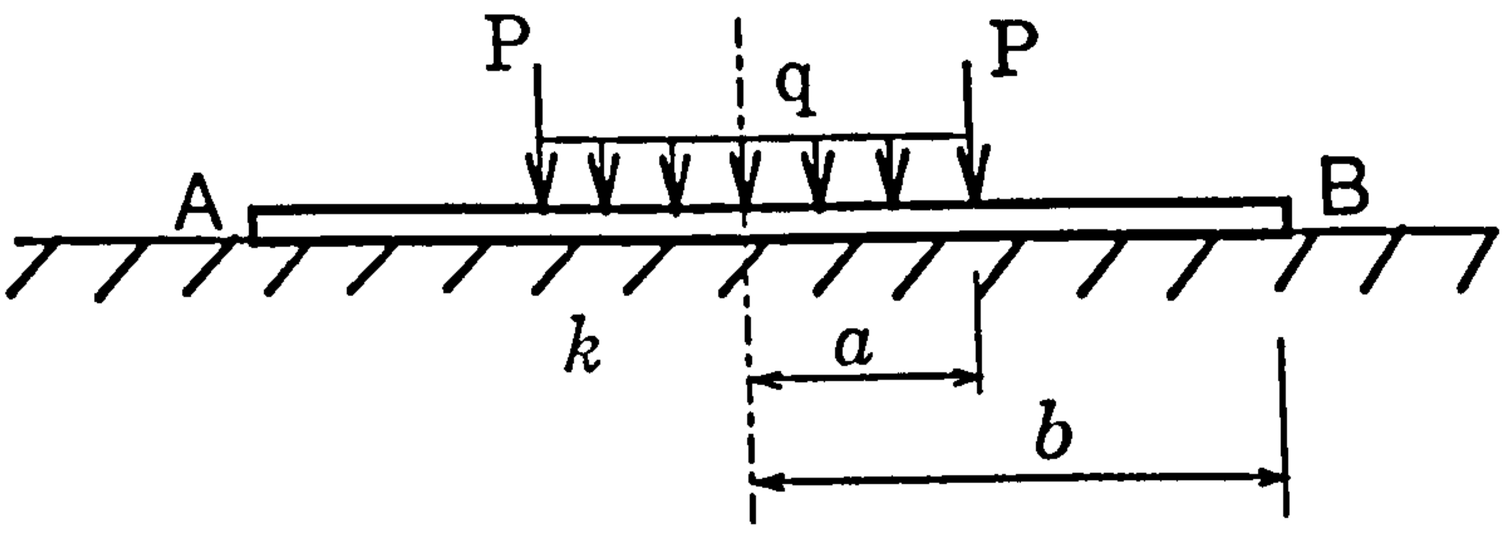

Fig 3.10 Beam on an elastic foundation subjected to concentrated and uniformly distributed loads

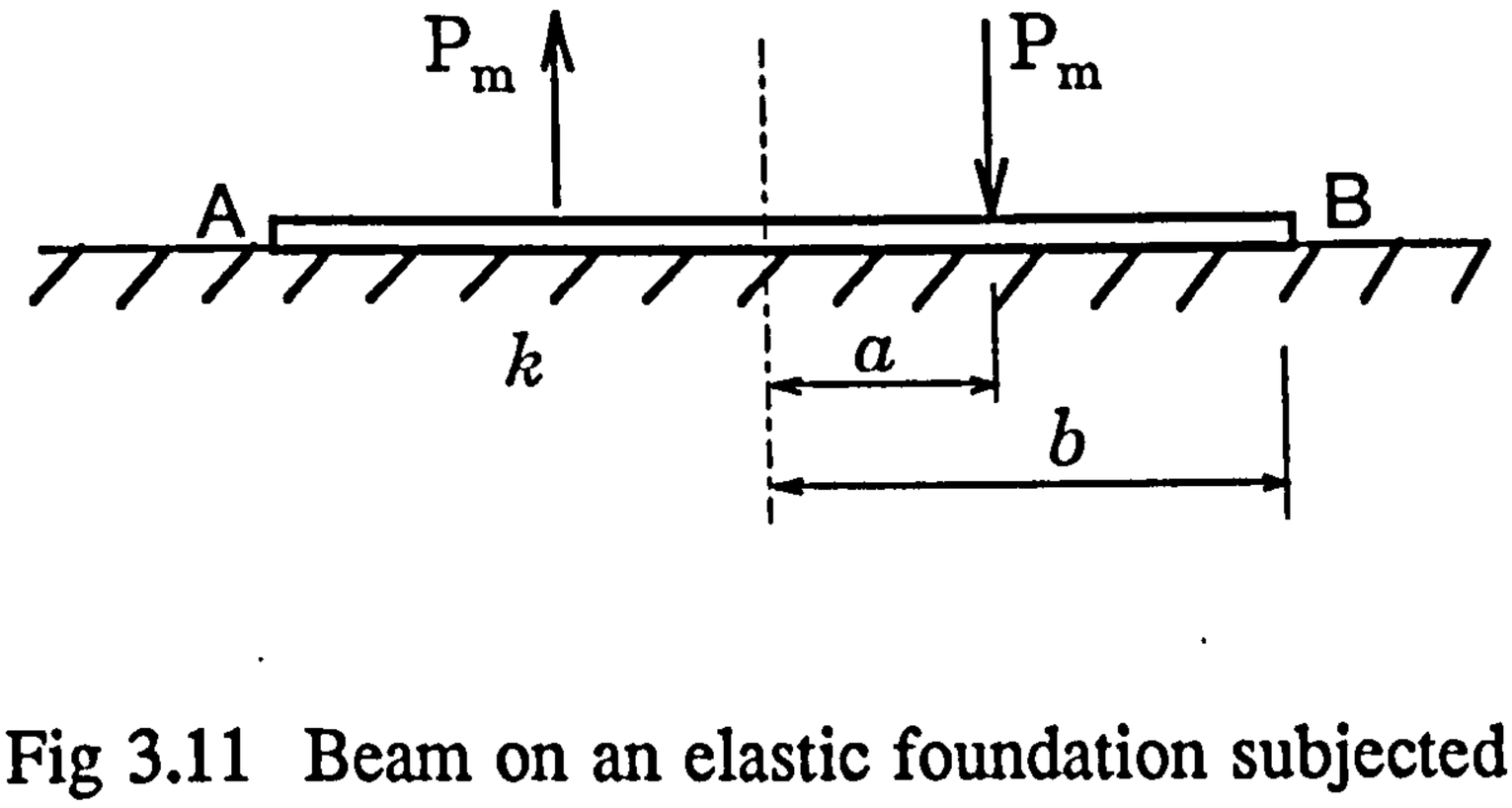

Fig 3.11 Beam on an elastic foundation subjected to a pair of antisymmetrical concentrated loads

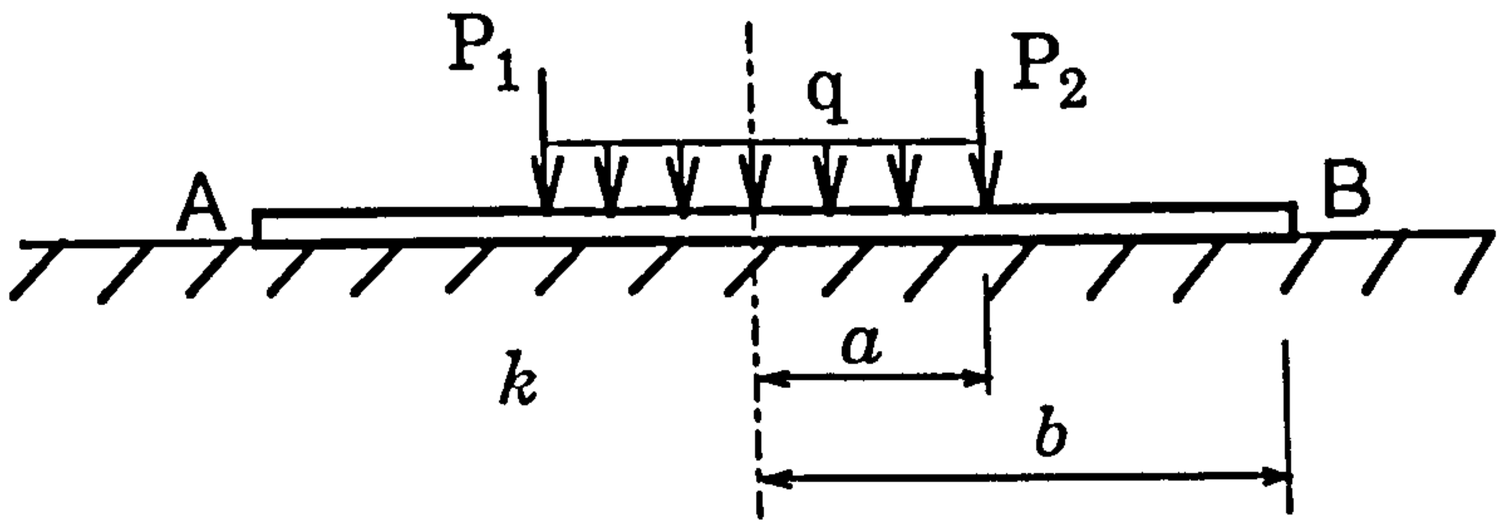

Fig 3.12 Beam on an elastic foundation subjected to concentrated and uniformly distributed loads

3.4.2 Determination of the initial rotational stiffness and the critical bending moment

As indicated, the superimposition of Fig 3.10 and Fig 3.11 models the original problem of Fig 3.9 that is subjected to the axial load P_c and the

bending moment M, or Fig 3.12 that is equivalent to Fig 3.9.

The deformation and internal forces of the problems in Fig 3.10 and Fig 3.11 are easily found if small deformation theory applies. The superimposition of both solutions gives that of the original problem in Fig 3.9.

Fig 3.10 is a symmetric beam subjected to a symmetric load. So, the rotation at the centre of the beam is zero. This implies that the rotation of the baseplate in Fig 3.9 is the same as that at the centre of the beam in Fig 3.11

$$\theta_1 = w_1^{(l)}|_{x=0} = \alpha(A_1 + B_1 - C_1 + D_1) \qquad (3.16)$$

where w_1 is the deflection of Fig 3.11 and given by Eq(3A.49) in Appendix A3.2. A_1, B_1, C_1 and D_1 are given by Eq(3A.51).

Alternatively, the rotation of the baseplate in Fig 3.9 can be measured using the differences of deflections which is similar to Eq(3.13). Due to the symmetry of Fig 3.10, its rotation is zero. Then, the rotation of Fig 3.12 is determined only by Fig 3.11 as

$$\theta_2 = \frac{\Delta_a^{(b)}}{a} = M.R_{11} \qquad (3.17)$$

where $\Delta_a^{(b)}$ is the deflection of the column edge in Fig 3.11, relative to the centre point of the baseplate, and is given by Eq(3A.52), R_{11} is given by Eq(3A.51) in Appendix A3.2.

The initial rotational stiffness of the baseplate therefore is defined in the similar way as that in Eq(3.14)

$$k_b^{\,1}=\frac{M}{\theta_1}=\frac{M}{\alpha(A_1+B_1-C_1+D_1)} \tag{3.18}$$

or

$$k_b^{\,2}=\frac{M}{\theta_2}=\frac{1}{R_{11}} \tag{3.19}$$

where $k_b^{\,1}$ is the rotational stiffness of the baseplate defined from the rotation of the baseplate centre, $k_b^{\,2}$ is defined from the difference of the deflections of the baseplate. However, $k_b^{\,2}$ is more appropriate to represent the rotational stiffness of the baseplate since it represents the average rotation across the column cross-section.

Bearing in mind that these results are based on the condition that the bending moment M is less then the critical moment M_0 when the whole elastic foundation is in compression. This implies that the combined deflection of Fig 3.10 and Fig 3.11 should not make any part of the baseplate uplift from the subgrade. Therefore, the downwards deflection at point *B* in Fig 3.10 should be equal to the upwards deflection at point B in Fig 3.11 when M is equal to M_0, that is:

$$w_2^{(a)}|_{x=b}=w_2^{(b)}|_{x=b} \tag{3.20}$$

where $w_2^{(a)}$ is the deflection of Fig 3.10, given by Eq(3A.35), and $w_2^{(b)}$ the deflection of Fig 3.11, given by Eq(3A.55) in Appendix 3.1 and 3.2, respectively.

Substituting Eq(3A.35) and Eq(3A.53) into Eq(3.18) produces

$$R_a = M.R_b$$

This bending moment is defined as critical bending moment, M_0, as

$$M_0 = \frac{R_a}{R_b} \qquad (3.21)$$

where R_a and R_b are the constants defined by Eq(3A.35) and Eq(3A.53), respectively.

A computer program BASEMK has been developed to carry out the calculation of the initial rotational stiffness and the critical bending moment [55].

3.5 Numerical illustration and conclusions

3.5.1 Examples

To illustrate the effectiveness of the analysis under consideration, a baseplate with different combinations of bending moments and axial loads, supported on a subgrade, is considered. They are shown in Fig 3.3 and Fig 3.5. The analysis was made using Frame Analysis Computer Program [46]. The numbering of the nodes for calculation is shown in Fig 3.7.

A typical baseplate manufactured by Dexion [58] has been used for the illustration. The modulus of elasticity for the baseplate is E_s=2.1x10^5 N/mm^2. The dimensions for the baseplate are L_2=200 mm, S_2=100 mm, t_1=4.5 mm, and those for the subgrade are k_s=0.1108 N/mm^3, E_c=2.0x10^4 N/mm^2, t_2=200mm, υ=0.167. The compression columns have a length of L=10 mm and a uniform interval between supports L_n=12.5 mm. The number of the compression columns is n=17 (see Fig 3.3 and Fig 3.7).

The axial compression rigidity of the compression columns, the axial and flexural rigidity of the beam in Fig 3.7 are obtained, from Eq(3.10a), Eq(3.11), and Eq(3.12), respectively, as follows

$$EA_i^c = 1.949 \times 10^5 \ N$$

$$EA_B = 9.450 \times 10^7 \ N$$

$$EJ_B = 1.600 \times 10^8 \ Nmm^2$$

The five load cases are considered as follows.

Case 1: The applied column loads are P=2.5x10^4 N, M=2.4x10^5 Nmm, and M/P=9.6 mm, which gives, from Eq(3.1)

$$q=125 \text{ N/mm}, \quad P_1=3.85\text{x}10^3 \text{ N}, \quad P_2=8.65\text{x}10^3 \text{ N}$$

Using the procedure in Section 3.3.3, the rotation of the baseplate can be obtained from Eq(3.13) where the deflections at node 5 and node 13 (n-4=17-4) in Fig 3.7 are taken to calculate Δ_c,

$$\theta=\frac{-0.089629+0.155039}{12.5\times 8}$$

$$=6.541\times10^{-4}\ rad$$

Then, the rotational stiffness of the baseplate is given by Eq(3.14)

$$k_b=\frac{M}{\theta}$$

$$=\frac{240000}{0.0006541}$$

$$=3.6691\times10^{5}\ kN.mm/rad$$

Case 2: Examine the case when the axial load increases from P=2.5x10^4 N in Case 1 to P=5.0x10^4 N. The other conditions remain unchanged. Here M/P=4.8 mm. The rotational stiffness in this case becomes

$$k_b=\frac{M}{\theta}=3.6692\times10^{5}\ kN.mm/rad$$

Case 3: The column loads are P=2.5x10^4 N and M=1.0x10^6 Nmm. Here M/P=40 mm. In this case, the calculated rotational stiffness of baseplate is k_b=1.1059x10^5 kNmm/rad.

Case 4: The column loads are P=5.0x10^4 N and M=1.0x10^6 Nmm. Here M/P=20 mm. The calculation gives k_b=3.6696x10^5 kN.mm/rad.

For comparison, the calculated results of the rotational stiffness of baseplate for the four load cases are listed in Table 3.1.

Table 3.1 The calculated rotational stiffness k_b

Load case	P (N)	M/P (mm)	k_b (kN.mm/rad)
1	25000	9.6	3.6691×10^5
2	50000	4.8	3.6692×10^5
3	25000	40	1.1059×10^5
4	50000	20	3.6696×10^5

It can be seen from Table 3.1 that the difference between the rotational stiffness in Case 1 and Case 2 are less significant. However, as shown in Case 3, the rotation stiffness decreases sharply, as the ratio of the bending moment to the axial force gets up to 40 mm. It is concluded that the ratio of the bending moment to the axial force has a dominant effect on the rotational stiffness of the baseplate. On the other hand, Case 2 and Case 4 shows that the rotational stiffness is constant below the ratio of M/P=20 mm. It is therefore deduced that a critical value of the ratio of M/P exists below which the rotational stiffness remains constant.

The implication of the ratio of the bending moment to the axial force indicates that the greater the ratio is, the greater the eccentricity of the loading system on the baseplate will be, thus resulting in decreasing the rotational stiffness of the baseplate.

Experimental studies conducted by Aston University in 1981 showed that the applied axial load has a marked effect on the rotational stiffness [32]. The conclusions of the theoretical investigation in this thesis agree with these experimental results.

The deflections and reaction forces on the baseplates for different load cases are shown in Fig 3.13 to Fig 3.16, respectively, where the horizontal axis represents the baseplate with the origin on the left end of the baseplate. Fig 3.13 shows the calculated deflection of baseplate for Load Case 4, where the contour of deformation of the baseplate and the rotation of the baseplate can be observed. Fig 3.14 shows the deflection of the baseplate for Load Case 3 and Load Case 4 for the comparison of the effects of the ratio of the bending moment to the axial load on the deformation of the baseplate. For the larger ratio of the bending moment to the axial load, Load Case 3 for example, the rotation deformation of the baseplate occurs more easily, thus the rotational stiffness decreases.

The deflections of the baseplate under four load cases are plotted in Fig 3.15, whilst the reaction force distributions are plotted in Fig 3.16. Looking at Table 3.1, the smallest rotational stiffness among the four calculated load cases is Load Case 3, where its rotational stiffness is about one third of the others. The other three load cases have very close rotational stiffness. These can be observed in Fig 3.16 where the baseplate under Load Case 3 rotates easily due to its small rotation-resistance. Its left hand side has been uplifted so the reaction force acting on it by the subgrade is zero, as shown in Fig 3.16.

Case 5: Now, the effects of the subgrade are examined. Increase the modulus of subgrade reaction from k_s=0.1108 N/mm^3 in Case 1 to k_s=2.216x10^{-1} N/mm^3, so the EA_i^c=2.756 x 10^5 N. The other parameters are the same as those in Case 1.

The rotational stiffness of the baseplate in this case becomes k_b=4.82x10^5 kN.mm/rad. The calculated deflection and reaction force distribution of the baseplate are given in Fig 3.17 and Fig 3.18, respectively. From the calculated deflections in Fig 3.17, it can be seen that small modulus of subgrade reaction caused large deflection and large rotation. This implies that small modulus of subgrade reaction has a small rotation resistance, thus small rotational stiffness.

Comparing the rotation stiffness k_b between the load case 1 where k_b=3.67x10^5 kN.mm/rad and the load case 5 where k_b=4.82x10^5 kN.mm/rad, it can be concluded that the modulus of subgrade reaction is one of the dominant factors of rotational stiffness of baseplate and increasing the modulus of subgrade reaction increases the rotational stiffness of baseplate.

In summary, the theoretical numerical studies have demonstrated that the ratio of the bending moment to the axial load is one of the main factors that determine the rotational stiffness of the baseplate. Increasing the ratio of the bending moment to the axial load will decrease the overturning resistance ability, thus decreasing the rotational stiffness of the baseplate. It has also been found that the modulus of subgrade reaction of foundation is another dominant factor in the rotational stiffness of the baseplate. The greater the modulus of subgrade reaction of foundation is, the greater the rotational stiffness of the baseplate.

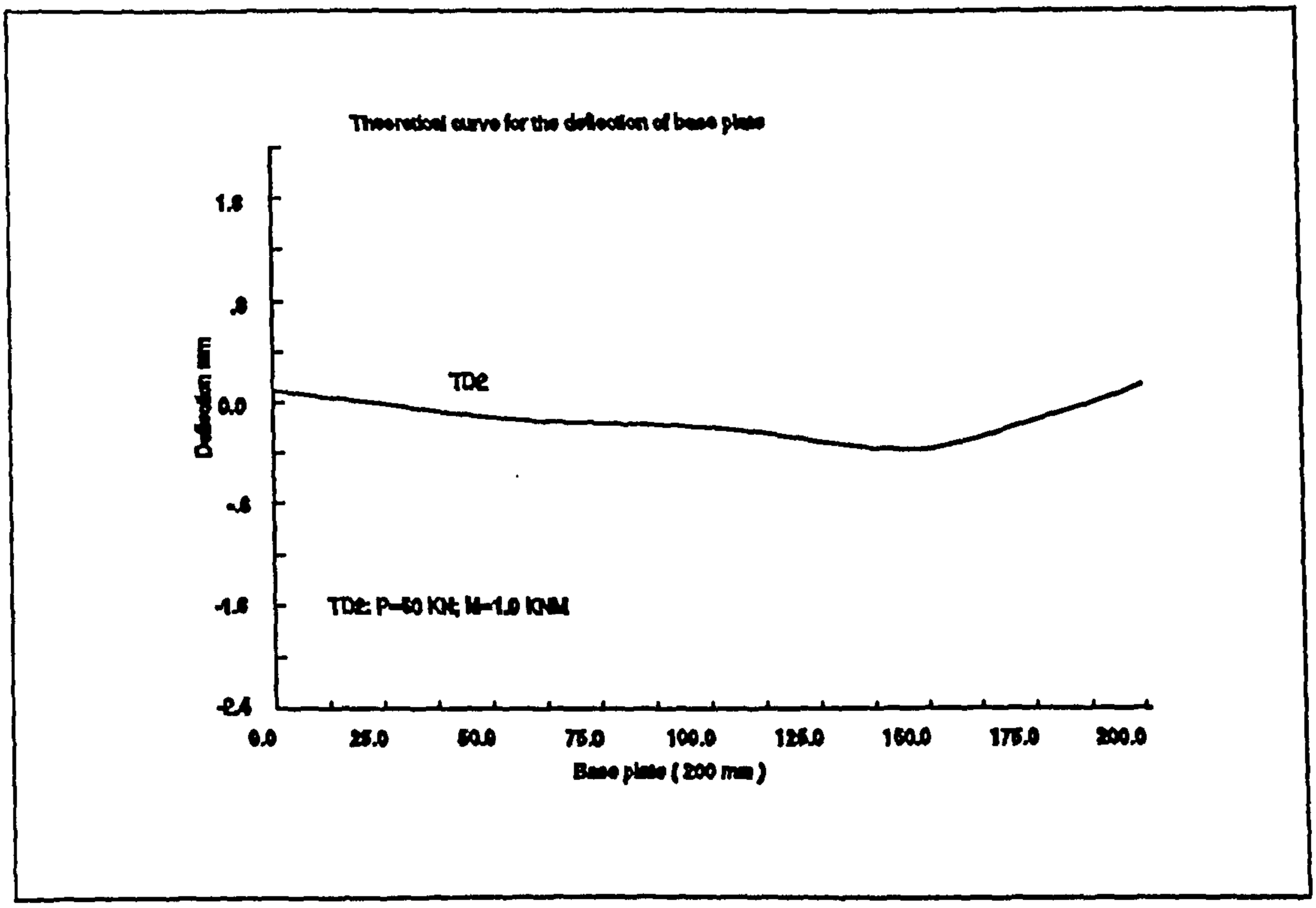

Fig 3.13 Deflection of the baseplate under Load Case 4

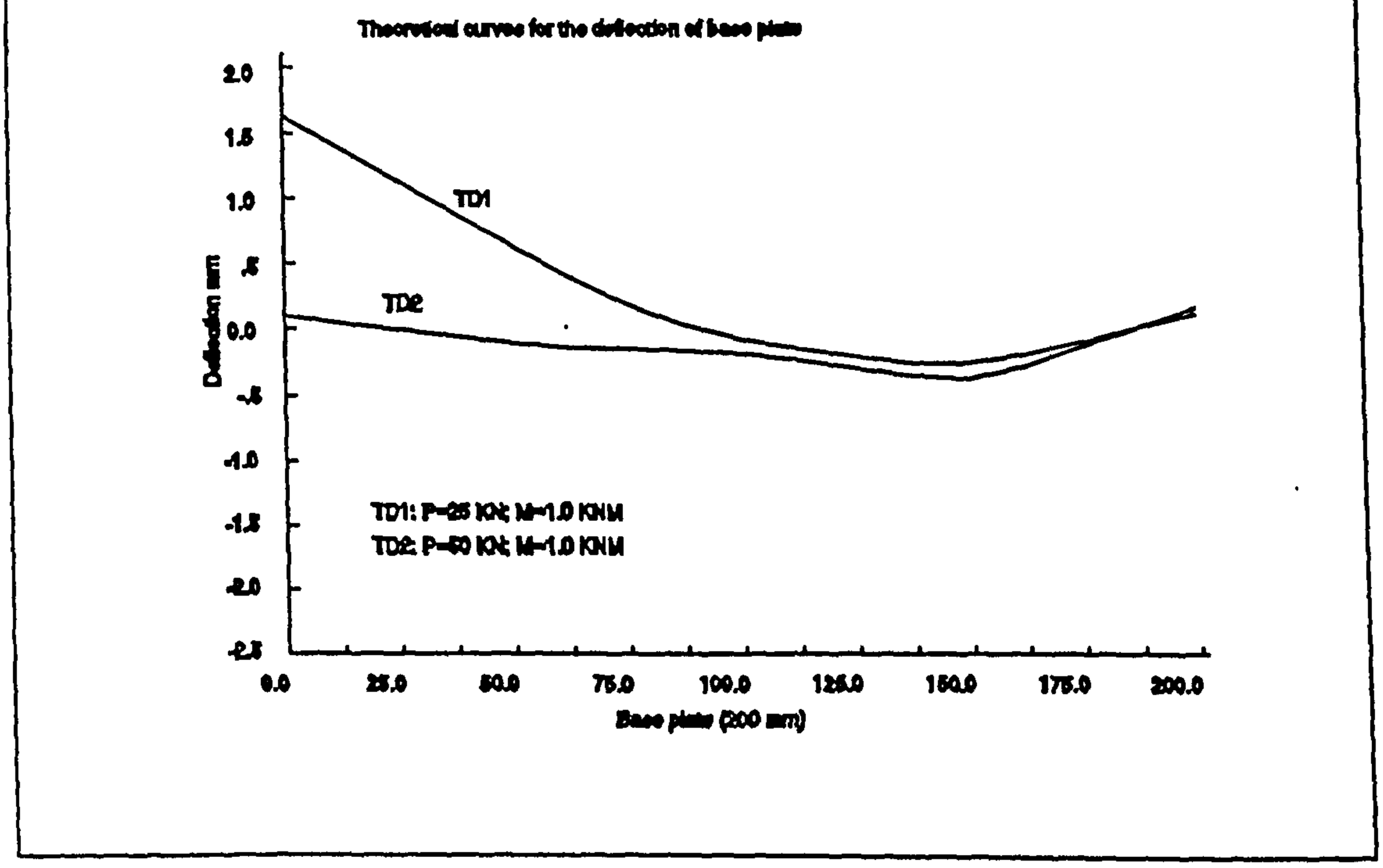

Fig 3.14 Deflection of the baseplate under Load Case 3
and Load Case 4

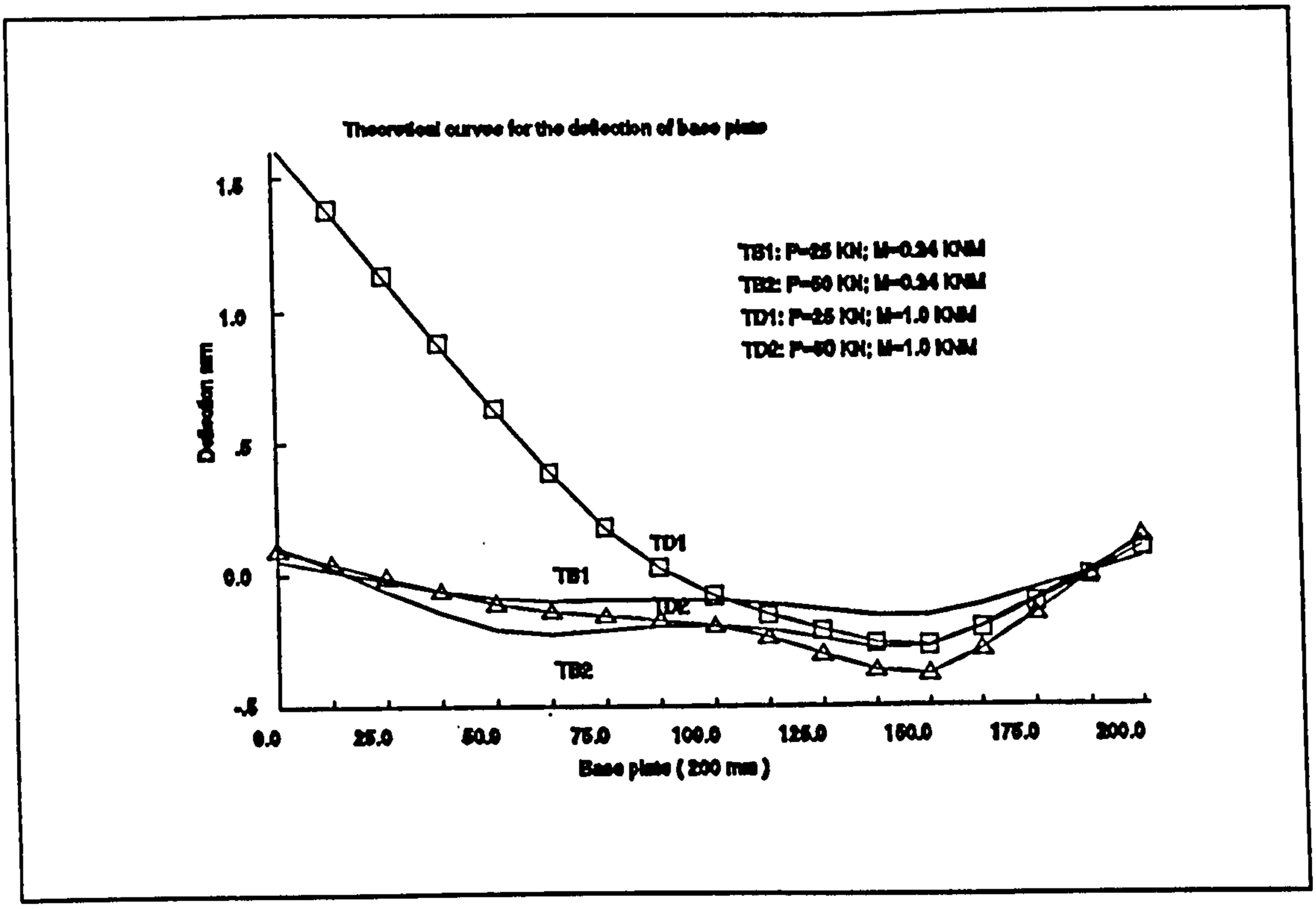

Fig 3.15 Deflection of the baseplate under four Load Cases

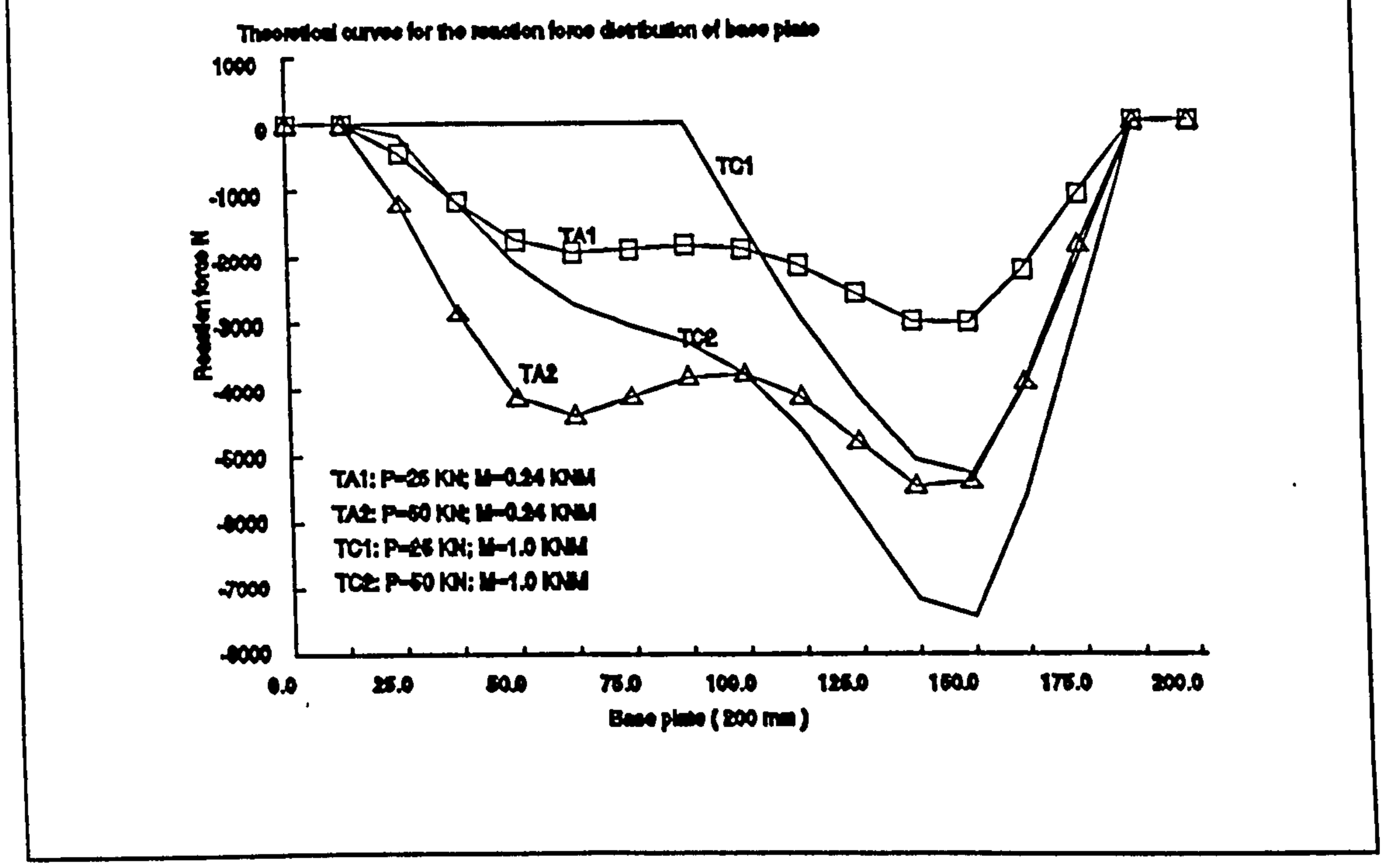

Fig 3.16 Reaction force distribution of baseplate for four Load Cases

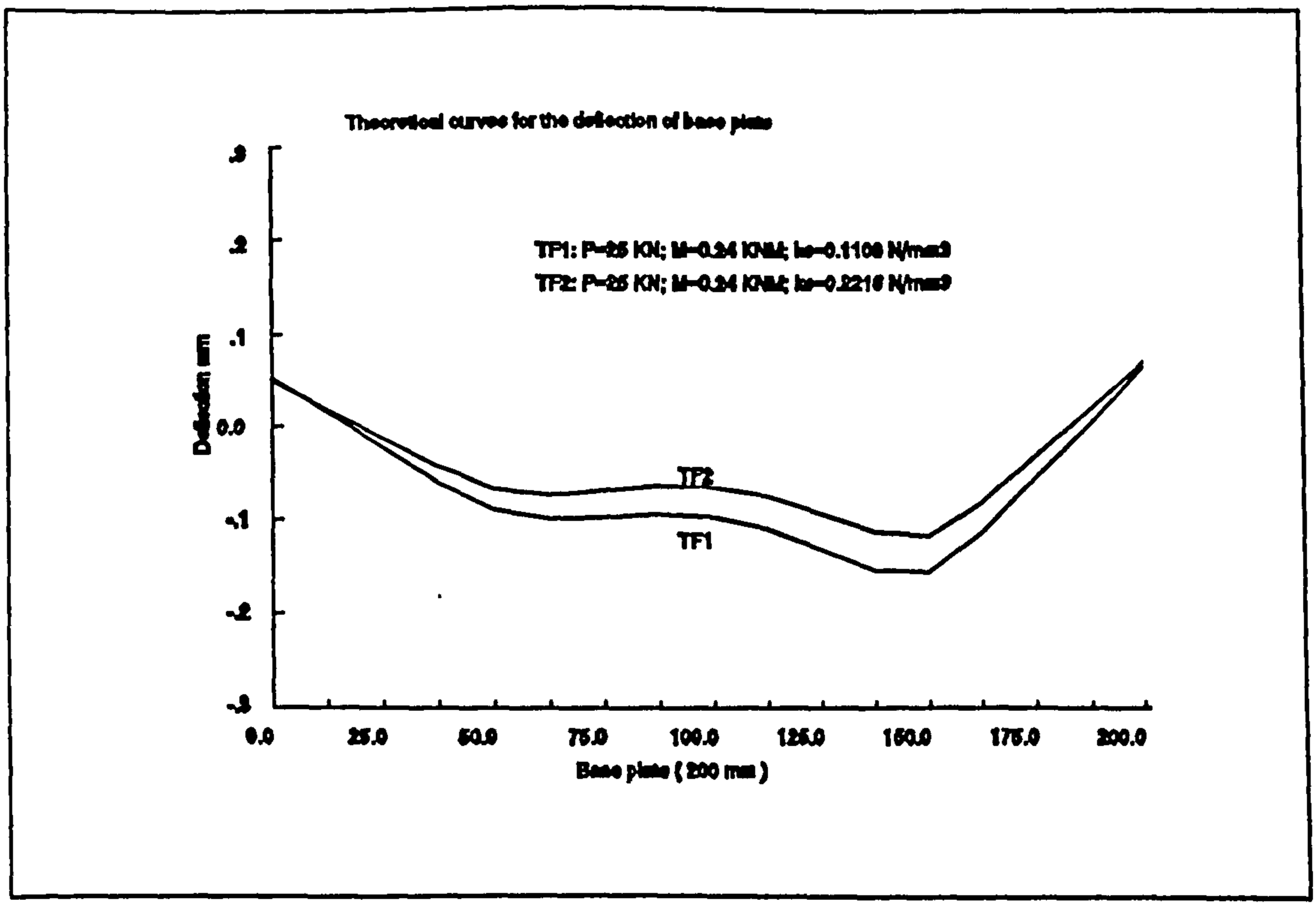

Fig 3.17 Deflection of baseplate under Load Case 5 with different subgrade

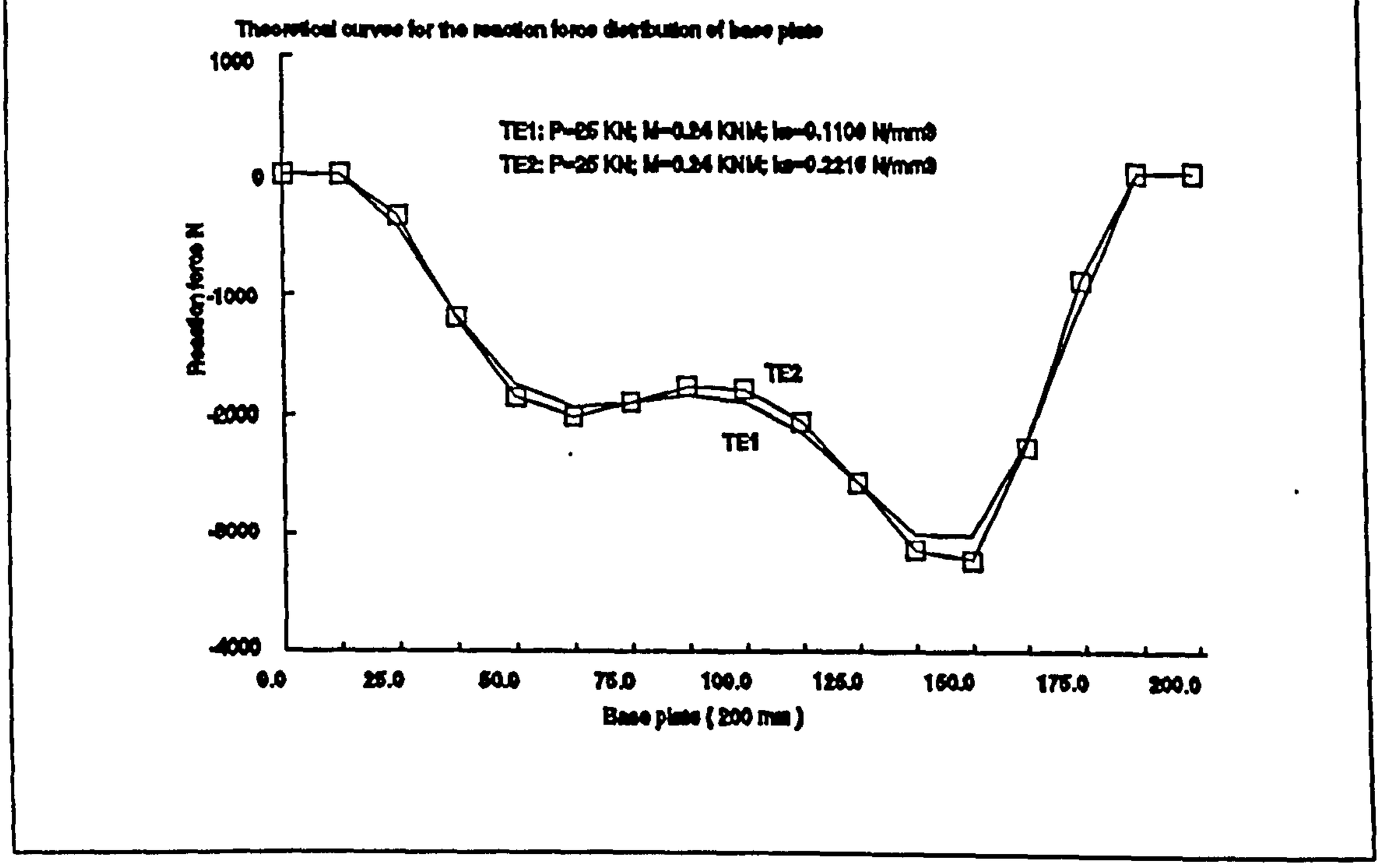

Fig 3.18 Reaction force distribution of baseplate for Load Case 5 with different subgrade

3.5.2 Conclusions

Baseplates in slender structures such as pallet racking systems, when unbolted or partially bolted or even completely bolted, usually have semi-rigid characteristics due to the interaction between baseplate and elastic subgrade. These phenomena are well known but the quantities of these semi-rigid characteristics are not available. In design, the rotational stiffness of baseplate has been determined empirically.

Theoretical investigations into the semi-rigid properties of baseplates have been carried out in this chapter. A simplified method has been presented to calculate the equivalent modulus of subgrade reaction and the moment-rotation relationship of baseplate, from which the rotational stiffness of the baseplate can be determined. The method takes into account the interaction between the baseplate, the subgrade which consists of concrete floor and soil foundation, and the applied column axial force and bending moment. This procedure can be implemented by a linear plane frame analysis computer program.

The theoretical studies demonstrated that the rotational stiffness of baseplate is determined by many factors. They include the geometry and material of baseplate, the modulus of subgrade reaction of baseplate and the applied axial loads. There exists a critical bending moment M_0, below which the rotational stiffness of baseplate is kept constant. When the bending moment M goes beyond the critical bending moment M_0, the rotational stiffness of the baseplate becomes nonlinear and dependent on the applied loads. The moment-rotation of baseplate was found by an iterative procedure. The secant stiffness of the moment-rotation curve is used to

represent the rotational stiffness of baseplate. The critical value M_0 can be determined by the geometry and material behaviour of the baseplate, the axial load and the modulus of subgrade reaction of the baseplate. By the implication of the critical bending moment, it has been formulated to give an efficient way to determine the critical bending moment.

It was demonstrated that the rotational stiffness of baseplate also depends on the dimensions and materials of baseplate and subgrade. Increasing the modulus of subgrade reactions will increase the rotational stiffness and increasing the thickness and Young's modulus of baseplate can also increase its rotational stiffness.

The theoretical model in this chapter has provided an efficient and practical way to deal with the rotational stiffness of baseplate. The predicted results are reasonable and the conclusions obtained are helpful in the understanding of the semi-rigid behaviour of baseplate.

CHAPTER 4: EXPERIMENTAL INVESTIGATION ON ROTATIONAL STIFFNESS OF SEMI-RIGID BASEPLATES

4.1 General outline

Experiments were conducted to investigate the behaviour of a non-rigid flat baseplate. A total of six specimens were tested. The variables used in the tests included axial load, bending moment and modulus of subgrade reaction. The tests were devoted to investigating the effects of applied axial loads, bending moments and the modulus of subgrade reaction on the rotational stiffness of the baseplate. The objectives of the tests were to confirm the effectiveness and reliability of the theoretical model and the methods proposed in Chapter 3 for predicting the rotational stiffness of baseplate.

A panel test rig was designed to achieve the above objectives. The test rig was able to apply both axial load and bending moment to a baseplate which was supported on a subgrade. The linear voltage displacement transducers were used to measure the deflections of the column, from which the rotations of the baseplate were obtained.

The Young's modulus of elasticity for the concrete and timber materials tested were determined by the compression tests of the materials. They were then used in the calculation of the rotational stiffness of

baseplate in Chapter 3.

The effects of the applied axial loads on the rotational stiffness of baseplate were tested where axial loads of 20kN, 40kN and 80kN were used. The effects of the ratio of the applied axial load to the bending moment were also investigated.

The significance of the modulus of subgrade reaction were demonstrated and were first studied by the present research. Two different materials of subgrade, concrete and timber, were tested. The corresponding moment-rotation curves were obtained.

The test rig specifically designed for the present research proved to be very successful in the investigation of the rotational stiffness of baseplate. The test results were reasonable to explain the theoretical model of the rotational stiffness of baseplate in the previous chapter.

4.2 Test configuration and design consideration

A panel test rig which could apply both axial load and bending moment to a baseplate supported on a subgrade was required. It was designed as shown in Fig 4.1 with a typical test panel located in it. The test rig consisted of a 230kN (23 tonne) servo-controlled hydraulic jack and a 100kN (10 tonne) hand-controlled hydraulic jack located in a reaction frame. The test panel was located between pinned spherical bearings at either end of the rig.

A	TEE.	J	LOAD CELL. (20^{TON})
B	H-JACK. RC-2510.	K	STEEL PLATE.
C	STEEL PLATE.	L	STEEL PLATE.
D	STEEL BALL.	M	STEEL BALL.
E	STEEL PLATE.	N	STEEL PLATE.
F	BASE PLATE.	P	LOAD CELL. (2^{TON})
G	COLUMN.	Q	STEEL PLATE.
H	CONCRETE BLOCK.	R	H-JACK. RC-1010.
I	STEEL PLATE.	S	COLUMN.

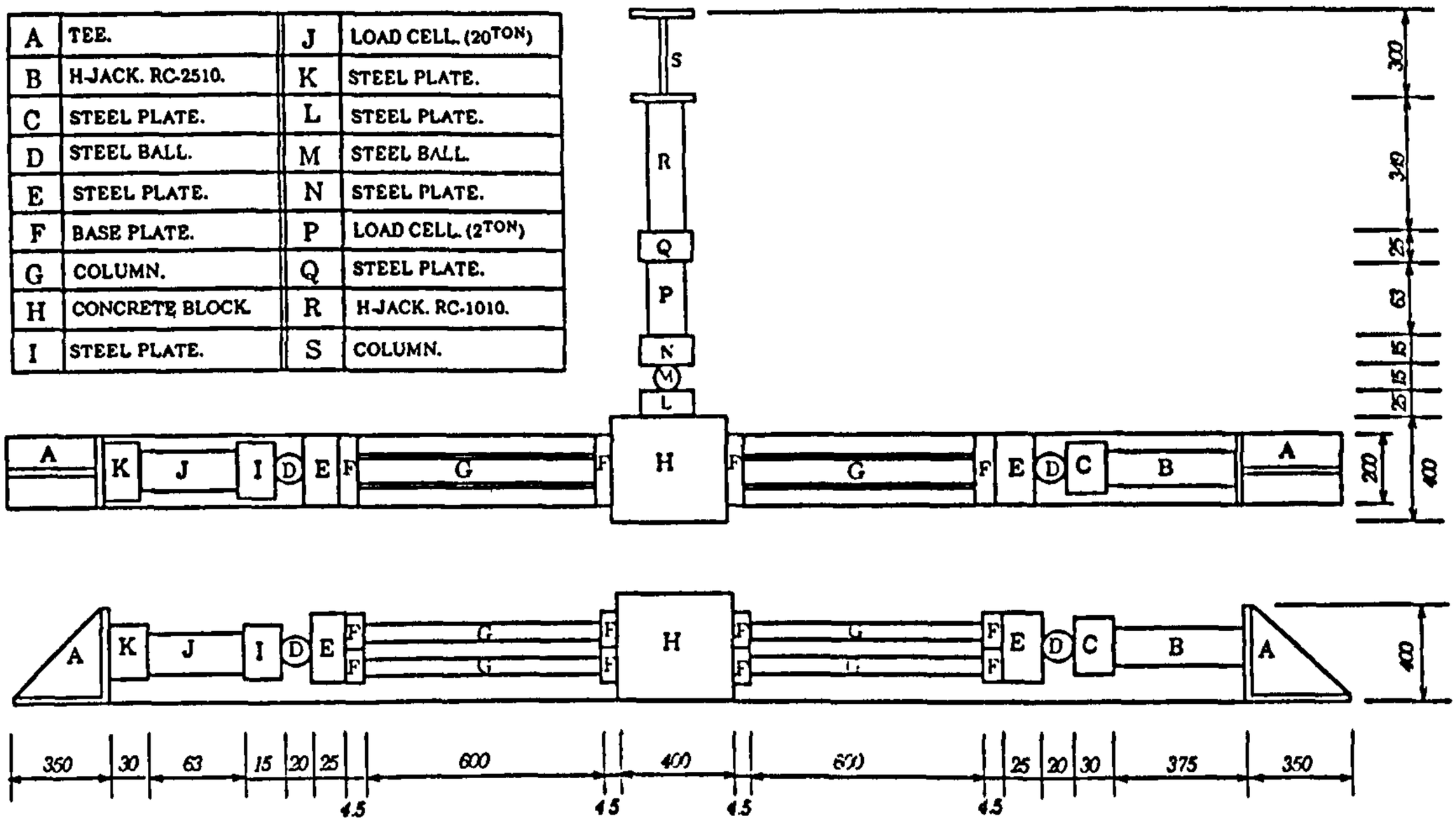

Fig 4.1(a) Schematic plan view of test rig and test panel

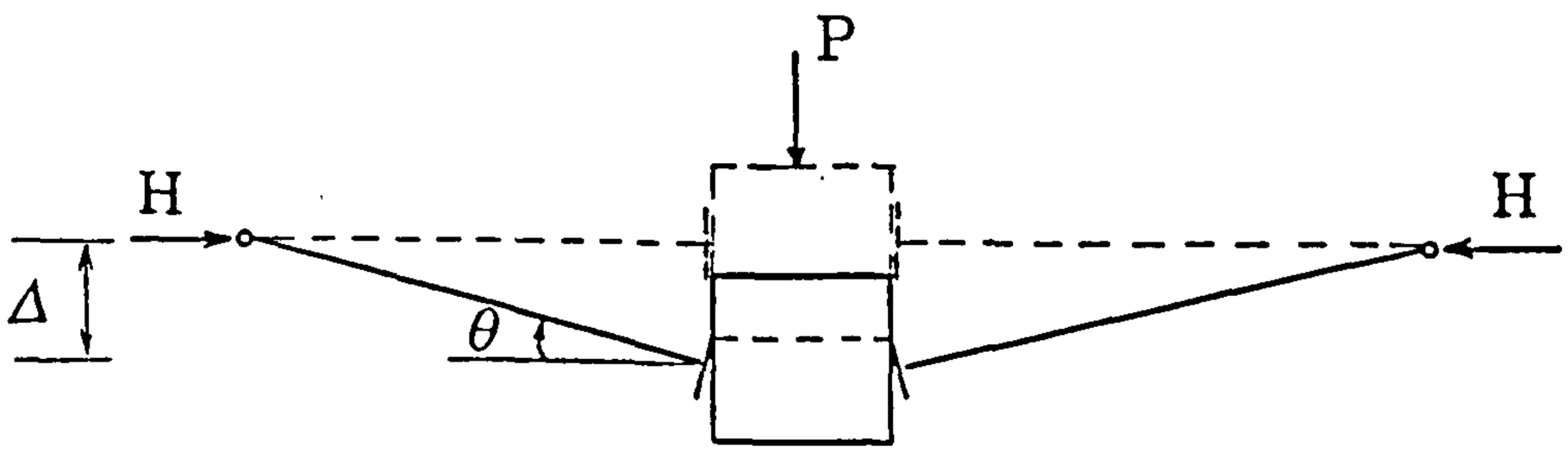

Fig 4.1(b) Loading and deformation of the experimental model

A full-scale baseplate and its upright were used in the test panel to make the experimental condition close to the practical condition.

The materials for testing, as shown in "H" in Fig 4.1, were concrete and timber blocks. They were used in the test panel as the foundation of the baseplate to investigate the effect of the subgrade on the rotational stiffness of the flat baseplate. The selection of concrete and timber blocks for testing was because the modulus of subgrade reaction for these two materials is significantly different.

Four base plates and uprights were used in each of the test panels to make an axisymmetric arrangement, so as to ensure that the test avoided torsional effects, as shown in "F" in Fig 4.1.

The base plate in the test panel was put onto the subgrade block without fixing bolts.

4.3 Experimental assembly

(1) Baseplate [58]:

Size:

188mm wide, 103mm deep and 4.5mm thick.

Holes:

A pair of 14mm diameter holes were punched in each baseplate.

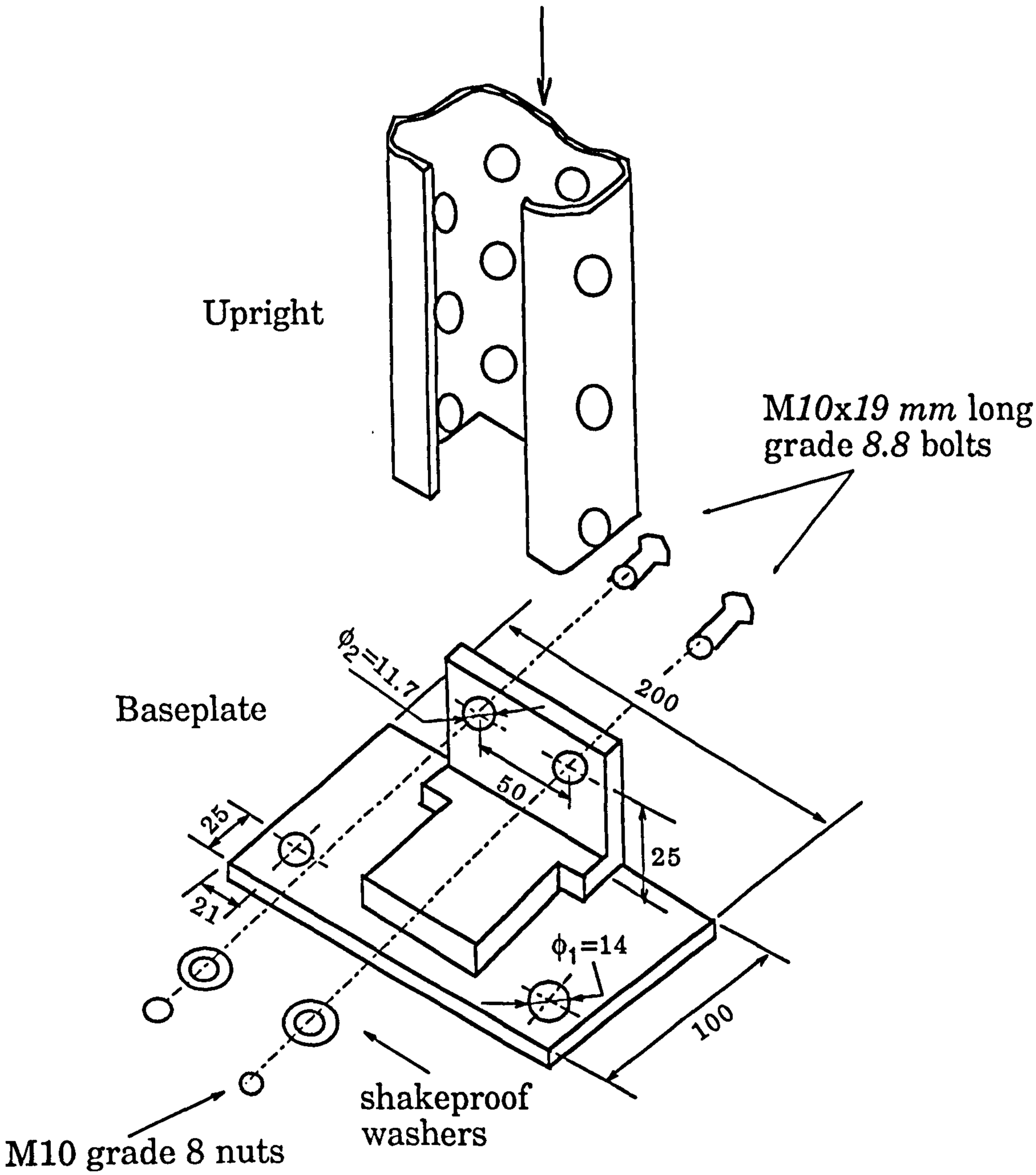

Fig 4.2 Baseplate description

These holes were 146mm apart, 21mm from the plate edges and 25mm from the back. In the angle cleat there were a pair of 11.7mm diameter holes, 50mm apart and 25mm from the plate surface. Fig 4.2 is a description of the baseplate tested.

Material:

The plate was made from steel grades HR43/35 or HR46/40 [47] to BS 1449: Part 1, and the angle cleat was a 73mm length of 50mm x 50mm x 5mm rolled steel angle to BS 4848: Part 4.

Finish:

Degreased and stove enamelled dark grey to BS 4800: 18B25.

Fixings:

Each plate was fixed to the upright by two M10 x 19mm deepstor bolts, nuts and 'shakeproof' washers, see Fig 4.2.

(2) Upright [58]:

Size:

103mm x 53mm x 3.05mm thick with 13.5 mm lips, see its description in Fig 4.3.

Material: Steel grade HR14 to BS 1449: Part 1.

(3) Subgrade block

(a) Concrete block (See Fig 4.4)

Size: 400mm x 400mm x 400mm

Material: E=21468.8 N/mm^2

where the Young's modulus of elasticity for concrete, E, was determined experimentally and described in Section 4.6.

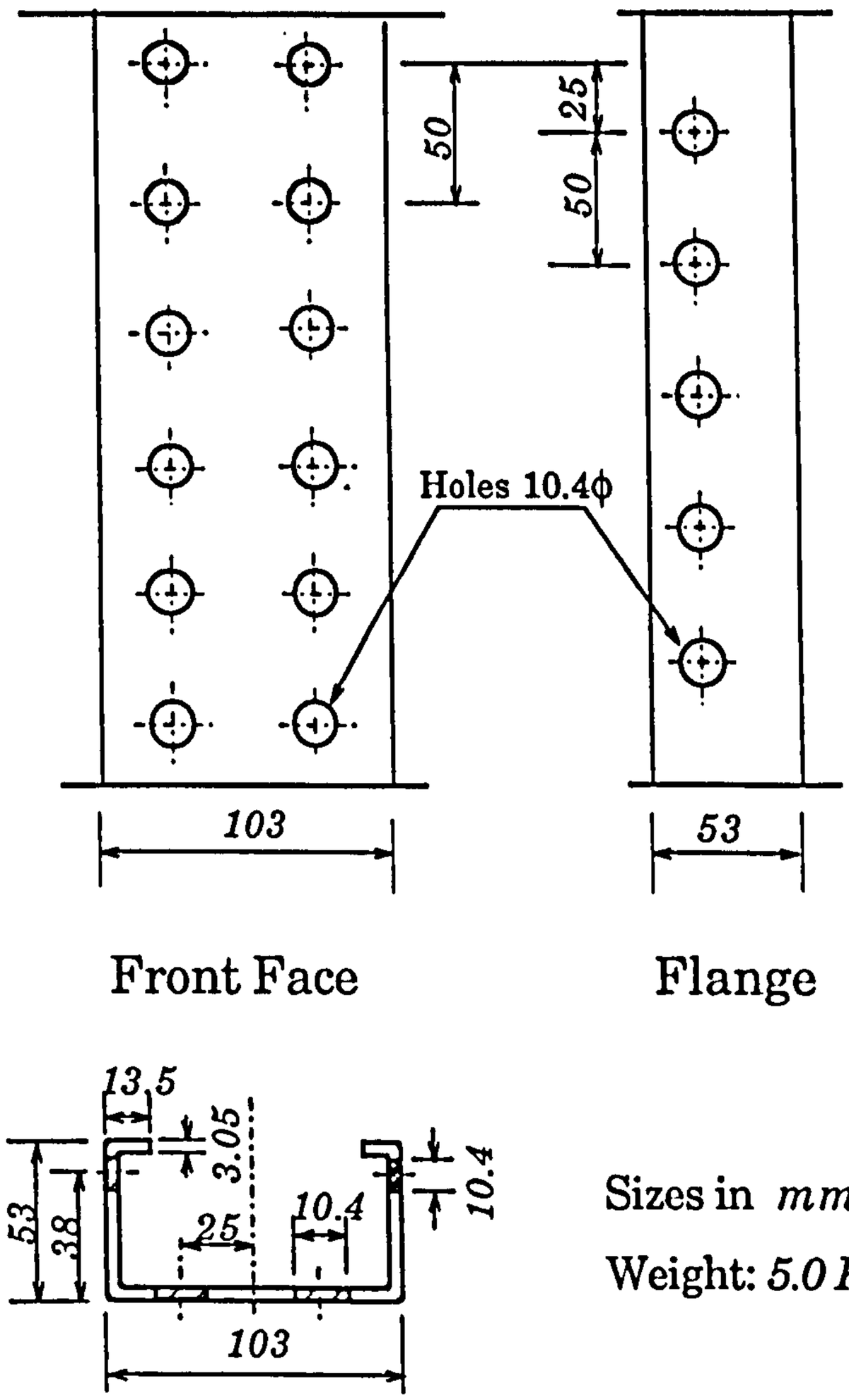

Fig 4.3 Upright description

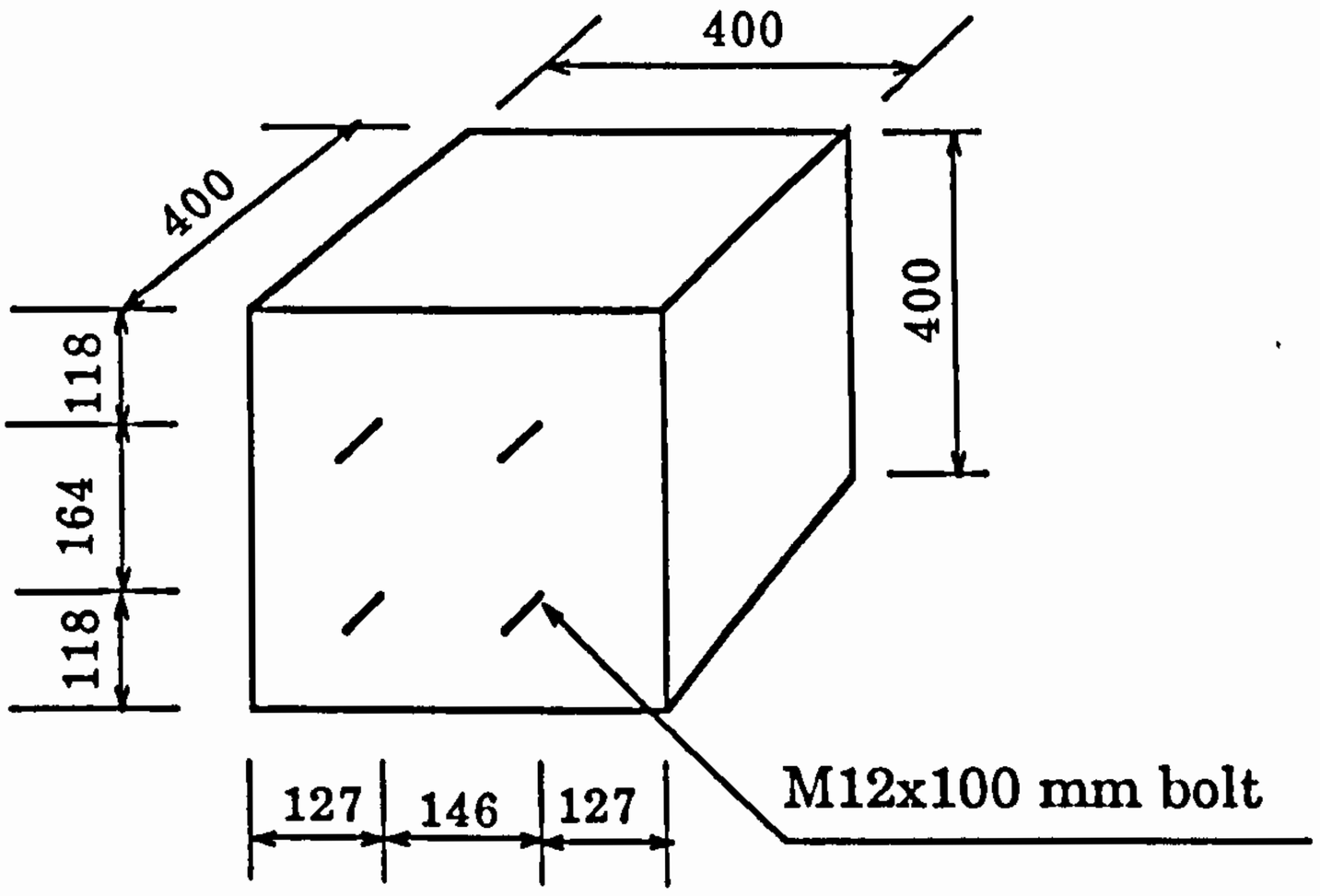

Fig 4.4 Concrete block

(b) Timber block (See Fig 4.5)

Size: 400mm x 400mm x 400mm

Material: E=182.36 N/mm^2

where the Young's modulus of elasticity for concrete, E, was determined experimentally and described in Section 4.6.

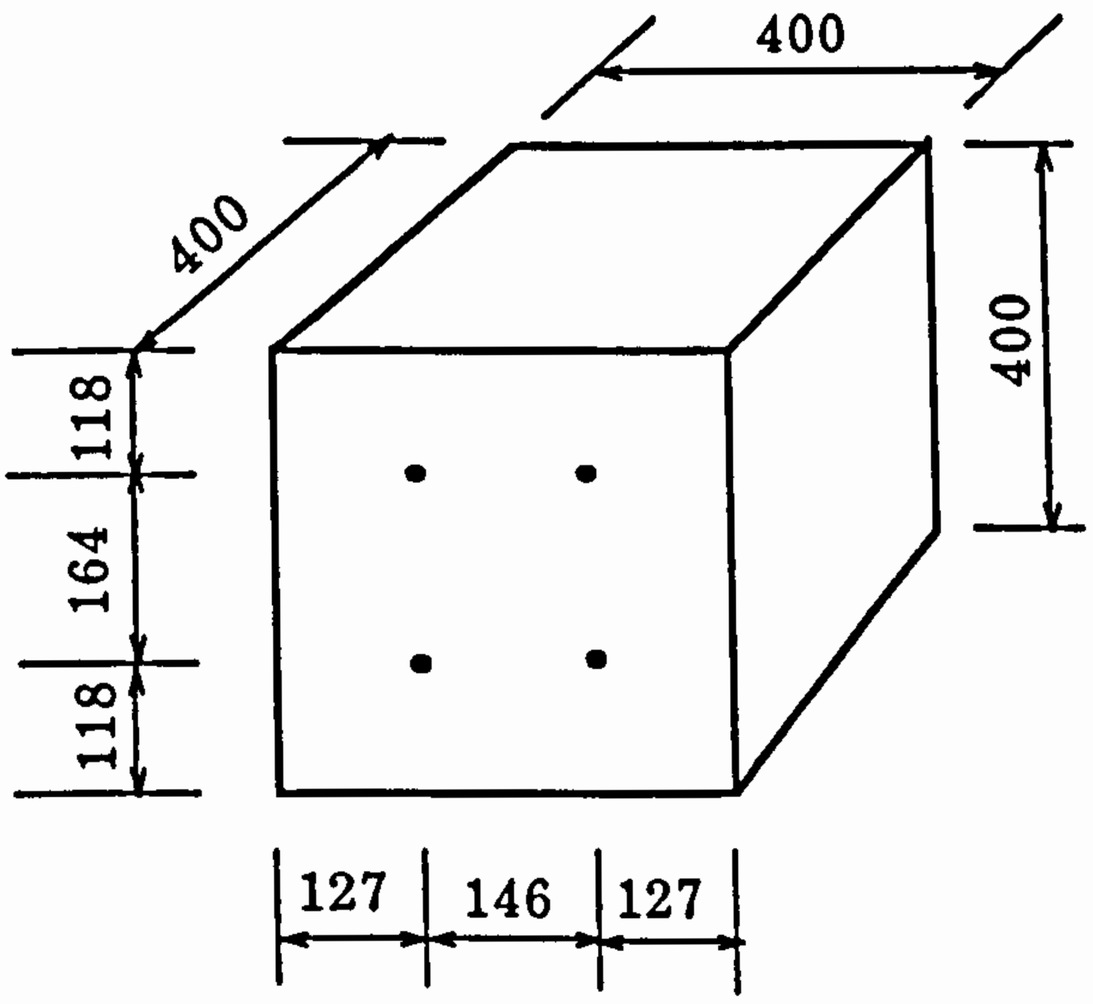

Fig 4.5 Timber block

4.4 Loading assembly

The constant axial load on the baseplate was applied by the servo-controlled hydraulic jack loaded on one end of the test panel, as shown in "B" in Fig 4.1.

The increased lateral load which was used to apply the increasing bending moment on the base plate was applied by the hand-controlled hydraulic jack loading on the centre of the subgrade block, as shown in "R" in Fig 4.1.

A plastic sheet was fitted between the subgrade block and reaction frame to ensure minimum friction force during the test.

4.5 Instrumentation

Three pairs of linear voltage displacement transducers (LVDT) were used during the test. Two pairs of them were located on each side of the columns to measure the lateral displacement. In addition, pairs of LVDTs were located on the subgrade block to allow the rotation of the block to be determined. The positions of the LVDTs are shown in Fig 4.6.

The applied loads were measured using two load cells. The locations of the load cells are also shown in "P" and "J" in Fig 4.6.

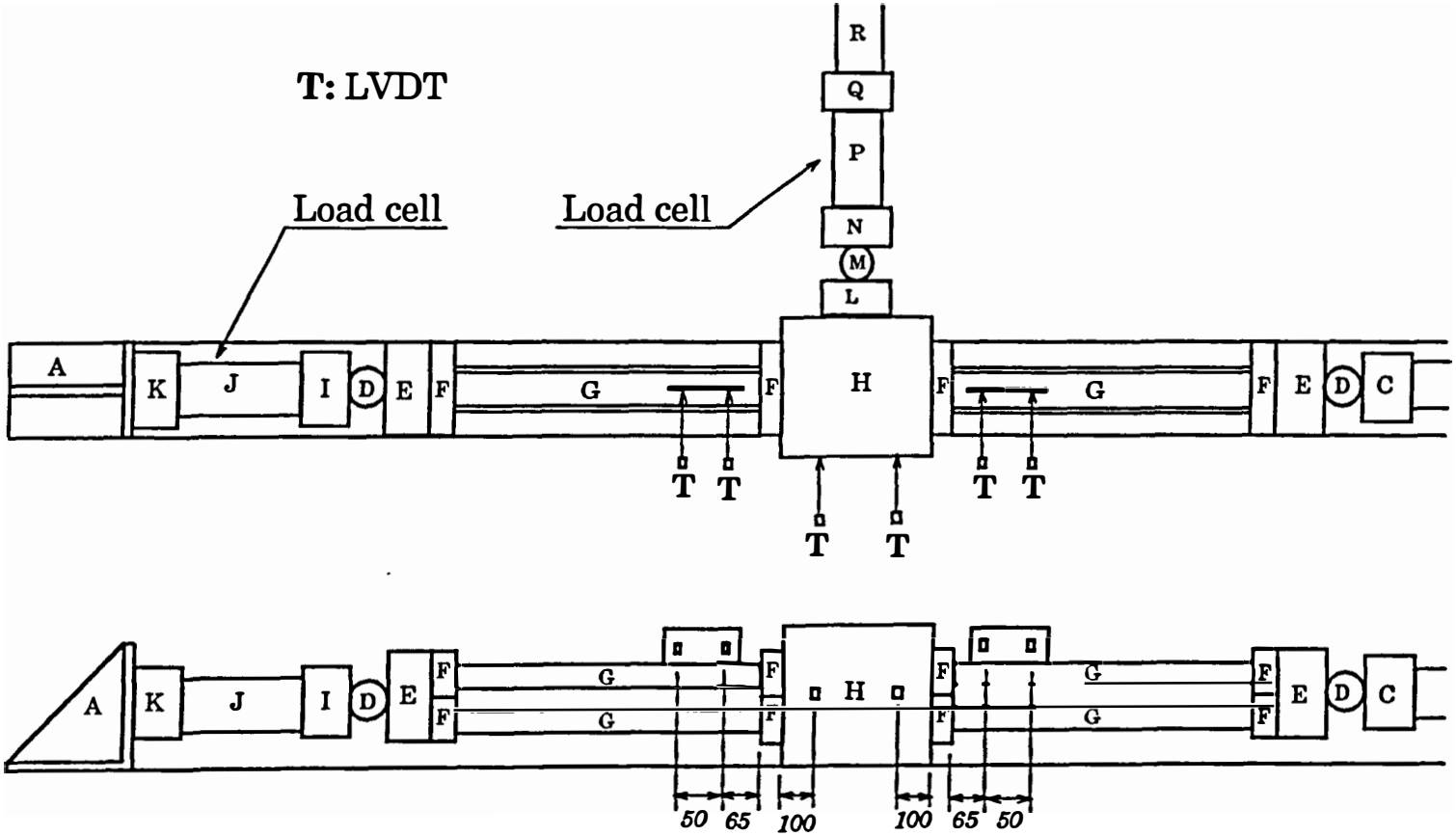

Fig 4.6 The position of LVDTs and load cells

All the load cells and transducers involved in the test were connected to a SPECTRA multi-channel data acquisition system which allowed almost simultaneous readings of all channels at any load level. The readings were recorded and stored by the computer.

4.6. Material properties of the concrete and timber

As has been discussed on the previous chapter the rotational stiffness of the baseplate was influenced by the modulus of subgrade reaction of the baseplate. In order to confirm the results from the theoretical analysis, an experimental study was carried out for the baseplate to estimate the influence of the modulus of subgrade reaction on the rotational stiffness of the baseplate. Two different kinds of materials, concrete and timber, were used in the tests. They were taken as the foundation block of the baseplate to model the action of the modulus of subgrade reaction.

In the analytical model for the rotational stiffness of the baseplate, the subgrade of the baseplate was modeled by using a group of compression springs. The compression stiffness of the springs was determined by the modulus of subgrade reaction of the baseplate. To determine the modulus of subgrade reaction of the baseplate in the test, the elastic modulus of the material of which the base block was made had to be defined. Therefore, further comparison study between the theoretical and experimental results can possibly be carried out to justify and prove the analytical model for the rotational stiffness of the baseplate.

The compression test of a concrete column was conducted to determine the Young's modulus of the concrete material. The test rig is shown in Fig 4.7. The concrete column was 150x150x350 mm^3 in size. The concrete column and the concrete block were cast at the same time using the same material to ensure that they would have the same properties. A pair of dial gauges were fixed on each side of the concrete column to measure the deformation of the column. The test was terminated when the failure occurred in the concrete column.

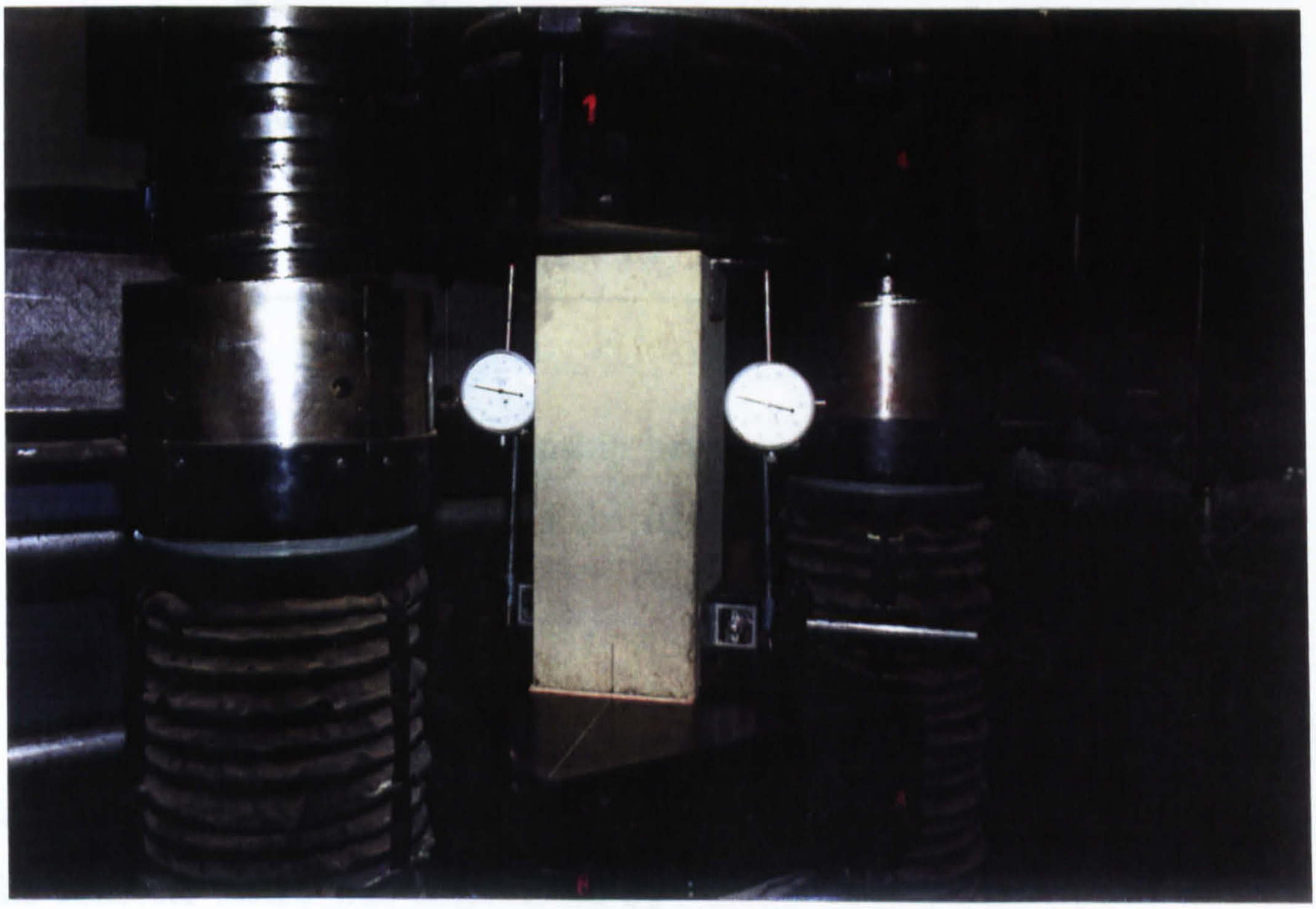

Fig 4.7 Compression test of concrete column
to determine its Young's modulus of elasticity

At a number of axial load increments, the deformation was measured. So the relationship between deformation and axial load was obtained and

then treated using Techni-Curve linear regression program. The results are shown in Fig 4.8.

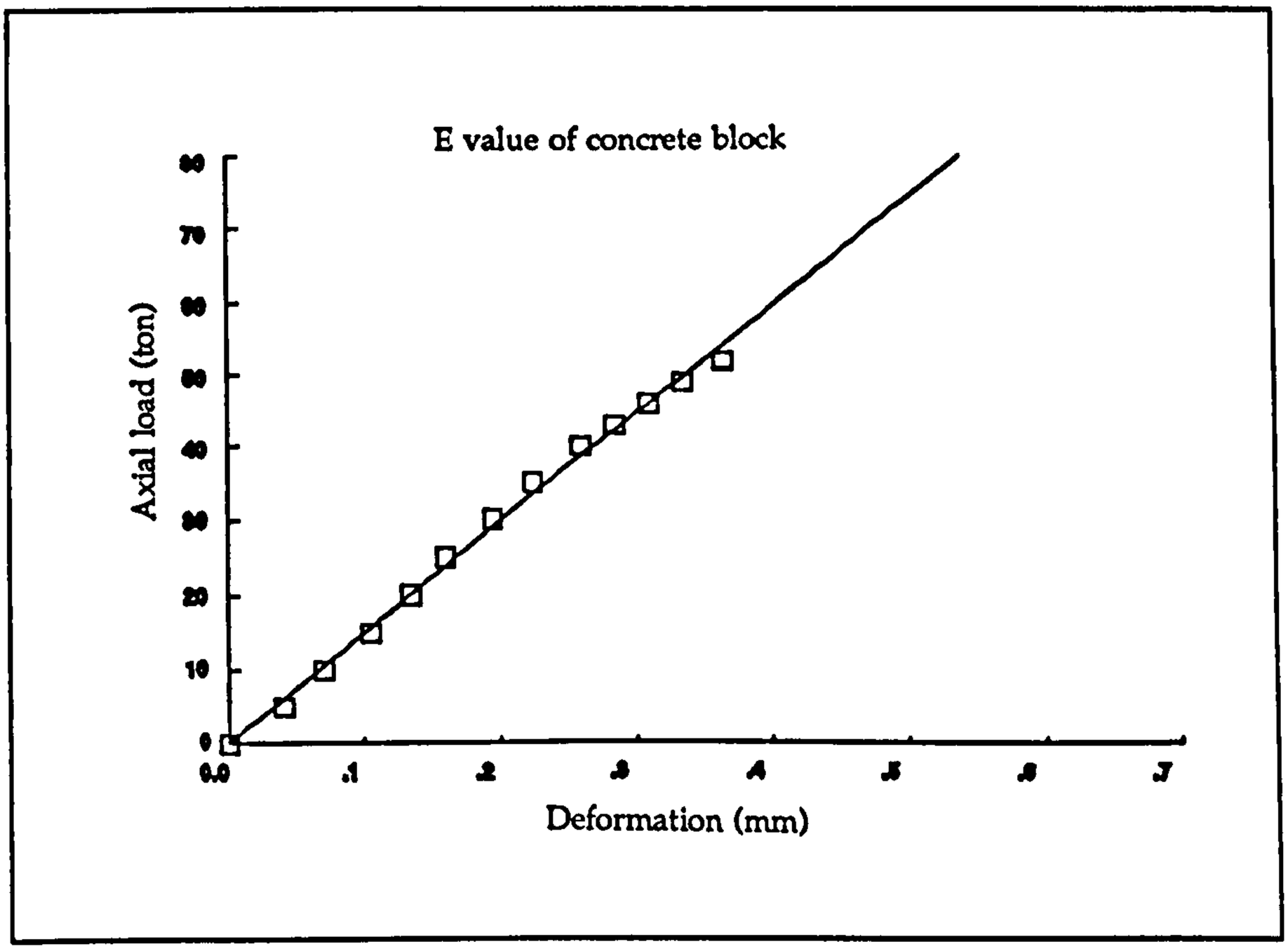

Fig 4.8 The relationship between deformation and axial load of the first concrete column

From the linear regression, the slope of the curve in Fig 4.8 was found to be α=1480.613. Therefore, the Young's modulus of elasticity for the concrete tested was determined by

$$E=\frac{\sigma}{\epsilon}=\frac{P}{A}.\frac{l}{\Delta l}=\frac{P}{\Delta l}.\frac{l}{A}=\alpha.\frac{l}{A} \qquad (4.1)$$

where l was the length of the column from which the deformation was measured. A was the cross-section area of the column.

In the test, the length of the column was 341 mm, the cross-section area of the column was 150x150 mm^2. So, substituting α,*l* and *A* into Eq(4.1) gives

$$E_{c1}=\alpha.l/A=1480.613x10^3x341x0.98/(150x150)=21990.72N/mm^2$$

The test was repeated for a second specimen of concrete column. The Techni-Curve linear regression curve for the testing data of the relationship between the deformation and the axial load is shown in Fig 4.9.

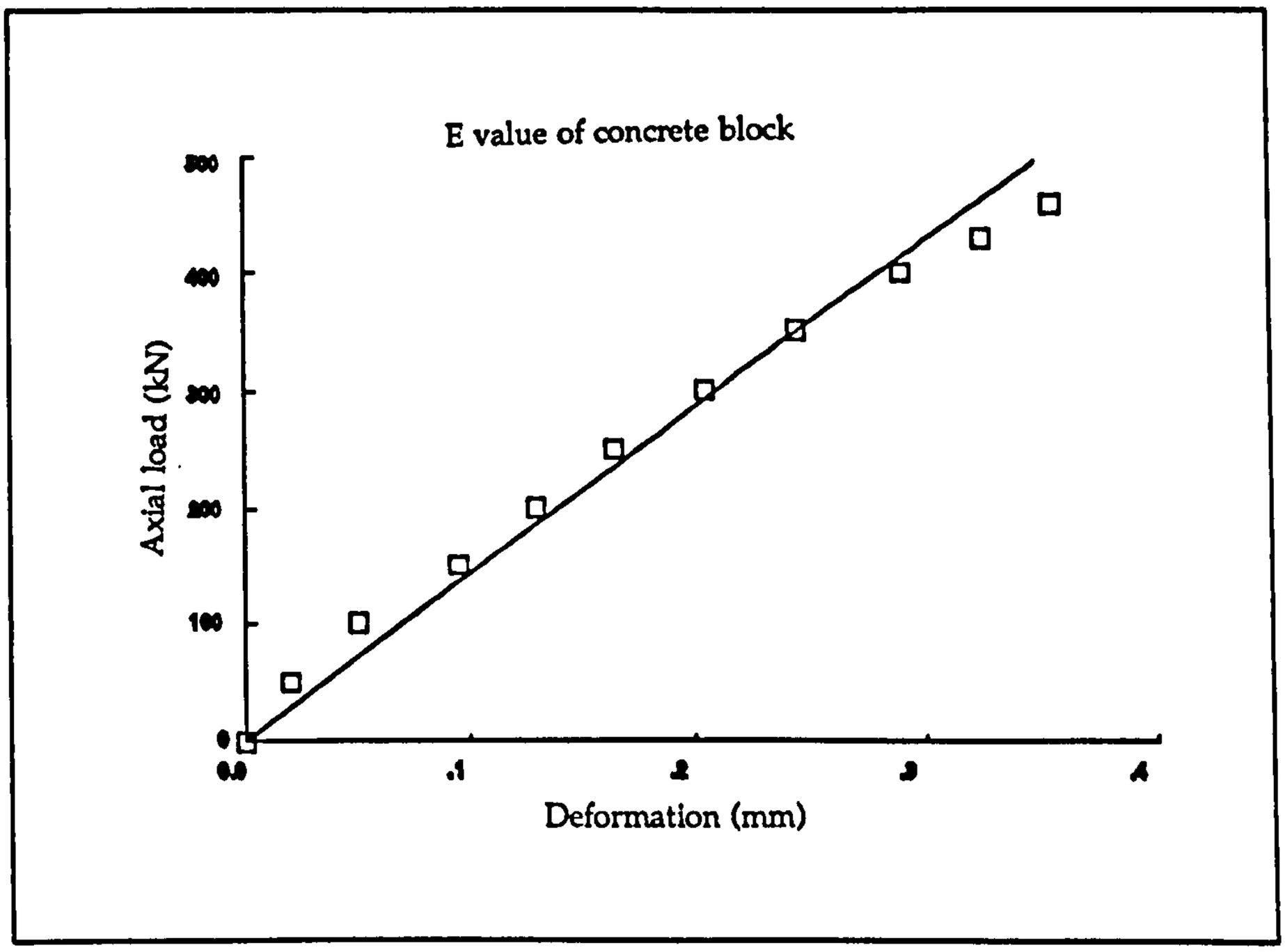

Fig 4.9 The relationship between deformation and axial load of the second concrete column

The slope of the curve in Fig 4.9 was found from the linear regression to be α=1424.958.

Substituting α, the column length *l* and the area of column cross-section *A* into Eq(4.1) yields

$E_{c2}=\alpha.l/A=1424.958x10^3x337.5x0.98/(150x150)=20946.88\ N/mm^2$.

Therefore, the average value of the Young's modulus of elasticity for the concrete block is given by

$E_c=(E_{c1}+E_{c2})/2=(21990.72+20946.88)/2=21468.8\ N/mm^2$

A similar compression test was carried out for the timber material tested so as to determine its Young's modulus of elasticity. A 400x400x400 mm^3 timber block was used in the test. A pair of dial gauges were used to measure the deformation of the timber block when the axial load was increased. A curve of the deformation and the axial load was obtained and, after using the Technic-Curve program to analyze the test data, it was given in Fig 4.10.

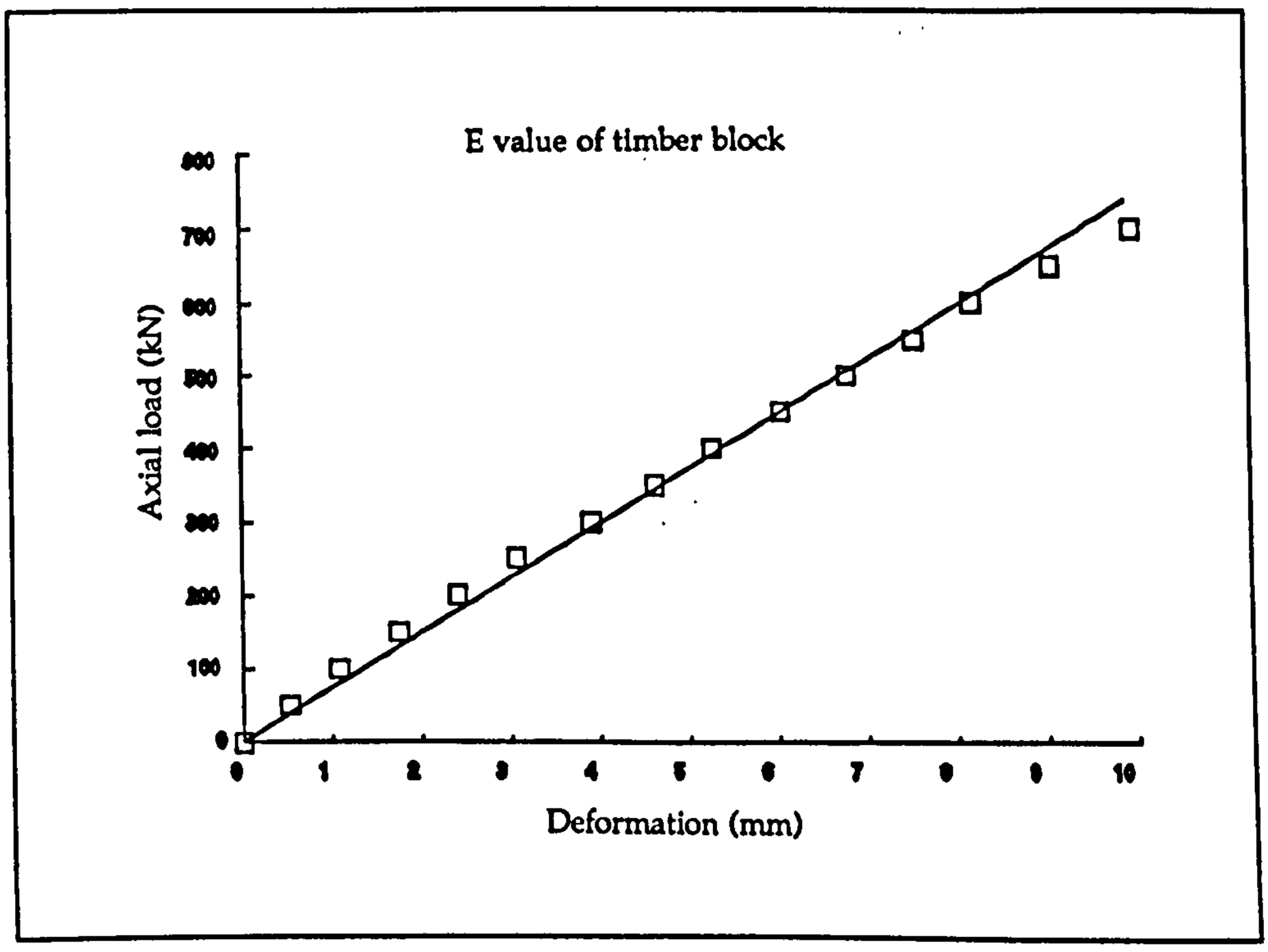

Fig 4.10 The relationship between deformation and axial load of the timber block

The slope of the curve was found to be α=74.43268. In the test, the length of the timber block was 400mm, the cross-section area of the block was 400x400 mm^2. Therefore, the Young's modulus of elasticity of the timber tested was determined by

$$E_t=\alpha.1/A=74.43268x10^3x400x0.98/(400x400)=182.36\ N/mm^2.$$

It was noted that the timber block tested was loaded across the grain. The modulus of elasticity obtained was therefore lower than that loaded parallel to the grain.

4.7 Test procedure

4.7.1 Test of modulus of subgrade reaction

The theoretical investigation showed that one of the principal factors that influence the rotational stiffness of baseplate is the modulus of subgrade reaction. In order to compare the theoretical results with the experimental investigations, an equivalent modulus of subgrade reaction has to be determined for the theoretical calculation. Therefore, tests to determine the modulus of subgrade reaction for the concrete and timber blocks were carried out.

Since the Young's modulus of elasticity for the concrete and timber blocks tested have been determined in Section 4.6, the modulus of subgrade reaction for concrete and timber blocks can be determined easily by considering the subgrade as a block instead of a semi-infinity subgrade, as shown in Fig 4.11.

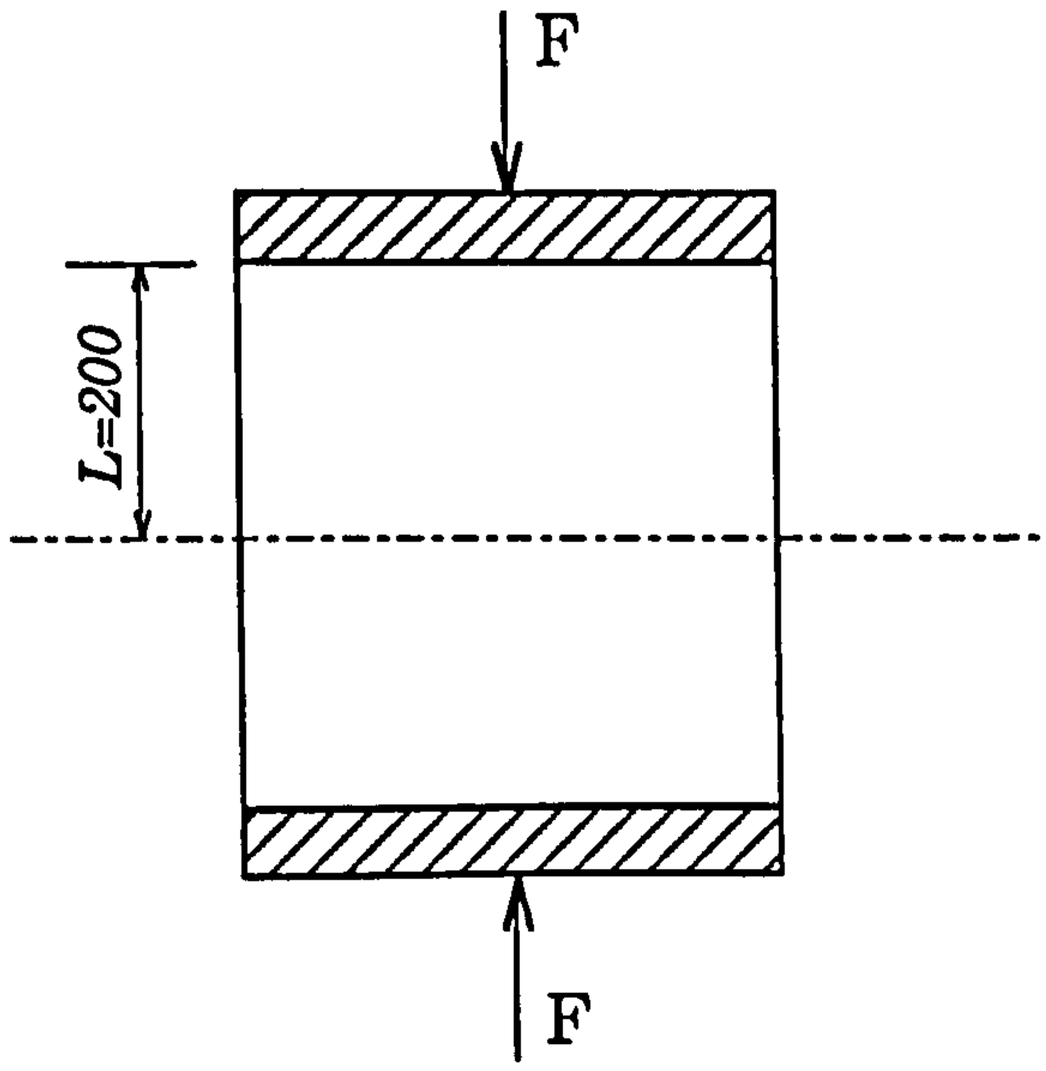

Fig 4.11 A block subjected to compression

By definition, the modulus of subgrade reaction k_s is referred to as the reaction per unit area of foundation for unit deflection. Thus, the modulus of subgrade reaction of concrete block k_{sc} can be written as

$$k_{sc}=F/(A\Delta) \qquad (4.2)$$

where F is the force acting on the concrete block, A is the area of the cross-section of the block and Δ is the deformation defined by

$$\Delta=FL/(AE_c)$$

Substituting Δ into Eq(4.2) gives

$$k_{sc}=E_c/L \qquad (4.3)$$

The Young's modulus of elasticity for the concrete block has been determined in the previous section as E_c=21468.8 N/mm^2 which is substituted into Eq(4.3) to give

$$k_{sc}=21468.8/200=107.344 \text{ N/mm}^3$$

Similarly, the modulus of subgrade reaction of the timber block k_{st} can be written as

$$k_{st}=F/(A\Delta) \qquad (4.4)$$

where F is the force acting on the timber block, A is the area of the cross-section of the block and Δ is the deformation defined by

$$\Delta=FL/(AE_t)$$

Δ is substituted into Eq(4.4) to produce

$$k_{st}=E_t/L \qquad (4.5)$$

The Young's modulus of elasticity for the timber block is E_t=182.36 N/mm^2. It is substituted into Eq(4.5) to give

$$k_{st}=182.36/200=0.9118 \text{ N/mm}^3$$

4.7.2 Steel tensile test of the baseplates

The baseplates used in the experiment were made of steel. When the test for the rotational stiffness of the baseplate is carried out, the baseplate is subject to bending. Therefore, the failure stress of the steel baseplate is required for both experimental and theoretical research of the rotational stiffness of the baseplate. In order to find out the maximum stress of the steel baseplate, a steel tensile test for the baseplate was carried out. Three baseplate samples were used in the test, as shown in Fig 4.12.

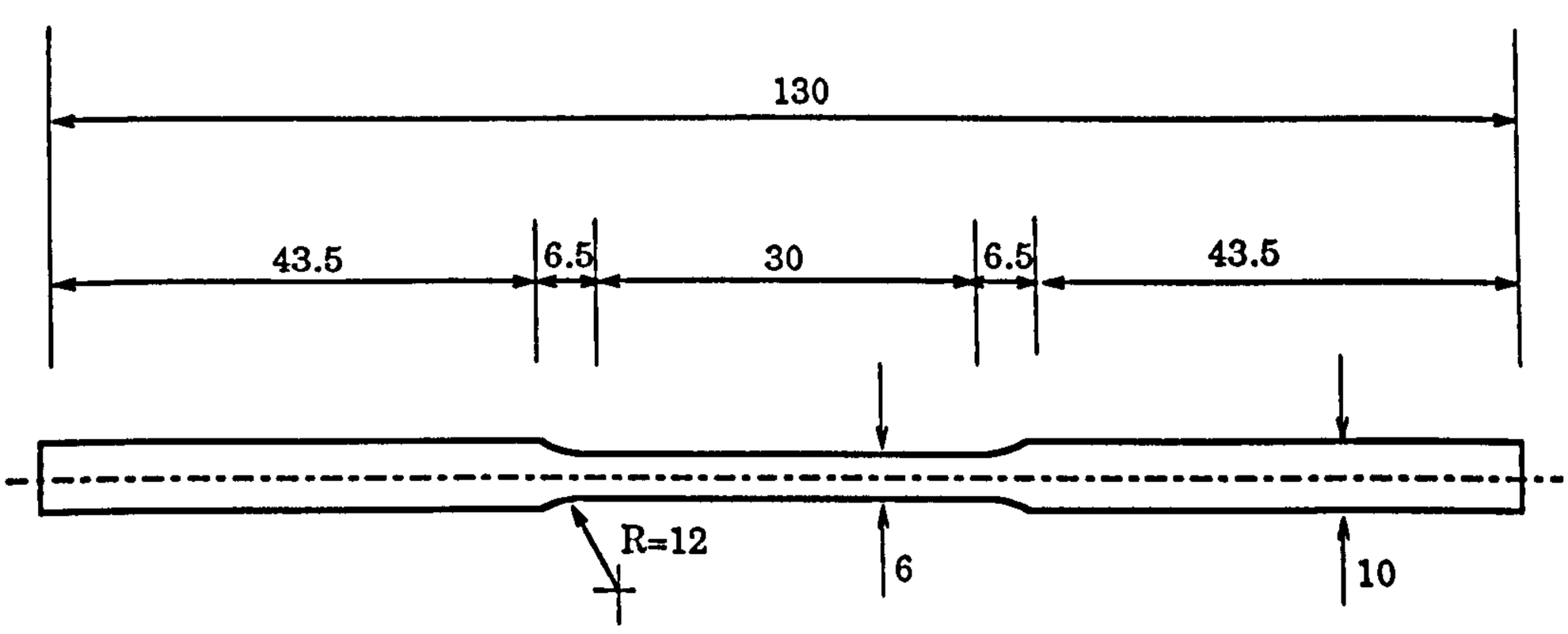

THICKNESS: *4.5 mm*
WIDTH: *6 mm ± 0.03.*

Fig 4.12 Three tensile test samples required as drawn.

The test results are shown in Fig 4.13, Fig 4.14 and Fig 4.15. They are summarised in table 4.1, which gives the yield load, maximum (ultimate) load and maximum stress of the specimen for the steel baseplate.

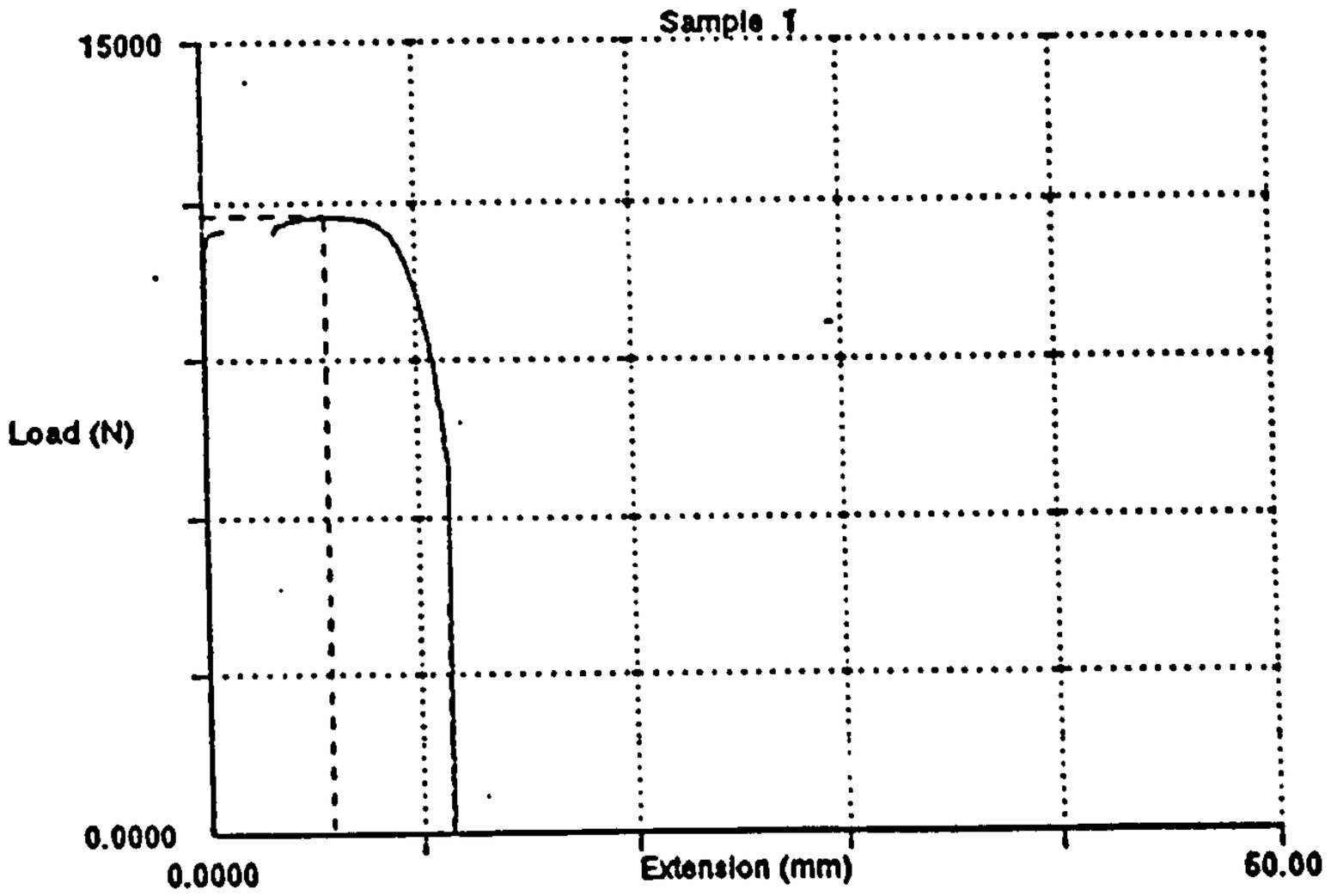

Maximum Load (N)	Load @ Off Yld (N)	Ext @ Off Yld (mm)	Fixed Strain (%)	Modulus of Elast (N/mm²)	Sample Width (mm)	Sample Thick' (mm)
11790	10920	0.1015	37.67	232500	5.953	4.498

Fig 4.13 The tensile test result of the steel baseplate for Sample 1

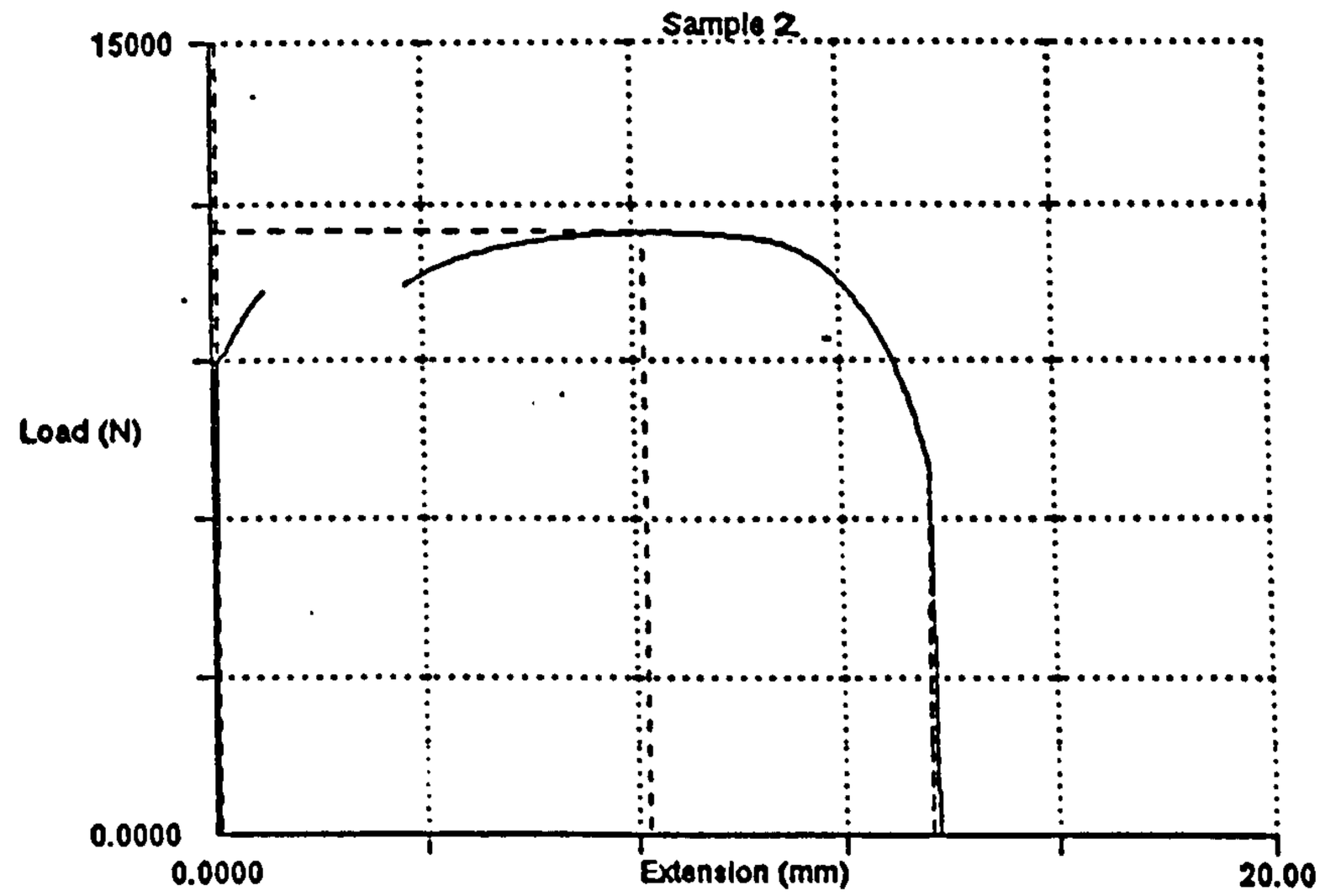

Maximum Load (N)	Load @ Off Yld (N)	Ext @ Off Yld (mm)	Fixed Strain (%)	Modulus of Elast (N/mm²)	Sample Width (mm)	Sample Thick' (mm)
11510	8998	0.0972	54.46	202200	5.765	4.470

Fig 4.14 The tensile test result of the steel baseplate for Sample 2

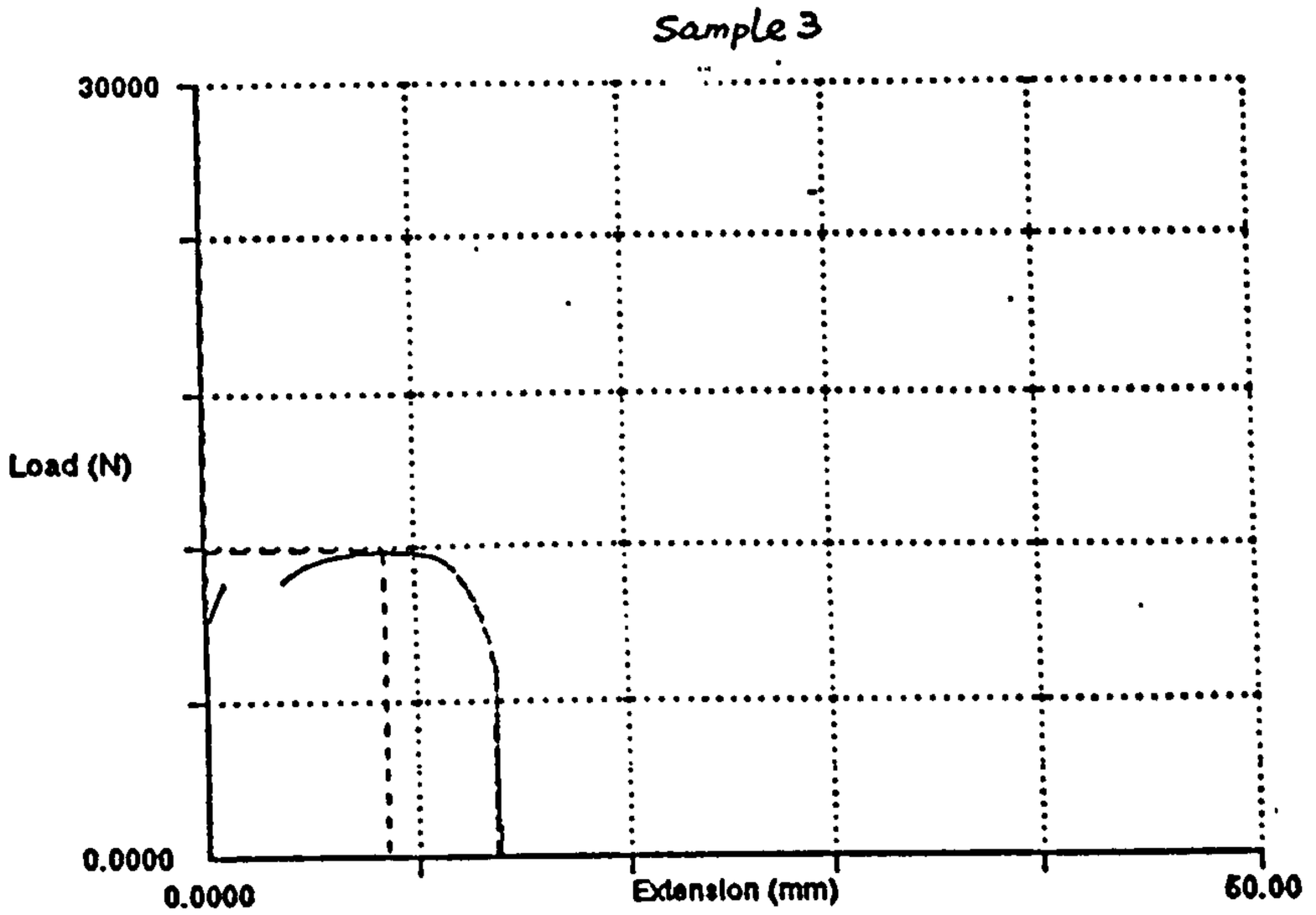

Maximum Load (N)	Load @ Off Yld (N)	Ext @ Off Yld (mm)	Fixed Strain (%)	Modulus of Elast (N/mm²)	Sample Width (mm)	Sample Thick' (mm)
11890	9243	0.0933	45.50	252500	5.921	··4.476

Fig 4.15 The tensile test result of the steel baseplate for Sample 3

Table 4.1 Summary of the steel tensile tests

Baseplate		Sample 1	Sample 2	Sample 3
Thickness (mm)	Top	4.501	4.470	4.487
	Middle	4.500	4.472	4.472
	Bottom	4.494	4.468	4.469
	Average	4.498	4.470	4.476
Width (mm)	Top	5.947	5.760	5.921
	Middle	5.961	5.753	5.925
	Bottom	5.952	5.781	5.918
	Average	5.953	5.765	5.921
Yield load (N)		10920	8993	9237
Maximum Load (N)		11790	11510	11890
Maximum stress (N/mm^2)	Average	440.31	446.65	448.64
	Maximum	441.15	447.78	449.57

4.7.3 The procedure for the rotational stiffness test of the baseplate

Before the test started, the positions of all the LVDTs and dial gauges were checked. The LVDTs and dial gauges were readjusted to suit the possible travel distances for each of the test. The LVDTs and the load cells were calibrated accurately. The correct conversion factors of the LVDTs and the load cells were put into the data logger and the figure was checked again before the test. The tape to be used in the test was also checked before the test to make sure that it would work during the test. The time period at which results were to be measured was entered into the data logger before the test. The tape was started running before the test begin.

A constant axial load and an increased horizontal load were applied for each of the test panels to supply a loading condition with a constant axial load and a gradually increased bending moment.

During the test, the axial load was applied first. When it reached the required magnitude, the servo-controlled hydraulic jack kept it constant throughout the test, while the lateral load was applied gradually by using the hand-controlled hydraulic jack until the ultimate bending moment was achieved. When the loading procedure was completed, the lateral load was removed first to keep the whole test panel stable, and then the axial load was reduced. All the readings were recorded once every five seconds and stored by the computer automatically. The test results will be described in the next section.

4.8 Test results

4.8.1 The moment-rotation curves

Two different test panels were chosen for the test to investigate the effects of the modulus of subgrade reaction. One had a concrete block subgrade, another had a timber block subgrade. Three tests were carried out for each of the test panels under axial loads of 20kN, 40kN and 80kN to include the effects of axial loads. The test results showing the moment-rotation curves for the subgrade of concrete blocks and timber blocks are plotted in Fig 4.16 and Fig 4.17, respectively.

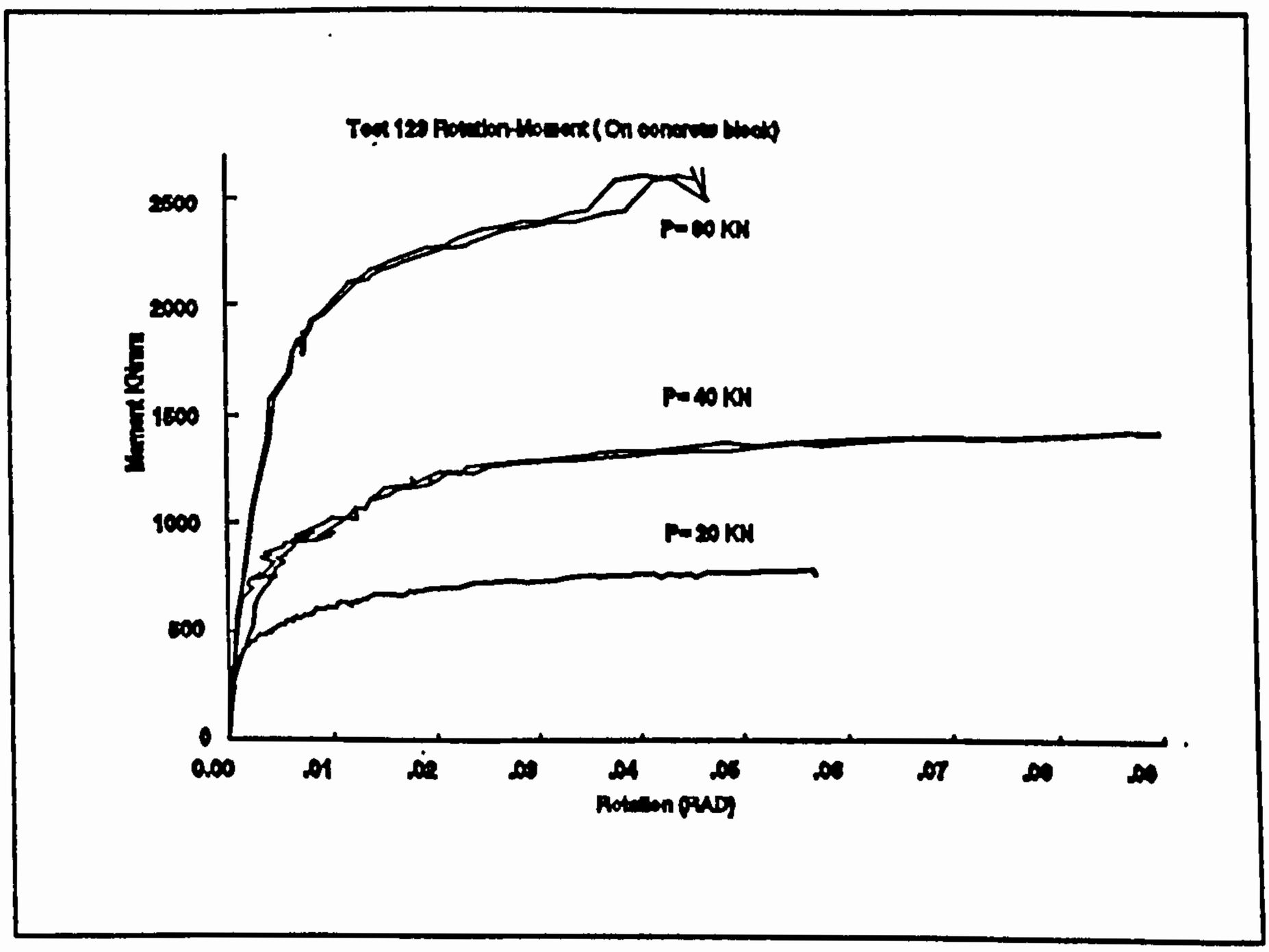

Fig 4.16 The moment-rotation curves of the baseplate supported on the concrete subgrade subjected to the axial loads of 20kN, 40kN and 80kN

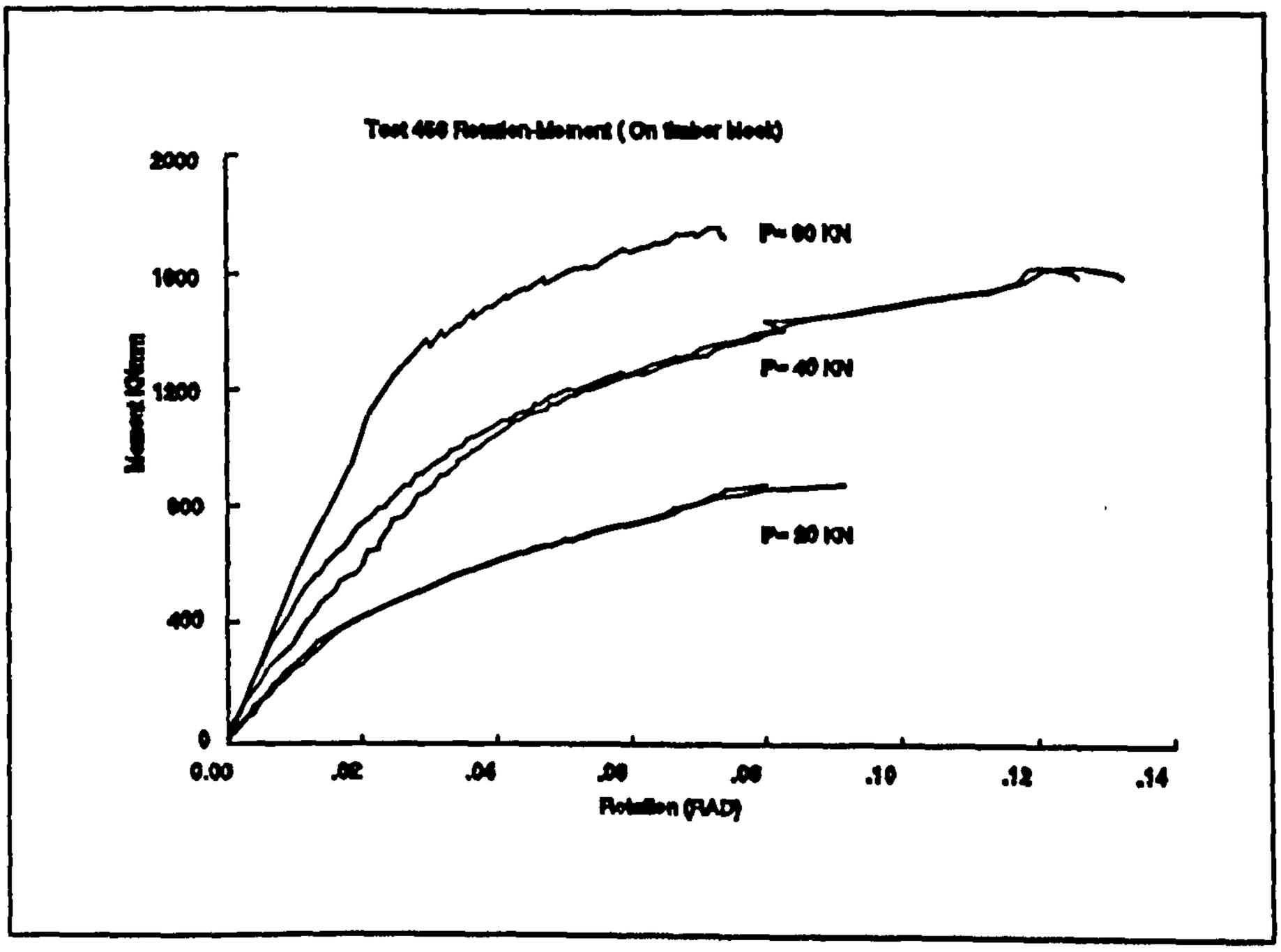

Fig 4.17 The moment-rotation curves of the baseplate supported on the timber subgrade subjected to the axial loads of 20kN, 40kN and 80kN

4.8.2 The effects of different axial loading conditions

Fig 4.16 gives a group of experimental baseplate rotation-moment curves based on the subgrade of concrete block under axial loads of 20kN, 40kN and 80kN. Fig 4.17 gives a group of experimental baseplate rotation-moment curves based on the subgrade of timber block under axial loads of 20kN, 40kN and 80kN. The two figures show clearly that the axial load has a great influence on the shape of the moment-rotation curves of the baseplate. The rotational stiffnesses of the baseplate are therefore affected, particularly in the regime of large rotations. The rotational stiffness of the

baseplate increases with the increasing axial load, no matter what kind of subgrade the baseplate is supported.

4.8.3 The effects of different modulus of subgrade reaction

A group of comparison results about the effects of different modulus of subgrade reaction on the rotational stiffness of the baseplate are shown in Fig 4.18, Fig 4.19 and Fig 4.20, with each being subjected to the same axial load.

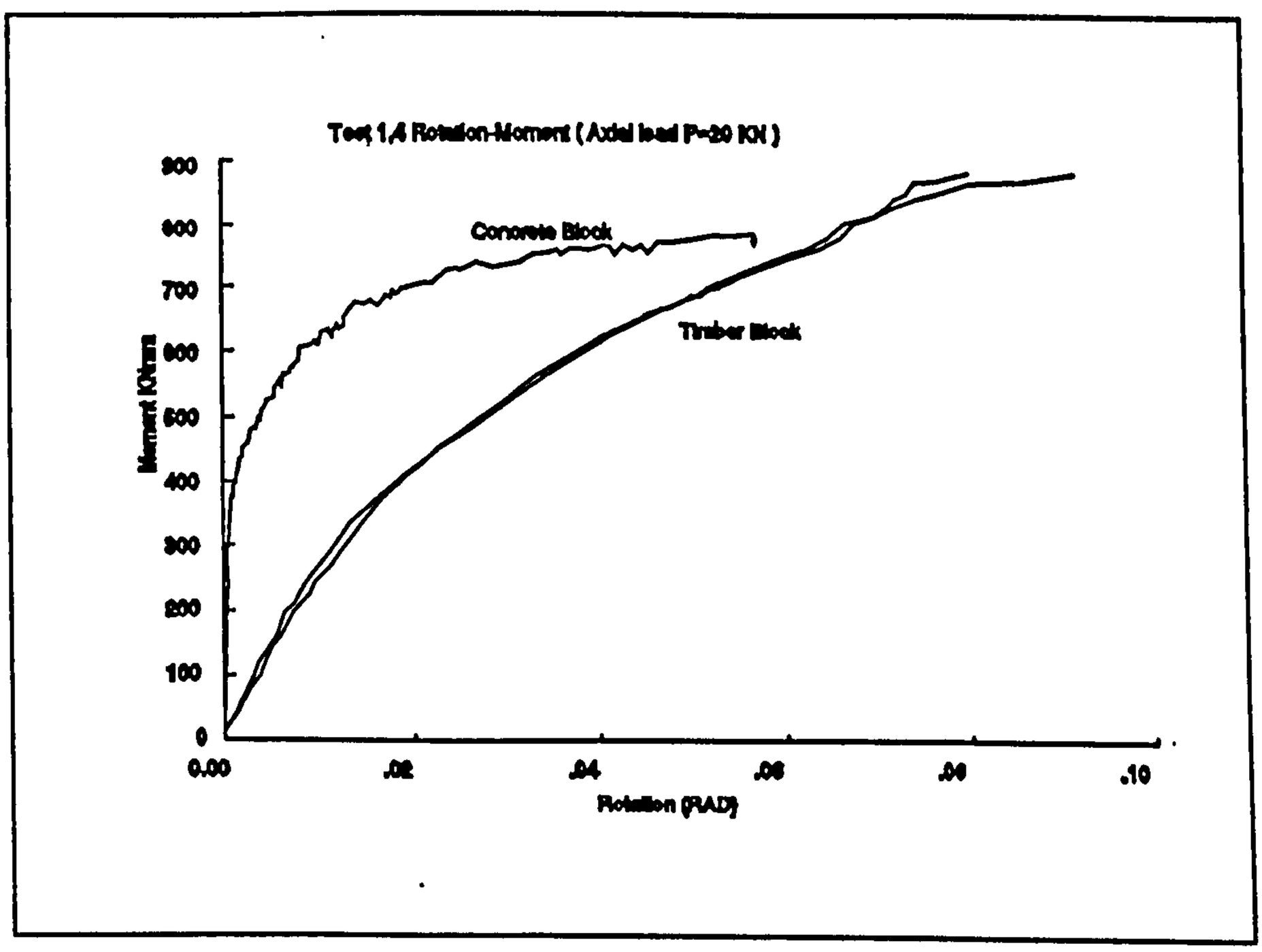

Fig 4.18 The moment-rotation curves of the baseplate supported on the concrete and timber subgrade subjected to the axial loads of 20kN

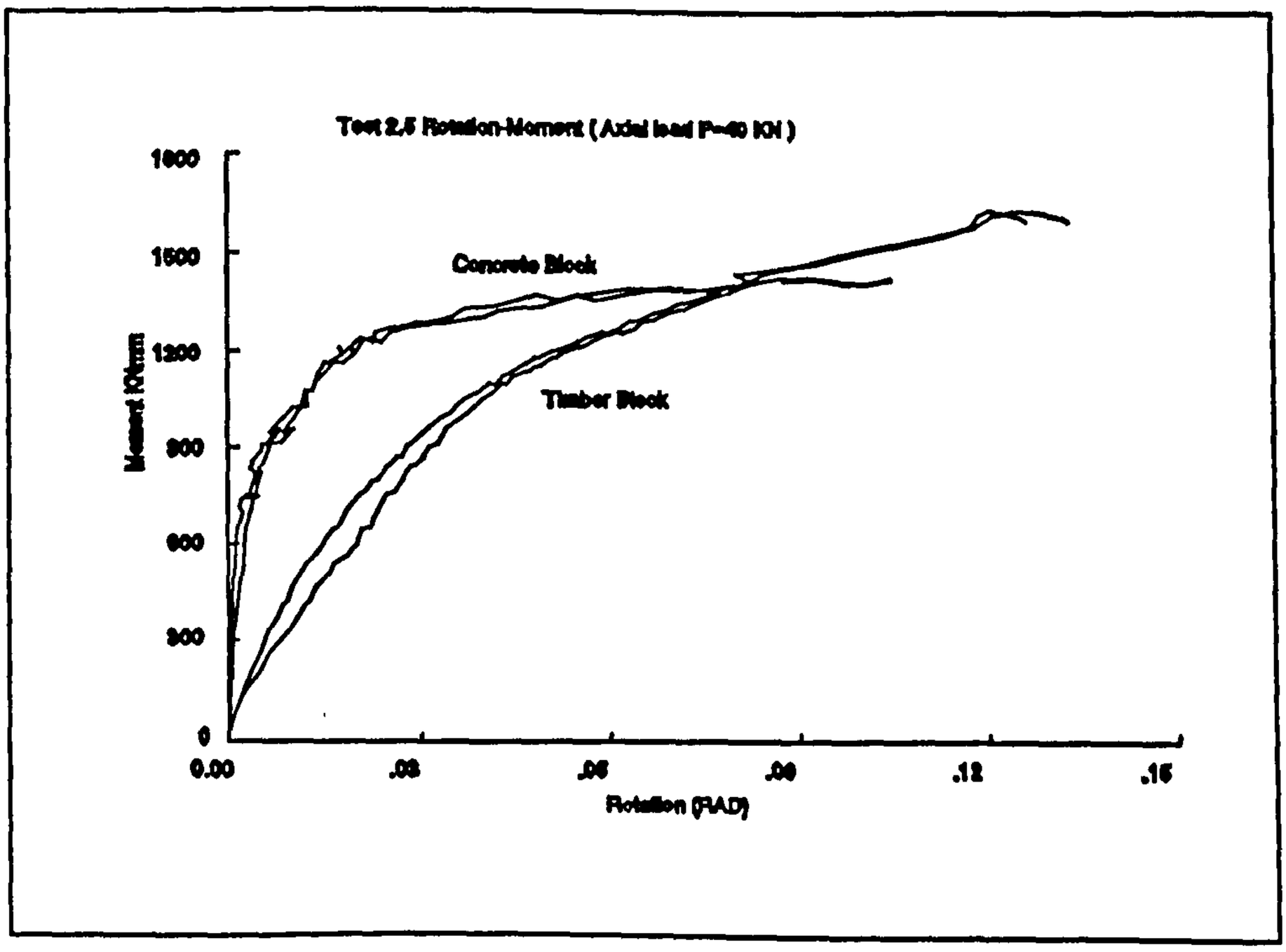

Fig 4.19 The moment-rotation curves of the baseplate supported on the concrete and timber subgrade subjected to the axial loads of 40kN

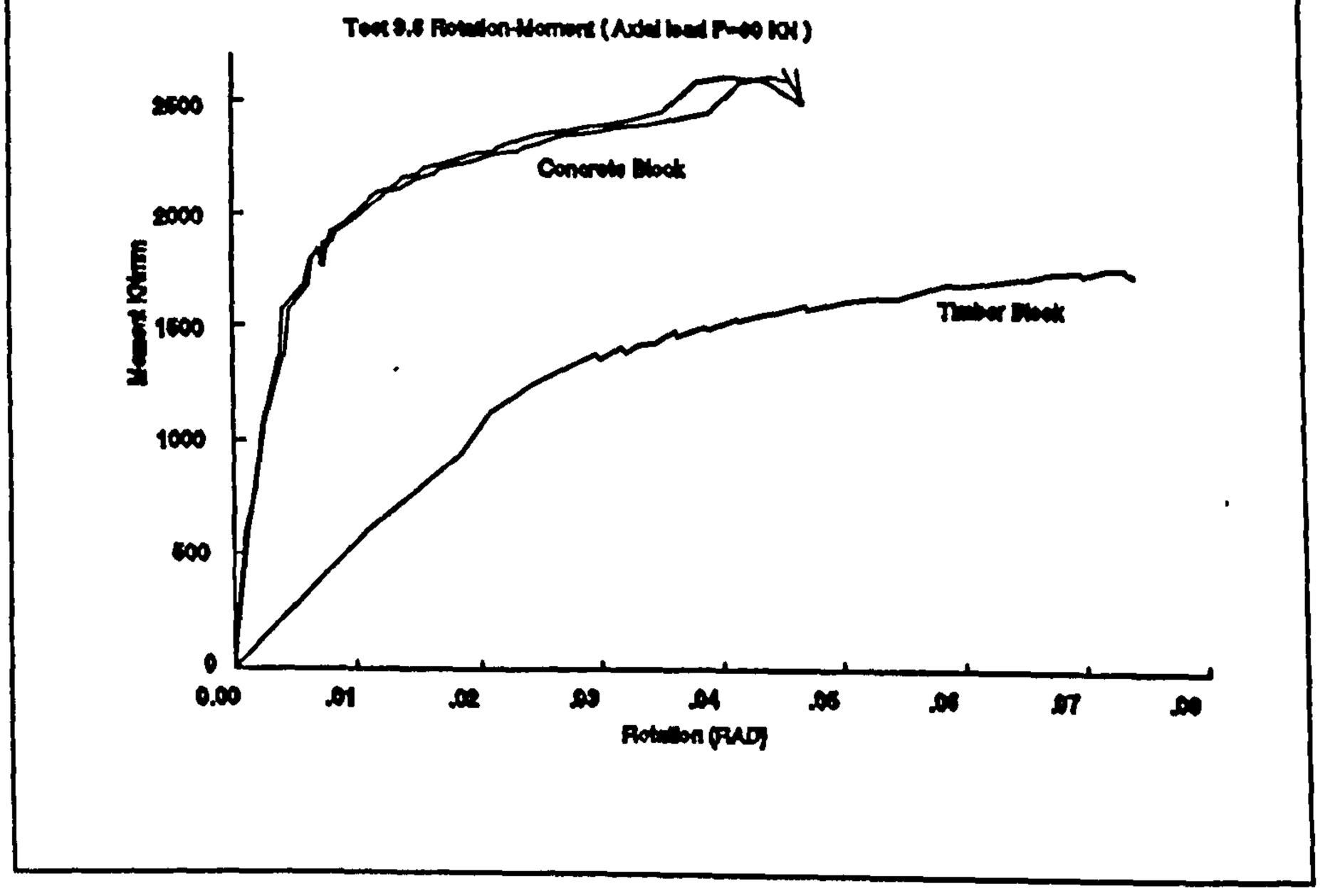

Fig 4.20 The moment-rotation curves of the baseplate supported on the concrete and timber subgrade subjected to the axial loads of 80kN

Fig 4.18 shows the experimental results of the moment-rotation curve of the baseplate under the concrete block subgrade and timber block subgrade when the axial load remained at 20kN. Fig 4.19 and Fig 4.20 are the similar moment-rotation curves, but subjected to axial loads of 40kN and 80kN, respectively. As indicated in these plots, the concrete block subgrade is much stiffer than the timber block subgrade. It is concluded that the rotational stiffness of the baseplate increases with the increasing modulus of subgrade reaction.

4.9 Summary

The experimental investigations into the rotational stiffness of semi-rigid baseplate have demonstrated that two of the major factors that influence the rotational stiffness of baseplate are the applied column axial loads and the modulus of subgrade reaction. The different scales of axial loads and two types of subgrade materials were used in the investigations.

The test rig specifically designed for the investigations is unique and has proved to be successful. It is easy to assembly and convenient to operate. The test data treatment is efficient and quick. It can be recommended for determining the rotational stiffnesses of baseplates.

CHAPTER 5 COMPARISON BETWEEN THEORETICAL PREDICTIONS AND EXPERIMENTAL RESULTS

5.1 General outline

The previous two chapters have been devoted to theoretical and experimental investigations into the rotational stiffness of a semi-rigid baseplate and the factors which influence the behaviour of the baseplate. The theoretical predictions and the experimental results will be compared in this chapter. It will be shown that the theoretical model proposed in Chapter 3 for investigating the rotational properties of unbolted baseplates is supported experimentally and therefore it can be used to predict the behaviour of the baseplate under various subgrade and applied axial loads.

The moment-rotation curves are firstly compared for both theoretical predictions and experimental results under two subgrade conditions (concrete block and timber block) and three applied axial loads (20kN, 40kN, and 80kN). This enables some conclusions to be drawn out about the effects of subgrade and the applied axial loads on the rotational stiffness of the baseplate. This section also gives details about how to construct the theoretical model and how to determine its parameters for a practical problem.

Next, the bifurcation bending moment for a set of applied axial loads

is defined, below which the rotational stiffness of a baseplate is independent of this set of applied axial loads. The bifurcation bending moments obtained from experimental investigations and the theoretical model for the subgrade of concrete and timber are compared with each other and, additionally, are compared with that computed by a specially derived formula in Chapter 3.

Then, the initial rotational stiffness and subsequent rotational stiffness of the baseplate are defined and their theoretical predictions are compared with the corresponding experimental results. A procedure to determine the initial rotational stiffness is given and some discussions are made.

Finally, conclusions are drawn from the above comparisons which enable the rotational behaviour of an unbolted semi-rigid baseplate subjected to various subgrade conditions and different applied axial loads to be understood.

5.2 The effects of subgrade and axial load on rotational stiffness of semi-rigid baseplate

The baseplate in the column-baseplate-subgrade system, shown in Fig 3.2 in Chapter 3, transmits forces uniformly from column to subgrade. Usually the baseplate exhibits semi-rigid behaviour, that is, the baseplate is allowed to rotate under the action of applied bending moment due to the deformable subgrade. The rotational stiffness of the baseplate is therefore directly dependent upon the stiffness of the subgrade. In addition, it is easy

to understand that the axial loads applied to the baseplate have a positive influence in resisting overturning, thus contributing further to the rotational stiffness of the baseplate. These effects will be demonstrated in detail in this section by the comparison of the theoretical predictions and the experimental results.

Firstly, experimental results, that is, moment-rotation curves for the concrete subgrade and timber subgrade, can be taken directly from Chapter 4. The theoretical predictions, on the other hand, must be made by using the parameters compatible with those of experiments. The computational model for theoretical prediction is shown in Fig 3.7 in Chapter 3, in which the continuous beam models a baseplate and the support columns model the subgrade. The columns in the model are assumed to be subjected to compression only for the simulation of the action of the subgrade. This model is now employed to analyse the baseplates supported on concrete blocks or timber blocks in the same way as the experiments. It is shown in Fig 5.1.

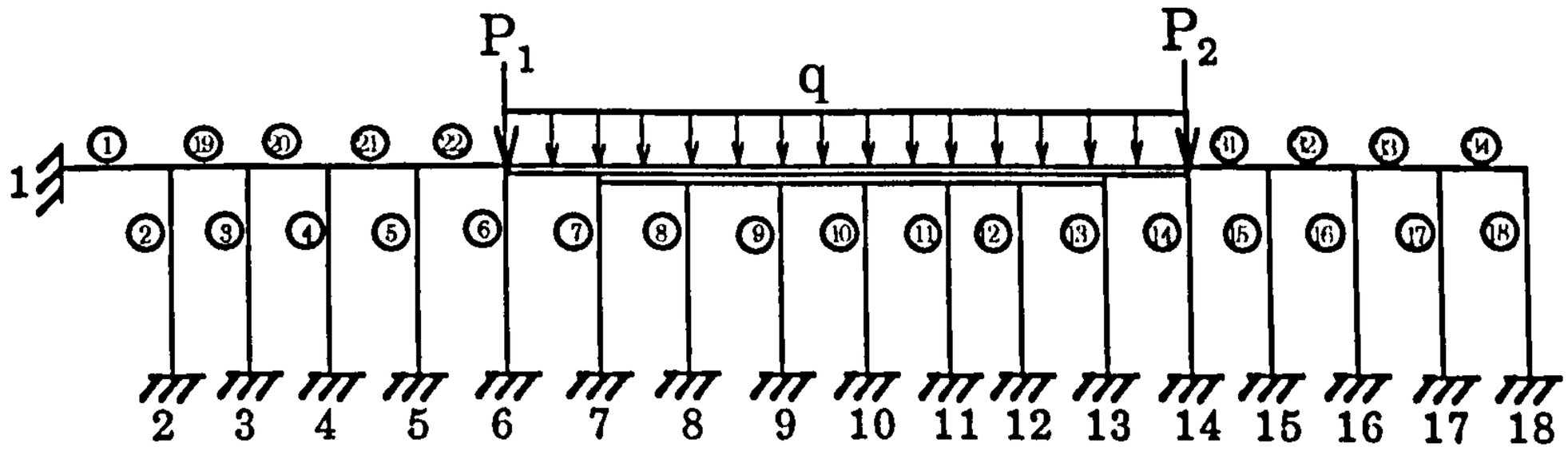

Fig 5.1 Computational model for theoretical predictions

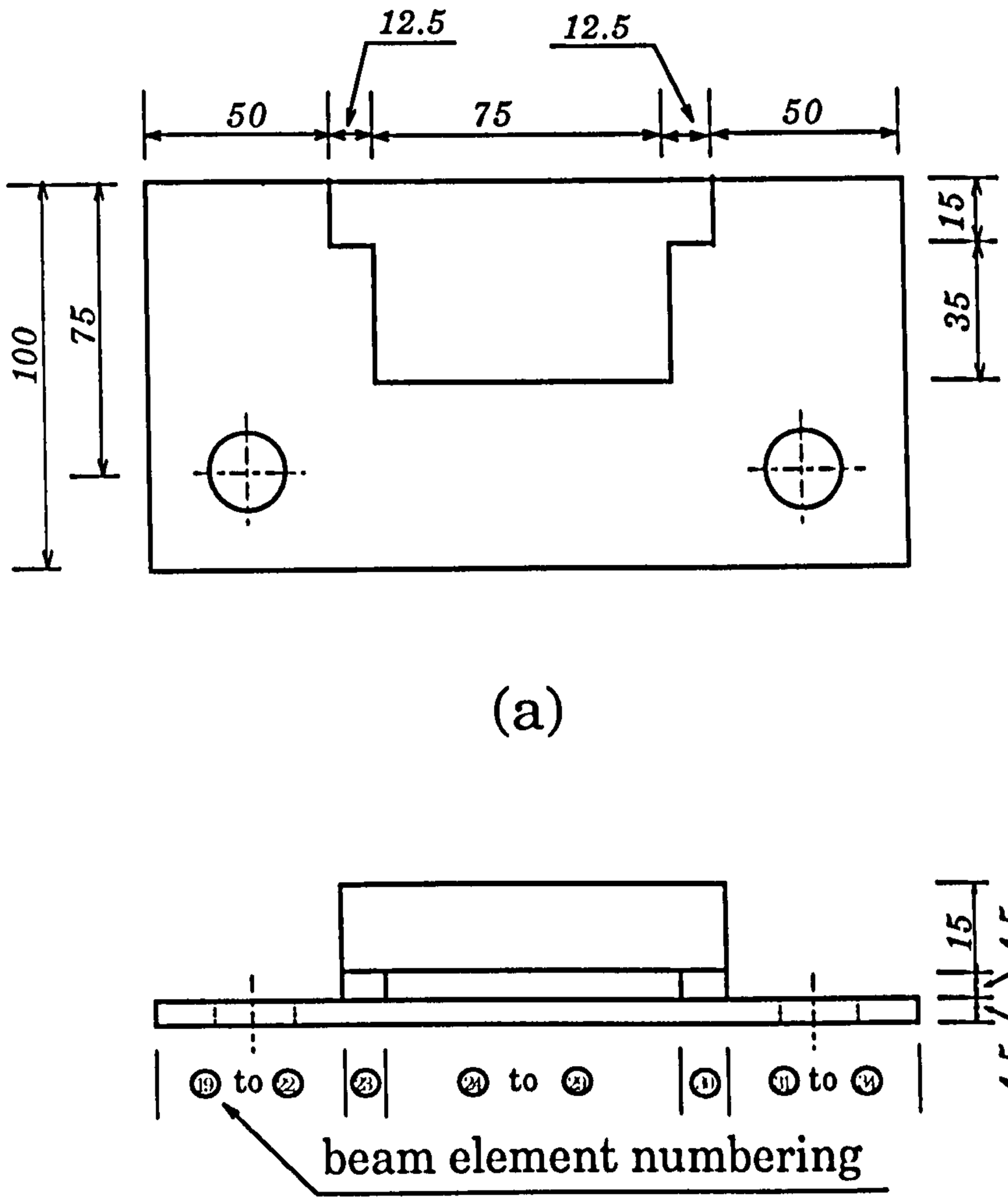

(a)

(b)

Fig 5.2 Baseplate tested(a) and its beam element numbering (b)

The parameters in the experimental model, see Fig 4.5 in Chapter 4, give the corresponding parameters in Fig 5.1 as:

(1) The part of the subgrade which directly supports the baseplate is treated as a series of uniform compression columns. In the current

example, the number of the columns is 17, so the length and the interval of the columns are L=10.0mm and l_n=200.0/(17-1)=12.5mm, respectively.

(2) The modulus of elasticity for the concrete block and the timber block have been experimentally determined as $E_c=2.15\times10^4$ N/mm^2 and $E_t=1.82\times10^2$ N/mm^2, respectively. Because the subgrade, concrete or timber block, is in fact not a semi-infinite body, the formula for calculating the axial compression rigidity of the compression columns, see Eq(3.10a) which was derived based on the assumption of semi-infinite body of subgrade, can be replaced simply by considering the axial rigidity of a small subgrade column with the length of L and width of l_n by a stiffness equivalent method, thus yielding $(EA)_c$=377.38 kN and $(EA)_t$=3.21 kN for the concrete subgrade and the timber subgrade, respectively.

(3) The baseplate, shown in Fig 5.2(a) and assumed to have an elastic modulus of $E_b=2.1\times10^5$ N/mm^2, is modelled by the beam elements numbered in Fig 5.1 and Fig 5.2(b), in which the axial rigidity and the flexural rigidity of the beam elements numbered from 19 to 22 and from 31 to 34 are

$$E_bA_1=(2.1\times10^5)(75.0\times4.5)$$
$$=7.10\times10^4 \text{ kN.mm}^2$$

$$E_bI_1=(2.1\times10^5)(75.0\times4.5^3/12)$$
$$=1.20\times10^5 \text{ kN.mm}^2$$

and those for the beam elements numbered 23 and 30 are

$E_bA_2=(2.1x10^5)(60.0x4.5+15.0x4.5+4.5x15.0)$

$=8.51x10^4$ kN.mm^2

$E_bI_2=(2.1x10^5)[60.0x4.5^3/12+15.0x9.0^3/12$

$+4.5x15.0^3/12+4.5x15.0x(7.5+4.5)^2]$

$=2.60x10^6$ kN.mm^2

and those for the beam elements numbered from 24 and 29 are

$E_bA_3=(2.1x10^5)(25.0x4.5+50.0x4.5+4.5x15.0)$

$=1.32x10^4$ kN.mm^2

$E_bI_3=(2.1x10^5)[25.0x4.5^3/12+50.0x4.5^3/12$

$+50.0x4.5^3/12+4.5x15.0x(7.5+4.5)^2]$

$=2.51x10^6$ kN.mm^2

(4) The boundary beam element, numbered 1, is added to model the boundary condition, which has an infinitely large axial rigidity and has no flexural rigidity, that is, EA=∞ and EI=0.0.

(5) The axial load, P=$2.5x10^4$N, and the bending moment, M=$2.4x10^5$Nmm, applied on the baseplate are equivalently converted into the action of an uniformly distributed load, q, and two concentrated loads, P_1 and P_2, by means of the static equilibrium of Eq(3.1), which gives

q=125.0 N/mm, P_1=3850.0 N, P_2=8650.0 N

(6) The continuous beam in Fig 5.1, which simulates the baseplate,

will bend under the combined action of the uniformly distributed load, q, and the concentrated loads, P_1 and P_2. The resulting bending moment in the beam, M_b, should be confined within the maximum bending moment, M_p, that the beam could possibly bear, that is, $M_b \leq M_p$. This constraint can be given from the type of steel used for the baseplate.

The maximum bending moment can be determined by

$$M_p = A/2 * \sigma_y * h/2$$

with A and h being the cross section area and the thickness of the baseplate, respectively; σ_y being the yield stress of the baseplate.

Usually two types of steel are used for thin-walled structures according to BS1449 [47]

(a) For steel grade HR43/35:

yield strength, R_e, minimum: 350 N/mm^2

tensile strength, R_m, minimum: 430 N/mm^2

(b) For steel grade HR46/40:

yield strength, R_e, minimum: 400 N/mm^2

tensile strength, R_m, minimum: 460 N/mm^2

The baseplate in the test was made from the steel grade HR46/40, so take σ_y= 460 N/mm^2 with which the maximum bending moment becomes the ultimate bending moment as

$$M_p = A/2 * \sigma_y * h/2$$

$$= 460/4 x (4.5 x 100) x 4.5$$

$$= 2.33 x 10^2 \text{ kN.mm}$$

Having determined the parameters in the computational model of Fig 5.1, we are now in a position to use the modified beam-column analysis computer program FPGRD [46]. We first note that the assumption of no axial tensile rigidity and flexural rigidity in the compression columns means that the solution procedure has to be repeated if some of the compression beams are in tension. This can be done simply by setting the axial rigidity of the compression columns concerned to be zero, and on the subsequent rounds of calculation these deleted compression columns have to be taken into account again if they appear to be compressed rather than tensile. This procedure is carried out until all the columns left are in compression. The rotation of the baseplate is defined as the relative rotation between the left end of the beam element 23 and the right end of the beam element 30, which is based on the average consideration of rotation of the baseplate.

Fig 5.3 shows the comparison of Moment-Rotation Curves for the concrete subgrade obtained from experiments and theoretical predictions with a series of axial loads acting on the baseplate, that is, P_1=20kN, P_2=40kN, and P_3=80kN; while Fig 5.4 gives those for the timber subgrade.

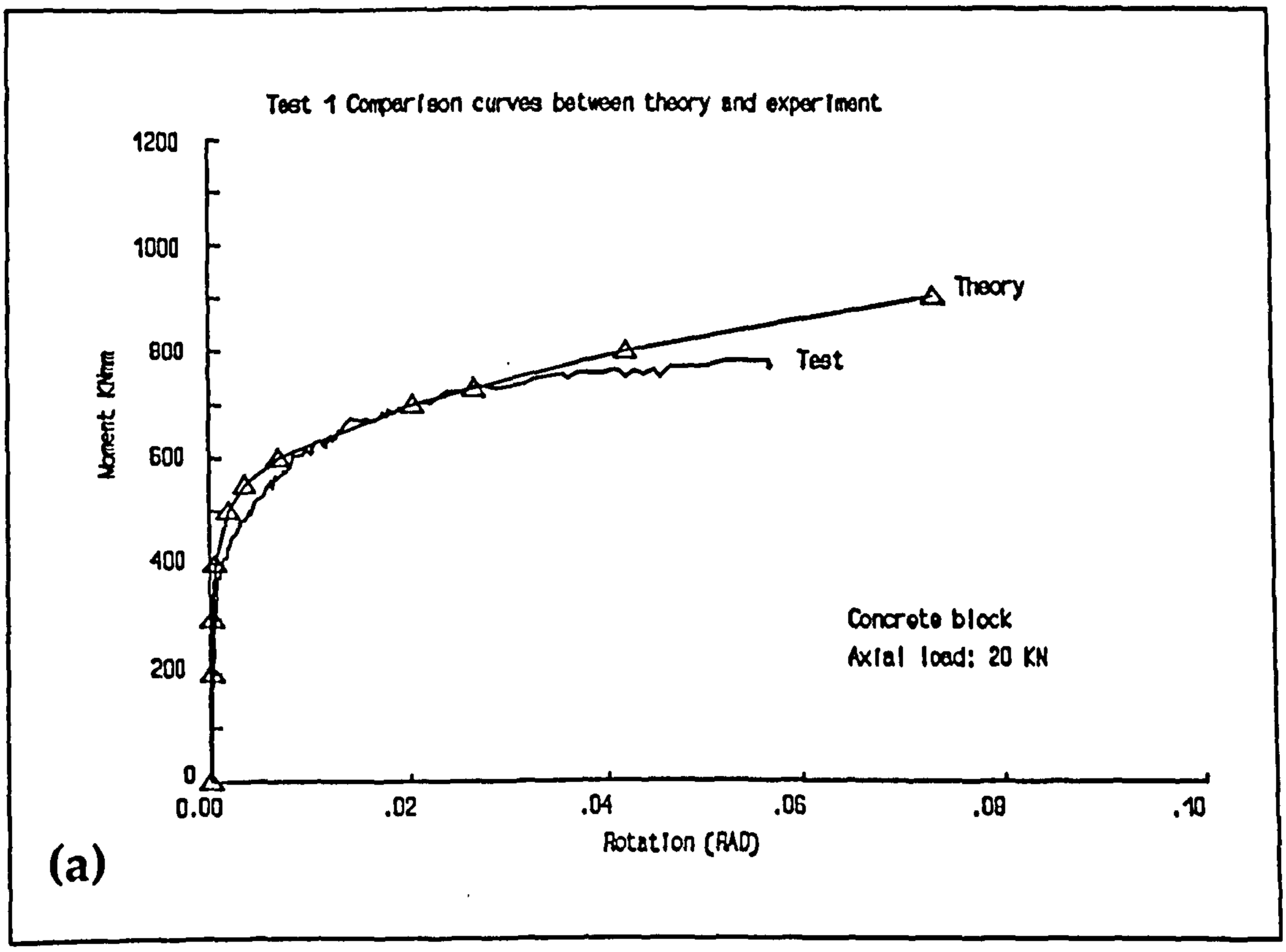
Test 1 Comparison curves between theory and experiment
Moment KNm
1200
1000
800
600
400
200
0
Theory
Test
Concrete block
Axial load: 20 KN
0.00
.02
.04
.06
.08
.10
Rotation (RAD)
(a)

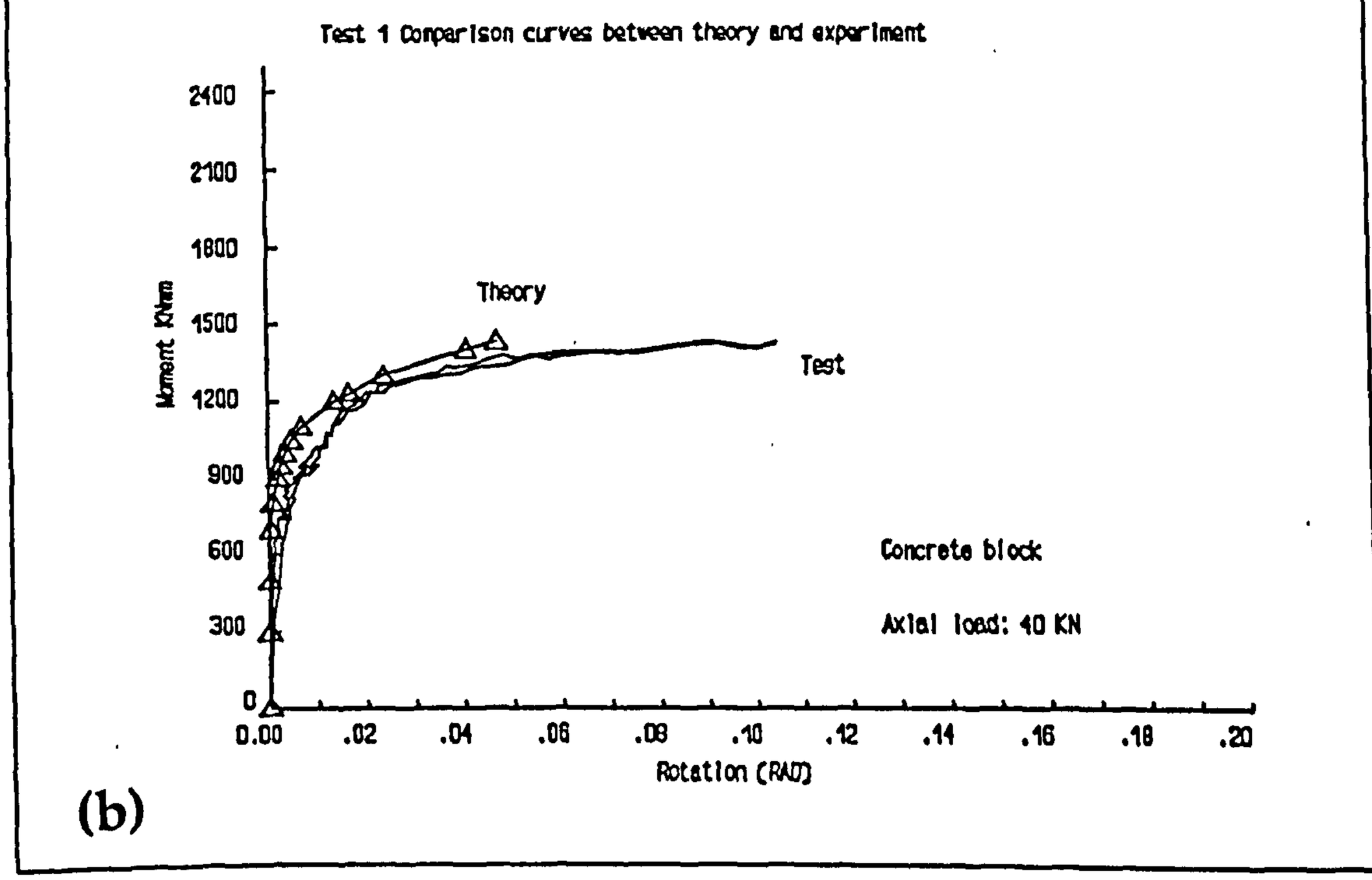
Test 1 Comparison curves between theory and experiment
Moment KNm
2400
2100
1800
1500
1200
900
600
300
0
Theory
Test
Concrete block
Axial load: 40 KN
0.00
.02
.04
.06
.08
.10
.12
.14
.16
.18
.20
Rotation (RAD)
(b)

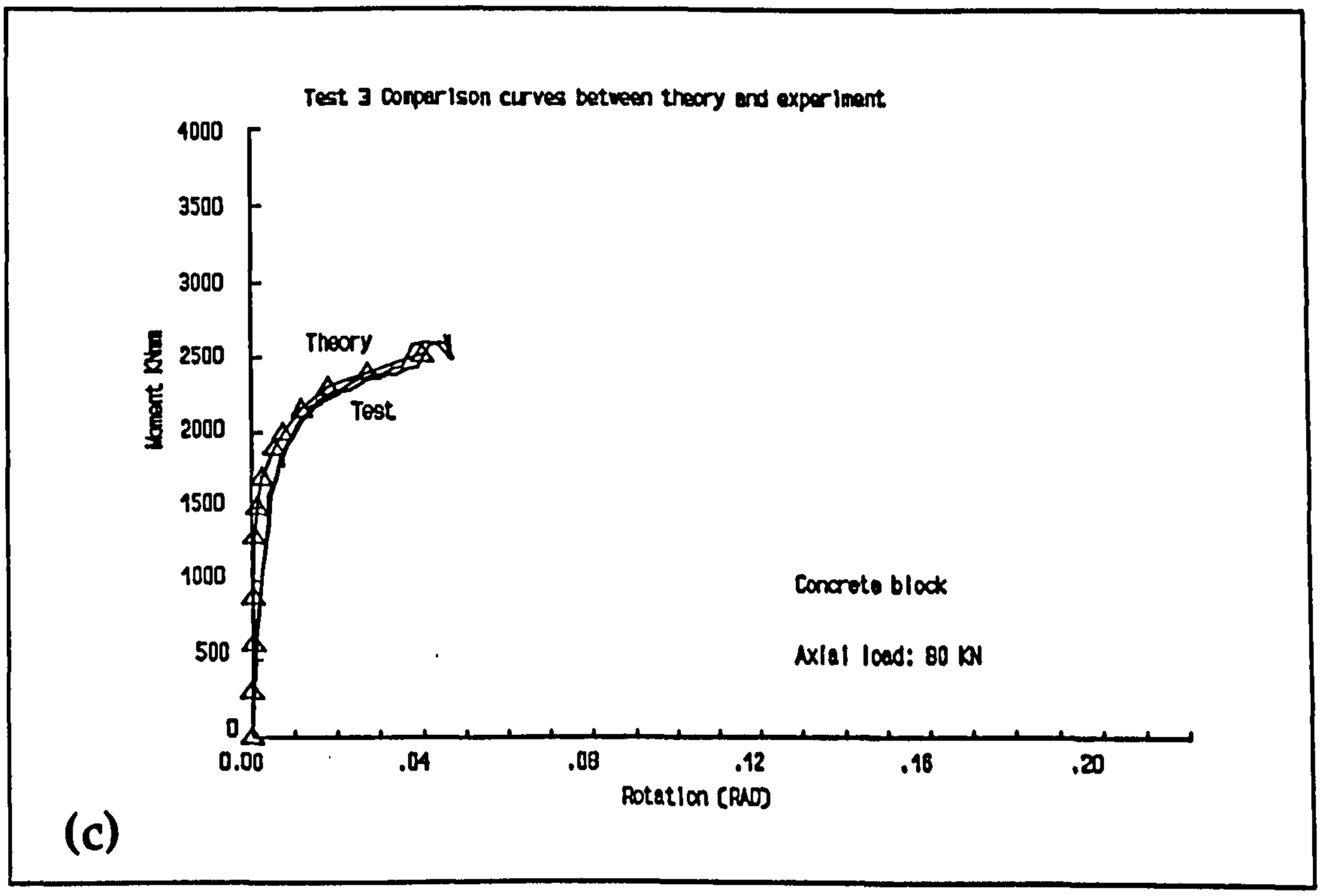

Fig 5.3 Moment-rotation curves for concrete Subgrade under different axial loads (a) P_1=20kN; (b) P_2=40kN; and(c) P_3=80kN

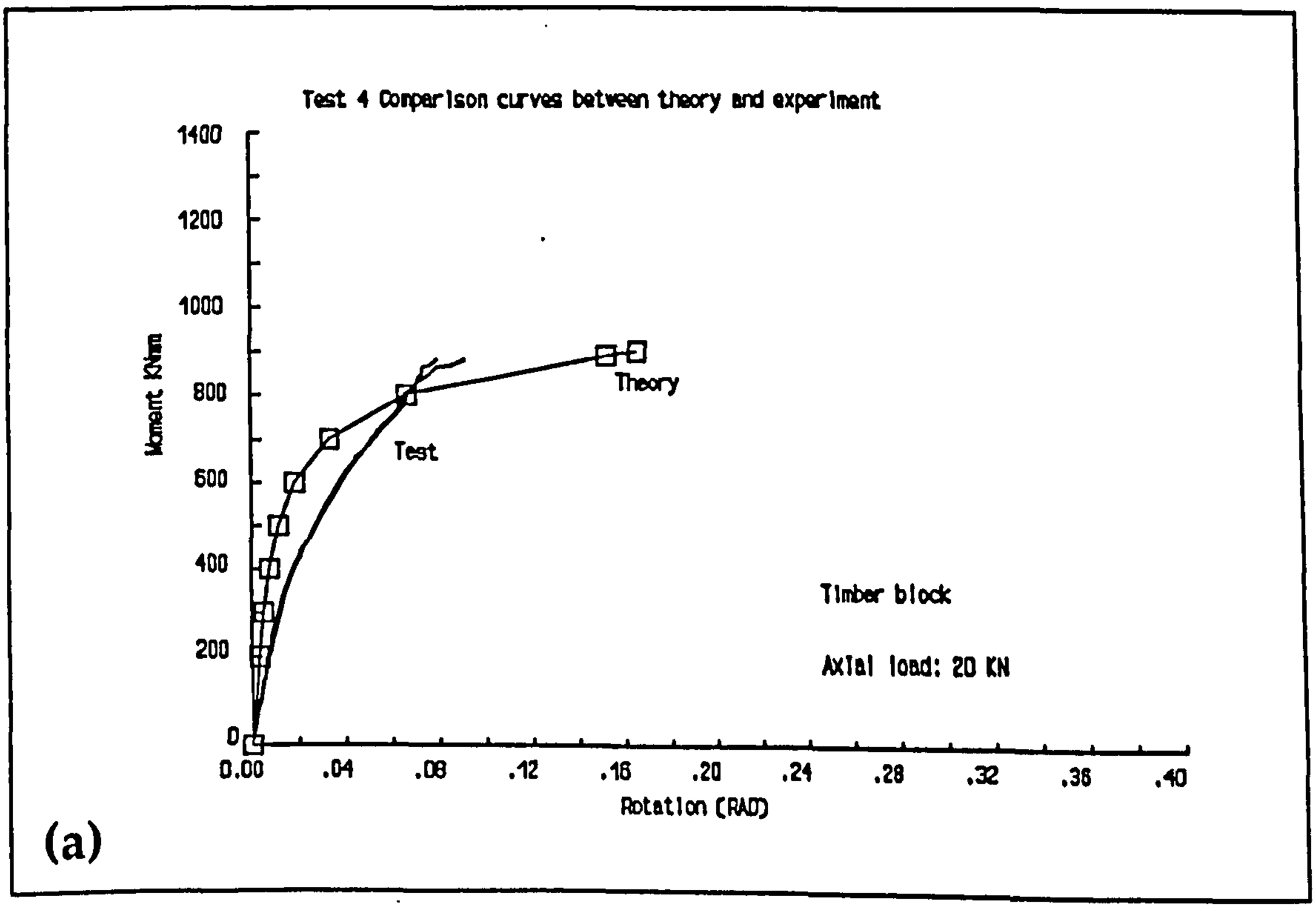

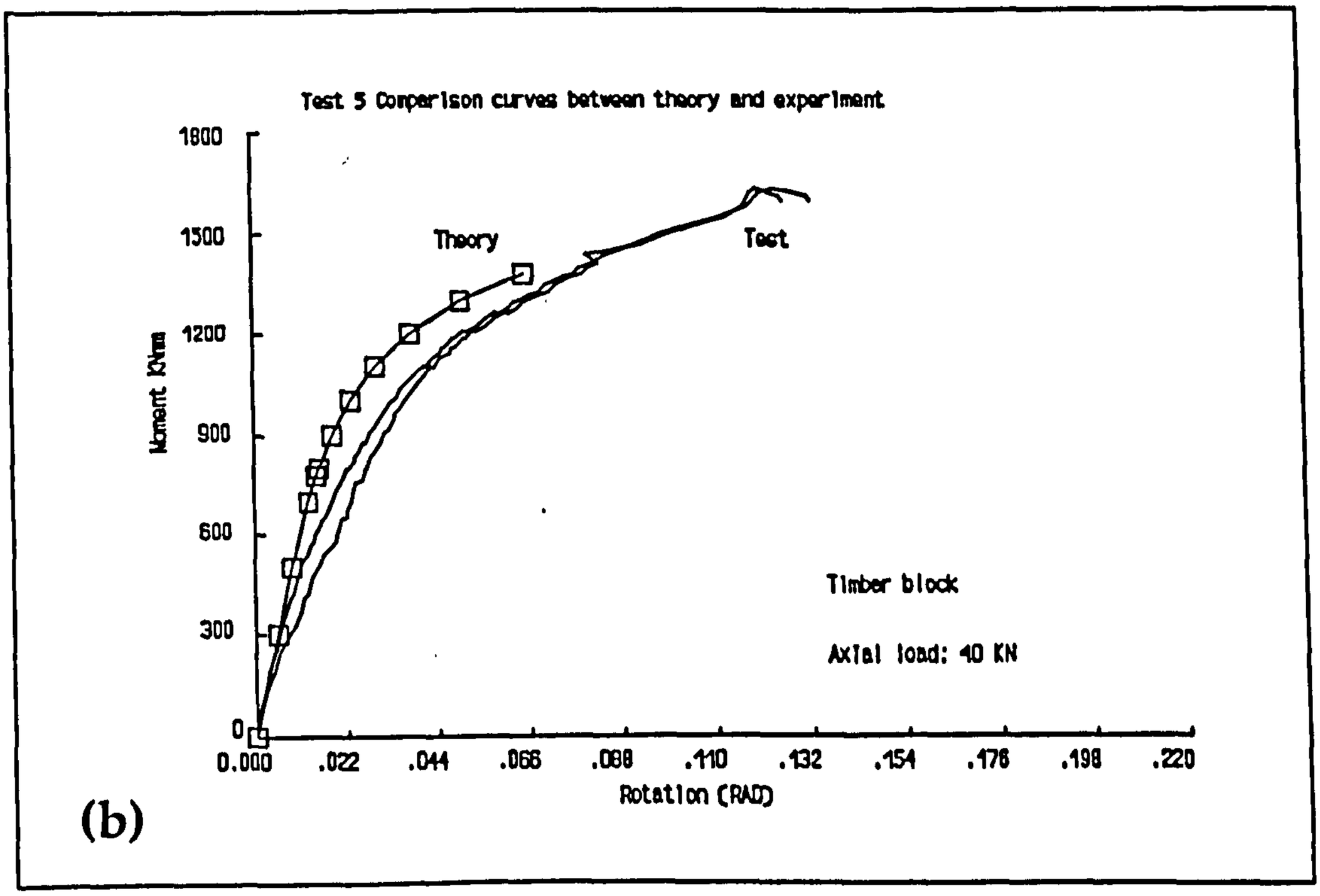

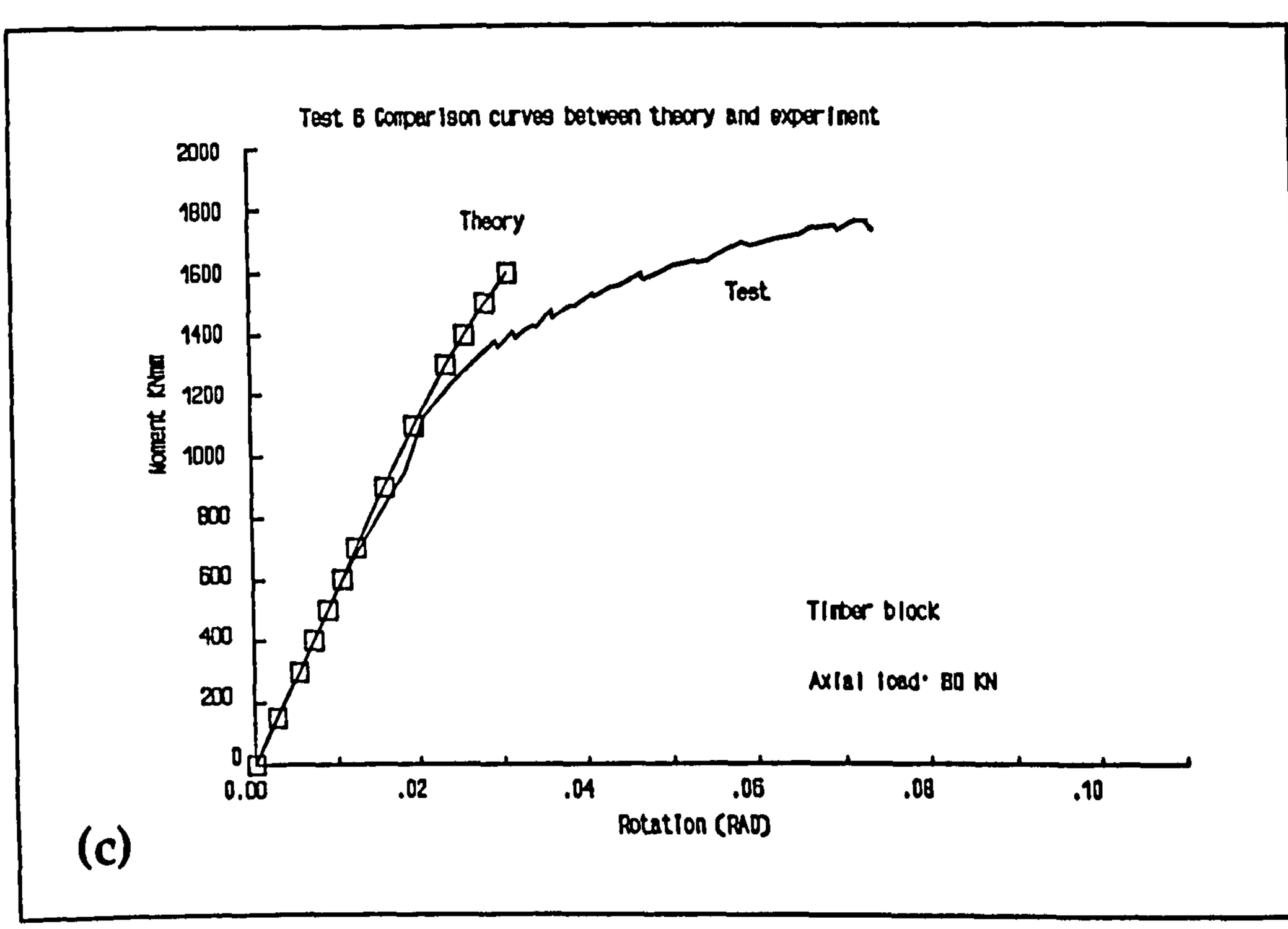

Fig 5.4 Moment-rotation curves for the timber subgrade under different axial loads (a) P_1=20kN; (b) P_2=40kN; and (c) P_3=80kN

It can be seen from Fig 5.3 for the concrete subgrade that the moment-rotation curves of theoretical predictions fit quite well with those of experiments. In the case of the timber subgrade, Fig 5.4, the curve fitting is good for small rotations, but for large rotations the gap between theoretical predictions and experiments becomes pronounced. This can be explained by the anisotropy of timber.

The above comparison between the theoretical predictions and experiments suggests that, as a whole, the theoretical model can give quite good moment-rotation curves for subgrades which were made of isotropic materials such as concrete, and it can also give reasonable results for small rotations for subgrade that were made of anisotropic materials such as timber.

The above calculation and comparison also allow us to conclude that the moment-rotation curves, or the rotational stiffness of the baseplate, are closely related to the rigidity of the subgrade, and to the applied axial loads as well. The rotational stiffness of the baseplate, defined as the secant stiffness of the moment-rotation curve, increases with increasing rigidity of the subgrade, and also increases with increasing axial loads. This is due to the positive effects of the applied axial loads on the stability of the baseplate.

5.3 Bifurcation bending moment

The preceding section demonstrated that the moment-rotation curves are different with the different axial loads that were applied to the baseplate. This gives rise to the question of whether there exists a coincident part of these moment-rotation curves. The answer is positive.

We assume that the baseplate is subjected to a series of axial loads, $P_1,P_2,...,P_n$, with the constraint of $P_i<P_{cr}$ (i=1,2,...,n) where P_{cr} is the critical load of the column joined to the baseplate. Section 5.2 and Section 3.3 indicated that there exists one moment-rotation curve for one applied axial load P_i (i=1,2,...,n), and there exists a bending moment which is defined as critical bending moment denoted as M_{0i} (i=1,2,...,n). The moment-rotation curve remains straight (or linear) until the applied bending moment exceeds the critical bending moment. The *Bifurcation Bending Moment* for a specified series of axial loads, $P_1,P_2,...,P_n$, is defined as

$$M_0=\min(M_{0i}) \quad \text{with } i=1,2,...,n$$

or

$$M_0=M_{01}$$

if this set of axial loads satisfy: $P_1<P_2<...<P_n$.

The physical meaning of the bifurcation bending moment is demonstrated schematically in Fig 5.5.

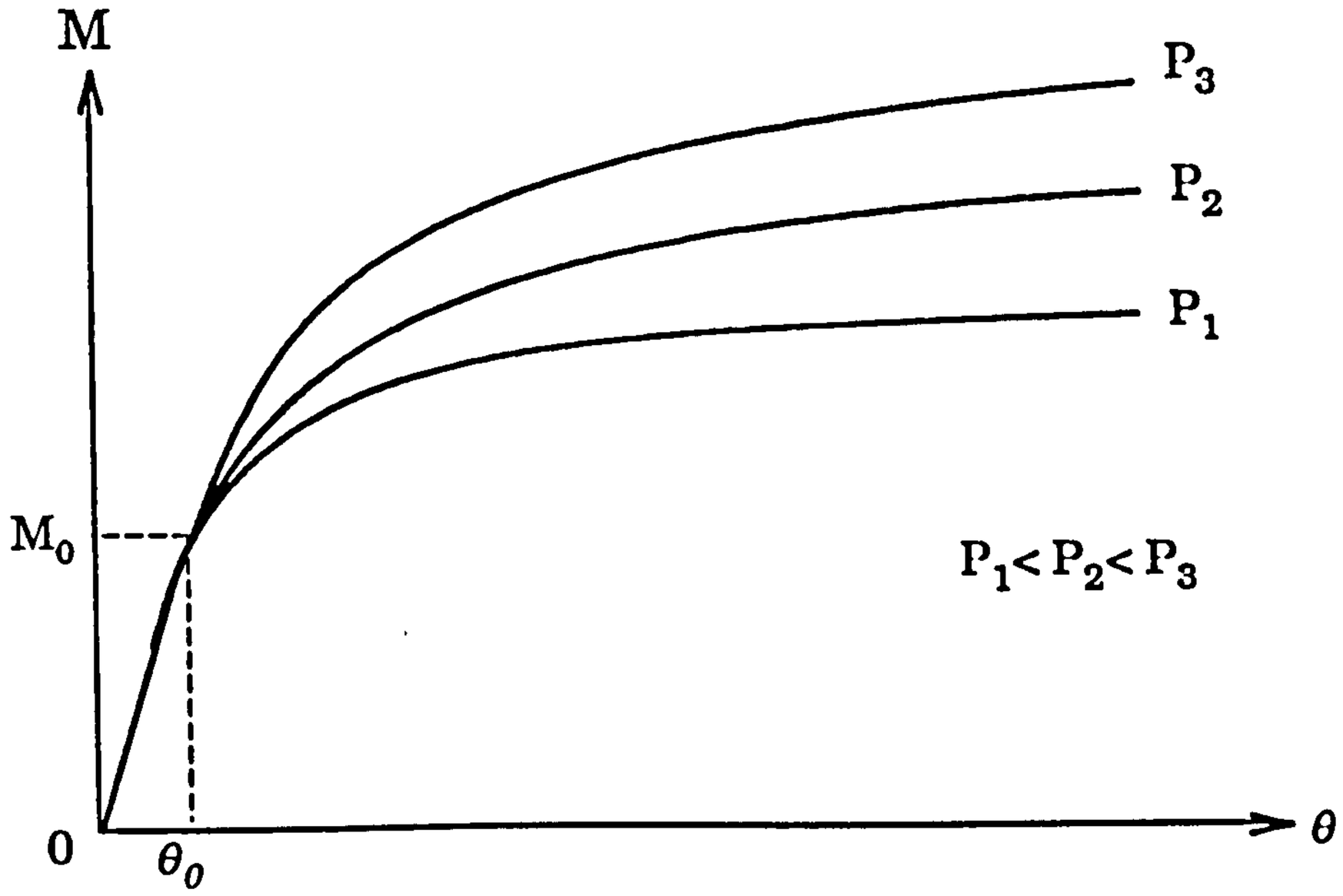

Fig 5.5 Bifurcation bending moment M_0

The above facts are confirmed by grouping into a single plot the three experimental moment-rotation curves of the baseplate subjected to the axial loads of P_1=20kN, P_2=40kN, and P_3=80kN, respectively, for the concrete subgrade, shown in Fig 4.16, and the same procedure for the timber subgrade, which is demonstrated in Fig 4.17. These two plots show that the bifurcation bending moment does exist.

Alternatively but more accurately, an analytical formulation for calculating the critical bending moment has been given in Section 3.4.2 of Chapter 3, the application of it to the current problems yields

$$M_0 = 205 \text{ kN.mm}$$

for the concrete block; and

$$M_0=31 \text{ kN.mm}$$

for the timber block.

The comparison of these two computed bifurcation bending moments with those of experiments in Fig 4.16 and Fig 4.17 gives reasonable agreement. It is seen from this comparison that the experiments can only give qualitative results to the bifurcation bending moment whilst the theoretical methods can give quantitative predictions.

As has mentioned, the bifurcation bending moment M_0 is dependent on the smallest axial load P_1 in a given series of axial loads, $P_1<P_2<...<P_n<P_{cr}$, acting on the baseplate. M_0 increases with increasing P_1, so the smallest axial load, P_1, of the load series, $P_1<P_2<...<P_n$, directly affects the stability of the baseplate.

5.4 Initial and subsequent rotational stiffness of baseplate

The previous section gave the bifurcation bending moment M_0 for a set of axial loads, below which the moment-rotation curves remain straight or linear. By definition of Section 3.3 in Chapter 3, the rotational stiffness of the baseplate is the secant of the moment-rotation curve, so the straight line in the moment-rotation curve implies that the rotational stiffness of the baseplate is a constant until the applied bending moment exceeds the bifurcation bending moment. This constant rotational stiffness is defined as the initial rotational stiffness of the baseplate, and the others are defined as subsequent rotational stiffness which is dependent on the applied axial

loads.

Fig 5.5 shows that the secant of the common straight line of the moment-rotation curves is axial load independent and is constant for a given subgrade. The method to determine the initial rotational stiffness of the baseplate k_0 has been discussed extensively in Chapter 3. The corresponding computer program is BEAMC [55]. The computed results of k_0 by BEAMC are $k_0=5.96\times10^5$ kN.mm/rad for the concrete subgrade and $k_0=3.6\times10^4$ kN.mm/rad for the timber subgrade. Compared with the experimental results, see Fig 4.16 and Fig 4.17, where $k_0=5.48\times10^5$ kN.mm / rad for the concrete subgrade and $k_0=3.46\times10^4$ kN.mm/rad for the timber subgrade which are obtained using the curve fitting techniques, it is concluded that the methodology used in Chapter 3 to determine the initial rotational stiffness of the baseplate is correct.

The subsequent rotational stiffness of the baseplate is nonlinear and axial load dependent. This occurs for large rotations of the baseplate or small axial loads acting on the baseplate. Nonlinearity due to large rotations of the baseplate is easily understood, while that due to small applied axial loads is because of the loss of the ability of overturning resistance contributed by the applied axial loads.

In general, due to the nonlinearity of the rotational stiffness of the baseplate, an iterative routine is usually to be adopted when the applied bending moment exceeds the bifurcation bending moment which will be further explained in Chapter 7.

The knowledge of the initial rotational stiffness of the baseplate, corresponding to a set of given axial loads, may be useful for the analyst to simplify the analysis and to estimate the range of effectiveness of the constant rotational stiffness model. Increasing the axial loads or the vertical loads acting on a column joined to a baseplate increases the stability of the baseplate, thus increasing the rotational stiffness. However, in this case we must consider the ability of column buckling resistance. Some compromise is often made between these two factors to adapt to practical needs.

5.5 Conclusions

The results of predictions and experiments have been compared and concluded in this chapter. The correctness and effectiveness of the theoretical model proposed in Chapter 3, the associated computational methods and the computer programs [55] have been examined and validated by good agreement between the predictions and the experimental results. The comparison suggested that the theoretical model is more suitable for predicting the rotational stiffness of the baseplate supported on subgrade with isotropic materials like concrete. However, it can also give reasonable results if rotations are limited for subgrade with anisotropic behaviour like timber. Therefore, the computational model and the methods proposed can replace experiments in some cases to predict the rotational stiffness of baseplate.

It has been demonstrated from both experimental studies and the theoretical model that the rotational stiffness of the baseplate has shown to

be closely dependent on the rigidity of the subgrade and on the applied axial loads. The rotational stiffness increases with increasing rigidity of the subgrade, and with increasing applied axial loads.

The investigations indicated that the bifurcation bending moment exists in predictions and experiments, which could be useful in practice. The effectiveness of the commonly used constant rotational stiffness model can be estimated in this way, and the appropriate column-baseplate-subgrade system can be designed to bear the applied loads. These properties of baseplate will be used in the subsequent chapters.

CHAPTER 6 BUCKLING ANALYSIS FOR CRITICAL LOADS AND BUCKLING MODES

6.1 General outline

A slender structure will usually fail by overall buckling if the axial loads acting on it reach their critical values.

An example of slender frame structure is the pallet rack system shown in Fig 3.1 commonly used in factories and stores for the storage of palletized goods. Such a slender structure is often made from cold-formed steel structural members with various shapes of thin-walled sections such as channel, hat sections and I-sections. With increasing applications in industry and supermarkets, this type of structure is being constructed with more storeys and greater storage heights. Thus, the structure is becoming higher and more slender, and the stability behaviour of the structure becomes even more dominant in the design.

As mentioned in Chapter 1, a simplified model and the associated computational approach are required by industry to analyze the stability behaviour of slender frame structures. It has been commonly accepted that the joints in cold-formed steel structures exhibit semi-rigid characteristics. For example, the beam-column joints in the pallet rack structure are often formed by hooks and slots, thus having semi-rigid behaviour. For the

column-baseplate joints, as described in Chapters 2 and 3, it has been shown that the rotational stiffness of the joints exhibits nonlinear characteristics, axial load dependence, and subgrade dependence. Therefore, the simplified model has to consider the semi-rigid behaviour of both beam-column joints and column-baseplate connections.

Upon the above considerations, a simplified structural model and associated computerized approach are developed in this chapter taking into account the semi-rigid characteristics of joints.

The first part of the chapter is to construct the structural model for buckling analysis. Significant consideration is given to the rotational stiffness of the beam-column and column-baseplate joints to simulate the action of the link beams and the baseplate upon the column. The second part derives the equivalent rotational stiffness of beam-column joints and column-baseplate connections. The equivalent beam-column rotational stiffness is obtained by considering the two beams, one on each side of the column with their own end semi-rigid properties. Meanwhile, the rotational stiffness of baseplate is provided by the previous chapters. The third part formulates the buckling equations. By the exact analysis of the column elements, the bending equilibrium at the joints of beam-column and column-baseplate is constructed, and a set of homogeneous linear matrix equations are obtained. The condition of non-trivial solution of the equations leads to the buckling equations for elastic critical loads. The fourth part presents an efficient algorithm to find the critical loads. The fifth part deals with the determination of the buckling modes corresponding to the fundamental buckling load. The sixth part gives some numerical illustrations of the application of the method to a multi-bay slender frame

structure with variable number of storeys, semi-rigid baseplates and beam-column joints. The comparison between the computed results and those of other methods is made to demonstrate the effectiveness of the simplified model and the associated computational method.

6.2 The simplified model for buckling analysis

It is easily understood that the deformation modes of unbraced slender frame structures subjected to both vertical and horizontal loads usually take the form of sway. Such unbraced slender frame structures normally consist of many bays with each identically loaded. We can therefore use a single column structural model based on a single bay to model such unbraced slender frame structures, as indicated in Fig 6.1, where the loads from the beams are equivalently applied to the centre line of the column as concentrated loads, the rotational stiffness of the column due to the restraint of beams is represented by an equivalent rotational stiffness.

The model in Fig 6.1 consists of n sections with each having a height of l_i (i=1,2,...,n), which are the same heights as those in the corresponding slender frame structure. k_0 is the rotational stiffness of semi-rigid column-baseplate joint, which has been investigated systematically in Chapters 3 and 4. k_i (i=1,2,...,n) are the equivalent rotational stiffness on the positions of beam-column joints, where the joints can displace horizontally. The external loads acting on it are assumed to be vertical axial loads only, which include the statically equivalent parts coming from the link beams.

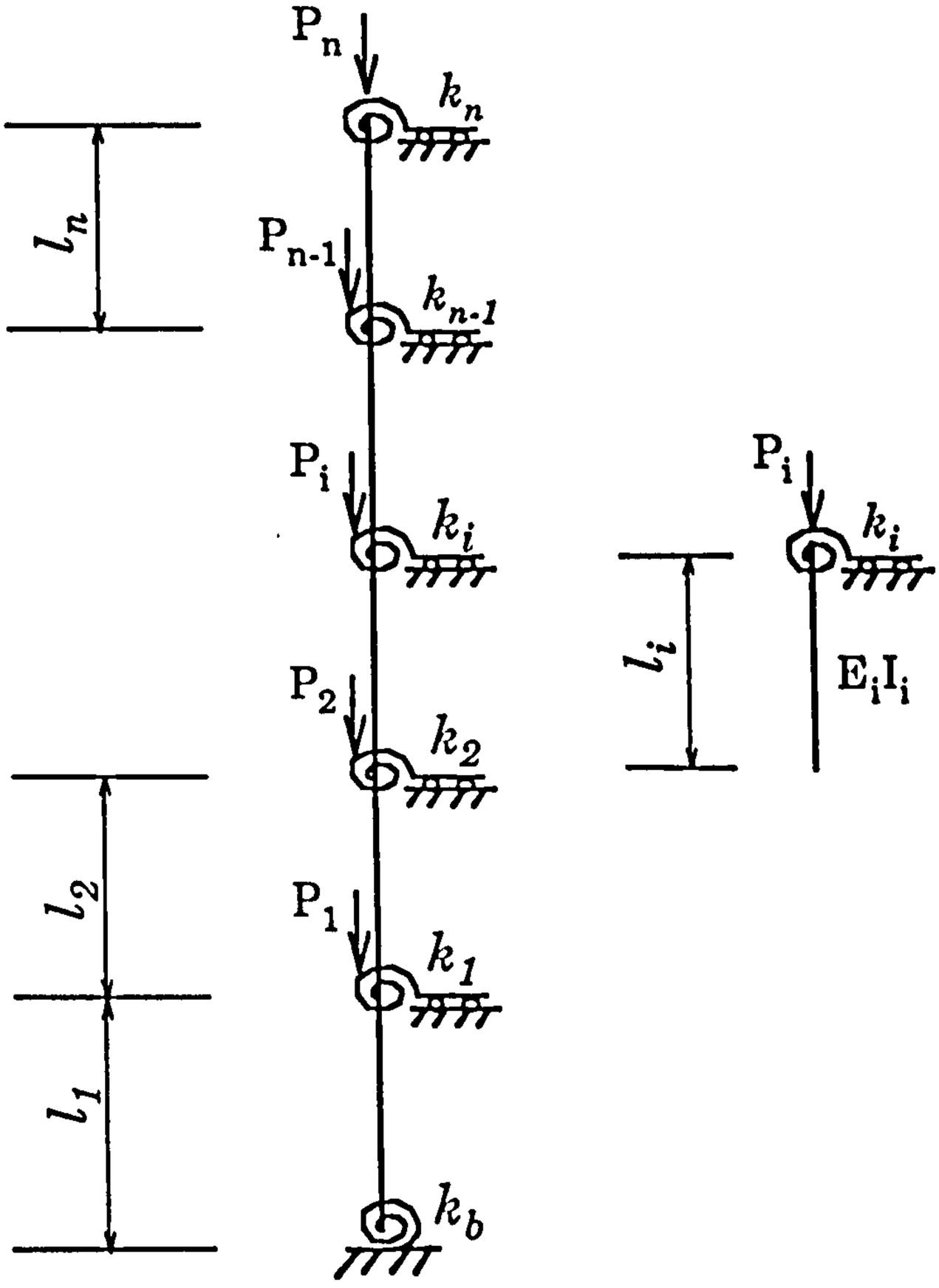

Fig 6.1 Structural model for buckling analysis

The typical i-th column element has length l_i, flexural rigidity E_iI_i, and semi-rigid column-beam rotational stiffness k_i. Fig 6.2 shows the possible buckling mode of the unbraced framework of Fig 6.1, corresponding to the lowest critical load.

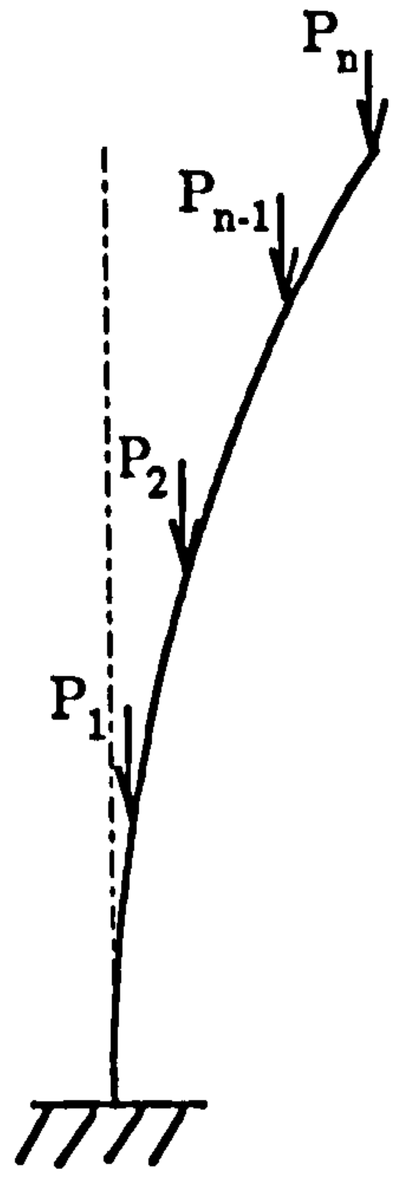

Fig 6.2 Possible buckling mode

This simplified model for unbraced slender frame structure will be used subsequently throughout this thesis but with a different external loading system in a Second-order Analysis in Chapter 7.

6.3 The equivalent rotational stiffness of beam-column connections

The rotational stiffness k_i (i=1,2,...,n) represents the rotational characteristics of the beam to column connections, i.e., the bending moment required to produce unit rotation on the column, while k_0 refers to the

rotational characteristics of the baseplate which has been given in Chapter 3.

Beam-to-column joints in cold-formed steel structures are of many types. For thin-walled steel section members, the beam-column joints are often formed by hooks and slots (see Fig 6.3). This kind of joint may have different rotational characteristics on the right end and the left end of the beam. So in the model for deriving the beam-to-column rotational stiffness at i-th beam level, shown in Fig 6.4, we assume that $k_{li} \neq k_{ri}$ where k_{li} and k_{ri} denote the rotational stiffness on the left end and the right end of beam element, respectively.

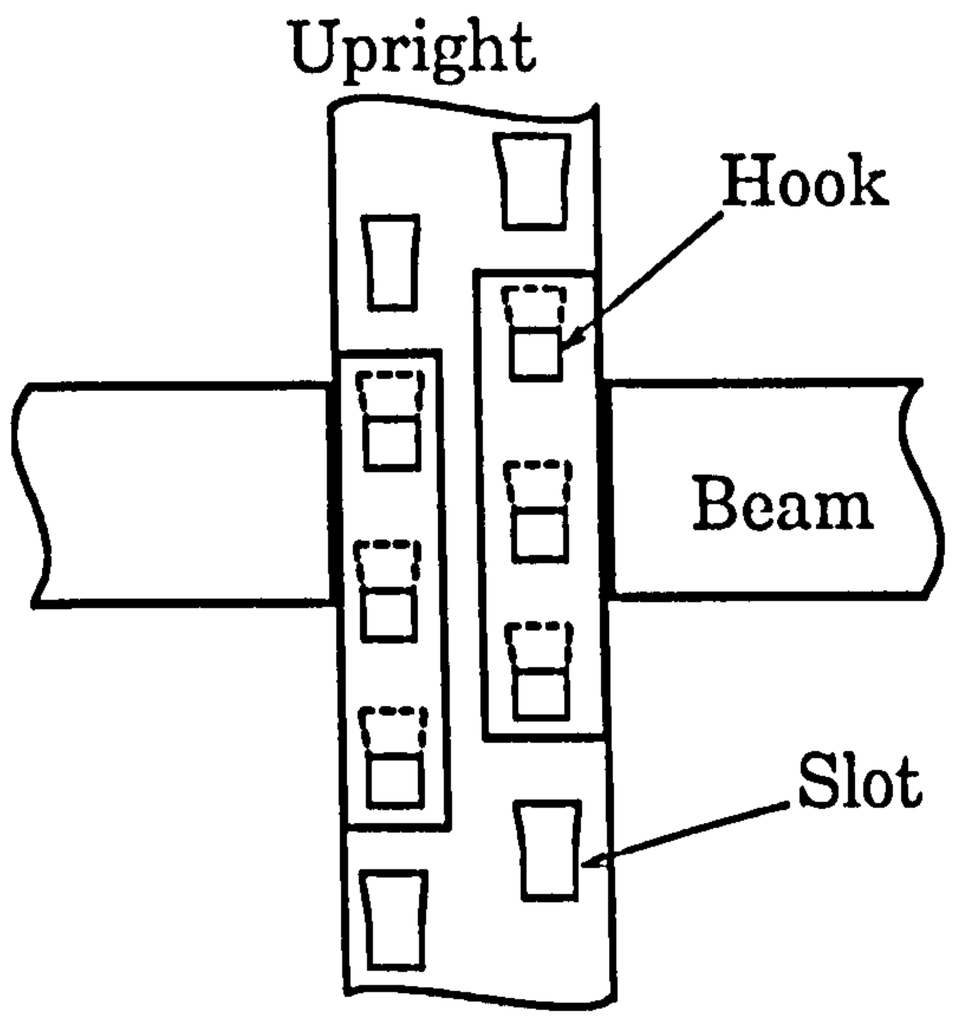

Fig 6.3 Typical beam-column hook and slot connection

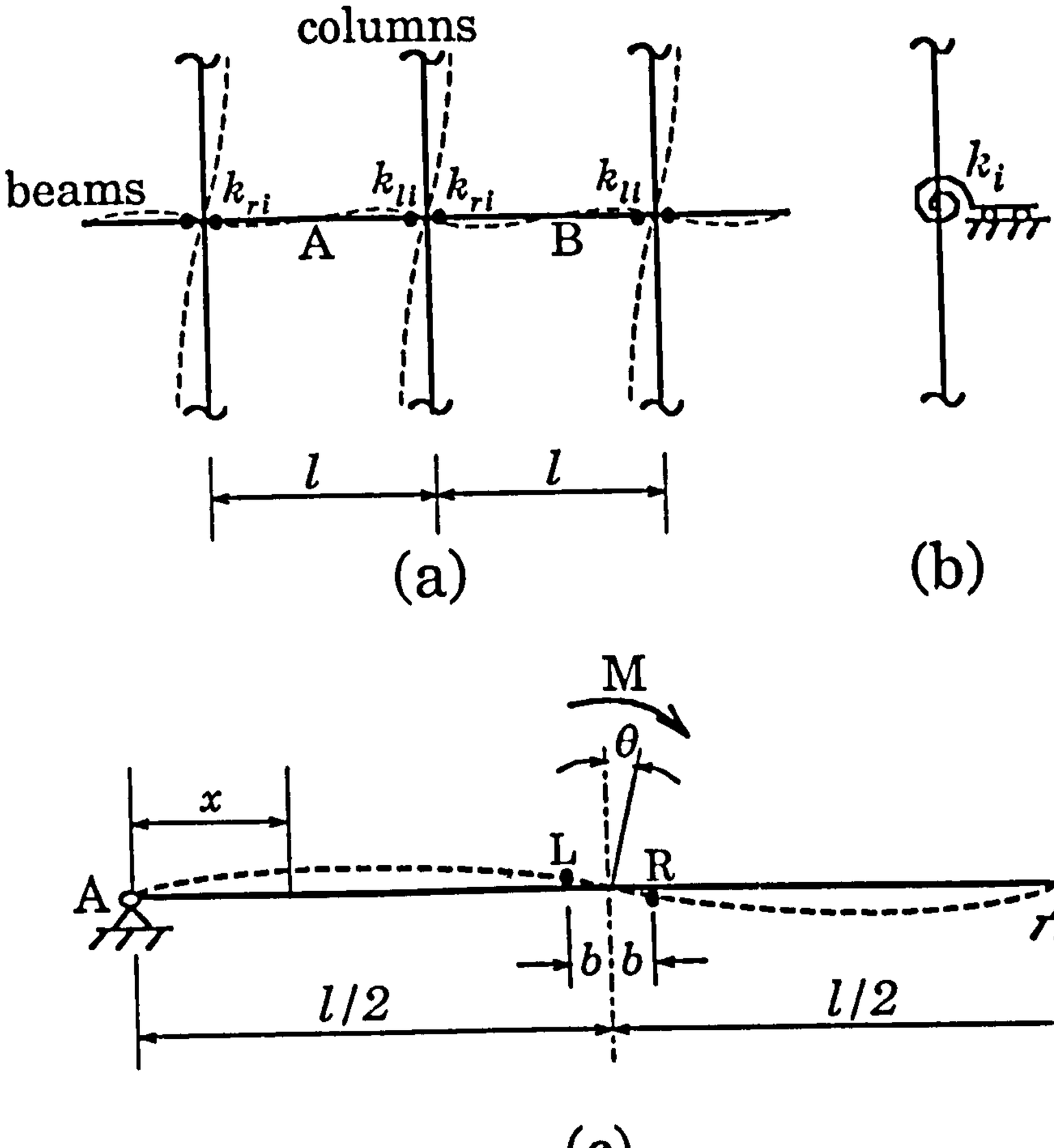

Fig 6.4 Equivalent rotational stiffness

Because we are considering a multi-bay slender frame structure with no sway bracing, the likely deformed shape of the beam is the dotted line in Fig 6.4(a). Fig 6.4(b) shows that the rotational restraint of beams on column on i-th level is taken as an equivalent rotational stiffness of column on that level, denoted as k_i.

The equivalent rotational stiffness k_i can be derived based on the model in Fig 6.4(c) which is taken from Fig 6.4(a). In this model, the semi-rigid joints of beams to column are simulated by springs L and R, their distance from the centre line of the column b is a small number.

The complementary energy of the structure in Fig 6.4(c) can be written as:

$$U=\int_0^{\frac{l}{2}-b}\frac{1}{2}.\frac{M^2(x)}{(EI)_i}dx+\int_{\frac{l}{2}+b}^{l}\frac{1}{2}.\frac{M^2(x)}{(EI)_i}dx+\frac{M_L^2}{2k_{li}}+\frac{M_R^2}{2k_{ri}} \qquad (6.1)$$

where M_L and M_R are the internal bending moments acting on the left spring L and the right spring R, respectively. M(x) represents the internal bending moment at the cross section of x. $(EI)_i$ is the flexural rigidity of the beam. k_{li} and k_{ri} are the rotational stiffness on the left and right springs, respectively.

Because the distance b is very small, the complementary energy in the beam segment LR is ignored and so it is not included in Eq(6.1).

Integrating Eq(6.1) gives

$$U=\frac{M^2}{2}[\frac{2}{3(EI)_i l^2}.(\frac{l}{2}-b)^3+\frac{1}{k_{li}l^2}.(\frac{l}{2}-b)^2+\frac{1}{k_{ri}l^2}.(\frac{l}{2}-b)^2] \qquad (6.2)$$

Because l/2 is far larger than b, we have the approximation, l/2-b≈l/2. Then, Eq(6.2) becomes,

$$U=\frac{M^2}{2}\left[\frac{l}{12(EI)_i}+\frac{1}{4k_{li}}+\frac{1}{4k_{ri}}\right] \qquad (6.3)$$

Taking the variation of complementary energy U with respect to bending moment M gives the rotation corresponding to M,

$$\frac{\partial U}{\partial M}=\theta=M\left[\frac{l}{12(EI)_i}+\frac{1}{4k_{li}}+\frac{1}{4k_{ri}}\right] \qquad (6.4)$$

By definition, rotational stiffness refers to the bending moment required to produce unit rotation. Thus, we obtain the equivalent rotational stiffness in Fig 6.4(b) as follows

$$k_i=\frac{1}{\left[\frac{l}{12(EI)_i}+\frac{1}{4k_{li}}+\frac{1}{4k_{ri}}\right]} \qquad (i=1,2,...,n) \qquad (6.5)$$

The equivalent rotational stiffness k_i in Eq(6.5) has incorporated the effects of the flexural rigidity of the beams joining the column and the effects of semi-rigid behaviour of the joints linking beam and column. If no semi-rigid behaviour of the beam-column joints is considered, that means that the beams have no relative rotations at the positions of beam-column joints, then k_i reduces to the common case of a rigid beam-column joint which is given by letting k_{li} and k_{ri} approach infinity as follows

$$k_i=12\frac{(EI)_i}{l} \qquad (6.6)$$

Alternatively, Eq(6.5) can also be derived following the procedure suggested by Chen and Lui [49].

6.4 Derivation of the buckling equations

The equilibrium equations for the simplified structural model in Fig 6.1 are now to be derived. Three steps are followed.

Firstly, consider the equilibrium of an isolated column element, as shown in Fig 6.5. It is subjected to the forces (P,Q_{AB},M_{AB}) and (P,Q_{BA},M_{BA}) acting on the element end A and end B, respectively, where P refers to the axial force, Q to the shear force and M to the bending moment. The deformation of the element is characterized by the relative transverse displacement Δ, the rotations θ_A and θ_B at ends A and B, respectively.

It is assumed that the axial rigidity of the column is large enough, relative to its flexural rigidity, to allow the axial deformation to be ignored.

By solving a second-order differential equation on bending equilibrium of the column element, the transverse displacement function w(x) can be expressed in terms of the end forces, the end bending moments, and the two unknown constants. After determining the unknown constants using the boundary conditions, the slope-deflection relations can be obtained as follows:

$$M_{AB}=4i\theta_A\varphi_2(v)+2i\theta_B\varphi_3(v)-6i\frac{\Delta}{l}\eta_3(v)$$

$$M_{BA}=2i\theta_A\varphi_3(v)+4i\theta_B\varphi_2(v)-6i\frac{\Delta}{l}\eta_3(v) \qquad (6.7)$$

$$Q_{AB}=Q_{BA}=-\frac{6i}{l}\theta_A\eta_3(v)-\frac{6i}{l}\theta_B\eta_3(v)+12i\frac{\Delta}{l^2}\eta_2(v)$$

and $\varphi_i(v)$,(i=1,2,3,4), $\eta_2(v)$, and $\eta_3(v)$ are transcendental functions in terms of v or P as follows

$$\varphi_2(v)=\frac{1-\frac{v}{tanv}}{\frac{\tan\frac{v}{2}}{\frac{v}{2}}}$$

$$\varphi_3(v)=\frac{\frac{v}{sinv}-1}{\frac{\tan\frac{v}{2}}{\frac{v}{2}}}, \qquad \eta_2(v)=\varphi_4(v)-\frac{v^2}{12} \qquad (6.8)$$

$$\eta_3(v)=\varphi_4(v), \quad \varphi_4(v)=\varphi_1(\frac{v}{2}), \quad \varphi_1(v)=\frac{v^2}{3(1-\frac{v}{tanv})}$$

where

$$i=\frac{EI}{l}, \qquad v=l\sqrt{\frac{P}{EI}},$$

and (EI/l) is the flexural rigidity of the element.

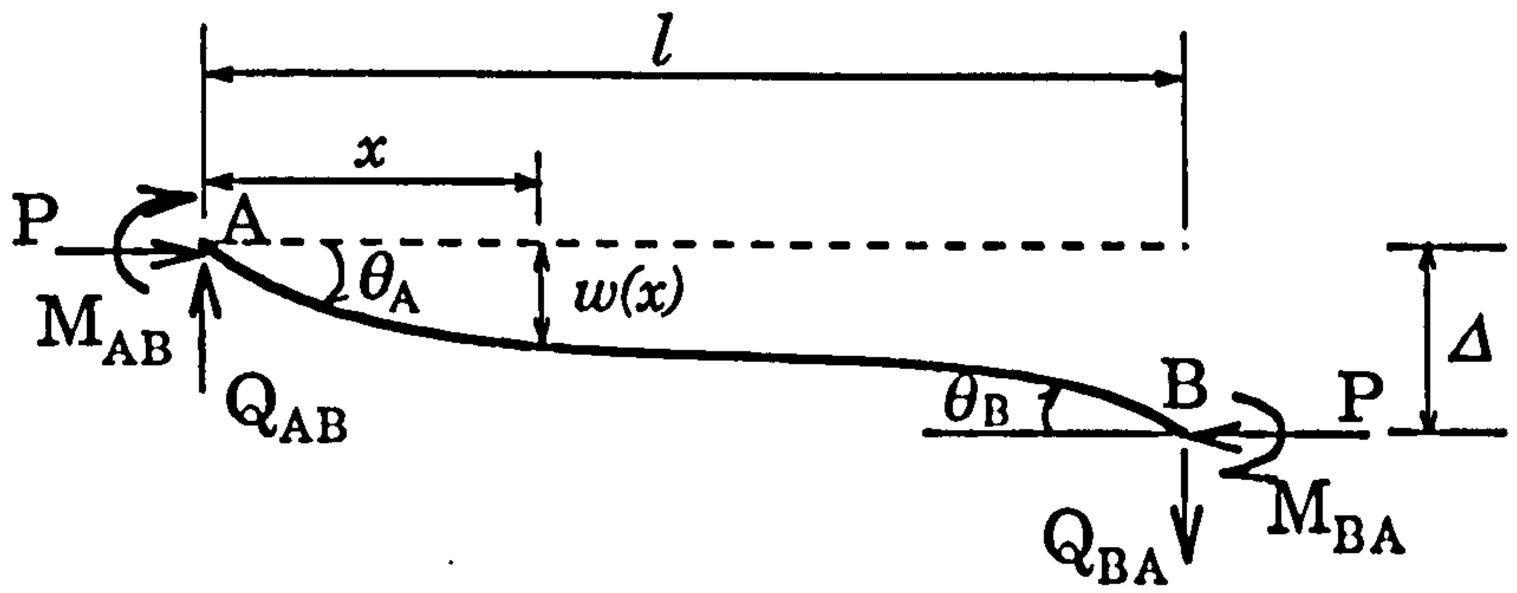

Fig 6.5 Column element analysis

As mentioned in Section 6.1, the unbraced slender frame structure under consideration is allowed to sway freely. This implies that the shear forces in the column element must vanish while the sway displacement Δ is arbitrary. Thus Fig 6.5 reduces to Fig 6.6. Substituting $Q_{AB}=Q_{BA}=0$ into Eq(6.7) gives:

$$M_{AB}=i\theta_A\frac{\nu}{tan\nu}-i\theta_B\frac{\nu}{sin\nu}$$

$$M_{BA}=-i\theta_A\frac{\nu}{sin\nu}+i\theta_B\frac{\nu}{tan\nu} \qquad (6.9)$$

where ν is the function of the axial load P, expressed in Eq(6.8).

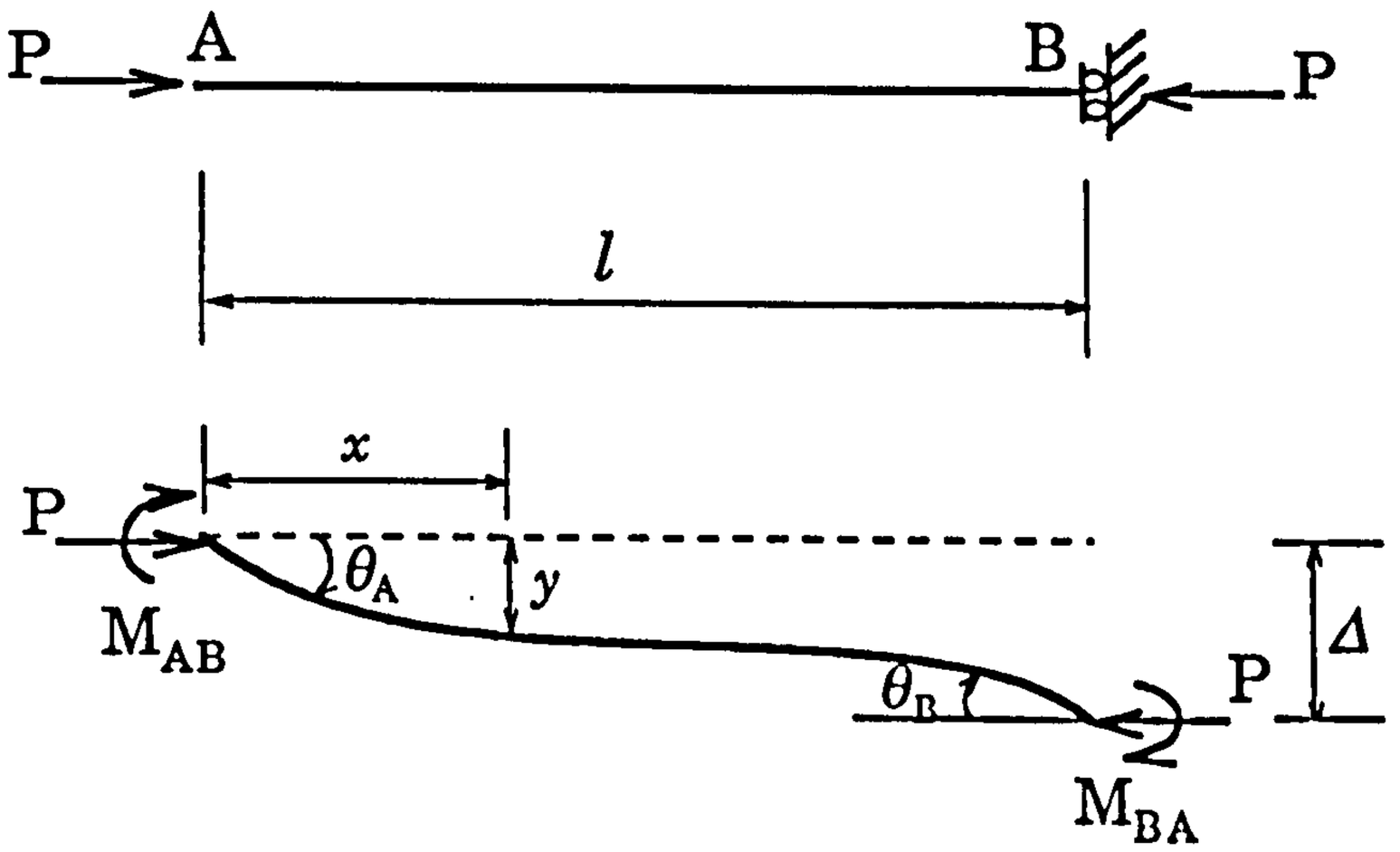

Fig 6.6 Element without end shear force

The reduction from Eq(6.7) to Eq(6.9) is not so obvious. The derivation is lengthy and tedious, so it is given in Appendix A6.1. To confirm the correctness of Eq(6.9), another derivation is provided as well in Appendix A6.1 based on the basic element in Fig 6.6.

Secondly, apply Eq(6.9) to the column elements in the model of Fig 6.1.

Fig 6.7 shows two adjacent column elements taken from Fig 6.1.

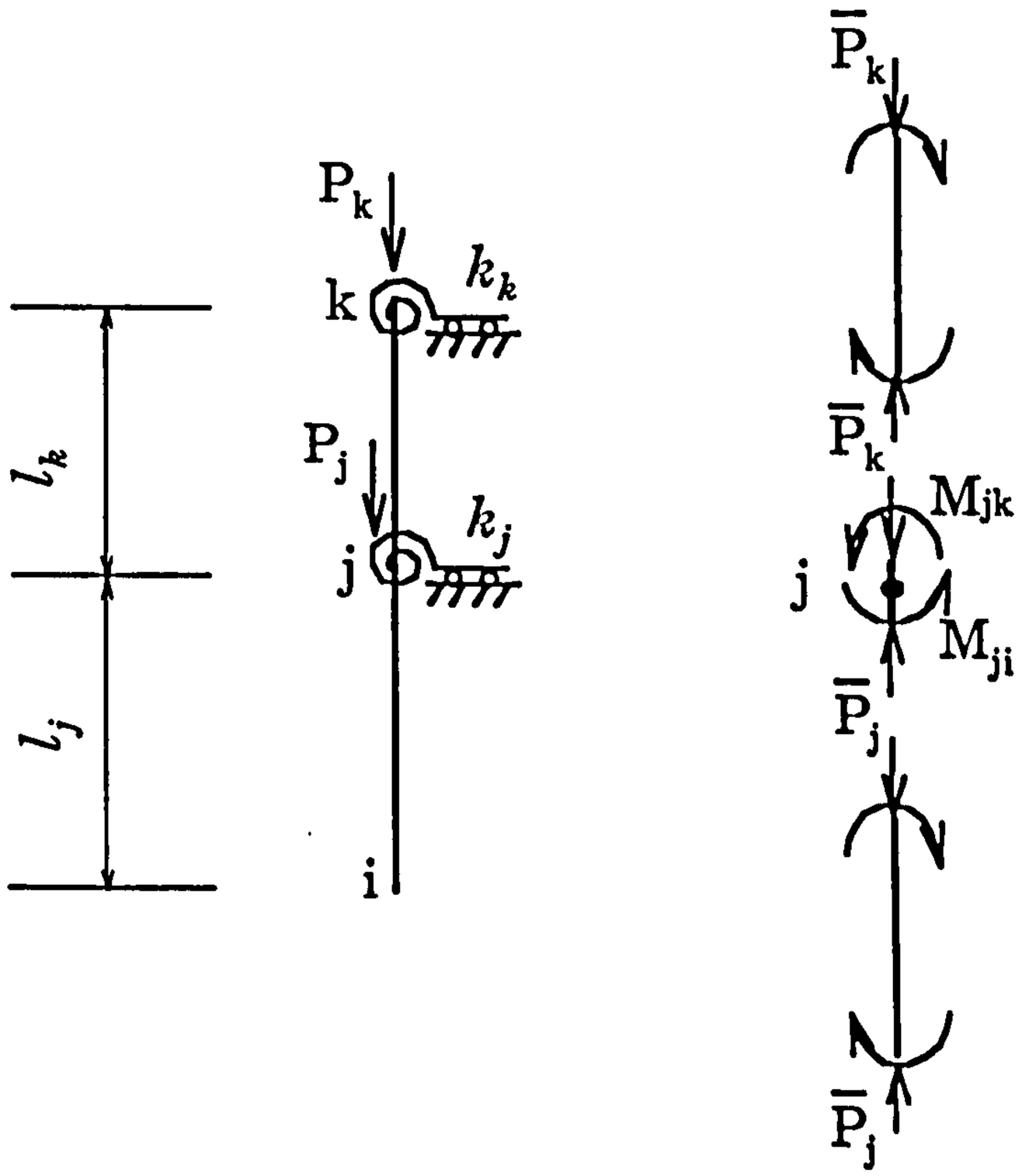

Fig 6.7 Compatibility and equilibrium of elements

Using Eq(6.9) for these two column elements produces, respectively

$$M_{ji}=-i_{ij}\theta_i\frac{v_{ij}}{sinv_{ij}}+i_{ij}\theta_j\frac{v_{ij}}{\tan v_{ij}} \qquad (6.10)$$

and

$$M_{jk}=i_{jk}\theta_j\frac{v_{jk}}{tanv_{jk}}-i_{jk}\theta_k\frac{v_{jk}}{sinv_{jk}} \qquad (6.11)$$

where

$$i_{ij}=\frac{E_jI_j}{l_j}, \qquad i_{jk}=\frac{E_kI_K}{l_k}$$

$$v_{ij}=l_j\sqrt{\frac{\bar{P}_j}{E_jI_j}}, \qquad v_{jk}=l_k\sqrt{\frac{\bar{P}_k}{E_kI_k}} \qquad (6.12)$$

In these equations, θ_i, θ_j, and θ_k are the rotations at the joints i, j and k respectively. M_{ji} and M_{jk} are the bending moments of the two elements joining at the joint j. The sign convention is the same as that in Fig 6.5. i_{ij} is the flexural rigidity of the element i-j, and i_{jk} is for j-k element. $\bar{P}_j$ and $\bar{P}_k$ refer to the internal axial forces on the i-j element and j-k element, respectively. They can be rewritten as the summation of the axial loads above them, i.e.

$$\bar{P}_j=\sum_{i=j}^{n} P_i \ , \qquad \bar{P}_k=\sum_{i=k}^{n} P_i \qquad (6.13)$$

Thirdly, the buckling equations are derived from the compatible and equilibrium conditions shown in Fig 6.7. The end rotations θ_i, θ_j, and θ_k must be compatible, and the bending moments M_{ji} and M_{jk} must be in equilibrium. The former condition can be met by letting the joint of two column elements have the same rotation. The latter one, however, must consider the bending equilibrium at joint j which can be written as

$$\sum M_j=-\theta_j k_j$$

or

$$M_{j1}+M_{jk}=-\theta_j k_j \qquad (j=1,2,...,n-1) \qquad (6.14)$$

where $\theta_j k_j$ represents the resistant bending moment exerted by the equivalent rotational stiffness k_j, which has taken into account the effects of flexural rigidity of beams and the semi-rigid behaviour of beam-column joints.

Substituting Eqs(6.10) and (6.11) into (6.14) produces

$$-i_{ij}\theta_i\frac{v_{ij}}{sinv_{ij}}+i_{ij}\theta_j\frac{v_{ij}}{tanv_{ij}}+i_{jk}\theta_j\frac{v_{jk}}{\tan v_{jk}}-i_{jk}\theta_k\frac{v_{jk}}{sinv_{jk}}=-\theta_j k_j$$

$$(j=1,2,...,n-1) \qquad (6.15)$$

There are two exceptions which are not included in Eq(6.15). The first one is for j=n, i.e., the top beam-column joint of the model in Fig 6.1. The equilibrium equation in this case becomes

$$M_{n,n-1}=-\theta_n k_n \qquad (6.16)$$

where k_n is the equivalent rotational stiffness of the top level beam-column joint, θ_n is the corresponding rotation, $M_{n,n-1}$ is the bending moment acting on this joint by the top level column element.

An equation similar to Eq(6.15) can be obtained by substituting Eq(6.10) into Eq(6.16)

$$-i_{n-1,n}\theta_{n-1}\frac{v_{n-1,n}}{sinv_{n-1,n}}+i_{n-1,n}\theta_n\frac{v_{n-1,n}}{\tan v_{n-1,n}}=-\theta_n k_n \qquad (6.17)$$

where

$$i_{n-1,n}=\frac{E_n I_n}{l_n}, \qquad v_{n-1,n}=l_n\sqrt{\frac{\bar{P}_n}{E_n I_n}} \qquad (6.18)$$

and $\bar{P}_n$ is the internal axial force on the top column element.

$$\bar{P}_n=P_n \qquad (6.19)$$

The second exception is for j=0, i.e., the bottom column-baseplate joint of the model in Fig 6.1. The equilibrium equation in this case becomes

$$M_{0,1}=-\theta_0 k_0 \qquad (6.20)$$

where k_0 is the baseplate rotational stiffness which has been studied systematically in Chapter 3 and 4, θ_0 is the corresponding rotation, $M_{0,1}$ is the bending moment acting on this joint by the bottom column element.

Applying Eq(6.11) to Eq(6.20) gives

$$i_{01}\theta_0\frac{v_{01}}{tanv_{01}}-i_{01}\theta_1\frac{v_{01}}{sinv_{01}}=-\theta_0 k_0 \qquad (6.21)$$

where

$$i_{01}=\frac{E_1 I_1}{l_1}, \qquad v_{01}=l_1\sqrt{\frac{\bar{P}_1}{E_1 I_1}} \tag{6.22}$$

and $\bar{P}_1$ is the internal axial force on the bottom column element.

$$\bar{P}_1=\sum_{i=1}^{n} P_i \tag{6.23}$$

Assume that the axial loads at each beam level in Fig 6.1 satisfy the condition of proportional loading, i.e., $P_i=\alpha_i P$, where α_i is a proportional factor at the i-th level. Then Eqs(6.13), (6.19), and (6.23) are incorporated into

$$\bar{P}_j=P\beta_j^2 \tag{6.24}$$

where

$$\beta_j^2=\sum_{i=j}^{n} \alpha_j \qquad (j=1,2,...,n)$$

Thus, v_{ij} in Eqs(6.12),(6.18) and (6.22) are grouped into

$$v_{j-1,\,j}=\beta_j l_j\sqrt{\frac{P}{E_j I_j}} \qquad (j=1,2,...,n) \tag{6.25}$$

where the subscript i has been substituted by j-1.

So far, the buckling equations of the structural model in Fig 6.1 have been derived in Eqs(6.21), (6.15), and (6.17), representing the bending equilibrium at the bottom, medium, and top beam-column joints, respectively. They can be expressed in the matrix form as follows

$$[C(P)]\{\theta\}=\{0\} \tag{6.26}$$

where $\{\theta\}$ is the unknown joint rotation vector

$$\{\theta\}^T=\{\ \theta_0,\ \theta_1,\ \theta_2,\ \ldots,\theta_n\ \}$$

and [C(P)] is a symmetric tri-diagonal matrix of order (n+1), having the following form

$$[C(P)]=\begin{bmatrix} c_{00} & c_{01} & & & & \\ c_{10} & c_{11} & c_{12} & & & \\ & \vdots & & & & \\ & & c_{jj-1} & c_{jj} & c_{jj+1} & \\ & & & \vdots & & \\ & & & c_{n-1,n-2} & c_{n-1,n-1} & c_{n-1,n} \\ & & & & c_{n,n-1} & c_{n,n} \end{bmatrix} \tag{6.27}$$

and

$$c_{00}=i_{01}\frac{v_{01}}{tanv_{01}}+k_0$$

$$c_{jj-1}=-i_{j-1j}\frac{v_{j-1j}}{sinv_{j-1j}}$$

$$c_{jj}=i_{j-1j}\frac{v_{j-1j}}{tanv_{j-1j}}+i_{jj+1}\frac{v_{jj+1}}{tanv_{jj+1}}+k_j \quad (j=1,2,\ldots,n-1)$$

$$c_{jj+1}=-i_{jj+1}\frac{v_{jj+1}}{sinv_{jj+1}}$$

$$c_{nn}=i_{n-1,n}\frac{v_{n-1,n}}{tanv_{n-1,n}}+k_n$$

where $v_{j-1,j}$, $i_{j-1,j}$ (j=1,2,...,n) are given in Eqs(6.25) and (6.12), respectively.

We can see that Eq(6.26) is a homogeneous linear equation. The non-trivial solution for {θ} in Eq(6.26) corresponds to the critical value of $P=P_{cr}$, at which buckling occurs. Thus the buckling equation for determining the buckling load P_{cr} is

$$\det[C(P)]_{P=P_{cr}}=0 \qquad (6.28)$$

where det[C(P)] is the determinant of matrix [C(P)].

6.5 An efficient algorithm for buckling loads

As shown in Eq(6.26), the coefficients of this homogeneous linear matrix equation are transcendental functions of the load P, and so is the buckling equation of Eq(6.28).

Because the coefficient matrix [C(P)] has a symmetric tri-diagonal form, it is easy to expand the buckling equation Eq(6.28) by the Gauss Elimination Procedure into an algebraical expression as follows

$$f(P)=\prod_{i=0}^{n} c_{ii}^{*}=0 \qquad (6.29)$$

where

$$c_{00}^{*}=c_{00}$$

$$c_{jj}^{*}=c_{jj}-c_{j-1j}\cdot\frac{c_{jj-1}}{c_{j-1j-1}^{*}} \qquad (j=1,2,\ldots,n)$$

Theoretically, the transcendental equation f(P)=0 in Eq(6.29) has (n+1) roots, representing the (n+1) buckling loads. However, the smallest positive root, corresponding to the fundamental buckling load, is the major concern in the structural design.

To find the fundamental critical load of the structure of Fig 6.1, P_{cr}, we will first determine a domain along P axis in which P_{cr} lies.

As we can see, the fundamental critical load of a column with both ends fixed is given by

$$P'=\frac{(2\pi)^2 EI}{l^2}$$

where (EI/l) is the flexural rigidity of the column.

Assuming that all the connections in the model of Fig 6.1 are clamped, the n critical values can be obtained corresponding to n clamped columns, respectively. As the critical load for each clamped column must be not less than the critical load for any other restricted column and the critical load for each individual column must be not less than the critical load for the whole structure, therefore it can be deduced that the fundamental critical load corresponding to the real structure of Fig 6.1, P_{cr}, must be less than the maximum value of all these n values, that is,

satisfying the following inequality

$$0<P_{cr}\leq P_{maxcr} \qquad (6.30)$$

where P_{maxcr} is the maximum fundamental critical load of the column elements in Fig 6.1 when their ends are clamped, and it is given below,

$$P_{maxcr}=\max\{\frac{(2\pi)^2(E_iI_i)}{l_i^2}\}_i \qquad (i=1,2,...,n) \qquad (6.31)$$

Eq(6.30) implies that the fundamental critical load lies within the domain $[0,P_{maxcr}]$ and within this domain at least one root of the transcendental equation Eq(6.29) exists. On this basis, a procedure is presented to find the fundamental critical load P_{cr} as follows,

(1). Pick up the maximum value P_{maxcr} among those calculated by Eq(6.31).

(2). The domain $[0,P_{maxcr}]$ is divided into m subdomains.

(3). Examine the sign of the value of f(P) at each subdomain in the order of P increase. This procedure is continued until the sign at a subdomain, for example, at $[B_1,C_1]$ in Fig 6.8, changes from positive to negative or vice versa.

(4). If the length of this subdomain $[B_1,C_1]$ in which the fundamental critical load P_{cr} lies is within the given tolerance, the fundamental critical load P_{cr} is believed to have been found. If not, go on to the next step.

(5). Divide this subdomain $[B_1,C_1]$ into m subdomains. Go back to Step 3.

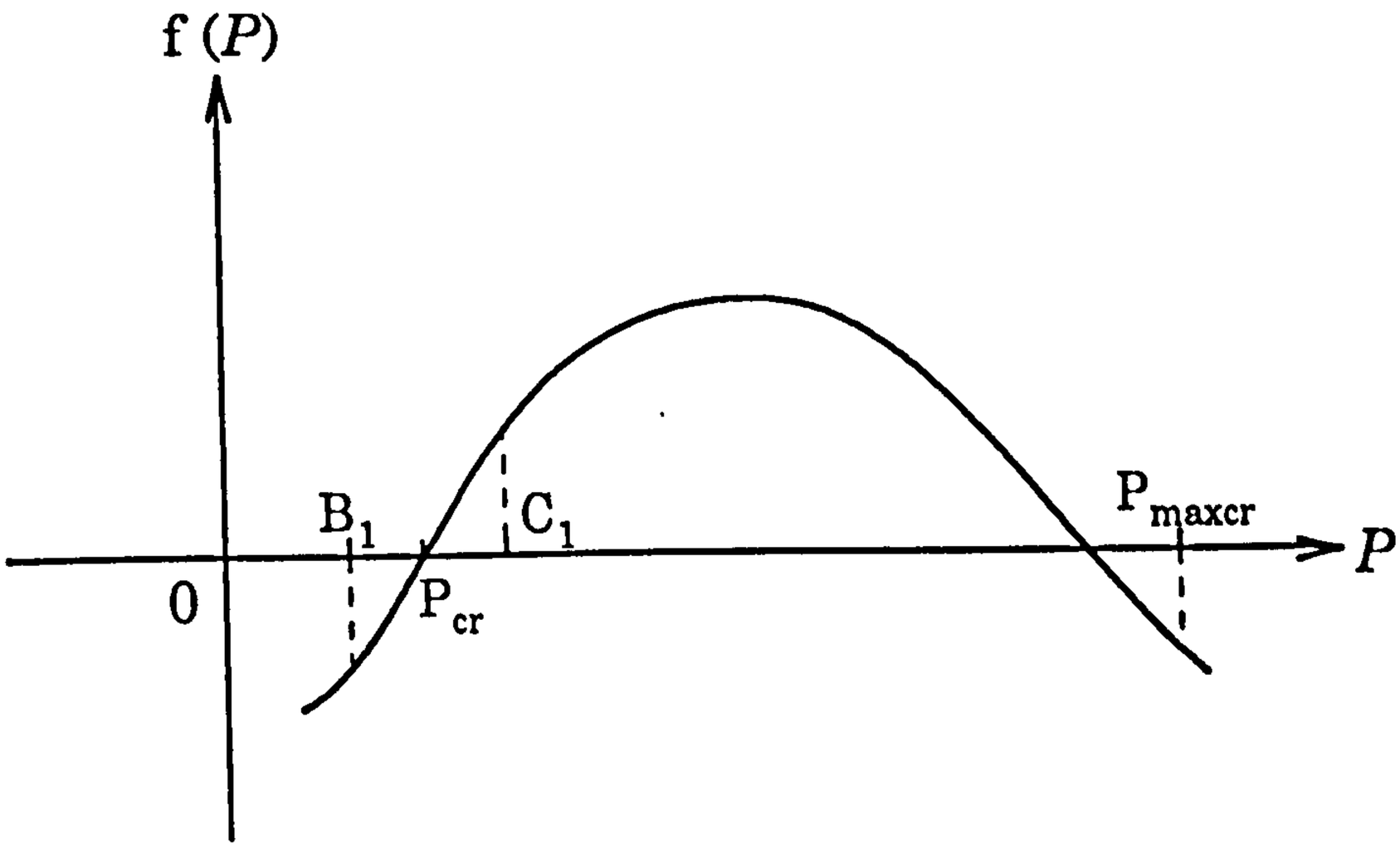

Fig 6.8 Algorithm for finding P_{cr}

This is a very efficient algorithm for finding the fundamental critical load P_{cr}. Obviously, if the number of subdomain m takes 2, that is, in each iteration the domain is divided into two subdomains, the algorithm reduces to the Interval Bisection Method.

After repetition of k times, the length of the subdomain in which the fundamental critical load P_{cr} lies will be $\delta^k=P_{maxcr}/m^k$. If $\delta^k<\varepsilon$, the fundamental critical load is obtained, where ε is a specified accuracy.

6.6 Determination of buckling modes

The preceding section has dealt with the determination of the fundamental buckling load P_{cr}. The associated buckling modes can be found from Eq(6.26) if P is substituted by P_{cr} instead.

$$[C(P_{cr})]\{\theta\}=\{0\} \tag{6.32}$$

It is easily understood that only n equations are independent among the (n+1) equations in Eq(6.32). By solving the first n equations, θ_1, θ_2, ..., θ_n can be expressed in terms of θ_0 as

$$\theta_1=-\frac{1}{c_{01}}(c_{00}\theta_0)$$

$$\theta_2=-\frac{1}{c_{12}}(c_{10}\theta_0+c_{11}\theta_1)$$

.....

$$\theta_n=-\frac{1}{c_{n-1,n}}(c_{n-1,n-2}\theta_{n-2}+c_{n-1,n-1}\theta_{n-1}) \tag{6.33}$$

where θ_0 is arbitrary and is set to 1.0 here.

On the other hand, if the end rotations θ_A and θ_B in the column element of Fig 6.7 are known, the corresponding relative transverse displacement Δ can be obtained from the third equation of Eq(6.7) by setting $Q_{AB}=Q_{BA}=0$.

$$\Delta=\frac{l}{2}.\frac{\eta_3(\nu)}{\eta_2(\nu)}[\theta_A+\theta_B] \qquad (6.34)$$

where $\eta_2(\nu)$, and $\eta_3(\nu)$ are given in Eq(6.8).

Corresponding to the joint rotations $\{\theta_0, \theta_1, \theta_2, ..., \theta_n\}$ determined by Eq(6.33), the relative transverse displacement modes $\{\Delta_1, \Delta_2, ..., \Delta_n\}$ can be obtained by applying Eq(6.34) as

$$\Delta_i=\frac{l}{2}.\frac{\eta_3(\nu)}{\eta_2(\nu)}[\theta_{i-1}+\theta_i] \qquad (i=1,2,...,n) \qquad (6.35)$$

$\{\Delta_1, \Delta_2, ..., \Delta_n\}$ is the buckling modes corresponding to the fundamental buckling load P_{cr}. Its schematic representation is shown in Fig 6.9(a).

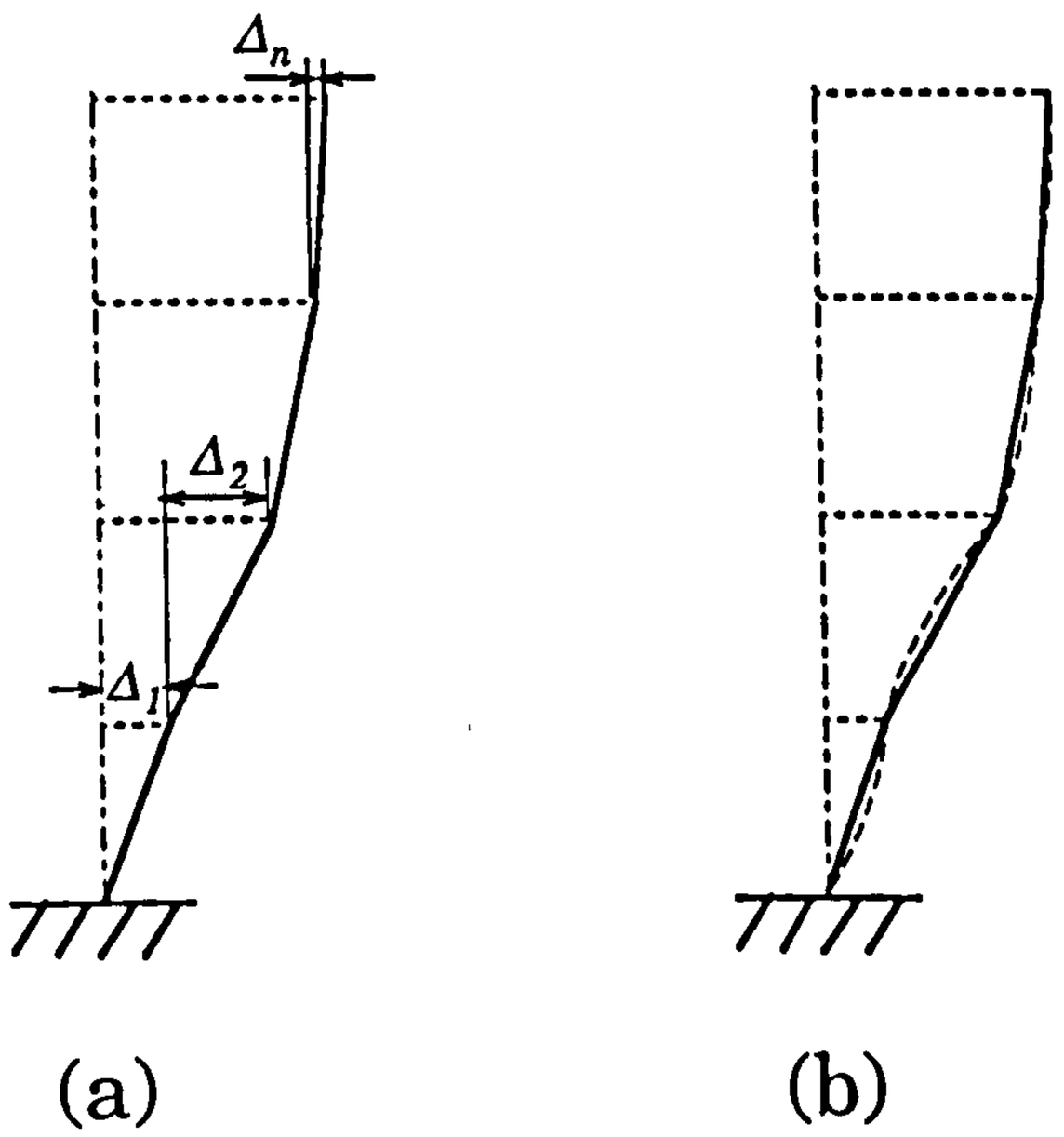

(a) (b)

Fig 6.9 Schematic representation of buckling modes

Further, to detail the buckling modes obtained from Eq(6.35) and described in Fig 6.9(a), solving the second-order differential equation on bending equilibrium of beams with the boundary conditions of Fig 6.6 gives

$$y=\frac{M_{AB}}{P}(\cos\frac{\nu x}{l}-1)+\frac{\theta_A}{\nu}\, l\, \sin\frac{\nu x}{l} \qquad (6.36)$$

where y is the deflection of the column element in Fig 6.6, and v is the same as that in Eq(6.7). The derivation of Eq(6.36) is given in more details in Appendix A6.1.

Applying the first equation of Eq(6.9) to Eq(6.36) produces

$$y=(\theta_A\frac{\nu}{tg\nu}-\theta_B\frac{\nu}{\sin\nu})\frac{i(\cos\frac{\nu x}{l}-1)}{P}+\frac{\theta_A l}{\nu}\sin\frac{\nu x}{l} \qquad (6.37)$$

where i=EI/l is the flexural rigidity of the column element in Fig 6.6.

Thus, Eq(6.37) is used to each column element in Fig 6.1 to smooth the buckling modes. The schematic representation of the buckling mode is given in Fig 6.9(b).

The above procedures have been incorporated in a computer program STAB3 [55]. As can be seen in Chapter 7, the buckling modes obtained may be used to describe the initial imperfection to predict the response of the slender frame structures to the applied loads.

Figure 6.10 presents the schematic illustrations of buckling modes for two cases with the same properties and loads but different restraints on the

top. The top in Fig 6.10(a) is free while the rotation at the top of Fig 6.10(b) is restrained to zero. The corresponding buckling curves are plotted in Fig 6.10(c).

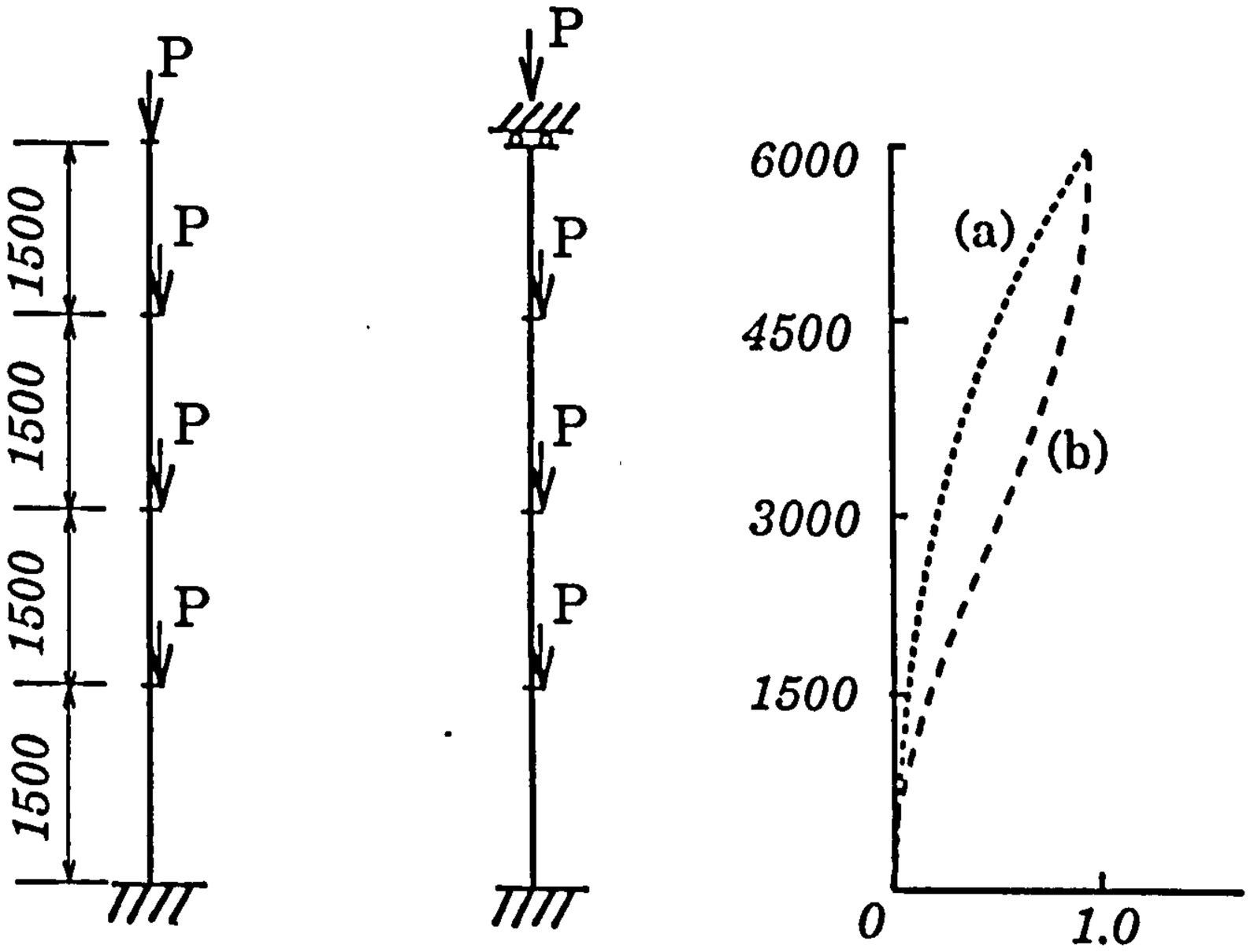

(a) (b) (c)

Fig 6.10 Schematic illustrations of buckling modes

6.7 Numerical examples

The simplified structural model in Fig 6.1, used to model slender frame structures, and the associated computational approach have been

incorporated and implemented in a computer program STAB3 [55]. It can be used to calculate the fundamental critical load and the associated buckling modes of structures.

Three examples are given to illustrate the effectiveness of the method in this chapter, and how to use the critical load calculation program STAB3.

Example 1:

Find the critical load of a single column when fixed at one end and free at the other , which is a cantilever strut as shown in Fig 6.11.

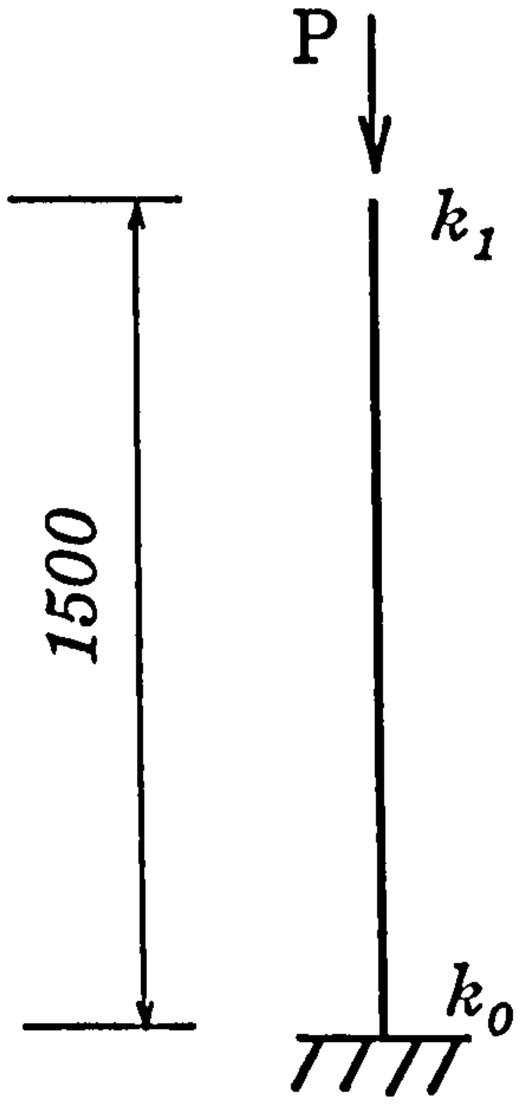

Fig 6.11 One end free and one end clamped column

Assume that the elastic modulus of the column is $E=2.10\times10^5$ N/mm^2. The moment of inertia $I=1.92\times10^5$ mm^4. The specified accuracy $\varepsilon=10^{-4}$.

Using the computer program STAB3, the input data file is:

[1] Number of stories n: 1;

[2] Young's modulus of elasticity of column E: 2.10×10^5 N/mm^2;

[3] The moment of inertia I: 1.92×10^5 mm^4;

[4] Length of column L: 1500 mm;

[5] Initial search step: 100;

[6] Accuracy of P_c: 10^{-4};

[7] Load factor for each story ($a_1,a_2,...,a_n$): 1.0

[8] Stiffness of each of the joints ($k_0,k_1,...,k_n$):

Joint 0: 2.6×10^{19} N.mm/rad; (On the fixed joint, k=infinity)

Joint 1: 0.0 N.mm/rad; (On the free rotation joint, k=0)

Run program: STAB3

Output: $P_c=4.4305\times10^4$ (N)

The theoretical solution to this problem is :

$$P_c=\frac{\pi^2 EI}{4l^2}$$

$$=\frac{3.14^2\times210000\times192390}{4\times1500^2}$$

$$=4.4305\times10^4(N)$$

Thus, the computer program STAB3 gives the correct result.

Example 2:

Find the critical load of a drive-in pallet rack system shown in Fig 6.12. The elastic modulus of the column is $E=2.10\times10^5$ N/mm^2. The moment of inertia $I=1.92\times10^5$ mm^4. The specified accuracy $\varepsilon=10^{-4}$.

Using the program STAB3, the input data file is:

[1] Number of stories n: 4;

[2] Young's modulus of elasticity of column E: 2.1×10^5 N/mm^2;

[3] The moment of inertia I: 1.92×10^5 mm^4;

[4] Length of column L: 1500 mm;

[5] Initial search step: 100;

[6] Accuracy of P_c: 10^{-4};

[7] Load factor for each story (a_1, a_2, ... , a_n):

1.0, 1.0, 1.0, 0.0;

[8] Stiffness of each of the joints (k_0, k_1, ... , k_n):

Joint 1 : 2.6×10^{19} N.mm/rad;

Joint 2 : 0.0 N.mm/rad;

Joint 3 : 0.0 N.mm/rad;

Joint 4 : 0.0 N.mm/rad;

Joint 5 : 2.6×10^{19} N.mm/rad.

Run program: STAB3

Output: $P_c=6.887\times10^3$ (N)

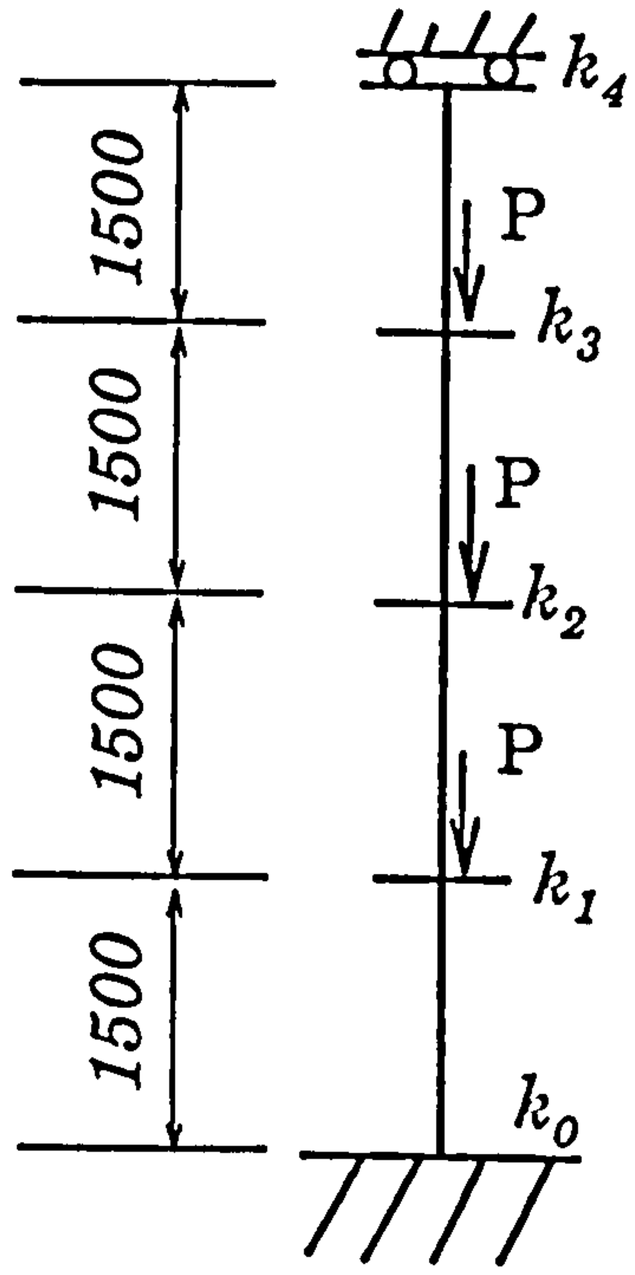

Fig 6.12 A drive-in pallet rack system

The two examples have also run by another finite element analysis computer program LUSAS which gives P_c= 4.430564x10^4 (N) for example 1 and P_c=6.88694x10^3 (N) for example 2 (see Appendix 6.2). It can be concluded by comparison that good agreement has been achieved.

Example 3:

The method proposed in this chapter has been used to analyze the same frames as used in [26], as shown in Fig 6.13.

The structure has the following properties:

Elastic modulus of steel: $E=2.1\times10^5$ N/mm^2;

Second moment of area of columns:$I_c=7.0\times10^5$ mm^4;

Second moment of area of beams: $I=5.5\times10^5$ mm^4;

Beam-column semi-rigid stiffness: $k_c=7.0\times10^4$ kN.mm/rad;

Baseplate stiffness: $k_b=9.0\times10^4$ kN.mm/rad;

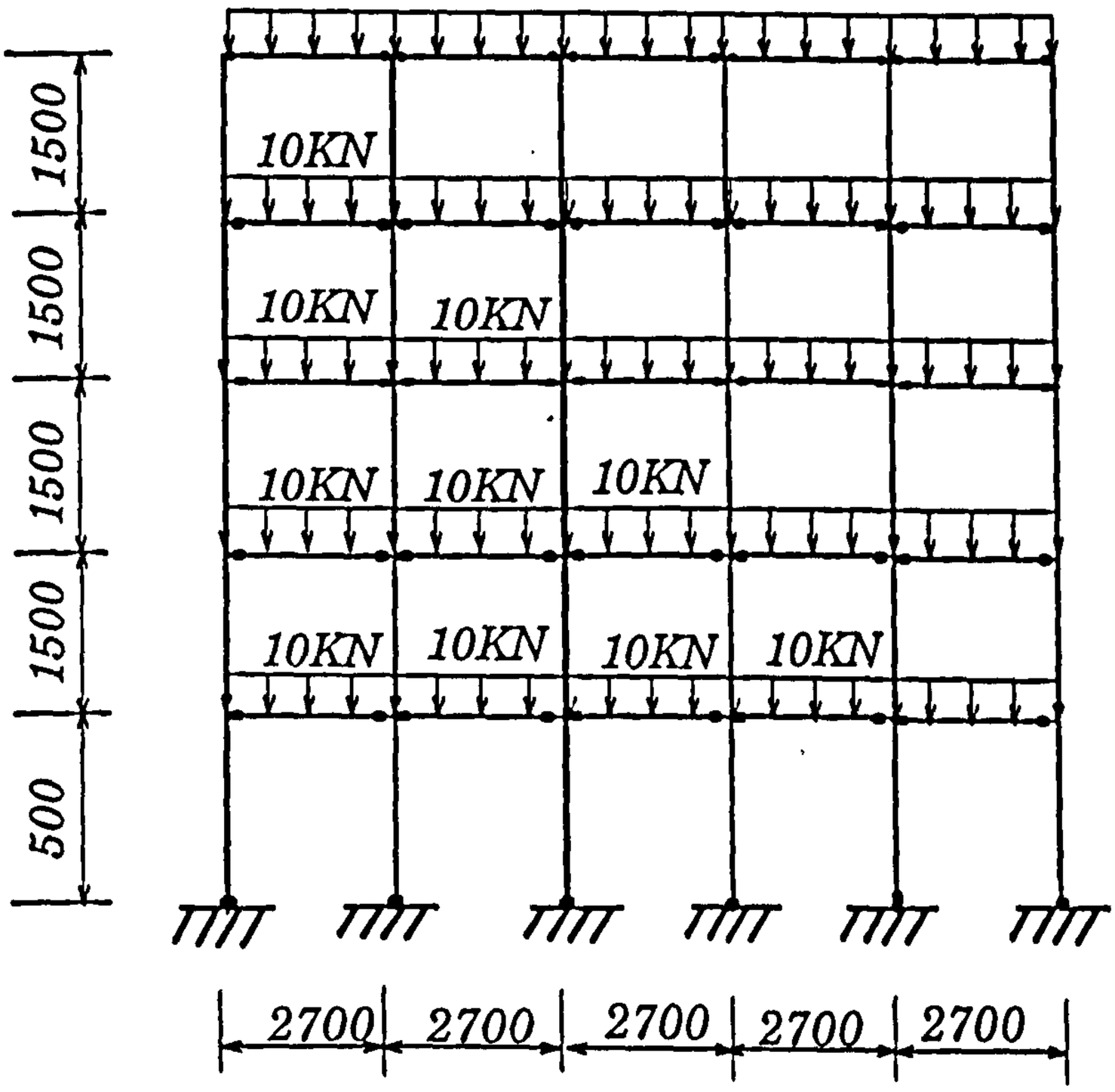

Fig 6.13 Frames for the verification of the method proposed

When the structure in Fig 6.13 is modelled by the simplified structural model of Fig 6.1, the equivalent beam-column rotational stiffness is calculated by Eq(6.5),

$$k^j_i = \frac{1}{\left[\frac{l}{12(EI)_i} + \frac{1}{4k_{li}} + \frac{1}{4k_{ri}}\right]}$$

$$= 1.1 \times 10^5 \text{ kN.mm/rad}$$

The structure consists of six uprights with corresponding baseplates, forming five bays. Therefore the equivalent beam-upright rotational stiffness k_i at level i is given by considering the combined action of the beams in five bays:

$$k_i = 5k^j_i = 5.5 \times 10^5 \text{ kN.mm/rad}$$

However, the aggregate baseplate rotational stiffness k_0 is given by considering all six baseplates and hence:

$$k_0 = 6k_b = 5.4 \times 10^5 \text{ kN.mm/rad.}$$

The aggregate second moment of area of the upright I_i is given by considering the combined action of six uprights and is equal to:

$$I_i = 6I_c = 4.2 \times 10^6 \text{ mm}^4$$

The results of elastic critical loads by different methods were given in [26], where the ratio of the notional horizontal to vertical load is known so that the second order plane frame analysis can be made and the elastic buckling load can be traced. The method presented in this chapter uses stability functions, see Eq(6.7), to derive the buckling equations and to define the buckling load, see Eq(6.29). All the methods should approach the same elastic buckling loads according to reference [15].

The comparison of the computed results is given in Fig 6.14 where

the vertical axis is the elastic critical load and the horizontal axis corresponds to a family of frames. Fig 6.14(a), 6.14(b) and 6.14(c) are the results of Horne/Davies[26], design method[26] and the method of this chapter, respectively, compared with those Davies obtained using "exact analysis" method and a second order plane frame program [26]. It can be seen that the results computed by the method of this chapter provide the best agreement to those of the "exact analysis".

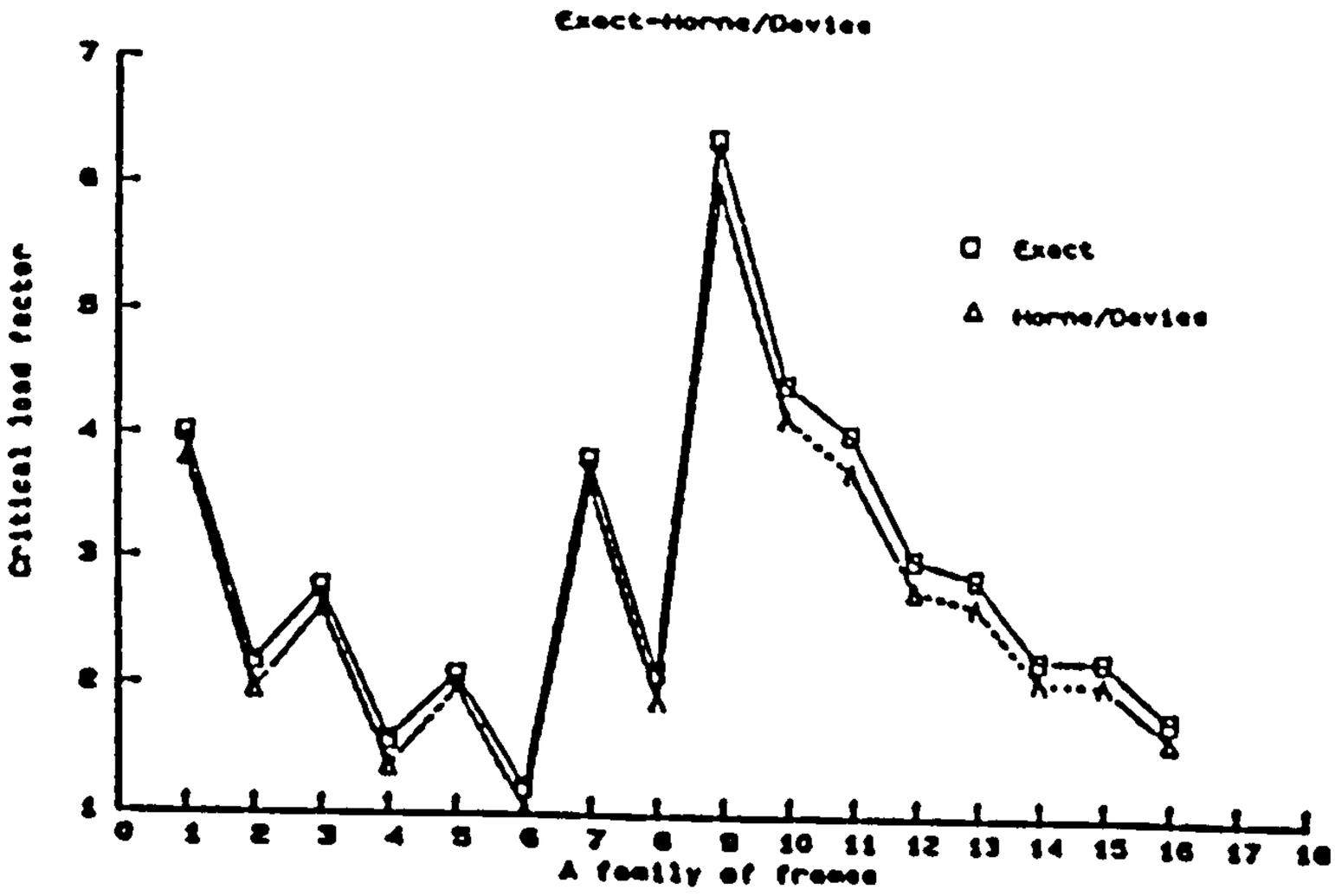

Fig 6.14(a) Comparison of the results between "Exact Analysis" and Horne/Davies

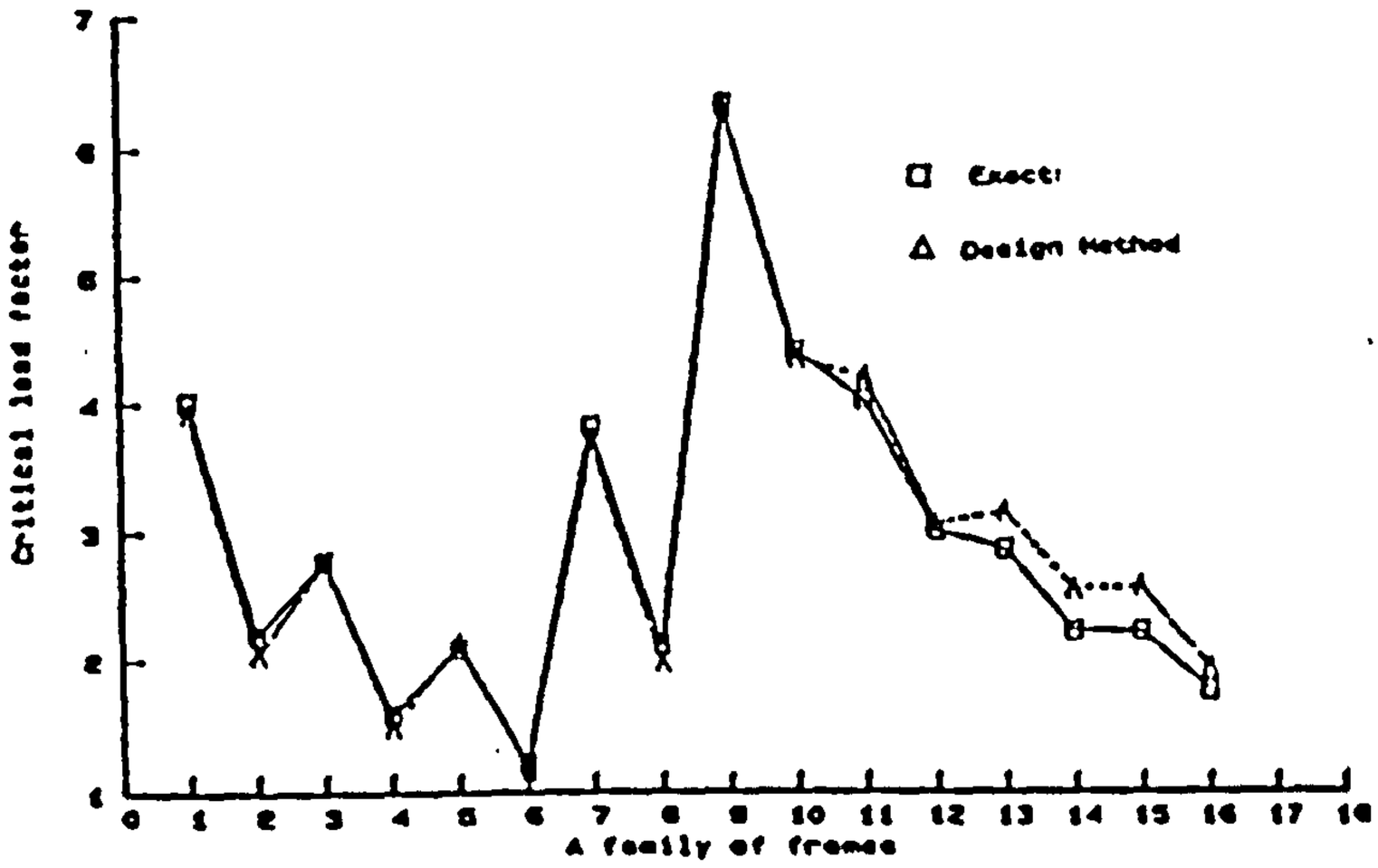

Fig 6.14(b) Comparison of the results
between "Exact Analysis" and Design Method

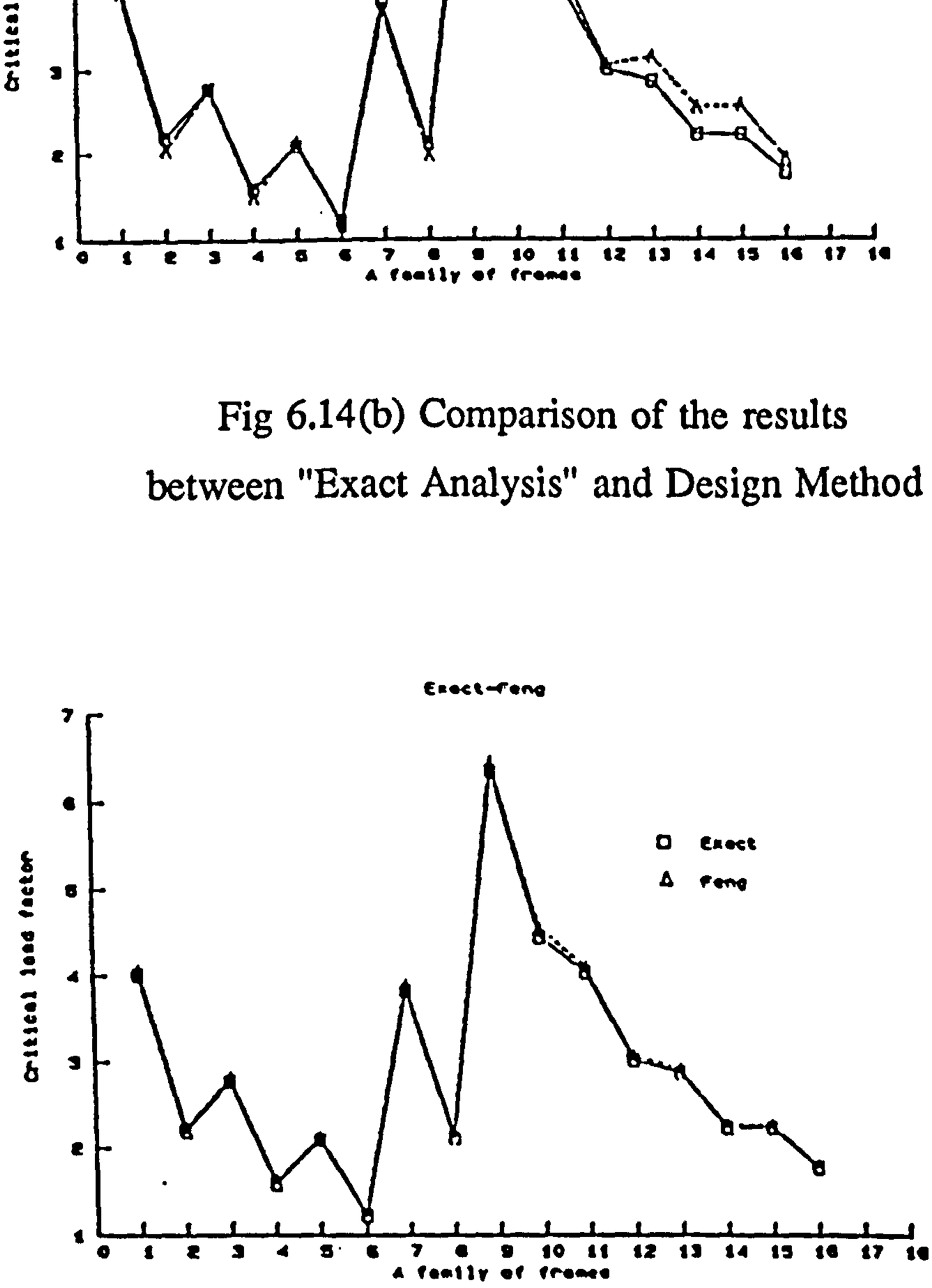

Fig 6.14(c) Comparison of the results
between "Exact Analysis" and the method of this chapter

6.8 Conclusions

Slender frame structures are normally made from cold-formed steel sections with semi-rigid beam to column joints and column to baseplate connections. This chapter has developed an effective method for the computerized buckling analysis of such structures.

The simplified model is very flexible and permits the modelling of slender frame structures under varied applied loads. The numerical illustration of the application of the associated computerised approach to multi-bay frame structures with variable number of storeys, semi-rigid baseplates and beam to column joints has shown good agreement with the "Exact Analysis".

The method not only provides a flexible way for modelling the original structure, allowing more factors to be involved in the analysis, but also develops a very efficient computerized procedure for the buckling analysis.

CHAPTER 7 SIMPLIFIED SECOND-ORDER ANALYSIS OF SLENDER FRAME STRUCTURES

7.1 General Outline

Semi-rigid slender frame structures, for example, Fig 7.1, when subjected to lateral loads, deflect laterally. However, if lateral loads and vertical loads both act on the structure, the vertical loads will interact with the lateral displacements produced by the lateral loads. This phenomenon is called the P-Δ effect. The consequence of this effect is an increase in deflection and an increase in overturning moment.

Besides P-Δ effects, the semi-rigid behaviour of the beam-column and the column baseplate connections makes the structural response to applied loads complex. This arises because most connections exhibit nonlinear responses almost from the start of loading. As described in Chapters 3 and 4, the column-baseplate rotational stiffness is nonlinear, being dependent upon the bending moment and the axial force acting on it, and upon the stiffness of subgrade on which the baseplate rests.

In order to determine accurately the final deflection and moment of semi-rigid slender frame structures with the P-Δ effect taken into account, it is necessary to use a second-order analysis based on the deformed geometry of the structure.

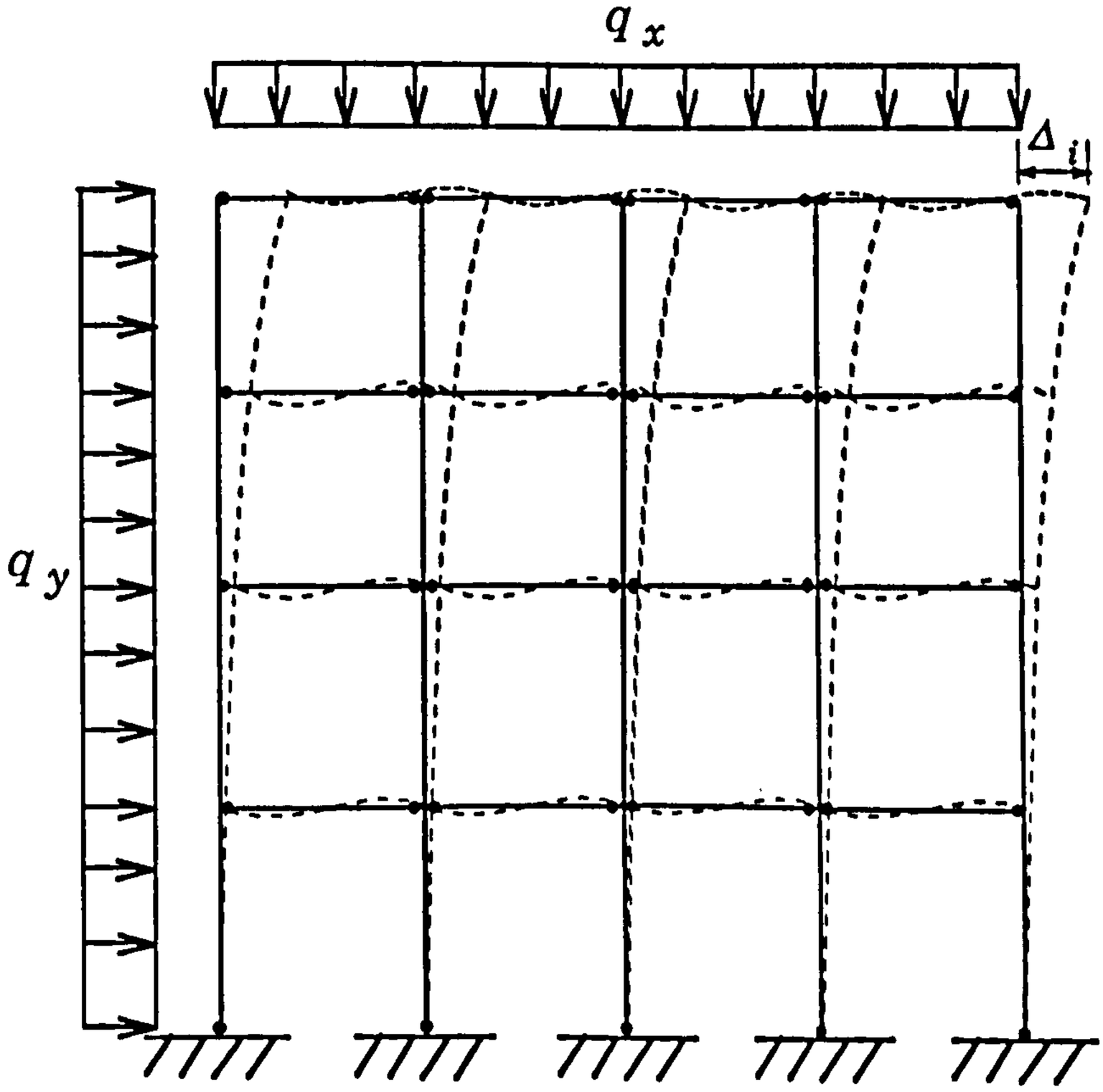

Fig 7.1 Semi-rigid slender frame structure

Second-order analysis usually entails an iterative process. However, in general, nonlinear iterative analyses are tedious and time-consuming. It is sometimes advantageous to resort to simplified models or techniques by which second-order effects are considered in an approximate manner.

In this chapter, a simplified model is presented to simulate semi-rigid slender frame structures. In the derivation of the stability stiffness functions of the beam-column elements, the member initial imperfection is accounted for. In the analysis of global equilibrium of the structure, the

initial deflection of the structure is also included.

7.2 A simplified model for second-order analysis

In a similar manner to the simplified model for buckling analysis, see Chapter 6, a simplified model for second-order analysis is shown in Fig 7.2(a),

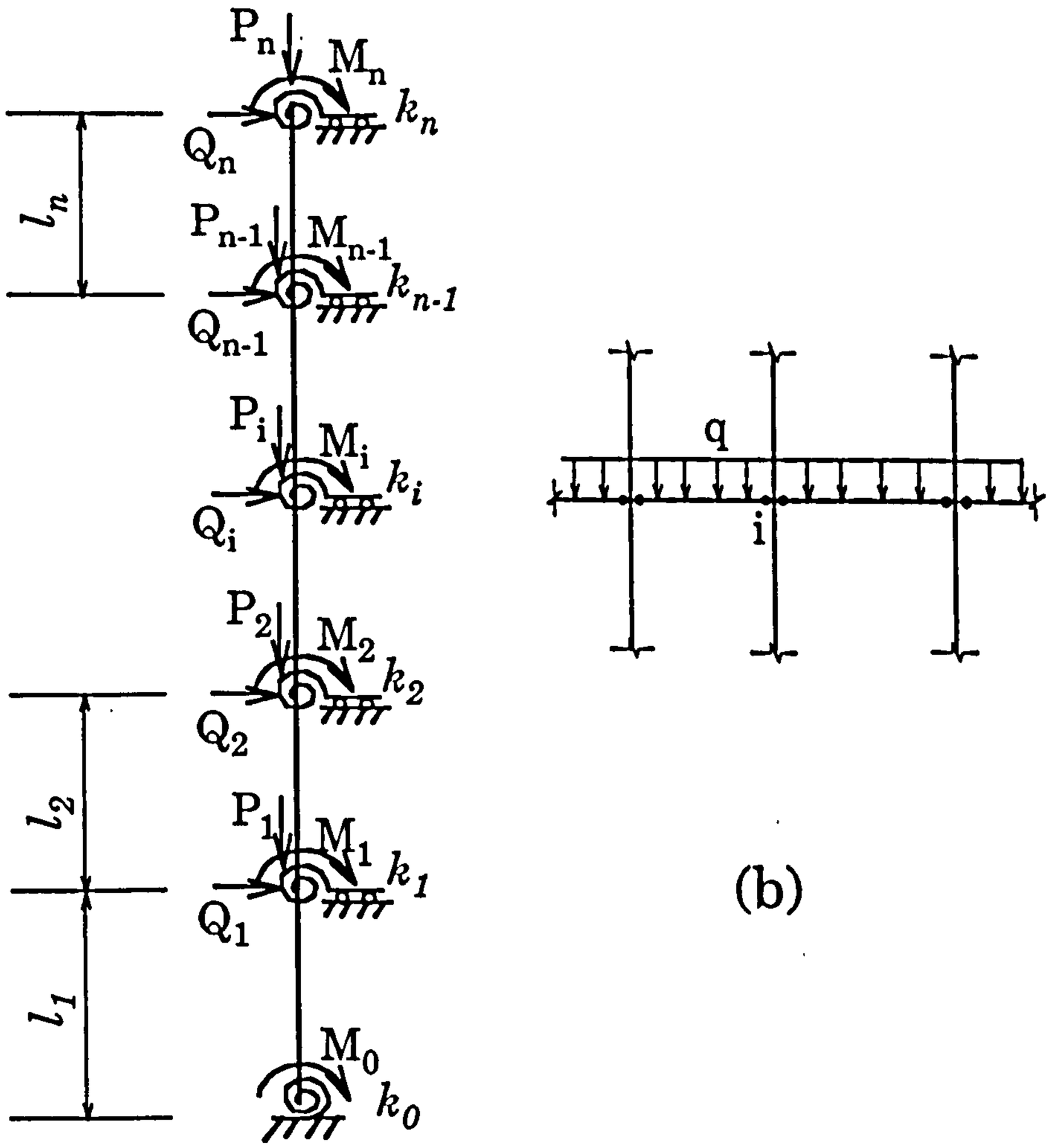

Fig 7.2 Simplified structural model

where Q_i, P_i and M_i *(i=1,2, ..., n)* are the statically equivalent lateral loads, vertical loads and bending moments, respectively, resulting from the loads on the i-th level link beams, see Fig 7.2(b), k_i *(i=1,2, ..., n)* are the equivalent rotational stiffness of beam-column joints which are the same as Eq(6.5) and k_0 is column-baseplate rotational stiffness which has been investigated theoretically and experimentally in Chapters 3 and 4.

Fig 7.2(a) is a sway model of semi-rigid slender frame structure. It describes the basic characteristics of deformation of this type of structure.

7.3 The equivalent loads on the model

The equivalent lateral loads Q_i, vertical loads P_i and bending moments M_i *(i=1,2, ..., n)* acting on the i-th beam-column connection, see Fig 7.2(a), are the total reactions transferred from the neighbouring link beams, see Fig 7.2(b). An illustration is given below to demonstrate how this process is performed.

Fig 7.3(a) shows a flexibly connected beam subjected to a uniformly distributed load q. The flexible connections are modelled by spring stiffness k_{li} and k_{ri}, respectively. Fig 7.3(a) can be decomposed into two load cases, Fig 7.3(b) and Fig 7.3(c), respectively. The first load case, Fig 7.3(b), corresponds to a simply-supported beam subjected to the uniformly distributed load. The second load case, Fig 7.3(c), represents the restraining effect on the beam from the flexible connections, where M_A and M_B are the bending reaction moments on ends A and B, respectively.

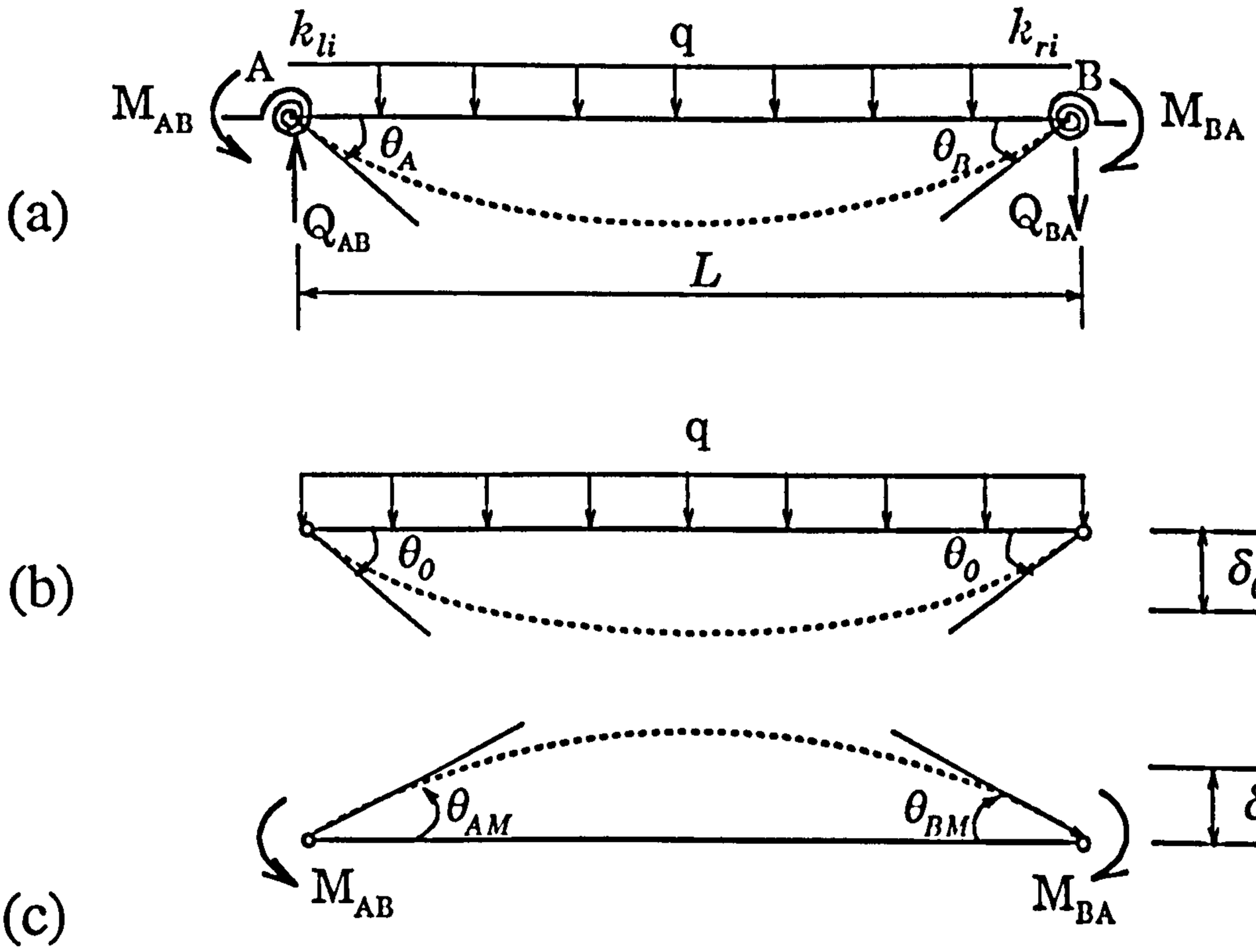

Fig 7.3 A flexibly connected beam

The compatibility of rotation at the ends requires that

$$\begin{aligned}\theta_A&=\theta_0+\theta_{AM}\\ \theta_B&=\theta_0+\theta_{BM}\end{aligned}\qquad(7.1)$$

where θ_A and θ_B are the rotational deformation of the connections A and B, respectively; θ_0 is the end rotation of the beam due to the uniformly distributed load, and θ_{AM} and θ_{BM} are the end rotations of the beam due to the restraining moments M_{AB} and M_{BA}, respectively.

By definition, we have

$$\theta_A=\frac{M_{AB}}{k_{li}}\ ,\qquad \theta_B=\frac{M_{BA}}{k_{ri}} \tag{7.2}$$

where M_{AB} and M_{BA} are the end moments at the connections A and B of Fig 7.3(c), respectively; k_{li} and k_{ri} are the corresponding connection stiffness.

From Figs 7.3(b) and 7.3(c), we obtain

$$\theta_0=\frac{qL^3}{24EI} \tag{7.3}$$

$$\begin{aligned}\theta_{AM}&=-\frac{M_{AB}L}{3EI}-\frac{M_{BA}L}{6EI}\\ \theta_{BM}&=-\frac{M_{AB}L}{6EI}-\frac{M_{BA}L}{3EI}\end{aligned} \tag{7.4}$$

where (EI/L) is the flexural rigidity of the element.

Substituting Eqs(7.2), (7.3) and (7.4) into Eq(7.1) and solving for M_{AB} and M_{BA} give

$$M_{AB}=\frac{2\bar{k}_{li}(6+\bar{k}_{ri})M_0}{3(12+4\bar{k}_{li}+4\bar{k}_{ri}+\bar{k}_{li}\bar{k}_{ri})}$$

$$M_{BA}=\frac{2\bar{k}_{ri}(6+\bar{k}_{li})M_0}{3(12+4\bar{k}_{li}+4\bar{k}_{ri}+\bar{k}_{li}\bar{k}_{ri})} \tag{7.5}$$

where

$$\bar{k}_u=\frac{k_u L}{EI}\ , \qquad \bar{k}_r=\frac{k_r L}{EI}$$

are the non-dimensional connection stiffnesses, and

$$M_0=\frac{qL^2}{8}$$

is the maximum moment of a uniformly loaded simply-supported beam, see Fig 7.3(b).

The lateral reaction forces of Fig 7.3(a), Q_{AB} and Q_{BA}, can be written as

$$\begin{aligned} Q_{AB}&=\frac{1}{L}\left(\frac{qL^2}{2}+M_{AB}-M_{BA}\right)\\ Q_{BA}&=-\frac{1}{L}\left(\frac{qL^2}{2}+M_{BA}-M_{AB}\right) \end{aligned} \qquad (7.6)$$

Eq(7.5) and Eq(7.6) give the end reaction forces and bending moments of a flexibly connected beam subjected to a uniformly distributed load, see Fig 7.3(a), which will contribute to the equivalent lateral loads Q_i, vertical loads P_i and bending moments M_i.

7.4 Derivation and solution of the basic equations

The basic equations governing the equilibrium of the structural model Fig 7.2(a) are formulated in this section. Firstly, an element equilibrium analysis is made. Then, the equations governing the equilibrium of the global structure are derived by considering the displacement compatibility

and force equilibrium at the joints of the structure. Finally, a procedure for transforming the coefficient matrix of the equations into a triangular matrix is presented.

7.4.1 Element Equilibrium Analysis

The beam-column element shown in Fig 7.4 is one of the structural members in the model Fig 7.2(a). The initial configuration of the element is denoted as y_0. The element is subjected to combined axial forces, P, shear forces, Q_{AB} *and* Q_{BA}, and bending moments, M_{AB} *and* M_{BA}. Under the action of these forces, the element will deflect locally and globally, denoted as y and Δ, respectively, until an equilibrium position is reached. During this process, the axial force P interacts with the lateral displacement caused by lateral forces Q_i and bending moment M_i. This is the P-Δ effect which has to be considered in the equilibrium of the element.

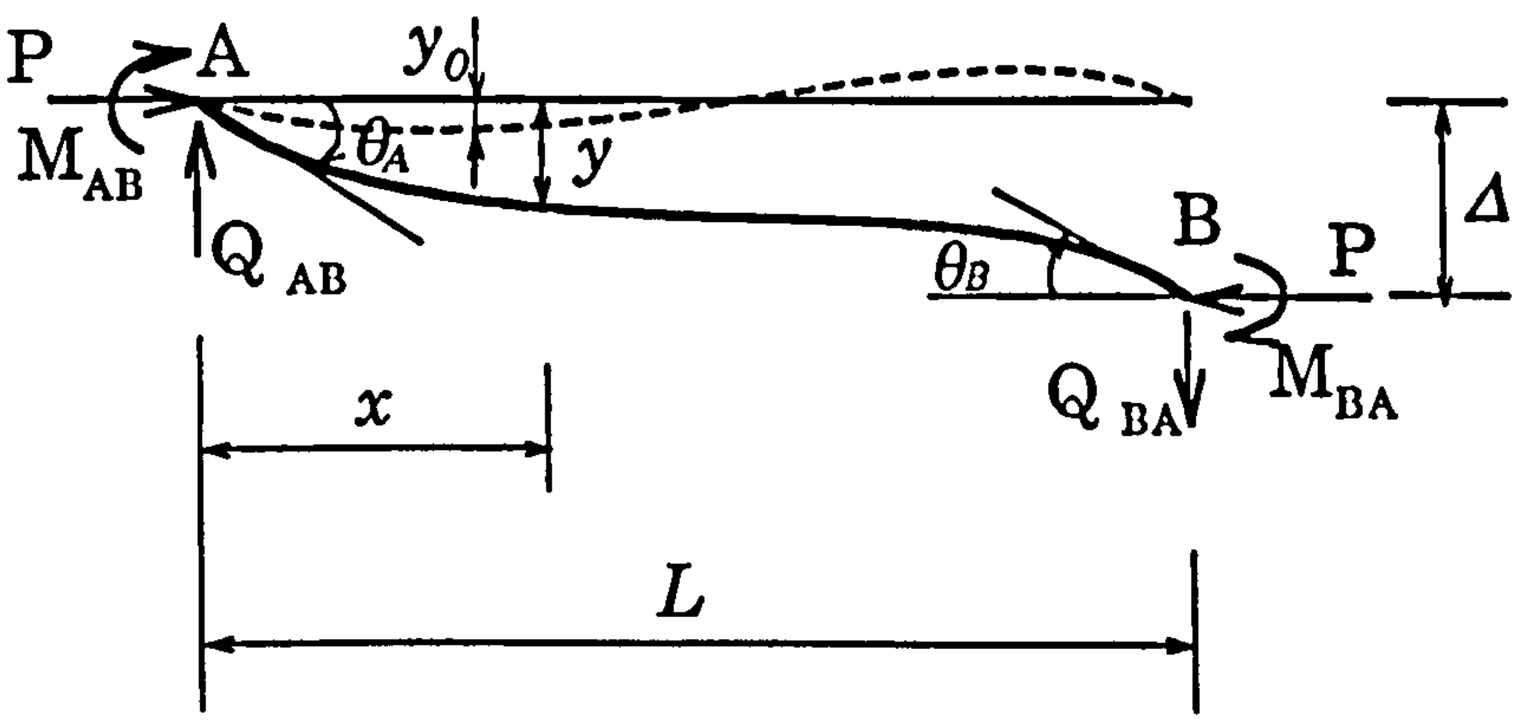

Fig 7.4 Element equilibrium analysis

The initial imperfection of the element is assumed to be a sinusoidal function as

$$y_0=a_0\sin\frac{m\pi x}{L} \qquad (7.7)$$

where a_0 is a specified constant representing the amplitude of the initial imperfection within the element; m=1 for braced frame and m=2 for unbraced frame.

The equation of bending equilibrium of the element can be written

$$M(x)=-EI\frac{d^2\bar{y}}{dx^2} \qquad (7.8)$$

where M(x) denotes the bending moment at the distance of x from the left end of the element, EI is the flexural rigidity of the element, and $\bar{y}$ represents the real deflection of the element, i.e.,

$$\bar{y}=y-y_0$$

Alternatively, Eq(7.8) can be expressed as

$$M_{AB}+Py+Q_{AB}x=-EI\frac{d^2(y-y_0)}{dx^2} \qquad (7.9)$$

Substitution of Eq(7.7) into Eq(7.9) gives

$$\frac{d^2y}{dx^2}+\alpha^2y=-a_0\left(\frac{m\pi}{L}\right)^2\sin\frac{m\pi x}{L}-\frac{M_{AB}}{EI}-\frac{Q_{AB}x}{EI} \qquad (7.10)$$

where

$$\alpha^2=\frac{P}{EI}$$

and P is the axial force of the element.

The corresponding boundary conditions are given as follows

$$y_{(x=0)}=0, \qquad y_{(x=L)}=\Delta \qquad (7.11a)$$

$$y'_{(x=0)}=\theta_A, \qquad y'_{(x=L)}=\theta_B \qquad (7.11b)$$

Solving Eqs(7.10) and (7.11) for θ_A and θ_B yields

$$\theta_A=C_2\alpha+H\frac{m\pi}{L}-\frac{Q_{AB}}{P}$$

$$\theta_B=-C_1\alpha\sin\alpha L+C_2\alpha\cos\alpha L+\frac{m\pi}{L}H\cos m\pi-\frac{Q_{AB}}{P} \qquad (7.12)$$

where

$$C_1=\frac{M_{AB}}{P}$$

$$C_2=\frac{1}{\sin\alpha L}\left[\Delta+\frac{M_{AB}}{P}(1-\cos\alpha L)+\frac{Q_{AB}}{P}L\right]$$

$$H=\frac{a_0}{1-\left(\frac{\alpha L}{m\pi}\right)^2}$$

Considering the equilibrium of the shear forces and the bending equilibrium with respect to end B gives

$$Q_{AB}=Q_{BA}$$
$$M_{BA}=-(M_{AB}+Q_{AB}L+P\Delta) \qquad (7.13)$$

Thus, we obtain the modified slope-deflection equations as follows from Eqs (7.12) and (7.13) considering the initial imperfection of the element:

$$M_{AB}=4i\theta_A\varphi_2(\nu)+2i\theta_B\varphi_3(\nu)-6i\frac{\Delta_B-\Delta_A}{L}\eta_3(\nu)+\bar{M}_{AB}$$

$$M_{BA}=2i\theta_A\varphi_3(\nu)+4i\theta_B\varphi_2(\nu)-6i\frac{\Delta_B-\Delta_A}{L}\eta_3(\nu)+\bar{M}_{BA}$$

$$Q_{AB}=Q_{BA}=-\frac{6i}{L}\theta_A\eta_3(\nu)-\frac{6i}{L}\theta_B\eta_3(\nu)+12i\frac{\Delta_B-\Delta_A}{L^2}\eta_2(\nu)+\bar{Q}_{AB} \qquad (7.14)$$

where

$$\bar{M}_{AB}=\frac{P}{S}.\frac{Hm\pi}{L}[\frac{\sin\alpha L}{\alpha}(\frac{tg\alpha L}{\alpha}-L)+\frac{tg\alpha L}{\alpha}(L-\frac{\sin\alpha L}{\alpha})\cos m\pi]$$

$$\bar{M}_{BA}=\frac{P}{S}.\frac{Hm\pi}{L}[\frac{tg\alpha L}{\alpha}(L-\frac{\sin\alpha L}{\alpha})+\frac{\sin\alpha L}{\alpha}(\frac{tg\alpha L}{\alpha}-L)\cos m\pi]$$

$$\bar{Q}_{AB}=\frac{P}{S}.\frac{Hm\pi}{L}[\frac{\sin\alpha L}{\alpha}(1-\cos\alpha L-\sin\alpha L.tg\alpha L)-\frac{tg\alpha L}{\alpha}(1-\cos\alpha L)\cos m\pi]$$

and

$$S=(1-\cos\alpha L)(L-\frac{tg\alpha L}{\alpha})-(L-\frac{\sin\alpha L}{\alpha}).(1-\cos\alpha L-\sin\alpha L.tg\alpha L)$$

and H is given in Eq(7.12), the relative deflection Δ has been replaced by $(\Delta_B-\Delta_A)$.

The stability functions in Eq(7.14), $\varphi_2(\nu)$, $\varphi_3(\nu)$, $\eta_2(\nu)$ and $\eta_3(\nu)$, are the same as those given in Eq(6.8) of Chapter 6.

It can be seen that Eq(7.14) will reduce to the normal slope-deflection equations if the initial imperfection of the element is not accounted for.

7.4.2. Equations Governing the Equilibrium of the Structure

As before, the beam-column element shown in Fig 7.4 is one of the structural members in the model of Fig 7.2(a). Now, we will apply the modified slope-deflection equation Eq(7.14) to the model in Fig 7.2(a).

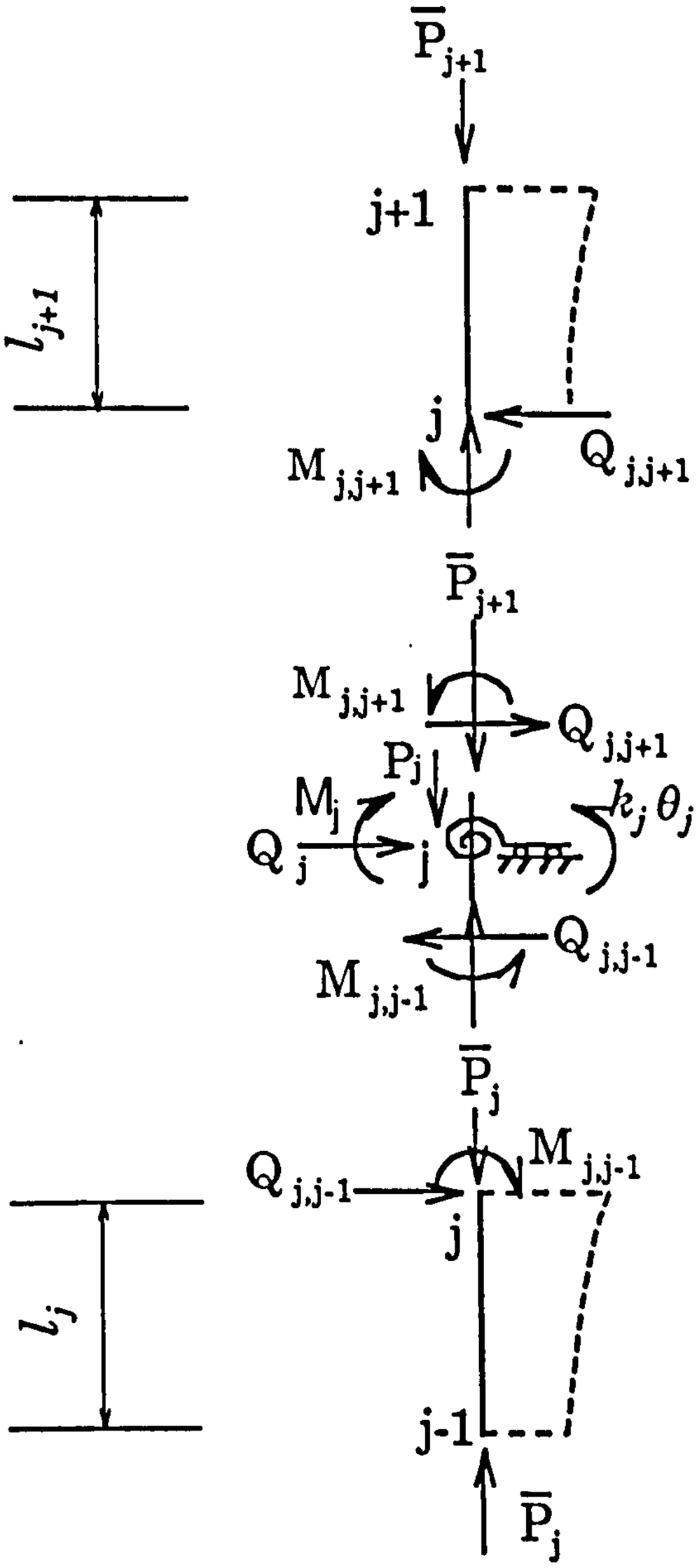

Fig 7.5 Compatibility and equilibrium at joint j

Fig 7.5 shows two isolated neighbouring beam-column elements , taken from the model, Fig 7.2(a), and their end reactions on the connection j. Compatibility of deflection requires that the rotation and deflection of these two elements take the same values at the common joint j. Equilibrium conditions of these two elements require that

$$M_{jj-1}+M_{jj+1}+k_j\theta_j=M_j \qquad (7.15a)$$

$$Q_{jj-1}-Q_{jj+1}=Q_j \qquad (j=1,2,...,n-1) \qquad (7.15b)$$

$$\bar{P}_j=\bar{P}_{j+1}+P_j \qquad (7.15c)$$

where P_j, Q_j and M_j are the external loads acting on the j-th joint, $k_j\theta_j$ is the restraining bending moment of the j-th beam-column joint, and the rest of the symbols are shown in Fig 7.5.

Eq(7.15) represents the bending equilibrium, shear equilibrium, and vertical (axial) equilibrium, respectively, at the joints j=1,2,...,n-1. The corresponding equilibrium equations at the top joint, j=n, reduce to

$$M_{n,n-1}+k_n\theta_n=M_n \qquad (7.16a)$$

$$Q_{n,n-1}=Q_n \qquad (7.16b)$$

and the equilibrium equation at the bottom joint, j=0, reduce to

$$M_{0,1}+k_0\theta_0=M_0 \qquad (7.17)$$

where k_0 is the rotational stiffness of column-baseplate.

Application of the modified slope-deflection equations Eq(7.14), respectively, to Eq(7.17), Eq(7.15), and Eq(7,16) yield

$$[4i_{01}\varphi_2(\nu_{01})+k_0].\theta_0+2i_{01}\varphi_3(\nu_{01}).\theta_1-$$
$$6\frac{i_{01}}{L_1}\eta_3(\nu_{01}).\Delta_1=M_0-\bar{M}_{01} \qquad (j=0) \qquad (7.18)$$

$$2i_{j-1j}\varphi_3(\nu_{j-1j}).\theta_{j-1}+[4i_{j-1j}\varphi_2(\nu_{j-1j})+4i_{jj+1}\varphi_2(\nu_{jj+1})+$$
$$+k_j].\theta_j+2i_{jj+1}\varphi_3(\nu_{jj+1}).\theta_{j+1}+6\frac{i_{j-1j}}{L_j}\eta_3(\nu_{j-1j}).\Delta_{j-1}+$$
$$+[-6\frac{i_{j-1j}}{L_j}\eta_3(\nu_{j-1j})+6\frac{i_{jj+1}}{L_{j+1}}\eta_3(\nu_{jj+1})].\Delta_j-$$
$$-6\frac{i_{jj+1}}{L_{j+1}}\eta_3(\nu_{jj+1}).\Delta_{j+1}=M_j-\bar{M}_{jj-1}-\bar{M}_{jj+1} \qquad (j=1,2,\ldots,n-1) \qquad (7,19a)$$

$$-6\frac{i_{j-1j}}{L_j}\eta_3(\nu_{j-1j}).\theta_{j-1}+[-6\frac{i_{j-1j}}{L_j}\eta_3(\nu_{j-1j})+6\frac{i_{jj+1}}{L_{j+1}}\eta_3(\nu_{jj+1}).\theta_j+$$
$$+6\frac{i_{jj+1}}{L_{j+1}}\eta_3(\nu_{jj+1}).\theta_{j+1}-12\frac{i_{j-1j}}{L_j}\eta_3(\nu_{j-1j}).\Delta_{j-1}+[12\frac{i_{j-1j}}{L_j}\eta_3(\nu_{j-1j})+$$
$$+12\frac{i_{jj+1}}{L_{j+1}}\eta_3(\nu_{jj+1})].\Delta_j-12\frac{i_{jj+1}}{L_{j+1}}\eta_3(\nu_{jj+1}).\Delta_{j+1}=Q_j-\bar{Q}_{jj-1}+\bar{Q}_{jj+1}$$
$$(j=1,2,\ldots,n-1) \qquad (7.19b)$$

$$2L_{n-1,n}\varphi_3(\nu_{n-1,n}).\theta_{n-1}+[4i_{n-1,n}\varphi_2(\nu_{n-1,n})+k_n].\theta_n+$$
$$+6\frac{i_{n-1,n}}{L_n}\eta_3(\nu_{n-1,n})\Delta_{n-1}-6\frac{i_{n-1,n}}{L_n}\eta_3(\nu_{n-1,n})\Delta_n=M_n-\bar{M}_{n,n-1}$$
$$(j=n) \qquad (7.20a)$$

$$-6\frac{i_{n-1,n}}{L_n}\eta_3(\nu_{n-1,n}).\theta_{n-1}-6\frac{i_{n-1,n}}{L_n}\eta_3(\nu_{n-1,n})\theta_n-$$

$$-12\frac{i_{n-1,n}}{L_n}\eta_2(\nu_{n-1,n})\Delta_{n-1}+12\frac{i_{n-1,n}}{L_n}\eta_2(\nu_{n-1,n})\Delta_n=Q_n-\bar{Q}_{n,n-1}$$

$(j=n)$ (7.20*b*)

In the above equations, $i_{j-1,j}$ and L_j (j=1,2,...,n) are the flexural rigidity and length, respectively, of the element with ends of (j-1) and j. $\nu_{j-1,j}$ are functions of the axial force $\bar{P}_j$. $\bar{M}_{j-1,j}$ and $\bar{Q}_{j-1,j}$ result from the initial imperfection of the elements. They are given by

$$i_{j-1,j}=\frac{E_jI_j}{L_j}$$

$$\nu_{j-1,j}=L_j\sqrt{\frac{\bar{P}_j}{E_jI_j}}$$

and

$$\bar{M}_{jj-1}=\frac{\bar{P}_j}{S_j}.\frac{H_jm\pi}{L_j}[\frac{tg\alpha_jL_j}{\alpha_j}(L_j-\frac{\sin\alpha_jL_j}{\alpha_j})+\frac{\sin\alpha_jL_j}{\alpha_j}(\frac{tg\alpha_jL_j}{\alpha_j}-L_j)\cos m\pi]$$

$$\bar{M}_{jj+1}=\frac{\bar{P}_{j+1}}{S_{j+1}}.\frac{H_{j+1}m\pi}{L_{j+1}}[\frac{\sin\alpha_{j+1}L_{j+1}}{\alpha_{j+1}}(\frac{tg\alpha_{j+1}L_{j+1}}{\alpha_{j+1}}-L_{j+1})+$$

$$+\frac{tg\alpha_{j+1}L_{j+1}}{\alpha_{j+1}}(L_{j+1}-\frac{\sin\alpha_{j+1}L_{j+1}}{\alpha_{j+1}})\cos m\pi]$$

$$\bar{Q}_{jj-1}=\frac{\bar{P}_j}{S_j}.\frac{H_jm\pi}{L_j}[\frac{\sin\alpha_jL_j}{\alpha_j}(1-\cos\alpha_jL_j-\sin\alpha_jL_j.tg\alpha_jL_j)-$$

$$-\frac{tg\alpha_j L_j}{\alpha_j}(1-\cos\alpha_j L_j)\cos m\pi]$$

$$\bar{Q}_{jj+1}=\frac{\bar{P}_{j+1}}{S_{j+1}}.\frac{H_{j+1}m\pi}{L_{j+1}}[\frac{\sin\alpha_{j+1}L_{j+1}}{\alpha_{j+1}}(1-\cos\alpha_{j+1}L_{j+1}-$$

$$-\sin\alpha_{j+1}L_{j+1}.tg\alpha_{j+1}L_{j+1})-\frac{tg\alpha_{j+1}L_{j+1}}{\alpha_{j+1}}(1-\cos\alpha_{j+1}L_{j+1})\cos m\pi]$$

$$S_j=(1-\cos\alpha_j L_j)(L_j-\frac{tg\alpha_j L_j}{\alpha_j})-(L_j-\frac{\sin\alpha_j L_j}{\alpha_j}).$$
$$.(1-\cos\alpha_j L_j-\sin\alpha_j L_j.tg\alpha_j L_j)$$

$$H_j=\frac{a_{0j}}{1-(\frac{\alpha_j L_j}{m\pi})^2}, \qquad \alpha_j=\sqrt{\frac{\bar{P}_j}{E_j I_j}} \qquad (7.21)$$

a_{0j} is the specified amplitude of the initial imperfection within the j-th element.

It is customary to express the lateral deflection using relative displacement. We therefore define

$$\delta_j=\Delta_j-\Delta_{j-1} \qquad (j=1,2,...,n) \qquad (7.22)$$

where δ_j is the displacement of the end j relative to the end (j-1), see Fig 7.5(b). For the bottom element, $\Delta_0=0$.

On the other hand, it is inevitable that the global structure has an initial imperfection, which is described in Fig 7.6 where Δ_j° and Δ_{j-1}° denote the nodal initial deflection at the j-th and (j-1)th nodes.

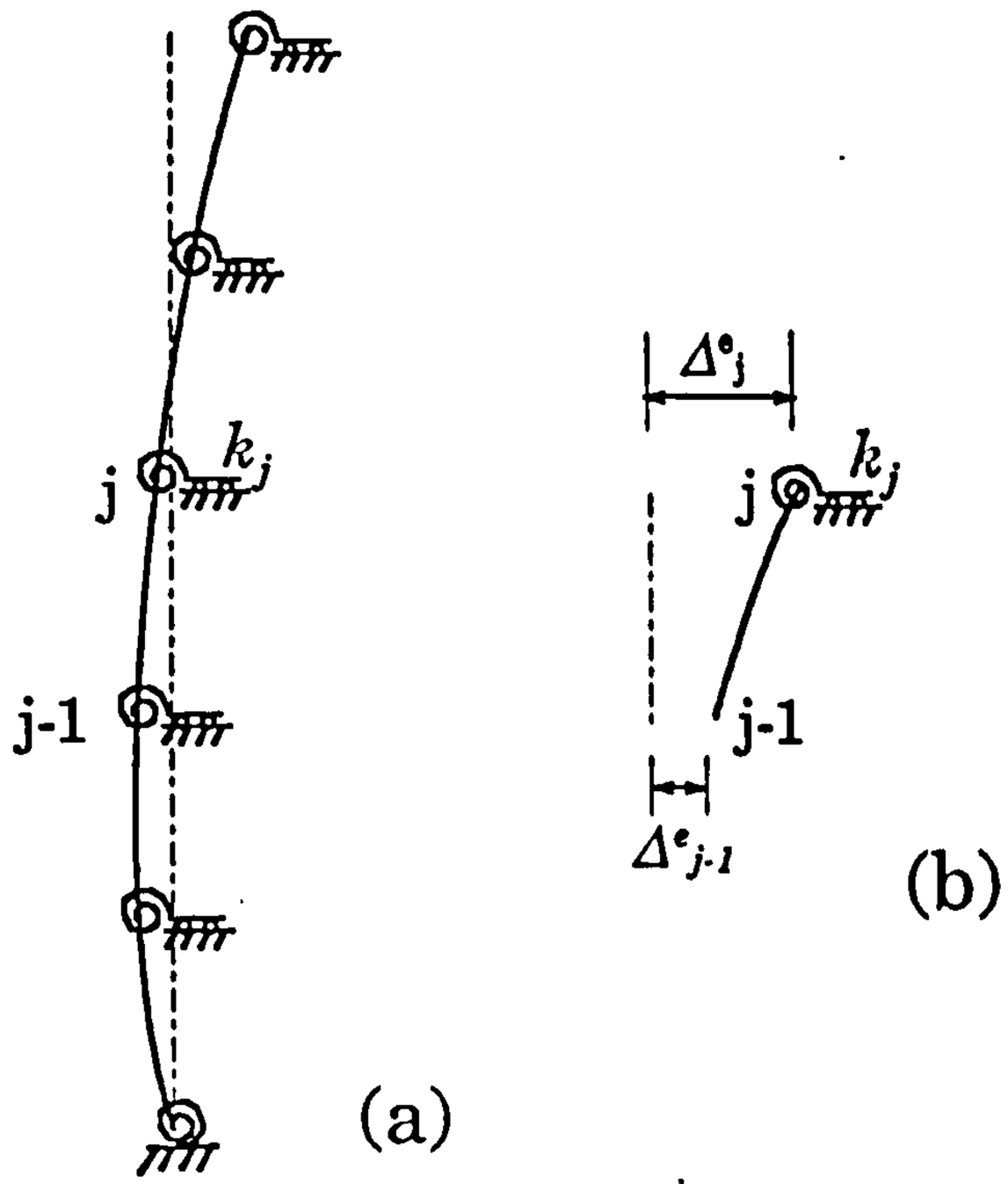

Fig 7.6 Initial imperfection of the structure

The initial imperfection of the structure can be specified in practice by an allowed maximum tolerance of nodal deflection. An alternative way is to assume that the shape of the initial deflection of the structure follows that of the buckling modes with the maximum deflection specified by an allowed tolerance, which may be the most disadvantageous to the structure. The buckling modes of the structure have been obtained in Chapter 6 and can be used here to describe initial imperfections of the structure.

In this case, Eq(7.22) becomes

$$\delta_j=(\Delta_j-\Delta_{j-1})-(\Delta_j^e-\Delta_{j-1}^e) \qquad (j=1,2,...,n) \qquad (7.23)$$

with $\Delta_0=0$ and $\Delta_0^e=0$.

Rearrangement of Eqs(7.18), (7.19) and (7.20) in terms of δ_j of Eq(7.23) gives the equations in matrix form as

$$[C]\{D\}=\{F\} \qquad (7.24)$$

where

$$\{D\}^T=\{\theta_0, \delta_1, \theta_1, \ldots, \delta_{2j-1}, \theta_{2j}, \ldots, \delta_n, \theta_n\}_{(2n+1)x1}$$

$$\{F\}^T=\{F_0, F_1, F_1, \ldots, F_{2j-1}, F_{2j}, \ldots, F_n, F_n\}_{(2n+1)x1}$$

$$[C] = \begin{bmatrix}
C_{00} & C_{01} & C_{02} & & & & & & & \\
C_{10} & C_{11} & C_{12} & C_{13} & C_{14} & & & & & \\
C_{20} & C_{21} & C_{22} & C_{23} & C_{24} & & & & & \\
 & & C_{32} & C_{33} & C_{34} & C_{35} & C_{36} & & & \\
 & & C_{42} & C_{43} & C_{44} & C_{45} & C_{46} & & & \\
 & & & \cdots\cdots & & & & & & \\
 & & & C_{2j-1,2j-2} & C_{2j-1,2j-1} & C_{2j-1,2j} & C_{2j-1,2j+1} & C_{2j-1,2j+2} & & \\
 & & & C_{2j,2j-2} & C_{2j,2j-1} & C_{2j,2j} & C_{2j,2j+1} & C_{2j,2j+2} & & \\
 & & & & & & \cdots\cdots & & & \\
 & & & & & & & C_{2n-1,2n-2} & C_{2n-1,2n-1} & C_{2n-1,2n} \\
 & & & & & & & C_{2n,2n-2} & C_{2n,2n-1} & C_{2n,2n}
\end{bmatrix}$$

where the coefficients of the 1st row are

$$C_{00}=4i_{0,1}\varphi_2(v_{0,1})+k_0$$

$$C_{01}=-6\frac{i_{0,1}}{L_1}\eta_3(v_{0,1}) \qquad (j=0) \qquad (7.25a)$$

$$C_{02}=2i_{0,1}\varphi_3(v_{0,1})$$

and those of the 2j-th row are

$$C_{2j-1,2j-2}=-6\frac{i_{j-1,j}}{L_j}\eta_3(v_{j-1,j})$$

$$C_{2j-1,2j-1}=12\frac{i_{j-1,j}}{L_j}\eta_2(v_{j-1,j})$$

$$C_{2j-1,2j}=[-6\frac{i_{j-1,j}}{L_j}\eta_3(v_{j-1,j})+6\frac{i_{j,j+1}}{L_{j+1}}\eta_3(v_{j,j+1})]$$

$$C_{2j-1,2j+1}=-12\frac{i_{j,j+1}}{L_{j+1}}\eta_2(v_{j,j+1})$$

$$C_{2j-1,2j+2}=6\frac{i_{j,j+1}}{L_{j+1}}\eta_3(v_{j,j+1}) \qquad (j=1,2,\ldots,n-1) \qquad (7.25b)$$

and those of the (2j+1)th row are

$$C_{2j,2j-2}=2i_{j-1,j}\varphi_3(v_{j-1,j})$$

$$C_{2j,2j-1}=-6\frac{i_{j-1,j}}{L_j}\eta_3(v_{j-1,j})$$

$$C_{2j,2j}=4i_{j-1,j}\varphi_2(v_{j-1,j})+4i_{j,j+1}\varphi_2(v_{j,j+1})+k_j$$

$$C_{2j,2j+1}=-6\frac{i_{j,j+1}}{L_{j+1}}\eta_3(v_{j,j+1})$$

$$C_{2j,2j+2}=2i_{j,j+1}\varphi_3(v_{j,j+1}) \qquad (j=1,2,\ldots,n-1) \qquad (7.25c)$$

and those of the 2n-th row are

$$C_{2n-1,2n-2}=-6\frac{i_{n-1,n}}{L_n}\eta_3(\nu_{n-1,n})$$

$$C_{2n-1,2n-1}=12\frac{i_{n-1,n}}{L_n}\eta_2(\nu_{n-1,n})$$

$$C_{2n-1,2n}=-6\frac{i_{n-1,n}}{L_n}\eta_3(\nu_{n-1,n}) \qquad (j=n) \qquad (7.25d)$$

and those of the (2n+1)th row are

$$C_{2n,2n-2}=2i_{n-1,n}\varphi_3(\nu_{n-1,n})$$

$$C_{2n,2n-1}=-6\frac{i_{n-1,n}}{L_n}\eta_3(\nu_{n-1,n})$$

$$C_{2n,2n}=4i_{n-1,n}\varphi_2(\nu_{n-1,n})+k_n \qquad (j=n) \qquad (7.25e)$$

The components of the load vector in the right hand side of Eq(7.24) are given by

$$F_0=M_0-\bar{M}_{0,1}-F_0^e$$

$$F_1=Q_1-\bar{Q}_{1,0}+\bar{Q}_{1,2}-F_1^e$$

$$F_2=M_1-\bar{M}_{1,0}-\bar{M}_{1,2}-F_2^e$$

... ...

$$F_{2j-1}=Q_j-\bar{Q}_{jj-1}+\bar{Q}_{jj+1}-F^e_{2j-1}$$

$$F_{2j}=M_j-\bar{M}_{jj-1}-\bar{M}_{jj+1}-F^e_{2j}$$

... ...

$$F_{2n-1}=Q_n-\bar{Q}_{nn-1}-F^e_{2n-1}$$

$$F_{2n}=M_n-\bar{M}_{nn-1}-F^e_{2n} \qquad (7.26)$$

where $\overline{M}_{j-1j}$, $\overline{M}_{jj+1}$, $\overline{Q}_{j-1j}$, and $\overline{Q}_{jj+1}$ are given in Eq(7.21) representing the effects of the initial imperfection of the beam-column elements, while F_{2j-1}^e and F_{2j}^e indicate the initial imperfections of the global structure, having the following expressions,

$$F^e_0=C_{01}\Delta^e_1 \qquad (j=0)$$

$$F^e_{2j-1}=C_{2j-1,2j-1}(\Delta^e_j-\Delta^e_{j-1})+C_{2j-1,2j+1}(\Delta^e_{j+1}-\Delta^e_j)$$

$$F^e_{2j}=C_{2j,2j-1}(\Delta^e_j-\Delta^e_{j-1})+C_{2j,2j+1}(\Delta^e_{j+1}-\Delta^e_j) \qquad (j=1,2,...,n-1)$$

$$F^e_{2n-1}=C_{2n-1,2n-1}(\Delta^e_n-\Delta^e_{n-1})$$

$$F^e_{2n}=C_{2n,2n-1}(\Delta^e_n-\Delta^e_{n-1}) \qquad (j=n) \qquad (7.27)$$

where Δ_j^e (j=0,1,2,...,n) are the initial deflections of the global structure, see Fig 7.6.

7.4.3 Solution of the equations

The coefficients in Eq(7.24) are transcendental functions in terms of the axial forces at each column element. Solving these equations usually entails an iterative process because of the interaction between the axial forces and the lateral displacements caused by lateral loads and bending moments. For example, the frame structure shown in Fig 7.1 falls into the category of statically indeterminate structures in which the axial forces at beams and columns are directly dependent upon the displacements and rotations of beam-column joints. However, for the structural model in Fig 7.2(a), the axial forces at each column element can be statically determined without considering the deformation geometry, which provides a straightforward way to solve Eq(7.24).

However, because the rotational stiffness of the column-baseplate exhibits nonlinear behaviour, an iterative procedure is still employed to find the solution.

Whatever solution procedure is used, transformation of the coefficient matrix of Eq(7.24) into an upper-triangular matrix seems particularly straightforward. This process is introduced below.

The objective of this process is to eliminate the elements below the diagonal of the matrix [C] in Eq(7.24). Assume that the elimination of the former (2j-1) rows has been finished. After the elimination procedure, the elements at 2j and (2j+1) rows of [C] and the corresponding elements of {F} become

$0, C'_{2j-1,2j-1}, C'_{2j-1,2j}, C'_{2j-1,2j+1}, C'_{2j-1,2j+2} \sim F'_{2j-1}$

$0, 0, C''_{2j,2j}, C''_{2j,2j+1}, C''_{2j,2j+2} \sim F''_{2j}$

(j=1,2, ...,n-1)

where

$$C'_{2j-1,2j-1}=C_{2j-1,2j-1}-C_{2j-1,2j-2}\frac{C''_{2j-2,2j-1}}{C''_{2j-2,2j-2}}$$

$$C'_{2j-1,2j}=C_{2j-1,2j}-C_{2j-1,2j-2}\frac{C''_{2j-2,2j}}{C''_{2j-2,2j-2}}$$

$$C'_{2j-1,2j+1}=C_{2j-1,2j+1}\ , \qquad C'_{2j-1,2j+2}=C_{2j-1,2j+2}$$

$$F'_{2j-1}=F_{2j-1}-C_{2j-1,2j-2}\frac{F''_{2j-2}}{C''_{2j-2,2j-2}}$$

and

$$C'_{2j,2j-1}=C_{2j,2j-1}-C_{2j,2j-2}\frac{C''_{2j-2,2j-1}}{C''_{2j-2,2j-2}}$$

$$C'_{2j,2j}=C_{2j,2j}-C_{2j,2j-2}\frac{C''_{2j-2,2j}}{C''_{2j-2,2j-2}}$$

$$C'_{2j,2j+1}=C_{2j,2j+1}\ , \qquad C'_{2j,2j+2}=C_{2j,2j+2}$$

$$F'_{2j}=F_{2j}-C_{2j,2j-2}\frac{F''_{2j-2}}{C''_{2j-2,2j-2}}$$

and

$$C''_{2j,2j}=C'_{2j,2j}-C'_{2j,2j-1}\frac{C'_{2j-1,2j}}{C'_{2j-1,2j-1}}$$

$$C''_{2j,2j+1}=C'_{2j,2j+1}-C'_{2j,2j-1}\frac{C'_{2j-1,2j+1}}{C'_{2j-1,2j-1}}$$

$$C''_{2j,2j+2}=C'_{2j,2j+2}-C'_{2j,2j-1}\frac{C'_{2j-1,2j+2}}{C'_{2j-1,2j-1}}$$

$$F''_{2j}=F'_{2j}-C'_{2j,2j-1}\frac{F'_{2j-1}}{C'_{2j-1,2j-1}}$$

and

$$C''_{00}=C_{00}\,,\quad C''_{01}=C_{01}\,,\quad C''_{02}=C_{02}\,,\quad F''_{0}=F_{0}$$

In the case when j=n, the elimination gives

$$0,\ C'_{2n-1,2n-1},\ C'_{2n-1,2n}\ \sim\ F'_{2n-1}$$

$$0,\ 0,\qquad C''_{2n,2n}\ \sim\ F''_{2n}$$

where

$$C'_{2n-1,2n-1}=C_{2n-1,2n-1}-C_{2n-1,2n-2}\frac{C''_{2n-2,2n-1}}{C''_{2n-2,2n-2}}$$

$$C'_{2n-1,2n}=C_{2n-1,2n}-C_{2n-1,2n-2}\frac{C''_{2n-2,2n}}{C''_{2n-2,2n-2}}$$

$$F'_{2n-1}=F_{2n-1}-C_{2n-1,2n-2}\frac{F''_{2n-2}}{C''_{2n-2,2n-2}}$$

and

$$C'_{2n,2n-1}=C_{2n,2n-1}-C_{2n,2n-2}\frac{C''_{2n-2,2n-1}}{C''_{2n-2,2n-2}}$$

$$C'_{2n,2n}=C_{2n,2n}-C_{2n,2n-2}\frac{C''_{2n-2,2n}}{C''_{2n-2,2n-2}}$$

$$F'_{2n}=F_{2n}-C_{2n,2n-2}\frac{F''_{2n-2}}{C''_{2n-2,2n-2}}$$

and

$$C''_{2n,2n}=C'_{2n,2n}-C'_{2n,2n-1}\frac{C'_{2n-1,2n}}{C'_{2n-1,2n-1}}$$

$$F''_{2n}=F'_{2n}-C'_{2n,2n-1}\frac{F'_{2n-1}}{C'_{2n-1,2n-1}}$$

The above procedure has transformed the non-triangular matrix [C] into a upper-triangular matrix from which the solutions can be obtained by back substitution.

A computer program NSTAB [55], which is based on the above theories and procedures, has been written. It has the facility of calculation of the displacements and the internal forces of semi-rigid slender frame structures subjected to both lateral and vertical loads.

7.5 Numerical examples and conclusions

Using the proposed simplified second-order analysis model and the associated computer program NSTAB [55], four numerical examples are given below.

Example 1:

Take the two-segment fixed-free column as the first example (Fig 7.7), where the elastic modulus $E=2.10\times10^5$ N/mm^2, the moment of inertia of the cross section $I=1.92\times10^5$ mm^4, the length of the column segment $l_1=l_2=1500$ mm. No rotational stiffness at the beam-column joints and the column-baseplate joint are considered in this example.

Firstly, the buckling mode, see Fig 7.7(a), is computed and is given by

$\beta=\{\ \beta_1, \beta_2\ \}^T=\{\ 0.31, 1.0\ \}^T$

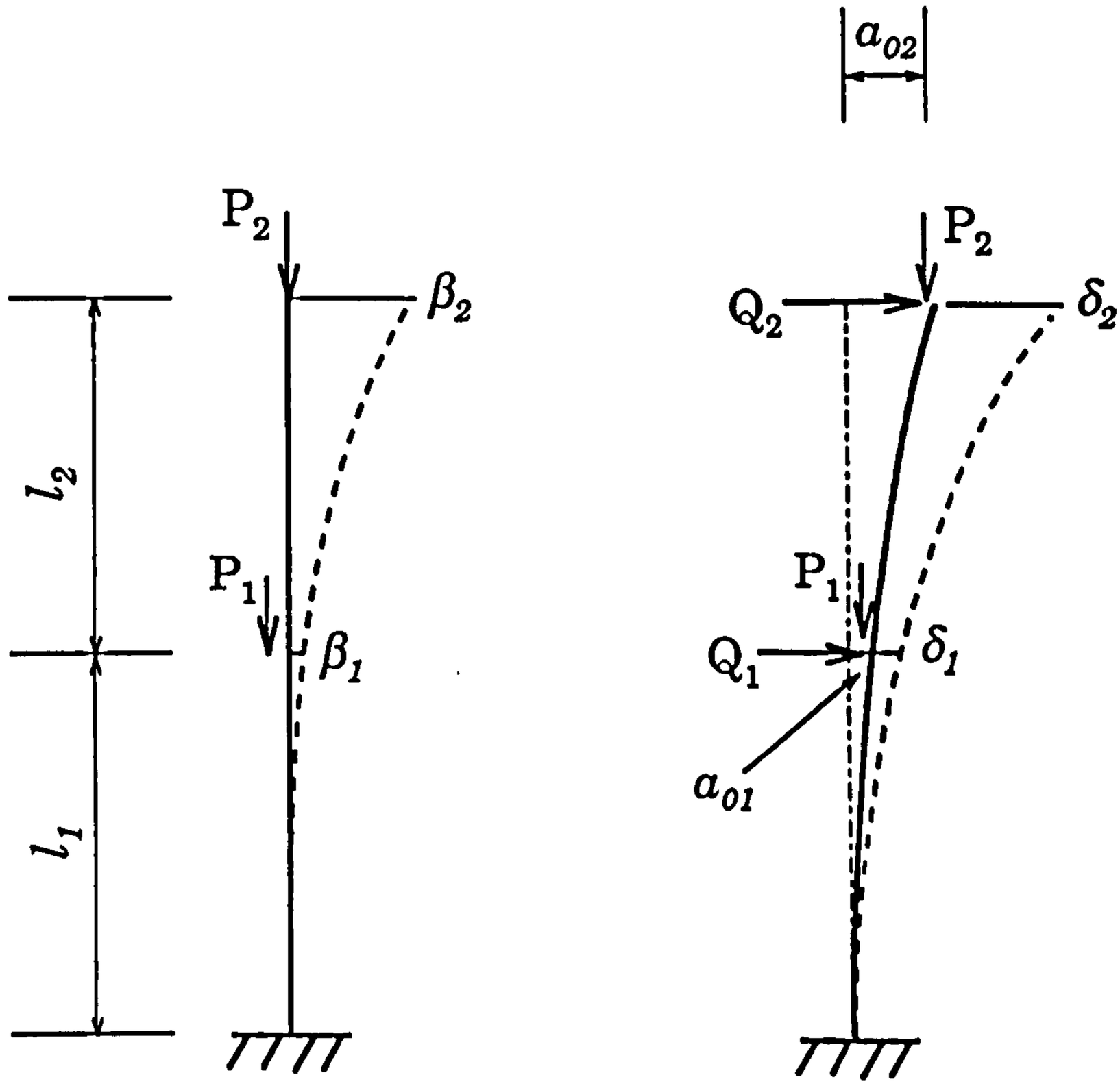

(a) (b)

Fig 7.7 Two-segment fixed-free column

(a) buckling mode, and (b) deformed curve

which will be taken as the initial imperfection of the structure, see Fig 7.7(b), by

$$a_0=\frac{l_1+l_2}{300}\beta$$

or

$$a_0=\{\ a_{01},\ a_{02}\ \}^T=\{\ 3.1,\ 10.0\ \}^T$$

Consider two load cases. The first one is that $P_1=P_2=2200N$ and $Q_1=Q_2=0$ which gives the computed deflection as

$$\{ \delta_1, \delta_2 \}^T=\{ 4.72, 15.05 \}^T$$

where the initial imperfection has been considered.

The second load case, $P_1=P_2=2200N$ and $Q_1=Q_2=11.0$ N, gives the computed deflection as

$$\{ \delta_1, \delta_2 \}^T=\{ 2.06, 6.31 \}^T$$

where no initial imperfection has been considered, and

$$\{ \delta_1, \delta_2 \}^T=\{ 6.78, 21.36 \}^T$$

where the initial imperfection has been considered.

From the above computed results, it can reasonably be seen that in the case when the initial imperfection is considered, the deflections with lateral loads are greater than those without lateral loads, and that the deflections with initial imperfections are greater than those without initial imperfections.

Example 2:

The second example is a four-segment fixed-free column shown in Fig 7.8. The results of this illustration will be compared with those of a general-purpose finite element analysis computer program LUSAS.

The structure in Fig 7.8 has the following parameters: the elastic modulus $E=2.10x10^5$ N/mm^2, the moment of inertia $I=1.92x10^5$ mm^4, the length of the column segment $l_1=l_2=l_3=l_4=1500$ mm. No beam-column

rotational stiffness and the column-baseplate rotation stiffness are accounted for.

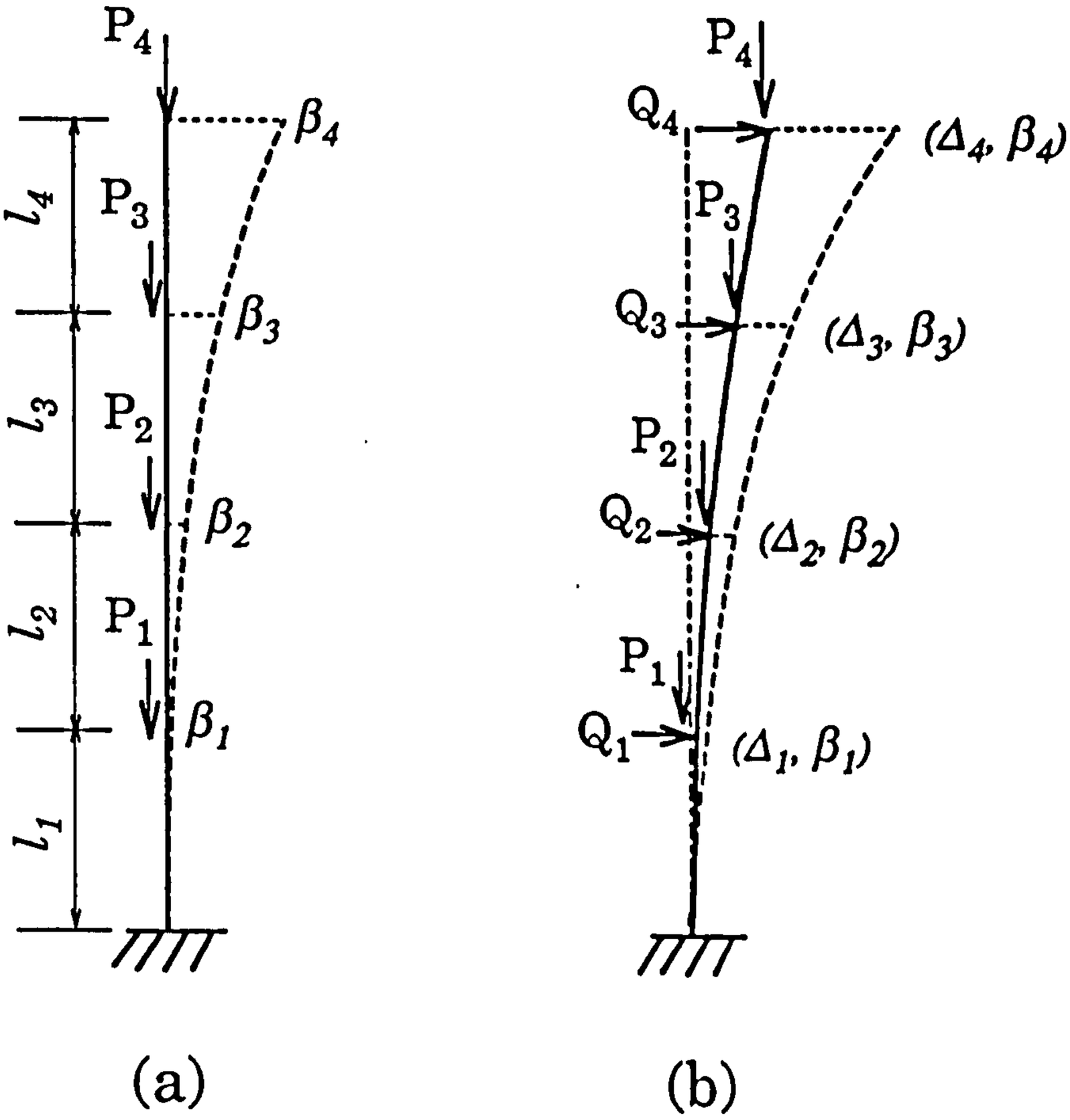

Fig 7.8 Four-segment fixed-free column
(a) buckling mode, and (b) deformed curve

Four load cases are considered as follows

Load Case 1: P_1=2000N, P_2=1000N, P_3=500N, P_4=250N,
Q_1=20N, Q_2=10N, Q_3=5N, Q_4=2.5N,

Load Case 2: P_1=4000N, P_2=2000N, P_3=1000N, P_4=500N,

Q_1=20N, Q_2=10N, Q_3=5N, Q_4=2.5N.

These are two load cases without considering initial imperfections of the structure. The other two load cases, Load Case 3 and Load Case 4 corresponding to the Load Case 1 and Load Case 2, respectively, take into account initial imperfections.

The initial imperfection of the structure is assumed to be the same shape as that of the associated buckling mode which is the most unfavourable case of all the possible deformation modes. The load factors at both Load Case 1 and Load Case 2 are the same as

$$\alpha=\{\ \alpha_1, \alpha_2, \alpha_3, \alpha_4\ \}^T=\{\ 8.0, 4.0, 2.0, 1.0\ \}^T$$

so they have the same buckling modes given by

$$\beta=\{\ \beta_1, \beta_2, \beta_3, \beta_4\ \}^T=\{\ 0.10, 0.35, 0.66, 1.00\ \}^T$$

According to design requirements, choose the initial imperfection curve as

$$a_0=\frac{\sum_{i=1}^{4} l_i}{600}\beta$$

or

$$\alpha_0=\{\ \alpha_{01}, \alpha_{02}, \alpha_{03}, \alpha_{04}\ \}^T=\{\ 1.0, 3.5, 6.6, 10.0\ \}^T$$

The computed results and those of LUSAS are listed in Table 7.1 and Table 7.2, in which the results of LUSAS are obtained by dividing each column segment into 8 beam elements.

Table 7.1 shows the rotations and the lateral displacements at the beam-column joints without the effects of initial imperfection. Table 7.2, on the other hand, gives the results of considering the effects of initial imperfection. Both tables list the results of LUSAS at the same time. The comparison of the results shows that the relative difference is very small for the case of no initial imperfection, and the maximum relative difference for the case of considering initial imperfection is 2.933% for Load Case 3 and 4.860% for Load Case 4.

Table 7.1 The Computed Rotations and Deflections without Initial Imperfection

	Load Case 1			Load Case 2		
	NSTAB	LUSAS	%	NSTAB	LUSAS	%
θ1	3.5992×10^{-3}	3.5991×10^{-3}	0.0028	6.0922×10^{-3}	6.0915×10^{-3}	0.0115
Δ1	3.0140	3.0139	0.0033	5.0076	5.0069	0.0140
θ2	5.1873×10^{-3}	5.1872×10^{-3}	0.0019	9.0328×10^{-3}	9.0318×10^{-3}	0.0111
Δ2	9.7809	9.7805	0.0041	16.6635	16.6613	0.0132
θ3	5.7333×10^{-3}	5.7331×10^{-3}	0.0035	10.0760×10^{-3}	10.0749×10^{-3}	0.0109
Δ3	18.0524	18.0517	0.0039	31.1483	31.1442	0.0132
θ4	5.8434×10^{-3}	5.8433×10^{-3}	0.0017	10.2883×10^{-3}	10.2872×10^{-3}	0.0107
Δ4	26.7624	26.7615	0.0034	46.4746	46.4685	0.0131

Table 7.2 The Computed Rotations and Deflections with Initial Imperfection

	Load Case 3			Load Case 4		
	NSTAB	LUSAS	%	NSTAB	LUSAS	%
θ1	4.21×10^{-3}	4.10×10^{-3}	2.683	8.17×10^{-3}	7.81×10^{-3}	4.609
Δ1	3.51	3.41	2.933	6.69	6.38	4.860
θ2	6.10×10^{-3}	5.97×10^{-3}	2.178	12.20×10^{-3}	11.72×10^{-3}	4.096
Δ2	11.45	11.16	2.599	22.40	21.44	4.478
θ3	6.76×10^{-3}	6.62×10^{-3}	2.115	13.64×10^{-3}	13.12×10^{-3}	3.963
Δ3	21.20	20.70	2.415	41.99	40.27	4.271
θ4	6.89×10^{-3}	6.75×10^{-3}	2.074	13.94×10^{-3}	13.41×10^{-3}	3.952
Δ4	31.47	30.76	2.308	62.75	60.23	4.184

Example 3:

The third illustration is an unbraced slender frame shown in Fig 7.9(a) in which the shaded part uses the simplified computational model of Fig 7.9(c), where the vertical loads P_j and the lateral load Q_j (j=1,2,3,4) are derived from the neighbouring connecting beams. From section 7.3, they are given by

Load Case 1: P_1=1600N, P_2=800N, P_3=400N, P_4=200N,
Q_1=8N, Q_2=4N, Q_3=2N, Q_4=1N,

Load Case 2: P_1=4000N, P_2=2000N, P_3=1000N, P_4=500N,
Q_1=20N, Q_2=10N, Q_3=5N, Q_4=2.5N.

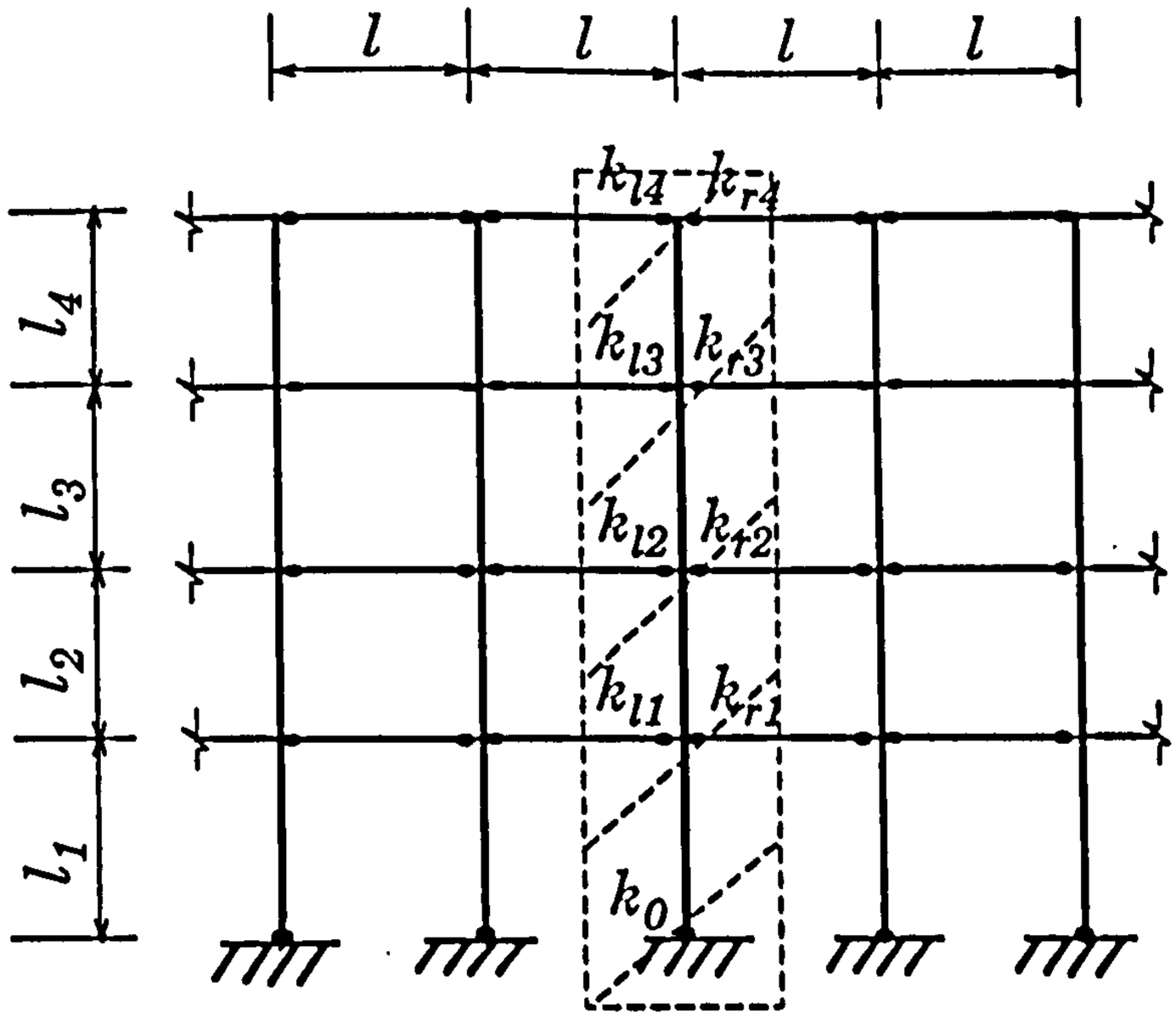

(a)

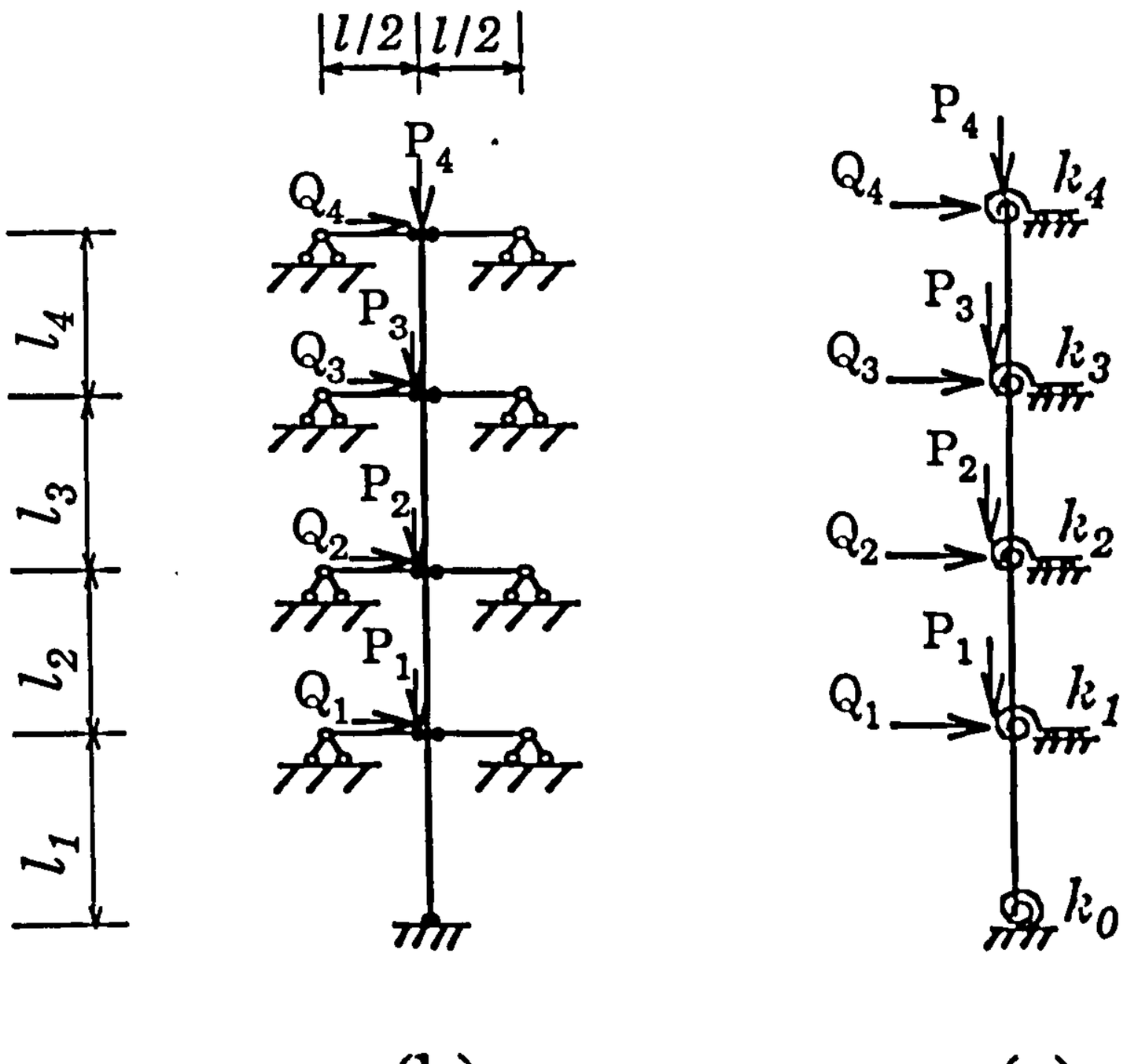

(b) (c)

Fig 7.9 (a) An unbraced frame structure
(b) a simplified model used for LUSAS, and
(c) the simplified model of this chapter

The semi-rigid stiffness of beam-column connections is computed by Eq (6.5)

$$k_i=\frac{1}{\left[\frac{L}{12(EI)_i}+\frac{1}{4k_{li}}+\frac{1}{4k_{ri}}\right]} \qquad (i=1,2,3,4)$$

where L and EI are the length and the flexural rigidity of the connecting beam, respectively; k_{li} and k_{ri} are the rotation stiffness of the left and right connecting beams, respectively; see Fig 7.9(a). Assuming that $E=2.10\times10^5$ N/mm^2, $I=8.62\times10^4$ mm^4, L=2000 mm, and all beam-column connections behave in the same way, i.e., $k_{li}=k_{ri}=7.3\times10^8$ N.mm/rad, we have

$k_i=1.17\times10^8$ N.mm/rad (i=1,2,3,4)

The semi-rigid stiffness of the column-baseplate connection is assumed to be $k_0=1.43\times10^9$ Nmm/rad. The heights of the storeys are assumed to be the same $l_1=l_2=l_3=l_4=1500$ mm. The elastic modulus and the inertia moment of the column are $E=2.10\times10^5$ N/mm^2 and $I=1.92\times10^5$ mm^4, respectively.

The computed rotations θ_i and the lateral deflection Δ_i (i=1,2,3,4) are shown in Table 7.3, where the comparison with the results of LUSAS, based on the model of Fig 7.9(b), has also been made. The relative differences between the results of NSTAB and LUSAS are given as well which shows that the results of NSTAB compared with those of LUSAS are reasonably good.

Table 7.3 Comparison of the Results between NSTAB and LUSAS

	Load Case 1			Load Case 2		
	NSTAB	LUSAS	%	NSTAB	LUSAS	%
θ_0	0.9956×10^{-5}	1.0195×10^{-5}	2.344	0.2583×10^{-4}	0.2655×10^{-4}	2.712
θ_1	1.1125×10^{-4}	1.1158×10^{-4}	0.296	2.9023×10^{-4}	3.0350×10^{-4}	4.372
Δ_1	0.1984	0.2084	4.798	0.5181	0.5469	5.266
θ_2	0.6692×10^{-4}	0.7172×10^{-4}	6.693	1.7296×10^{-4}	1.8560×10^{-4}	6.810
Δ_2	0.3820	0.4097	6.761	0.9955	1.0733	7.249
θ_3	0.2993×10^{-4}	0.3277×10^{-4}	8.666	0.7645×10^{-4}	0.8430×10^{-4}	9.312
Δ_3	0.4758	0.5150	7.612	1.2365	1.3459	8.128
θ_4	0.1081×10^{-4}	0.1235×10^{-4}	12.470	0.2742×10^{-4}	0.3150×10^{-4}	12.952
Δ_4	0.5133	0.5584	8.077	1.3321	1.4570	8.572

Example 4:

The fourth example is a four-bay frame structure with an equal span of L and different heights of l_i (i=1,2,3,4) on different level, shown in Fig 7.10(a). It is assumed that L=2000 mm, $l_1=l_2=l_3=l_4=1500$ mm; and the elastic modulus $E=2.10\times10^5$ N/mm, the moment of inertia of the beam cross section is $I_b=8.62\times10^4$ mm^4 and the column cross section is $I_c=1.92\times10^5$ mm^4. The beam-column connections and the column-baseplates are assumed to be semi-rigidly connected and the rotational stiffness of beam-column connection $k_i=k_r=7.3\times10^8$ N.mm/rad, column-baseplate $k_0=1.43\times10^9$ N.mm/rad.

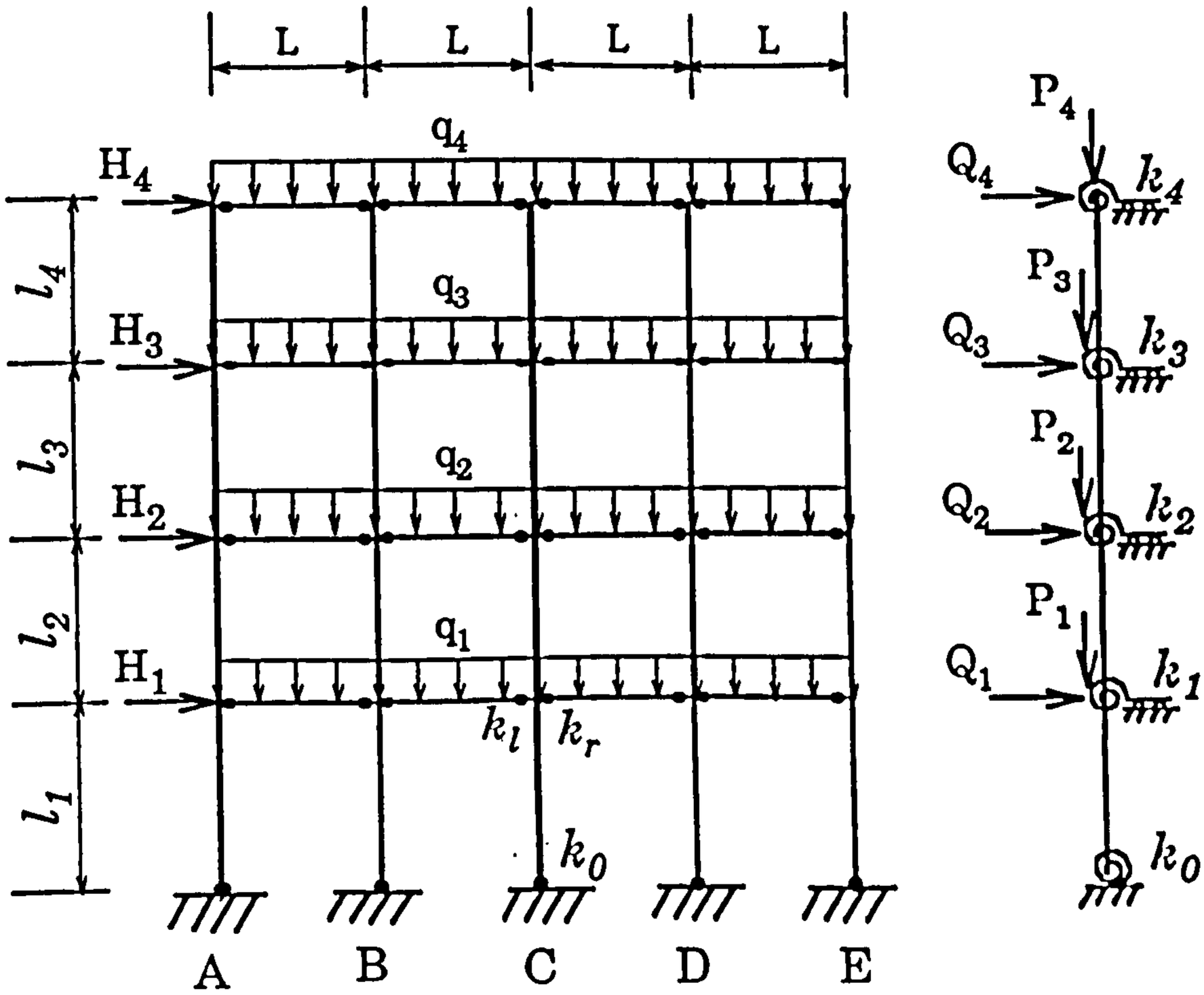

(a) (b)

Fig 7.10 A four-bay frame structure subjected to vertical and horizontal loads (a), and its simplified second-order analysis model (b)

The frame structure is subjected to the uniformly distributed loads, q_1=2.0N/mm, q_2=1.0N/mm, q_3=0.5N/mm, and q_4=0.25N/mm, respectively, on beams and the horizontal loads, $H_i=\lambda(4q_iL)$ (i=1,2,3,4), on i-th level, where λ=1/160, so H_1=100.0N, H_2=50.0N, H_3=25.0N, and H_4=12.5N.

Fig 7.10(b) shows the simplified computational model proposed in this chapter, where the column-baseplate rotational stiffness, k_0, is the same as that of the original structure in Fig 7.10(a), the equivalent rotational stiffness, k_i (i=1,2,3,4), is calculated from Eq(6.5) in Chapter 6, giving $k_i=1.173\times10^8$ Nmm/rad.

It should be noted that the frame structure only has four bays in this example while the derivation of the equvalent rotational stiffness, k_i, is based on the assumption of multi-bay slender frame structures, see Section 6.4 of Chapter 6. The modification of k_i, so as to make it applicable to the case where the frame is composed of only a few bays, is

$$k_i'=\gamma k_i$$

with $\gamma=n/(n+1)$ where n is the number of bays and (n+1) is the number of columns of the frame. This substitution implies that the total energy stored in the *n* pairs of semi-rigid connections, including the two single semi-rigid connections on both outer columns of the frame, for example, column A and E in Fig 7.10(a), is distributed uniformly by the "equivalent semi-rigid connections" on (n+1) columns. It can be seen that the coefficient, γ, is approximately equal to 1.0 for the case of multi-bay frame structure where n is very large. In this example, $\gamma=4/5$, so $k_i'=9.39\times10^7$ Nmm/rad, which will be used to substitute k_i (i=1,2,3,4) in the simplified model of Fig 7.10(b).

No bending moments act on the simplified model of Fig 7.10(b), that is, $M_i=0$ (i=1,2,3,4), because of the symmetric conditions of the structure itself and the loading on both sides of a column. The vertical loads, P_i, are equivalently derived from the corresponding uniformly distributed loads, q_i. Application of Eq(7.6) gives

$$P_i=q_iL \quad (i=1,2,3,4)$$

or

$$P_1=4000N,\ P_2=2000N,\ P_3=1000N,\ \text{and}\ P_4=500N.$$

On the other hand, the total horizontal load on the i-th level, H_i, is shared by 5 columns, which gives the horizontal load acting on each column as

$$Q_i = H_i/5 = 4\lambda P_i/5 \qquad (i=1,2,3,4)$$

or

$$Q_1=20N,\ Q_2=10N,\ Q_3=5N,\ \text{and}\ Q_4=2.5N.$$

In order to further confirm the effectiveness of the simplied model for second-order analysis, a full frame structure, Fig 7.10(a), is calculated using LUSAS for the purpose of comparison with the results of the simplified model. The parameters used by LUSAS are such that the equivalent concentrated vertical loads, q_iL (i=1,2,3,4), are applied on the beam-column connections on Column B, C, and D, while $q_iL/2$ on the beam-column connections on Column A and E; the total horizontal load, H_i (i=1,2,3,4), is distributed to the five columns uniformly with each beam-column connections loaded by $H_i/5$. The application of LUSAS to this problem gives the rotations, θ_i, and the lateral displacements, Δ_i, on the central columns B and C, which are listed in Table 7.4. At the same time are listed the results of NSTAB, a computer program developed based on the simplified theories proposed in this chapter.

Table 7.4 Comparison of the Results of a Frame with those of the Simplified Model

	NSTAB	LUSAS		MAX %
		Column B	Column C	
θ_0	0.288115×10^{-4}	0.285767×10^{-4}	0.283844×10^{-4}	1.52
θ_1	0.369345×10^{-3}	0.359593×10^{-3}	0.365039×10^{-3}	2.70
Δ_1	0.6010	0.5926	0.5926	1.42
θ_2	0.227617×10^{-3}	0.237054×10^{-3}	0.239718×10^{-3}	5.05
Δ_2	1.1877	1.2044	1.2044	1.39
θ_3	0.102420×10^{-3}	0.111492×10^{-3}	0.113502×10^{-3}	9.78
Δ_3	1.4913	1.5368	1.5368	2.96
θ_4	0.388412×10^{-4}	0.404402×10^{-4}	0.449267×10^{-4}	13.55
Δ_4	1.6152	1.6804	1.6804	3.88

The last column of Table 7.4 gives the maximum relative difference between the results of NSTAB and LUSAS (Column B or Column C), which shows that good agreement has been obtained.

The above four examples have been designed to demonstrate how the theory of simplified second-order analysis works and how the model is used in practice. The first two examples were devoted to demonstrating how the effects of initial imperfections were considered. The last two examples shows how frame structures are simplified to enable the analysis carried out by the model presented in this chapter.

By comparing the results with those of LUSAS, reasonable agreement

has been obtained. It can therefore be concluded that the theory and the associated structural model proposed in this chapter are a practical simplified choice. The associated computer program NSTAB is reliable and efficient.

CHAPTER 8 THE ANALYSIS OF TELESCOPIC STEEL PROPS

8.1 Introduction

Telescopic steel props serve as compressed components of falsework and are usually used on construction sites for supporting floor formwork. They can be regarded as a specific type of slender structure since they may be extended up to a maximum length of 6 metres in an upright position according to the German Standards[29] or 5.5 metres according to the Euro-Norm[30]* whilst their diameters are relatively small.

A telescopic steel prop is composed of cylindrical tubes with a coarse adjustment via a pin and a fine adjustment via a screwed connection, as shown schematically in Fig 8.1, where the prop head transmits axial loads in an axial direction, through the tubes, down to the prop baseplate and then to the subgrade. It is designed to incorporate a means of adjusting its length for repeated use on construction sites.

This specific slender structure, though very complex in the connections and in the adjustable parts, can be calculated by means of a

---

* Appendix A8.1 presents the major differences between the Euro-Norm and the German Standards.

general-purpose finite element program like LUSAS. However, it is tedious to prepare data and very time-consuming on the computer. So, for industrial use, it is important to produce a simplified method and to develop a specialised computer program for the automated analysis of telescopic steel props.

This chapter, therefore, by fully considering the specific characteristics of the telescopic steel props and by conforming to the Euro-Norm [30] and the German Standards [29], aims at presenting a computerised approach to determine the capacity of ultimate loading, deformations and internal forces of the props under various loading and end conditions.

8.2 Computational model

The main types of prop currently in use are adjustable telescopic steel props [29], as shown in Fig 8.1. The adjustable device, X, is designed to extend the prop to different heights so that the prop head is able to support the axial loads. The prop baseplate rests on the ground. There are two common types of props, with an exposed thread and with an enclosed thread, respectively, which are shown in elevation in Figs 8.2(a) and 8.2(b). Eccentricities are assumed at the prop head and at the prop base due to possible eccentric loading and due to possible existence of a gap at the

base. The prefabrication of props and the existence of the clearance between tubes imply that preflexure may exist along the prop. In addition, the baseplate connection is believed to exhibit elastic-plastic behaviour [29].

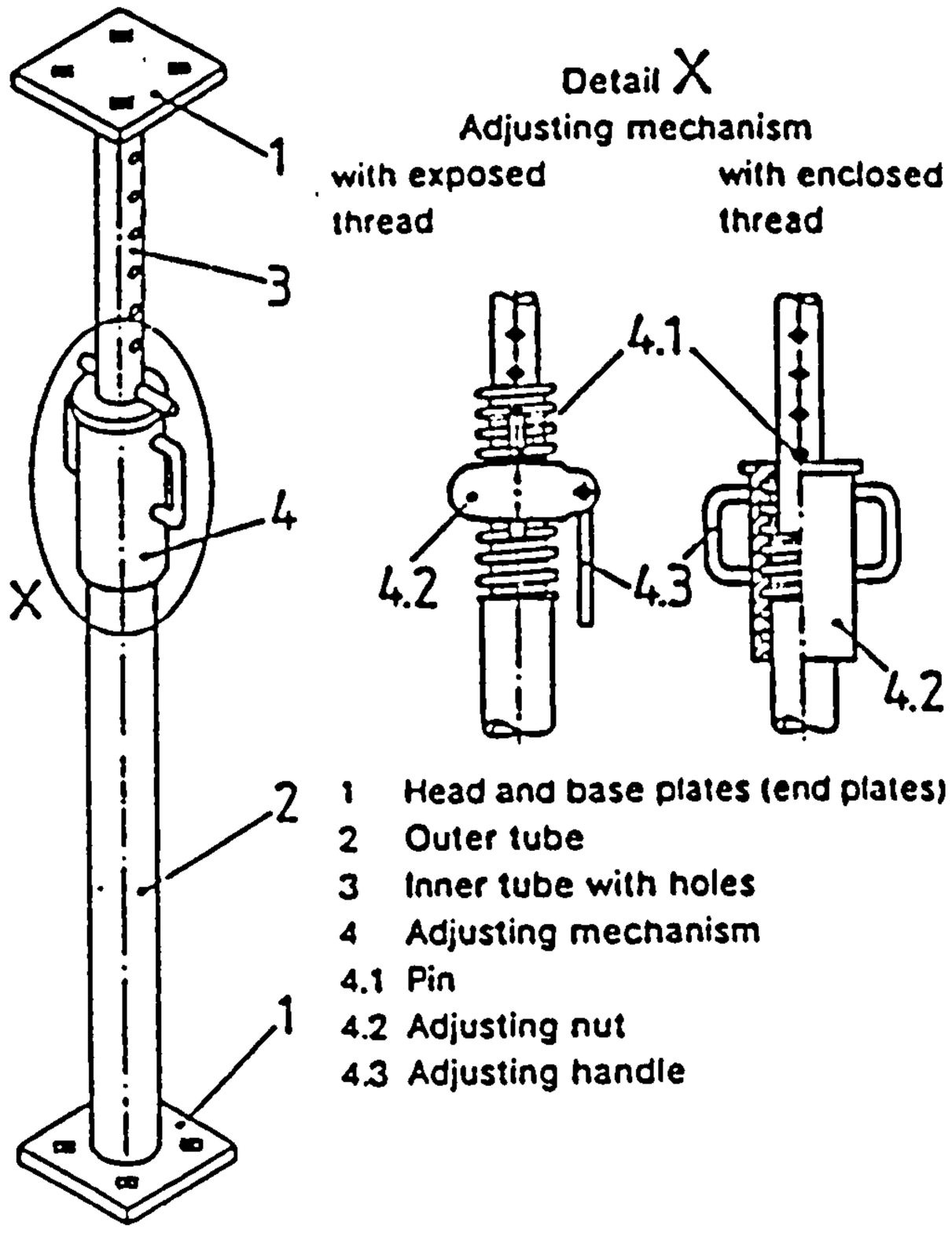

Fig 8.1 Adjustable telescopic steel prop

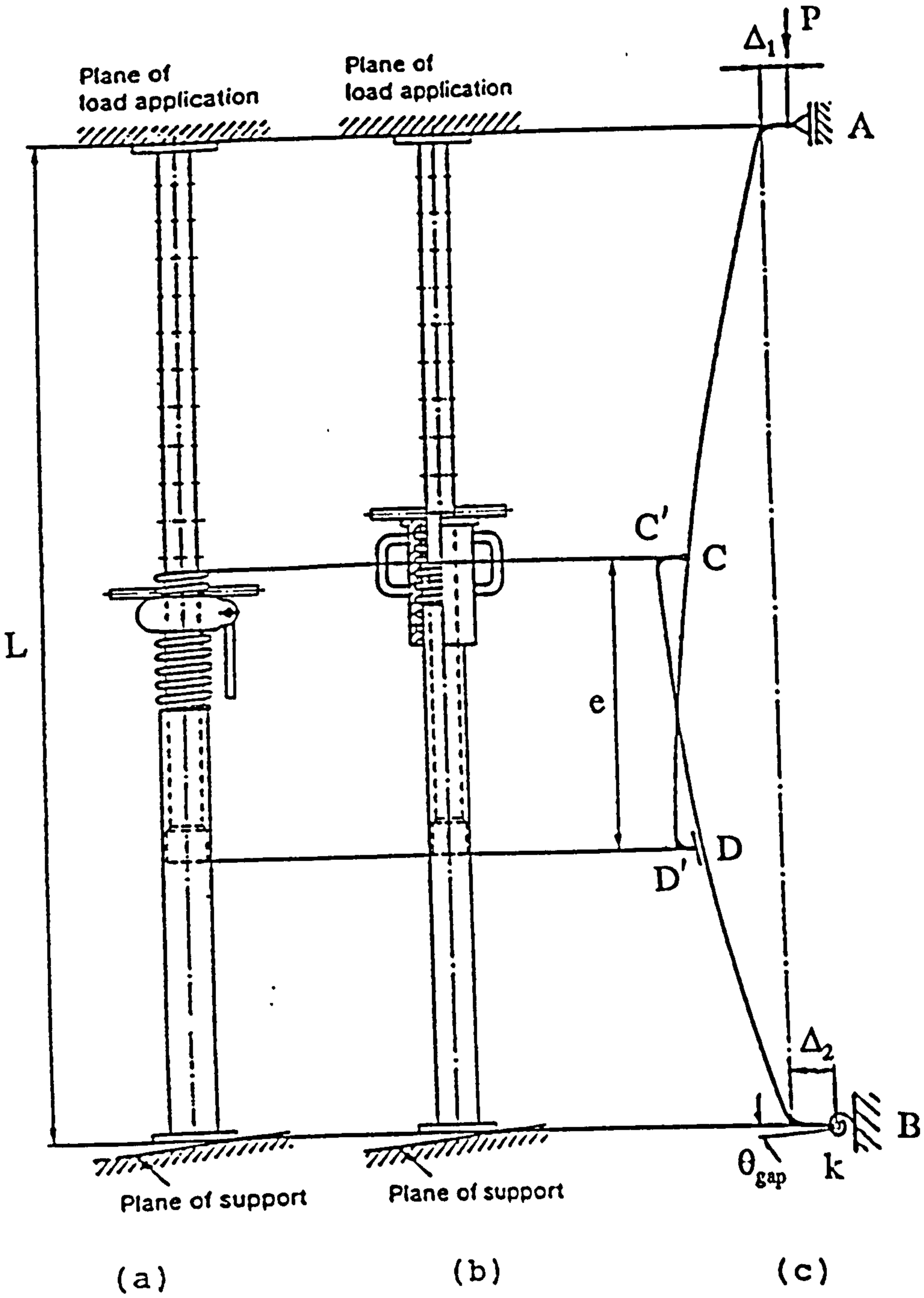

Fig 8.2 Props (a) with exposed thread, (b) with enclosed thread; and (c) computational model

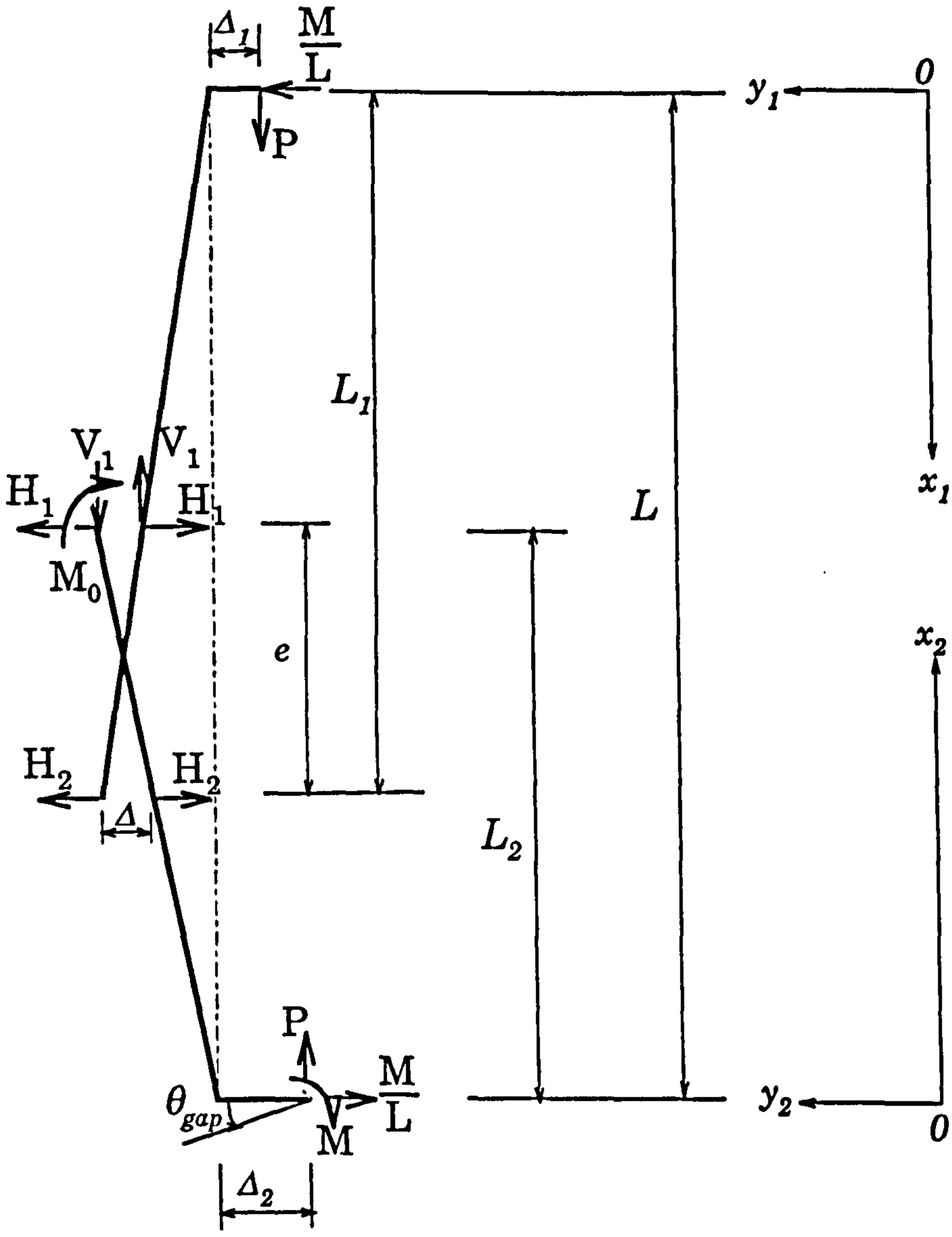

Fig 8.3 Forces, sizes, and coordinate systems on isolated elements

Based on the above assumptions, a computational model can be created as shown in Fig 8.2(c). Both end baseplates are modelled using

hinges where the top end baseplate, A, is moveable in the vertical direction while the bottom one, B, is restrained by a rotational spring modelling its semi-rigid behaviour with k as its rotational stiffness. The adjustable part is modelled using two hinges in which C is a fixed one while D is moveable in the axial direction of the prop. Under the action of the applied load, P, the prop will be in a combined state of compression and bending because of eccentricities. The bending deflection is further increased in the adjustable part of the prop because of the discontinuity of the flexural rigidity between the top half and bottom half of the prop.

The action and reaction forces on the isolated elements of the prop are given in Fig 8.3, in which M is the reaction bending moment applied by the rotational spring B in Fig 8.2(c), M_0 is the reaction bending moment acting on node C′ and can be expressed as $M_0=V_1\Delta$. Δ is the radius difference between the top and bottom prop while Δ_1 and Δ_2 are the load eccentricities on the top and bottom baseplates. θ_{gap} is the given baseplate gap. e is the length of overlap zone of the top and bottom parts of the prop. The top half of the prop, with a length of L_1, is defined using the x_1-y_1 coordinate system while the bottom half, with a length of L_2, is defined using the x_2-y_2 coordinate system. The total length of the prop is L.

8.3 Derivation of basic equations

8.3.1 Initial imperfections

It is inevitable that initial imperfections exist during fabrication of

props and application of loading. These include eccentricities, angle of inclination, and preflexure.

The eccentricities are referred to as the inclination of the applied vertical load from the central axis of the prop and are denoted by Δ_1 and Δ_2 in Fig 8.3. According to [30], the following initial eccentricities shall be assumed:

$$\Delta_1=10 \text{ mm, at the top of the prop,}$$

and

$$(\Delta_2)_0=0.4D$$

$$(\Delta_2)_{crit}=0.5D+t_1, \text{ at the base of the prop,}$$

where D is the outer diameter of the adjacent tube, t_1 is the wall thickness of a provided mantle tube piece [30] which can be a cover tube.

Fig 8.4 shows the eccentricity-rotation relation, or M_b/N-ψ_b curve, at the base of the prop where ψ_b is the rotation of the baseplate and $\Delta_2=M_b/N$ indicates the corresponding eccentricity, assumed by the Euro-Norm [30].

As a comparison, the eccentricities assumed by the German Standard [29] are

$$\Delta_1=5 \text{ mm at the prop head,}$$

and

$$\Delta_2=0.4D \text{ at the prop base.}$$

The angle of inclination, $\Delta\psi_0$ or Δ in Fig 8.5, is caused by the

clearance between the tubes in the overlap zone, which should be determined from the nominal dimensions of the components as $\Delta\psi_0=2\Delta/e$.

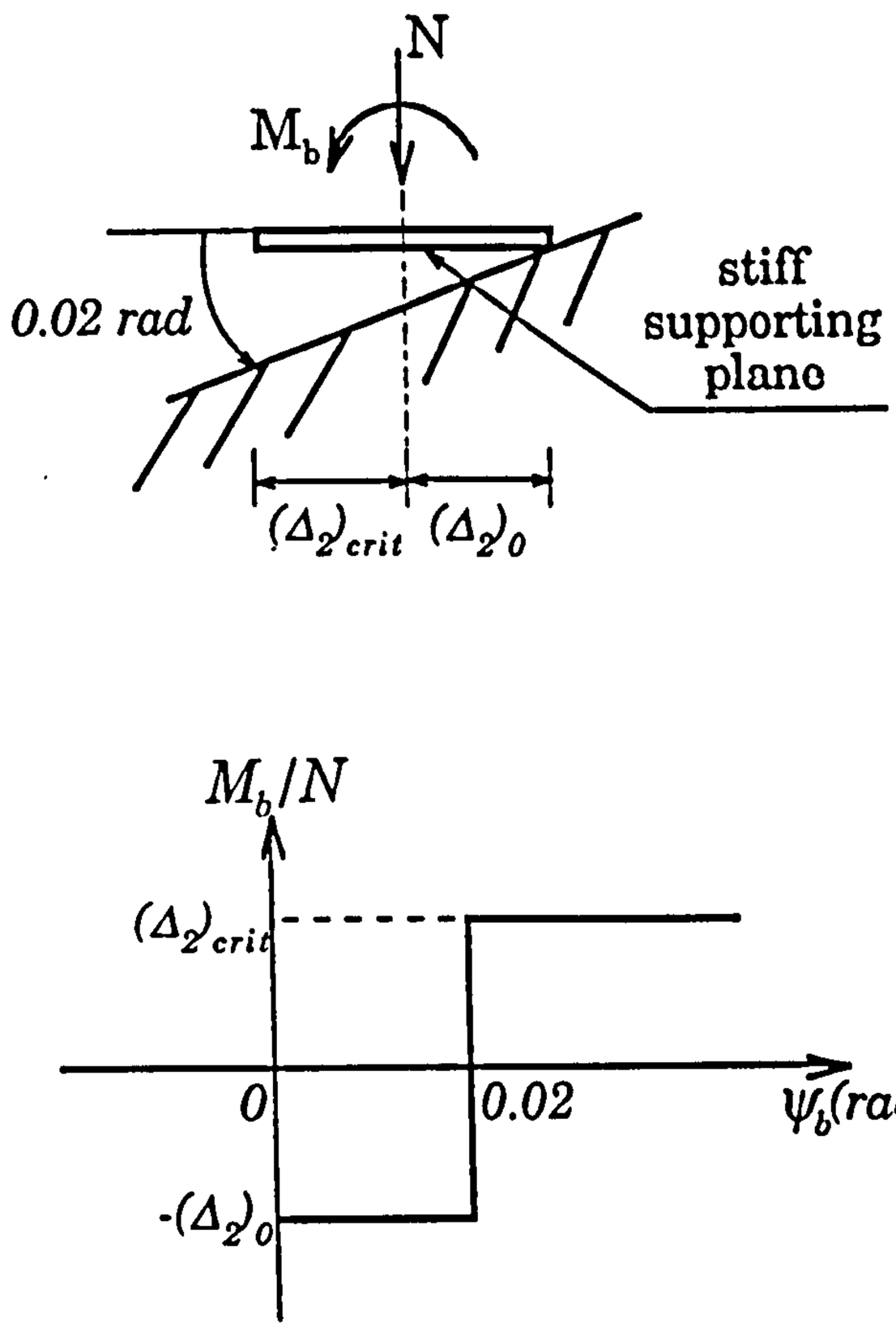

Fig 8.4 Eccentricity-rotation relation for the base of a prop

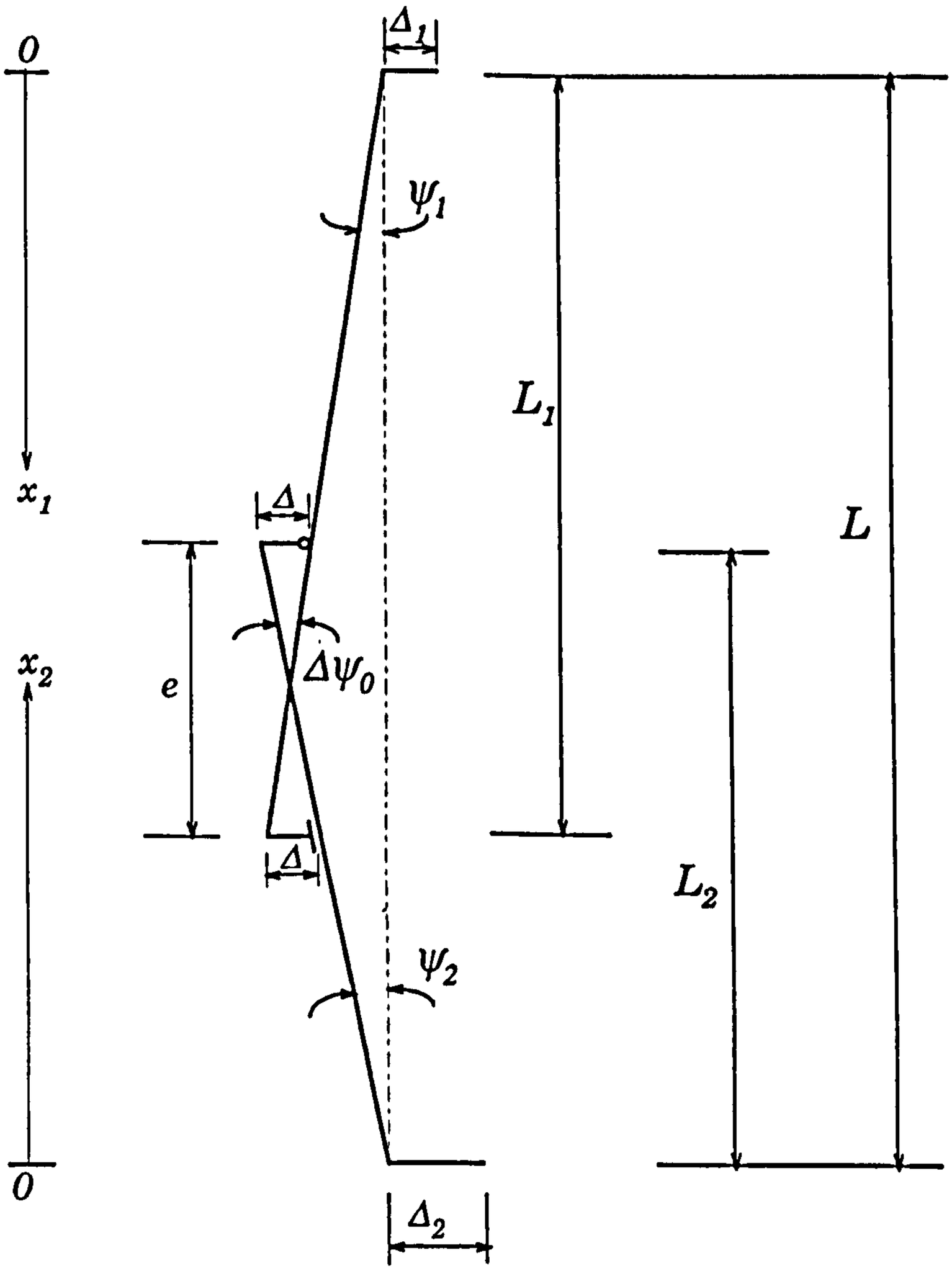

Fig 8.5 Angle of inclination and eccentricities

The geometrical relations in Fig 8.5 give

$$(L_1\sin\Psi_1+\Delta_1-\Delta)=(L_2-e)\sin\Psi_2+\Delta_2$$

$$(L_2\sin\Psi_2+\Delta_2-\Delta)=(L_1-e)\sin\Psi_1+\Delta_1 \qquad (8.1)$$

The assumption of small rotations implies that

$$\sin\Psi_1 \approx \Psi_1$$

$$\sin\Psi_2 \approx \Psi_2 \qquad (8.2)$$

Substituting Eq(8.2) into Eq(8.1) and solving for Ψ_1 and Ψ_2 give

$$\Psi_1 = \frac{\Delta(2L_2 - e) + e(\Delta_2 - \Delta_1)}{eL}$$

$$\Psi_2 = \frac{\Delta(2L_1 - e) + e(\Delta_1 - \Delta_2)}{eL} \qquad (8.3)$$

The preflexure of the prop is defined in [29] and [30] to be a single half sine wave as

$$y_0 = a_0 \sin\frac{\pi x}{L} \qquad (8.4)$$

with a maximum offset of L/1000 required by [30] or L/500 by [29], that is, a_0=L/1000 or L/500, respectively, where L is the extension length considered, shown in Fig 8.6.

The total initial deflections include those related to preflexure, eccentricities, and angle of inclination. Bearing in mind that the assumption of small deformations is made throughout the analysis, so the total initial deflection, y_{10}, for the top-half prop is expressed as

$$y_{10}=a_0\sin\frac{\pi x_1}{L}+\Delta_1+\Psi_1 x_1 \qquad (8.5a)$$

or

$$y_{10}=a_0\sin\frac{\pi x_1}{L}+\Delta_1+\frac{\Delta(2L_2-e)+e(\Delta_2-\Delta_1)}{eL}x_1 \qquad (8.5b)$$

and, y_{20}, for the bottom-half prop, is expressed as

$$y_{20}=a_0\sin\frac{\pi x_2}{L}+\Delta_2+\Psi_2 x_2 \qquad (8.6a)$$

or

$$y_{20}=a_0\sin\frac{\pi x_2}{L}+\Delta_2+\frac{\Delta(2L_1-e)+e(\Delta_1-\Delta_2)}{eL}x_2 \qquad (8.6b)$$

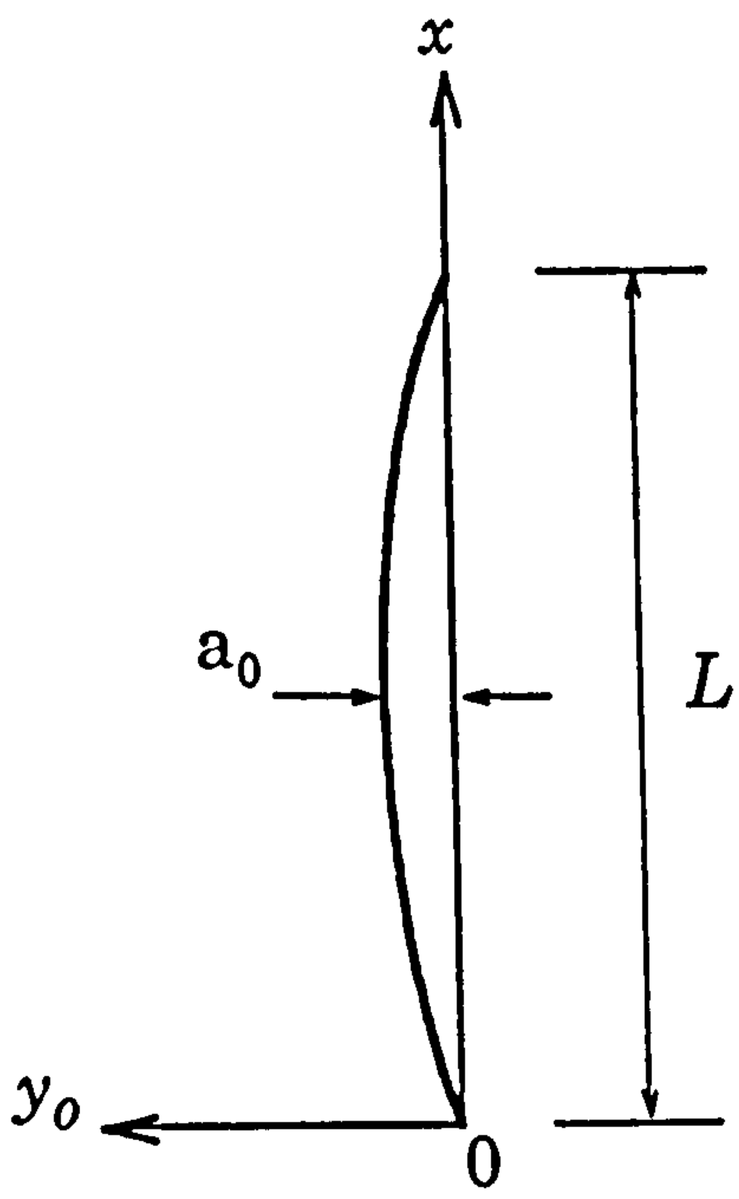

Fig 8.6 Preflexure of the prop

8.3.2 Bending equilibrium

The isolated elements in Fig 8.3 are subjected to the action and reaction forces, which contribute to the bending equilibrium of the prop as

$$EI_1\frac{d^2y_1}{dx_1^2}=-P(y_1+y_{10})+\frac{M}{L}x_1 \qquad (0\le x_1\le L_1-e) \qquad (8.7)$$

and

$$EI_1\frac{d^2y_{1a}}{dx_1^2}=-P(y_{1a}+y_{10})+\frac{M}{L}x_1$$

$$-H_1(x_1-L_1+e)+V_1(y_{1a}+y_{10}-y_{1m}-y_{10m})$$

$$(L_1-e\le x_1\le L_1) \qquad (8.8)$$

for the top-half prop, where EI_1 is the corresponding flexural rigidity; y_1 and y_{1a} are the deflections in the regions of $0\le x_1\le L_1-e$ and $L_1-e\le x_1\le L_1$, respectively; y_{10} is the initial deflection given in Eq(8.5); P, M, H_1, and H_2 are forces and moment indicated in Fig 8.3; and y_{1m} and y_{10m} are the values of y_1 and y_{10} at the position of $x_1=L_1-e$. That is:

$$y_{1m}=y_1|_{x_1=L_1-e}$$

$$y_{10m}=y_{10}|_{x_1=L_1-e}$$

Similar to Eqs(8.7) and (8.8), the bending equilibrium for the bottom-

half prop is given by

$$EI_2\frac{d^2y_2}{dx_2^2}=-P(y_2+y_{20})-\frac{M}{L}x_2+M \qquad (0\le x_2\le L_2-e) \qquad (8.9)$$

and

$$EI_2\frac{d^2y_{2a}}{dx_2^2}=-P(y_{2a}+y_{20})-\frac{M}{L}x_2+M-H_2(x_2-L_2+e)$$

$$(L_2-e\le x_2\le L_2) \qquad (8.10)$$

where EI_2 is the flexural rigidity of the bottom-half prop; y_2 and y_{2a} are the deflections in the regions of $0\le x_2\le L_2$-e and L_2-e$\le x_2\le L_2$, respectively; y_{20} is the initial deflection given in Eq(8.6); P, M, H_1, and H_2 are forces and moment indicated in Fig 8.3.

The four equations, from Eq(8.7) to Eq(8.10), constitute the bending equilibrium of the prop shown in Fig 8.3.

Integration of these four equations gives their general solutions with constants to be determined:

$$y_1=C_1\cos(\alpha_1x_1)+C_2\sin(\alpha_1x_1)+\Gamma_1\sin\frac{\pi x_1}{L}+\frac{M}{PL}x_1-(\Delta_1+x_1\Psi_1)$$

$$(0\le x_1\le L_1-e) \qquad (8.11)$$

$$y_{1a}=\frac{1}{EI_1}\left[\frac{Mx_1^3}{6L}-\frac{H_1(x_1-L_1+e)^3}{6}-V_1(y_{1m}+y_{10m})\frac{x_1^2}{2}\right]+C_5x_1+C_6$$

$$(L_1-e\le x_1\le L_1) \qquad (8.12)$$

$$y_2=C_3\cos(\alpha_2 x_2)+C_4\sin(\alpha_2 x_2)+\Gamma_2\sin\frac{\pi x_2}{L}-\frac{M}{PL}x_2-(\Delta_2+x_2\Psi_2)+\frac{M}{P}$$

$$(0\le x_2\le L_2-e) \qquad (8.13)$$

$$y_{2a}=C_7\cos(\alpha_2 x_2)+C_8\sin(\alpha_2 x_2)+\Gamma_2\sin\frac{\pi x_2}{L}$$

$$-\frac{1}{P}(\frac{M}{L}+H_2)x_2-(\Delta_2+x_2\Psi_2)-\frac{1}{P}H_2(e-L_2)+\frac{M}{P}$$

$$(L_2-e\le x_2\le L_2) \qquad (8.14)$$

where

$$\alpha_1=\sqrt{(\frac{P}{EI_1})};\qquad \alpha_2=\sqrt{(\frac{P}{EI_2})}$$

$$\Gamma_1=\frac{a_0}{(\frac{\pi^2 EI_1}{PL^2}-1)};\qquad \Gamma_2=\frac{a_0}{(\frac{\pi^2 EI_2}{PL^2}-1)} \qquad (8.15)$$

and C_i (i=1,2,...,8) are constants to be determined from the boundary conditions and compatibility conditions.

8.3.3 Boundary conditions and compatibility conditions

The deflections on different parts of the prop must satisfy (1) the boundary conditions at the top and bottom baseplates, A and B, shown in Fig 8.2, and (2) the compatibility conditions at C and D. Then, the constants of Eqs(8.11), (8.12), (8.13), and (8.14) can be determined.

The top baseplate is not allowed to move horizontally, which implies that

$$y_1|_{x_1=0}=0 \tag{8.16}$$

Similarly, on the bottom baseplate we have

$$y_2|_{x_2=0}=0 \tag{8.17}$$

Since the bottom column-baseplate-subgrade system behaviours semi-rigidly, the rotational reaction moment, M, produced by the spring, see Fig 8.3, can be written as

$$M|_{x_2=0}=0 \qquad when \quad \frac{dy_2}{dx_2}<\theta_{gap} \tag{8.18a}$$

$$M|_{x_2=0}=k(\frac{dy_2}{dx_2}-\theta_{gap})|_{x_2=0} \qquad when \quad \frac{dy_2}{dx_2}\geq\theta_{gap} \tag{8.18b}$$

$$M|_{x_2=0}=M_{u,Gr} \qquad when \quad M\geq M_{u,Gr} \tag{8.18c}$$

k is the rotational stiffness of the bottom baseplate which shall be assumed to be a constant of 4000 kN.cm/rad according to [29]; θ_{gap} is the gap between baseplate and subgrade before loading which is 0.02 rad [29]; dy_2/dx_2 is the rotation due to deflection y_2.

Eq(8.18) implies a trilinear characteristic of the spring as shown in Fig 8.7.

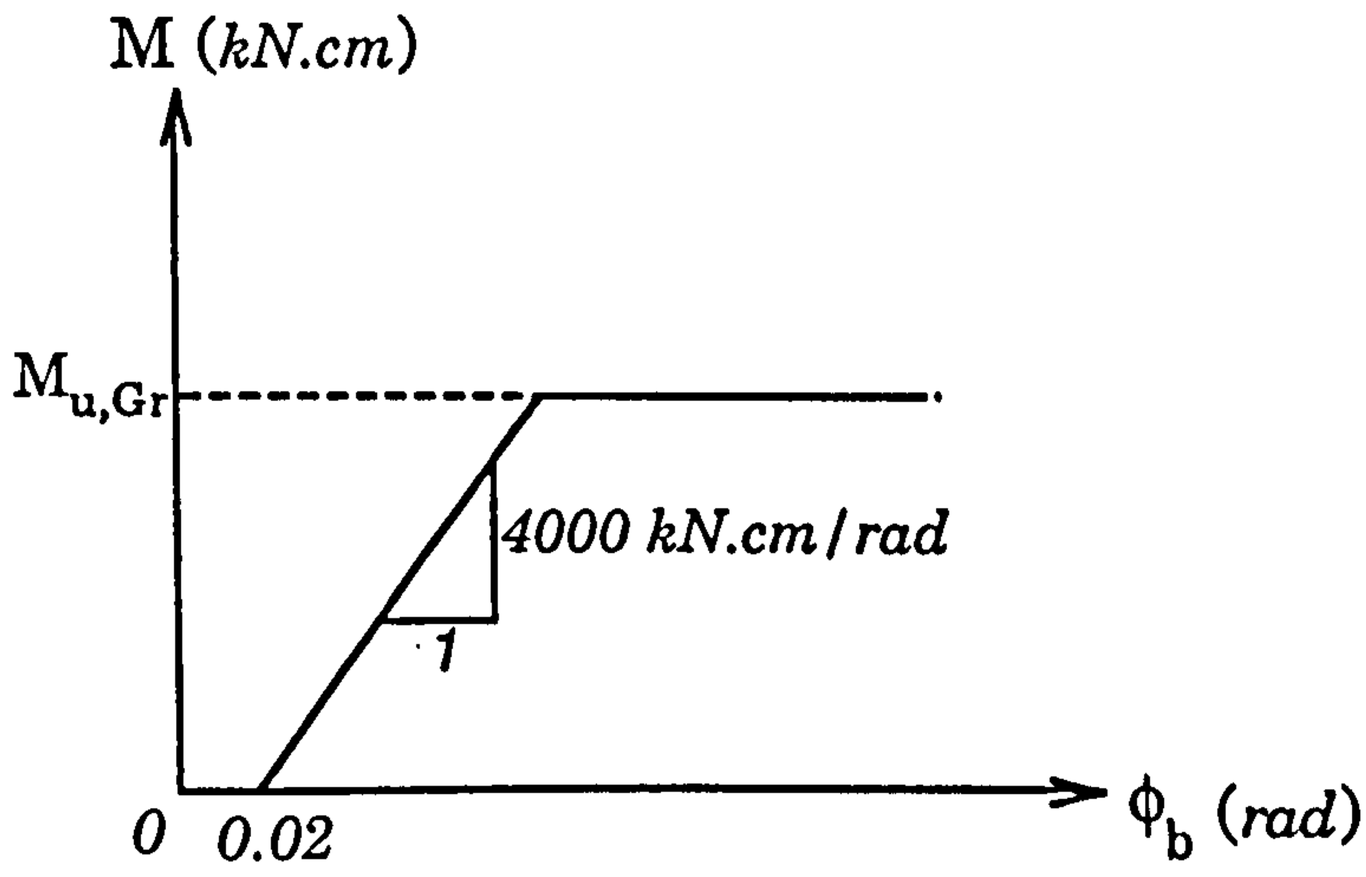

Fig 8.7 Trilinear characteristics of spring

The plastic limiting moment $M_{u,Gr}$ in Fig (8.7) at the prop base is given [29] by

$$M_{u,Gr}=\frac{\beta_s * b * t_p^2}{6} * \frac{1+2.6\frac{D}{b}}{1-\frac{D}{b}} \qquad (8.19)$$

where β_s is the tensile yield point of the end plate material; b is the smallest width of or the maximum diameter of an inscribed circle on the end plate; t_p is the end plate thickness and D is the external diameter of the lower tube.

However, the plastic limiting moment, denoted as $M_{b,crit}$ in [30], shall

be calculated from

$$M_{b,crit}=N.e_{crit}\leq M_{pl,N}$$

and

$$M_{pl,N}=M_{pl}.\cos(\frac{\pi}{2}.\frac{N}{N_{pl}})$$

where $M_{pl,N}$ is the reduced plastic resistance moment allowing for axial force; M_{pl} is the moment resistance of the cross-section; N is the actual normal force; N_{pl} is the compression resistance of the cross-section; e_{crit} is 0.4D, the critical eccentricity of the tube at the base of the prop.

So, in this case, Eq(8.18) is replaced by

(1) Before the gap is closed

$$\frac{dy_2}{dx_2}<\theta_{gap} \qquad (8.20a)$$

then, M=0 and $M_b=P\Delta_2$ with $\Delta_2=(\Delta_2)_0$, where M is the bending moment due to the spring, see Fig 8.3; P is the actual normal force, M_b is the bending moment at the bottom of the lower tube, see Fig 8.4.

(2) When the gap is closed

$$\frac{dy_2}{dx_2}=\theta_{gap} \qquad (8.20b)$$

then $M_b=P\Delta_2^1\leq M_{b,crit}$ with $\Delta_2^1=-(\Delta_2)_{crit}$, where $M_{b,crit}$ is the limiting moment just mentioned.

(3) When the gap is open again in the opposite direction

$$\frac{dy_2}{dx_2} > \theta_{gap} \tag{8.20c}$$

then $M=0$ and $M_b=P\Delta_2^1$ with $\Delta_2^1=-(\Delta_2)_{crit}$.

On the hinge position, D, the compatibility conditions among the deflections are given by

$$y_{1a}|_{x_1=L_1} = y_2|_{x_2=L_2-e} \tag{8.21}$$

$$y_2|_{x_2=L_2-e} = y_{2a}|_{x_2=L_2-e} \tag{8.22}$$

$$\frac{dy_2}{dx_2}|_{x_2=L_2-e} = \frac{dy_{2a}}{dx_2}|_{x_2=L_2-e} \tag{8.23}$$

where the first two equations represent the deflection compatibility while the last one the rotation compatibility.

Similarly, the compatibility conditions for the hinge position, C, are given by

$$y_{2a}|_{x_2=L_2} = y_1|_{x_1=L_1-e} \tag{8.24}$$

$$y_1|_{x_1=L_1-e} = y_{1a}|_{x_1=L_1-e} \tag{8.25}$$

$$\frac{dy_1}{dx_1}|_{x_1=L_1-e} = \frac{dy_{1a}}{dx_1}|_{x_1=L_1-e} \tag{8.26}$$

where the Eqs(8.24) and (8.25) represent the deflection compatibility while Eq(8.26) represents the rotation compatibility.

The global static equilibrium of the prop, i.e., vertical, horizontal and rotational equilibrium, respectively, gives

$$V_1=P \tag{8.27}$$

$$\frac{M}{L}+H_2=H_1 \tag{8.28}$$

$$H_2L_1+V_1(y_{1m}+y_{10m})=H_1(L_1-e) \tag{8.29}$$

where y_{1m} and y_{10m} are the same as those defined in Eq(8.8).

8.3.4 Solution procedure

The solutions of the deflections on each part of the prop, denoted from Eq(8.11) to Eq(8.14), can now be determined by the above boundary conditions and compatibility conditions.

Substitution of Eq(8.11) into Eq(8.16) gives

$$C_1=\Delta_1 \tag{8.30}$$

and Eq(8.13) into Eq(8.17),

$$C_3+\frac{1}{P}M=\Delta_2 \tag{8.31}$$

and Eq(8.13) into Eq(8.18),

$$\alpha_2 C_4-(\frac{1}{PL}+\frac{1}{k})M=\Psi_2-\Gamma_2\frac{\pi}{L}+\theta_{gap} \tag{8.32}$$

Substituting Eqs(8.12) and (8.13) into Eq(8.21) give

$$C_3\cos\alpha_2(L_2-e)+C_4\sin\alpha_2(L_2-e)-L_1C_5-C_6$$

$$=(\frac{L_1^3}{6EI_1L}-\frac{L_1}{PL})M-\frac{e^3}{6EI_1}H_1-\frac{V_1}{EI_1}(y_{1m}+y_{10m})\frac{L_1^2}{2}$$

$$-\Gamma_2\sin\frac{\pi(L_2-e)}{L}+\Delta_2+(L_2-e)\Psi_2 \tag{8.33}$$

Eqs(8.13) and (8.14) into Eq(8.22) give

$$(C_3-C_7)\cos\alpha_2(L_2-e)+(C_4-C_8)\sin\alpha_2(L_2-e)=0 \tag{8.34}$$

Eqs(8.13) and (8.14) into Eq(8.23) give

$$\alpha_2(C_7-C_3)\sin\alpha_2(L_2-e)+\alpha_2(C_4-C_8)\cos\alpha_2(L_2-e)+\frac{1}{P}H_2=0 \tag{8.35}$$

Eqs(8.11) and (8.14) into Eq(8.24) give

$$C_1\cos\alpha_1(L_1-e)+C_2\sin\alpha_1(L_1-e)-C_7\cos\alpha_2L_2-C_8\sin\alpha_2L_2+\frac{e}{P}H_2$$

$$=\Gamma_2\sin\frac{\pi L_2}{L}-\Delta_2-L_2\Psi_2-\Gamma_1\sin\frac{\pi(L_1-e)}{L}+\Delta_1+(L_1-e)\Psi_1 \tag{8.36}$$

Eqs(8.11) and (8.12) into Eq(8.25) give

$$C_1\cos\alpha_1(L_1-e)+C_2\sin\alpha_1(L_1-e)-(L_1-e)C_5-C_6$$

$$=\frac{1}{EI_1}\left[\frac{M(L_1-e)^3}{6L}-V_1(y_{1m}+y_{10m})\frac{(L_1-e)^2}{2}\right]$$

$$-\Gamma_1\sin\frac{\pi(L_1-e)}{L}-\frac{M}{PL}(L_1-e)+\Delta_1+(L_1-e)\Psi_1 \qquad (8.37)$$

Eqs(8.11) and (8.12) into Eq(8.26) give

$$-C_1\alpha_1\sin\alpha_1(L_1-e)+C_2\alpha_1\cos\alpha_1(L_1-e)-C_5$$

$$=\frac{1}{EI_1}\left[\frac{M(L_1-e)^2}{2L}-V_1(y_{1m}+y_{10m})(L_1-e)\right]$$

$$-\Gamma_1\frac{\pi}{L}\cos\frac{\pi(L_1-e)}{L}-\frac{M}{PL}+\Psi_1 \qquad (8.38)$$

The twelve equations, from Eq(8.27) to Eq(8.38), can now be used simultaneously to solve for twelve unknowns H_1, H_2, V_1, M and C_i (i=1,2,...,8).

The two unknowns, V_1 and C_1, can be obtained explicitly from Eq(8.27) and Eq(8.30), respectively, as

$$V_1=P \quad \text{and} \quad C_1=\Delta_1 \qquad (8.39)$$

The rest of the unknowns interact with each other. They are grouped in a vector form as

$$\{C\}^T=\{C_2,C_3,C_4,C_5,C_6,C_7,C_8,M,H_1,H_2\} \qquad (8.40)$$

So, this set of ten equations, Eqs(8.28),(8.29),(8.31) to (8.38), are expressed in a matrix form,

$$[A]\{C\}=\{F\} \tag{8.41}$$

where

$$\{F\}^T=\{F_1,F_2,F_3,F_4,F_5,F_6,F_7,F_8,F_9,F_{10}\}$$

and C_{ij} in matrix [A], F_j in right-hand vector {F} (i,j=1,2,...,10) are the coefficients of Eqs(8.28),(8.29),(8.31),(8.32),...,(8.38), corresponding to the order of {C}, which have not been listed out to save space.

8.3.5 Internal forces

The unknown vector, {C} in Eq(8.40), can be found by solving the matrix equation, Eq(8.41), using a Gaussian algorithm. The deflections of the prop, y_1, y_{1a}, y_2, and y_{2a}, can then be determined from Eqs(8.11), (8.12), (8.13), and (8.14), respectively, upon which the internal forces of the prop can be calculated.

By definition, the bending moments at different parts of the prop are written as

$$M_1=-EI_1\frac{d^2y_1}{dx_1^2} \qquad (0\le x_1\le L_1-e) \tag{8.42}$$

$$M_{1a}=-EI_1\frac{d^2y_{1a}}{dx_1^2} \qquad (L_1-e\le x_1\le L_1) \qquad (8.43)$$

$$M_2=-EI_2\frac{d^2y_2}{dx_2^2} \qquad (0\le x_2\le L_2-e) \qquad (8.44)$$

$$M_{2a}=-EI_2\frac{d^2y_{2a}}{dx_2^2} \qquad (L_2-e\le x_2\le L_2) \qquad (8.45)$$

Application of the solutions y_1, y_{1a}, y_2, and y_{2a} in Eqs(8.11), (8.12), (8.13), and (8.14)to the above four equations, respectively, will give the corresponding bending moments.

Alternatively, by static equilibrium of the isolated elements in Fig 8.3, the bending moments at different parts of the prop are expressed as

$$M_1=P(y_1+y_{10})-\frac{M}{L}x_1 \qquad (0\le x_1\le L_1-e) \qquad (8.42)'$$

$$M_{1a}=H_1(x_1-L_1+e)+V_1(y_{1m}+y_{10m})-\frac{M}{L}x_1$$

$$(L_1-e\le x_1\le L_1) \qquad (8.43)'$$

$$M_2=P(y_2+y_{20})+\frac{M}{L}x_2-M \qquad (0\le x_2\le L_2-e) \qquad (8.44)'$$

$$M_{2a}=P(y_{2a}+y_{20})+\frac{M}{L}x_2-M+H_2(x_2-L_2+e)$$

$$(L_2-e\le x_2\le L_2) \qquad (8.45)'$$

Similarly, the shear forces at different parts of the prop are written as, by definition,

$$V_1=-EI_1\frac{d^3y_1}{dx_1^3} \qquad (0\le x_1\le L_1-e) \qquad (8.46)$$

$$V_{1a}=-EI_1\frac{d^3y_{1a}}{dx_1^3} \qquad (L_1-e\le x_1\le L_1) \qquad (8.47)$$

$$V_2=-EI_2\frac{d^3y_2}{dx_2^3} \qquad (0\le x_2\le L_2-e) \qquad (8.48)$$

$$V_{2a}=-EI_2\frac{d^3y_{2a}}{dx_2^3} \qquad (L_2-e\le x_2\le L_2) \qquad (8.49)$$

or, they are alternatively expressed as, by static equilibrium of the isolated elements in Fig 8.3

$$V_1=P(cq_1+cq_5)-\frac{M}{L} \qquad (0\le x_1\le L_1-e) \qquad (8.46)'$$

$$V_{1a}=H_1-\frac{M}{L}x_1 \qquad (L_1-e\le x_1\le L_1) \qquad (8.47)'$$

$$V_2=P(cq_2+cq_6)+\frac{M}{L} \qquad (0\le x_2\le L_2-e) \qquad (8.48)'$$

$$V_{2a}=P(cq_4+cq_6)+\frac{M}{L}+H_2$$

$$(L_2-e\le x_2\le L_2) \qquad (8.49)'$$

where

$$cq_1=-C_1\alpha_1\sin\alpha_1x_1+C_2\alpha_1\cos\alpha_1x_1+\Gamma_1\frac{\pi}{L}\cos\frac{\pi x_1}{L}+\frac{M}{PL}-\Psi_1$$

$$cq_2=-C_3\alpha_2\sin\alpha_2x_2+C_4\alpha_2\cos\alpha_2x_2+\Gamma_2\frac{\pi}{L}\cos\frac{\pi x_2}{L}-\frac{M}{PL}-\Psi_2$$

$$cq_4=-C_7\alpha_2\sin\alpha_2x_2+C_8\alpha_2\cos\alpha_2x_2+\Gamma_2\frac{\pi}{L}\cos\frac{\pi x_2}{L}-\frac{1}{P}(\frac{M}{L}+H_2)-\Psi_2$$

$$cq_5=a_0\frac{\pi}{L}\cos\frac{\pi x_1}{L}+\Psi_1$$

$$cq_6=a_0\frac{\pi}{L}\cos\frac{\pi x_2}{L}+\Psi_2$$

So, the bending moments and shear forces of the prop can be calculated without difficulty once the deflections of the prop have been determined.

8.4 Development of the computer programs

8.4.1 Outline

The governing bending equilibrium equations for adjustable telescopic steel prop have been formulated in previous section, based on the computational model in Fig 8.2(c). This has led to the solutions of a matrix equation, Eq(8.41), upon which the deflections and internal forces at different parts of the prop can readily be obtained.

This procedure is quite straightforward but the calculation is very tedious and complicated. Two computer programs, PROP800 and PROP500 based on the Euro-Norm [30] and the German Standards [29], respectively, have therefore been developed for this purpose.

8.4.2 Adaptation to the Standards

For industrial use, the computer program is required to incorporate the requirements of the Standards such as materials, configurations, strength and load bearing capacity.

For example, telescopic steel props are classified into Standard Type Props and Heavy-duty Type Props, according to their safe working loads, denoted by P_N and P_G, respectively. They are calculated and constrained by

$$P_j=\beta_j\frac{L_{max}}{L^2}\leq P_{maxj} \qquad (j=1,2)$$

with $P_1=P_N$ and $P_2=P_G$, where $\beta_1=68.0$, $\beta_2=102.0$, and $P_{max1}=51.0$ kN, $P_{max2}=59.5$ kN.

It may have been noted that there are normally some pin holes on the top prop to serve as a coarse adjustment. This will no doubt reduce the moment of inertia of the cross-section, resulting in the reduction in the moment resistance of the cross-section. The net cross-section values should, instead, be considered [30], and are given by (see Fig 8.8)

$$A_{gr}=\pi(R^2-r^2)$$

$$I_{gr}=\frac{\pi}{4}(R^4-r^4)$$

$$A_n=2(\psi_R\ R^2-\psi_r\ r^2)-d\ (\sqrt{(R^2-\frac{d^2}{4})}\ -\sqrt{(r^2-\frac{d^2}{4})}\ )$$

$$I_n=\frac{R^3}{2}[\psi_R\ R-\frac{d}{6}\sin\psi_R\ (3+2\sin^2\psi_R)]$$

$$-\frac{r^3}{2}[\psi_r\ r-\frac{d}{6}\sin\psi_r\ (3+2\sin^2\psi_r)]$$

$$I_i=I_{gr}\ \frac{1}{1+2\frac{d}{a}(\frac{I_{gr}}{I_n}-1)}$$

where A_{gr} and A_n are the areas of gross and net cross-sections, I_{gr} and I_n are

the corresponding moments of inertia, I_i is the equivalent inertia moment of the cross-section, and

$$\psi_R=\cos^{-1}(\frac{d}{2R}), \qquad \psi_r=\cos^{-1}(\frac{d}{2r})$$

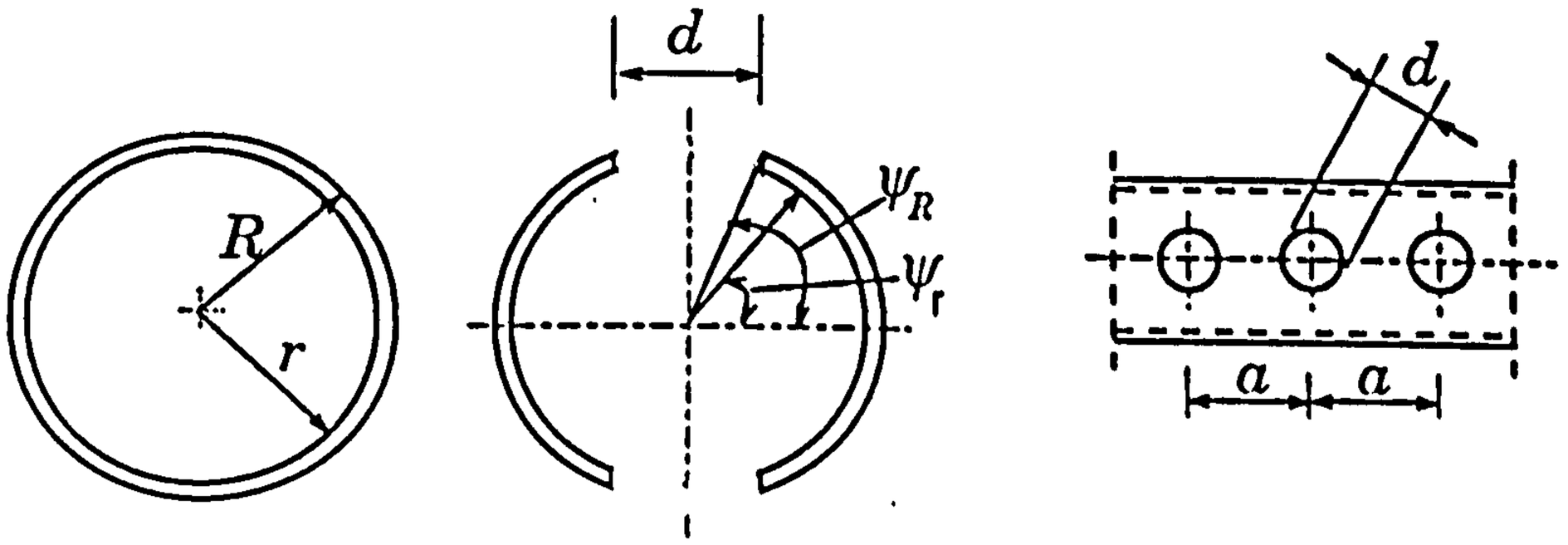

(a) (b) (c)

Fig 8.8 (a) Gross cross-section, (b) net cross-section, and (c) pin holes on the top prop

As a comparison, A_{gr} and I_{gr} are assumed as the German Standard [29]

$$A_{gr}=\pi(R^2-r^2)$$

$$I_{gr}=\frac{\pi}{4}(R^4-r^4)$$

Regarding the initial eccentricities, the Euro-Norm [30] requires that the following values be taken,

$$e_t=10 \text{ mm}$$

at the top of the prop, and

$$e_{b,0}=0.4D$$

$$e_{b,crit}=0.5D+t_1$$

at the base of the prop, where D is the outer diameter of the adjacent tube, t_1 is the wall thickness of a provided mantle tube piece [30].

8.5 Numerical examples and discussions

The development of the computer programs PROP800 and PROP500 [59] has met the objective of this chapter to analyse telescopic steel props by producing programs to provide proof that props at least reach the safe working load values [29] for any extended length. Some numerical illustrations are presented in this section.

Five types of prop are analyzed using PROP500, and for the purpose of comparison, using LUSAS as well. The parameters used in the calculation are given below. Table 8.1 gives the total length of the props *L*. Table 8.2 shows the length of overlap part of props, *e* in Fig 8.5, and the length of bottom props L_2. The length of top props are from these values. Table 8.3 gives the minimum characteristic strength of props.

Table 8.1 Lengths of Props (BS4074[50])

Prop type	Length fully closed (m)	Length fully extended (m)	Mass (kg) (approximation)
0	1.07	1.82	15.0
1	1.75	3.12	22.7
2	1.98	3.35	23.6
3	2.59	3.95	26.3
4	3.20	4.87	35.6

Table 8.2 Overlap of tubes for Props (BS4074[50])

Prop type	Length of outer tube (m)	Minimum tube overlap (mm)
0	1.02	230
1	1.68	293
2	1.68	293
3	1.68	293
4	2.04	357

Table 8.3 Minimum Characteristic Strength of Props (BS4074[50])

Prop type	Cases of props	Length (m)	Min characteristic strength (kN)
0	fully closed	1.07	50.8
	fully extended	1.82	50.8
1	fully closed	1.75	50.8
	fully extended	3.12	25.4
2	fully closed	1.98	50.8
	fully extended	3.35	23.2
3	fully closed	2.59	36.3
	fully extended	3.95	16.7
4	fully closed	3.20	37.7
	fully extended	4.87	13.0

The rest of the parameters include:

D=2.40 mm, D_1=5 mm, D_2=24.12 mm,

a_0=3.64 mm, P=0.2x10^5 N, E=2.05x10^5 N/mm^2

S_{gy1}=355.0 N/mm^2, S_{gy2}=195.0 N/mm^2,

k=0.4x10^8 N.mm/rad, θ_{gap}=0.02 rad,

dx_1=50.0 mm, dx_2=50.0 mm,

R_1=48.3 mm, t_1=3.2 mm, R_2=60.3 mm,

t_2=3.6 mm, M_{bu}=846467.0 N.mm.

where D is the radius difference between top prop and bottom prop, D_1 the top end eccentricity, D_2 the eccentricity of baseplate, a_0 the factor of preflexure curve, P the applied axial load, E the modulus of elasticity, S_{gy1} the design tensile yield stress of top prop, S_{gy2}, the design tensile yield stress of bottom prop, *k* the baseplate rotational stiffness, θ_{gap} the baseplate gap, dx_1 the step length of the calculation point on top prop, dx_2 the step length of the calculation point on bottom prop, R_1 the outside diameter of top prop, t_1 the wall thickness of top prop, R_2 the outside diameter of bottom prop, t_2 the wall thickness of bottom prop, M_{bu} the plastic limiting moment.

Table 8.4 Results of Fully Extended Props

Prop type	Ultimate load (kN)			Max displacement (mm)			Max moment (kN.mm)		
	A*	B*	|%|	A*	B*	|%|	A*	B*	|%|
0	45.18	48.34	6.5	17.45	19.76	12.	17.66	20.78	15.
1	26.87	26.83	0.2	59.41	62.87	5.5	20.58	22.36	7.9
2	25.08	24.99	0.4	66.31	68.40	3.1	21.09	22.49	6.2
3	21.35	21.01	1.6	76.14	87.75	13.	20.18	22.98	12.
4	15.34	15.09	1.6	128.2	134.6	4.8	21.51	23.20	7.3

* Note: A is program PROP500, B is program LUSAS.

Table 8.5 Results of Fully Extended, Half Extended and Fully Closed Props by PROP500

Prop type	Cases of props	Ultimate load (kN)	Max displacement (mm)	Max moment (kN.mm)
0	fully extended	45.18	17.45	17.66
	half extended	56.47	7.31	15.91
	fully closed	61.70	2.84	14.95
1	fully extended	26.87	59.41	20.58
	half extended	46.96	31.38	17.42
	fully closed	57.10	9.84	15.78
2	fully extended	25.08	66.31	21.09
	half extended	42.96	33.29	17.98
	fully closed	54.27	13.08	16.25
3	fully extended	21.35	76.14	20.18
	half extended	34.90	41.51	18.97
	fully closed	45.36	24.10	17.62
4	fully extended	15.34	128.2	21.51
	half extended	26.45	66.88	20.12
	fully closed	37.78	38.02	18.68

Table 8.4 makes the comparison between the predicted results by PROP500 and those by LUSAS which are shown in the same table, and presents the relative errors between them. It follows that both predict fairly similar results. However, if taking into account the data preparation and the computer CPU time, PROP500 has significant advantages over LUSAS.

Table 8.5 presents the predicted results by PROP500 of the three cases of props: fully extended, half extended, and fully closed. It follows from this table that the ultimate load for the fully extended prop is roughly half of the fully closed one, whilst the half extended prop falls between them. However, the maximum displacement for the fully extended prop is much larger (over three times at least) than that of the fully closed one, and also the maximum bending moment has the similar trends. It is therefore suggested that considerable attention be given to the fully extended prop in design as this is the most unfavourable case.

As a comparison, PROP500 and PROP800 were used to calculate the load capacity of a same prop with the following parameters: L=3380 mm, L_1=1673 mm, L_2=2000 mm, D=2.4 mm, initial load P=7000 N, E=2.05x10^5 Mpa, S_{gy1}=355 Mpa, S_{gy2}=195 Mpa, dx_1=80 mm, dx_2=80 mm, R_1=48.3 mm, t_1=3.2 mm, R_2=60.3 mm, t_2=3.6 mm. The other parameters used for PROP500, according to German Standards[29], include D_1=5 mm, D_2=24.12 mm, a_0=16.9 mm, k=0.4x10^8 N.mm/rad, gap=0.02 rad, M_{bu}=8.46x10^5 N.mm, and those used for PROP800, according to Euro-Norm[30], include D_1=10 mm, a_0=3.38 mm, gap=0.025 rad, d=17.0 mm, and a=140 mm.

PROP500 gives the gap closed load P_{gap}=10640 N and the ultimate load P_u=22850 N, whilst PROP800 gives P_{gap}=11490 N and P_u=22500 N.

The comparison indicates that the two Standards predict very close load capacities of the telescopic steel props. Actually, the German Standards[29] and the Euro-norm[30] are two different ways of predicting load capacity of telescopic steel props. Though with different considerations, as outlined in Appendix A8.1, they should be able to predict load capacity of props without a big difference. This has been confirmed by the above illustrations.

8.6 Conclusions

The standard telescopic steel props used in the construction industry have been investigated in this chapter where the initial imperfection, the eccentric loading condition, the semi-rigid baseplate and the initial gap of the baseplate are taken into account. The capacity of ultimate loading and the gap close loading, the deformations and the internal forces of the prop can be predicted using the specifically developed nonlinear computer programs PROP500 and PROP800 [59]. The position of the plastic hinge can also be predicted.

Fairly good agreement between the results of PROP500(PROP800) and another finite element analysis program LUSAS have been presented from the numerical studies. However, PROP500(PROP800) shows considerable advantage over LUSAS in data preparation and on computer CPU time. Meanwhile, the results for the cases of the fully extended, half extended and fully closed props are also presented which exhibit a quite reasonable trend. It should be possible to use PROP800 and PROP500 in the design of telescopic steel props.

The work of this chapter was a first attempt to obtain an adequate analysis method which would deal more readily with the investigation of the influence of nonlinear semi-rigid connections and baseplates on props and other slender structures when different sit conditions and subgrade effects are considered.

CHAPTER 9 SOME DESIGN CONSIDERATIONS AND LOAD CAPACITY PREDICTIONS

9.1 General outline

The previous chapters have investigated semi-rigid rotational stiffnesses of beam-column connections and baseplates and their effects on the buckling and deformation behaviour of slender frame structures and telescopic steel props. A good understanding of these aspects is helpful in the design and load capacity prediction of adjustable telescopic steel props and slender frame structures.

Design of steel frame structures deals with aspects of structural behaviour such as buckling, stiffness and strength [31,51,52]. It is difficult to talk comprehensively about the design of structures and this is not the objective of the present research. This chapter will be focused on discussions about design requirements and the general procedures in load capacity checks. The discussions are based on a knowledge of semi-rigid connections and baseplates and their influence on slender structures, which are the results achieved in the previous chapters.

9.2 Design consideration of baseplates

The model developed in Chapter 3 has proved to be successful and effective in predicting the rotational stiffness of the column-baseplate-subgrade system in pallet rack structures. It needs to be bore in mind that the baseplates investigated are unbolted or lightly bolted. This is the most unfavourable case. The results showed that the rotational stiffness of baseplates was closely related to the rigidity of the subgrade and the applied axial loads. A bifurcation bending moment, at which the moment-rotation curves for different applied axial loads bifurcate, exists for each value of the axial load. The rotational stiffness remains constant, which is defined as initial rotational stiffness of baseplate, until the bifurcation moment. After that, the rotational stiffness is no longer constant. It is dependent upon axial loads and increases with increasing axial load and with increasing rigidity of subgrade. So, as is commonly known, the applied axial loads in a pallet rack, normally the weight of the stored goods, play a positive role in resisting the overturning of the rack. However, the increase in the applied loads could induce another problem, that is the possible buckling of the structure, either globally or locally. So axial loads should not surpass their upper bounds controlled by the buckling criteria.

On the other hand, the application of lateral loads such as wind loads on the structures is one of the sources that create the bending moment at the baseplate. For a given set of applied axial loads, the possible maximum lateral loads can be predicted that will not cause the structure to overturn.

As indicated in section 5.3, of a given set of applied axial loads, the minimum one determines the bifurcation bending moment from which the

initial rotational stiffness can be calculated. The moment-rotation curve is linear for all applied axial loads when the applied moment falls below the bifurcation moment. It follows that the minimum applied axial load can be regarded as one of the control factors for the design of baseplates in pallet racks.

The results of Chapter 3 were based on the assumptions that the baseplates are unbolted or lightly bolted. This gave conservative predictions of the baseplate rotational stiffness. In reality, baseplates are bolted to some extent, sometimes completely fixed. This offers extra safety to resist the overturning of the structures.

9.3 Adjustable telescopic steel props

The standards of design of adjustable telescopic steel props, the Euro-Norm [30] and the German Standards [29], stipulate the principles and rules for materials, configurations, strength and load bearing capacity of the structures. The working loads, which are defined for Standard Type Props and Heavy-duty Type Props, and the initial eccentricities, preflexure, net cross-section areas at the positions of pin holes, etc, differ between the two Standards. All these differences should be considered in design.

The work done in Chapter 8 and the computer programs [55], PROP800 and PROP500 in Appendix A8.2, developed thereafter which are respectively in accordance with the Euro-Norm and the German Standards, should wherever possible be employed in the design and load capacity

prediction of adjustable telescopic steel props. Fully closed, half extended, or fully extended props can have their ultimate loading capacity, their maximum deformation and their maximum bending moment determined by using PROP500 or PROP800, as indicated in detail in Chapter 8.

9.4 Load capacity checks for semi-rigid slender structures

9.4.1 Load capacity checks

For a slender structure, a pallet rack system for example, of a given configuration, it is necessary to predict the load capacity which is defined as the ability to resist external actions without failure.

Normally, the analysis and design of a slender structure is based on the assumption that the beam-column connections and baseplates are rigidly joined or perfectly pinned. Evidently, for the assumption of rigidly joined connections, the load capacity is overestimated, whilst for the assumption of perfectly pinned connections, the load capacity is underestimated. The reasonable estimation of load capacity should be based on the assumption of semi-rigid connections and baseplates, which is the emphasis of the present research and will be addressed in this section.

In accordance with the current Eurocode 3: Design of Steel Structures [53,54], steel structures and their components are designed using the concepts of *Ultimate Limit State* associated with collapse or with other forms of structural failure, for example, by excessive deformation or by loss

of stability of the structures. Load capacity checks for the given configuration of a slender structure should be firstly based on the global buckling analysis and deformation analysis. Meanwhile, a local buckling check is necessary for cold-formed members from which pallet rack structures are often made. Though the local buckling does not necessarily mean immediate collapse of the section, it does reduce the stiffness of the overall structure causing collapse to take place at a lower load than if it had not been present.

9.4.2 Structural model

As discussed in the previous chapters, a slender structure was simplified by an equivalent model where the restraint of beams on columns was replaced by an equivalent beam-column rotational stiffness and the action of the baseplate was replaced by a baseplate rotational stiffness. The equivalent model was then used to predict the buckling and deformation behaviour of slender frame structures, see Chapter 6 and Chapter 7, respectively. The assumptions made in the model are that the most likely deformation modes for the original slender frame structure under the action of both lateral and vertical loads are the unbraced sway modes.

The procedure for the load capacity checks of semi-rigid slender structures is based on a similar model which is plotted in Fig 9.1. The slender frame structure in Fig 9.1(a) possesses semi-rigidity at its beam-column connections and baseplates, marked as black spots. It is simplified as Fig 9.1(b) where the equivalent rotational stiffness k_i (i=1,2,...,n) denotes the action of beams on columns, and k_b denotes the baseplate rotational

stiffness. Fig 9.1(c) represents beam end rotational stiffness, k_{ll} and k_{rl}, which are replaced by the equivalent rotational stiffness k_l, as shown in Fig 9.1(d). As indicated in Chapter 3, the initial baseplate rotational stiffness k_{b0} is calculated by Eq(3.19), and after bifurcation bending moment, the baseplate rotational stiffness k_b is nonlinear and calculated from the moment-rotation curve of the baseplate by secant stiffness of the moment-rotation curve. The equivalent beam-column rotational stiffness k_l is calculated by Eq(6.5), as indicated in Chapter 6. This is the basis for the load capacity checks of the structures concerned.

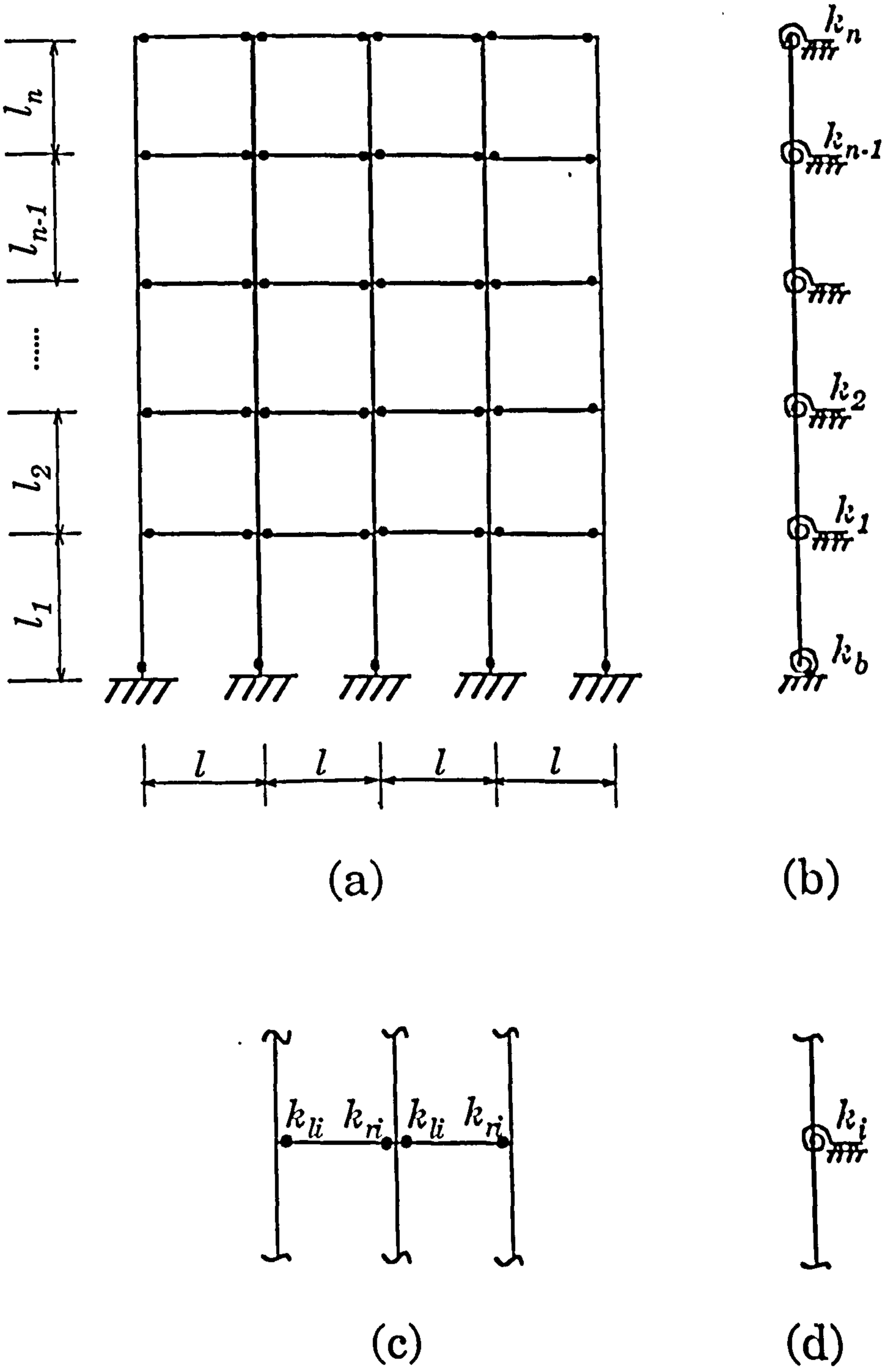

Fig 9.1 Structural model for load capacity checks, (a) slender frame structure with semi-rigid connections marked by black spots, (b) its simplified model with rotational stiffness of k_b and k_i (i=1,2,...,n), (c) beam end rotational stiffness k_{li} and k_{ri} , and (d) the equivalent rotational stiffness k_i

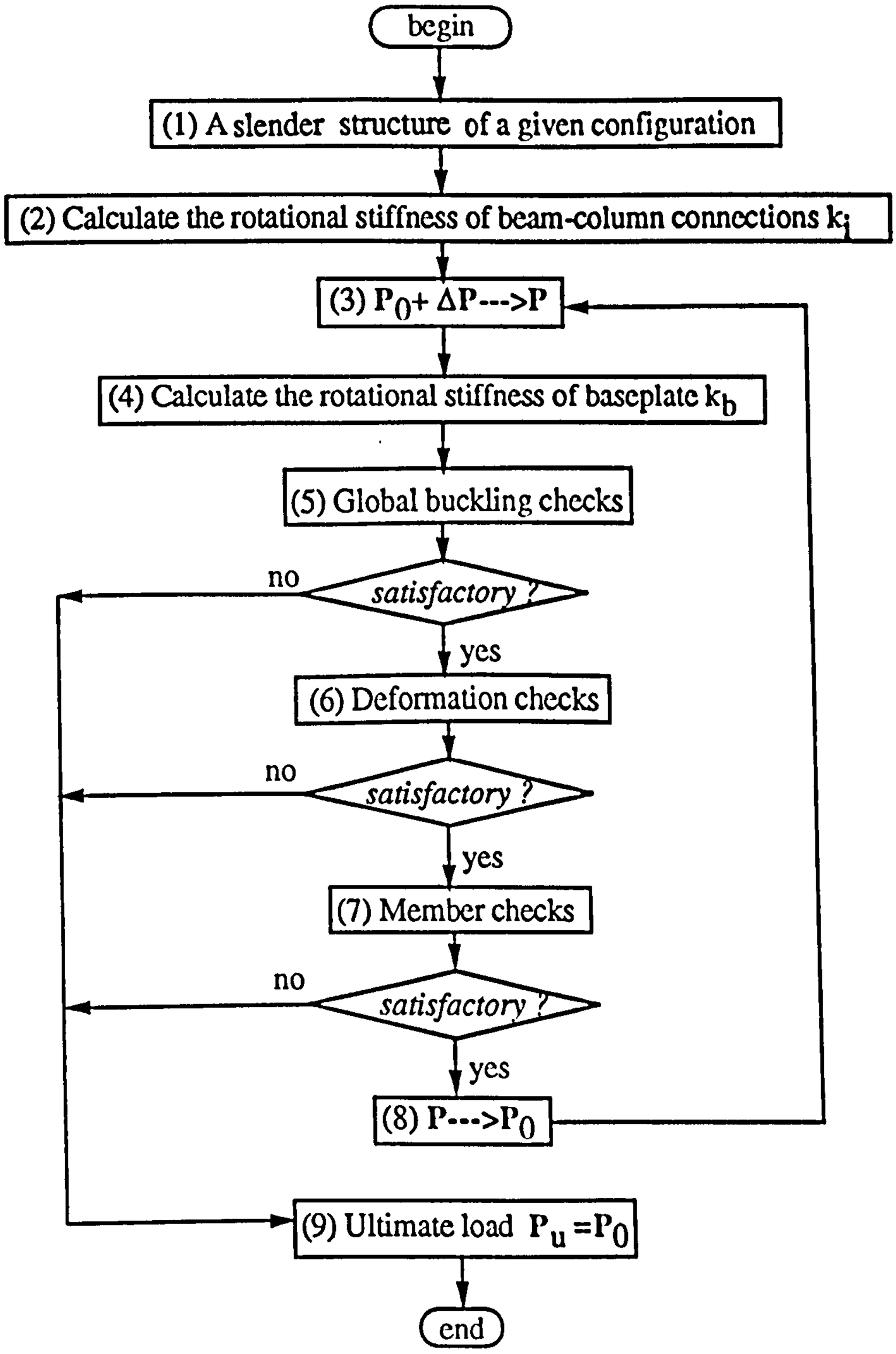

Fig 9.2 Flow diagram for load capacity checks of semi-rigid slender frame structures

9.4.3 Flow diagram for load capacity checks

The flow diagram for load capacity checks is given in Fig 9.2. The square boxes indicate the function boxes whilst diamond ones indicate the identification of the functions.

Box(1): Assume that a slender frame structure of a given configuration is known, see Fig 9.1(a). Input its geometric and material parameters which include: the span l, the height l_i (i=1,2,...,n) where n is the number of storeys, the areas of cross-section of beams and columns, the beam end rotational stiffness k_{li} and k_{ri}, the flexural rigidity of the beams and columns, the sizes of the baseplate, the modulus of subgrade reactions, etc.

Box(2): Calculate the equivalent rotational stiffness of beam-column connections, k_i (i=1,2,...,n), from Eq(6.5) where $(EI)_i$ is the flexural rigidity of the beam.

Box(3): Make incremental loading analysis.

Increment loading approach is used to consider the P-Δ effects and the nonlinearity of moment-rotation relationship of the baseplate for slender frame structures. The structures are subjected to both horizontal and vertical loads which are denoted by P. The initial load P_0 at the present load incremental step, obtained from the previous incremental loading step, plus a load increment ΔP, is assigned to the load variable P, that is $P_0+\Delta P \text{-->} P$. Then the structure subjected to load variable P is analyzed, which is based on the structural configuration of the previous incremental

loading step.

Note that at the first load incremental step, P_0 can be set to be zero.

Box(4): Calculate the rotational stiffness of the baseplate, k_b, which is not only dependent on the geometry and material properties of the baseplate, but also the axial load and the modulus of subgrade reaction of the baseplate. It is a constant, denoted as k_{b0}, when the moment M is less than the bifurcation bending moment M_0 and calculated from Eq(3.19). It becomes nonlinear when $M>M_0$ and calculated from moment-rotation relationship of the baseplate by secant stiffness. Both k_{b0} and k_b can be obtained by means of the computer programs [55].

Box(5): A global buckling check is to be made which uses the procedure of Chapter 6 and the computer programs [55].

The load capacity against global buckling, P_{cr}, can be predicted using the procedure of Chapter 6, and using the computer programs [55]. If the vertical components of the load variable P is smaller than P_{cr} which implies the load variable is not large enough to cause failure of the structure by buckling, the procedure goes to the next step, Box(6), for deformation checks. If the vertical components of the load variable P is larger than P_{cr}, it is believed that the ultimate load P_u has been achieved and then go to Box(9) where the ultimate load P_u takes the initial load P_0 at the present incremental loading step. After this, the whole check procedure is terminated.

Box (6): Make deformation check.

Following the procedures of Chapter 7, the nonlinear static analysis of the structures is made. This considers the P-Δ effects that represent the interaction between the lateral deflection and the axially applied loads. It also considers the initial imperfection of the structures that takes the form of offset from the central axes of the structures.

If the maximum deflection of the structure falls within the limits of the Standards[53], go to Box(7) for member checks. Otherwise, it is assumed that the ultimate load capacity has been reached, as indicated in Box(9).

Box(7): For thin-wall cross-sections of structural members, local buckling is likely to occur. This includes torsional buckling, flexural buckling, or the combination of both.

The necessity of a torsional buckling check lies in the fact that many of the cold-formed sections have either no axis of symmetry or only one, Z and channels for example. This means that these sections have a natural inclination to twist under most load actions. Quantitatively, the resistance of a section to twist is measured by its torsional stiffness which is directly proportional to the cube of its thickness. Therefore many cold-formed sections offer only small resistance to torsional effects due to their small torsional stiffnesses and also due to the shape of their cross-sections.

Check in this step if the requirements for member buckling are met or not according to the Standards[53]. If satisfactory, this will end a round of incremental loading and go to Box(8) for a new round of incremental loading. If not, it is believed that the ultimate load capacity P_u has been

realised which takes the initial load P_0 at the present incremental loading step, as indicated in Box(9). After this, the whole check procedure is terminated.

Box(8): Prepare for a new round of incremental loading which begins again from Box(3). But before that, assign the load variable P at the present incremental loading step to P_0 which is used as an initial load of the new round of incremental loading step.

Box(9): The ultimate load capacity, P_u, is achieved which takes the initial load P_0 at the present incremental loading step. After this, the whole procedure of load capacity checks is terminated.

Using the above procedures, the load capacity can be predicted for a semi-rigid slender structure of a given configuration. Some key points can be drawn out from the procedures. First is the necessity of considering semi-rigid characteristics of beam-column connections and baseplates in the prediction of load capacity. Second, load capacity is controlled either by global buckling behaviour, or by excessive deformation, or by local behaviour of members. Any of these factors failing to meet the requirements of the Standards[53] will lead to collapse of the structure, thus the load capacity of the structures, or say the ultimate load, is achieved. Third, load capacity checks are carried out following a series of load increments. This can take into account nonlinear effects occurring in the structure such as P-Δ effects and semi-rigid characteristics of baseplates. Except for the member checks such as torsional buckling of members, the present research provides all the theories and the computer programs for example, required to carry out the prediction of the load capacity of a semi-

rigid slender structure.

9.5 Summary

This chapter presented some aspects of design considerations concerning baseplates, adjustable telescopic steel props and slender frame structures. It also discussed the procedures for load capacity predictions of the structures.

It was suggested that one of the factors that should be taken into account in the design of column-baseplates in slender frame structures such as pallet racks is the rotational stiffness. The investigation revealed that the stiffness remains constant when the applied moment is less than the bifurcation bending moment. After the bifurcation moment, the stiffness not only depends on the geometric and material properties of the baseplate and the supporting subgrade, but also depends on the axial loads acting on it, and the stiffness increases with increasing axial load. However, increasing axial loads may result in the possibility of column buckling which should be considered in design.

The simplified model for the analysis of adjustable telescopic steel props, based on the Euro-Norm and the German Standards, provided designers with automated evaluation of ultimate loading capacity and maximum deformation of the props. It should be possible to use the associated computer programs, PROP500 and PROP800, in the design of the props.

The procedure for load capacity checks of semi-rigid slender frame structures has been outlined. It emphasized the considerations of the semi-rigid characteristic of beam-column connections and baseplates in load capacity predictions. It made use of the results obtained from the analysis of the previous chapters. These included the equivalent rotational stiffness of beam-column connections, the baseplate rotational stiffness, the global buckling analysis and the second-order deformation analysis. The computer programs [55] developed in this thesis can be used in load capacity checks for semi-rigid slender structures.

CHAPTER 10 CONCLUSIONS AND FURTHER WORK

10.1 Introduction

The influence of semi-rigid beam-column connections and baseplates on the behaviour of slender structures has been investigated in this thesis. Emphasis was given to the theoretical and experimental investigations of the semi-rigid behaviour of baseplates, to the simplified evaluation of buckling behaviour of the structures, to the nonlinear deformation behaviour of the structures and to the analysis of adjustable telescopic steel props. Some aspects of design considerations and load capacity predictions for these structures were also discussed. These investigations have offered a better understanding of the behaviour of semi-rigid slender structures.

10.2 Conclusions

The experimental and theoretical investigations of the rotational behaviour of an unbolted or lightly bolted semi-rigid baseplate in pallet rack structures, which is subjected to different subgrade conditions and applied axial loads, revealed that a given set of applied axial loads corresponds to a unique bifurcation bending moment. When the applied moment is less than the bifurcation moment, the rotational stiffness of the baseplate is a constant and independent of any applied axial load. The applied axial load on the baseplate enables the baseplate to resist the overturning moment and,

the larger its applied load, the stronger its resistance to overturning. It follows that lightly loaded pallet rack structures overturn more readily under the action of horizontal loads, whilst heavily loaded pallet racks have a higher overturning resistance. It is therefore suggested that the overturning resistance of a baseplate be controlled by the possible lowest loading conditions. On the other hand, though the stability of the structure may be guaranteed by increasing the axial loads, attention should still be drawn to the possible buckling of columns induced by excessive axial loading. These conclusions can be used as a guide in design.

The buckling behaviour of slender frame structures considering semi-rigid connections was investigated by a simplified model where the equivalent rotational stiffness of beam-column connections was derived and the baseplate rotational stiffness was determined from the present work. The model was validated by the numerical analysis of a multi-bay slender frame structure with variable number of storeys which showed a good a agreement with the results of other methods.

The deformation behaviour of slender frame structures with semi-rigid beam-column connections and baseplates was demonstrated by a simplified second-order analysis to determine the displacements and bending moments when subjected to both lateral and vertical loads. The comparison between the predictions and the results of the finite element analysis program LUSAS showed good agreement, so the proposed simplified model was validated. The results showed that the consideration of semi-rigid baseplates and beam-column connections contributed significantly to the lateral displacements and bending moments.

The analysis of adjustable telescopic steel props is a matter of interest as industry requires automated predictions of the load bearing capacity of such structures. The development of the design-oriented computer programs, PROP800 and PROP500, which are based on the Euro-Norm and the German Standards respectively, was successful.

Some aspects of design considerations of the relevant structures or structural components were discussed to draw attention to the understanding and the possible improvement of design based on the knowledge of the baseplates, adjustable telescopic steel props and the slender frame structures. The factors that influence the behaviour and design were demonstrated. The procedures of load capacity predictions for a slender structure of a given configuration were presented, which summarized the application of present research to practice.

The computer programs developed for the above subjects have proved to be efficient in computation, simple in preparation of input data and easy in use. They have higher efficiency, compared with the general-purpose finite element analysis computer programs and compared with full scale structural models. They spent less CPU time to achieve the required accuracy. What is more, they can solve the problems that other programs would find difficult. These, for example, include the automated prediction of moment-rotation curve of a baseplate, simplified buckling analysis and second-order analysis of slender structures considering semi-rigid connections and baseplates, analysis of telescopic steel props.

10.3 Further work

The work just summarised has fulfilled the objectives of the thesis outlined in Section 1.2. The results have been successful in experiments, theories and applications. However, future development of the present subjects can be very broad and extensive. This may include the following:

i) Plastic global analyses or elastic-plastic analyses may need to be carried out for some cases [53].

ii) Though some aspects of design considerations have been addressed based on the results of the present research and the flow diagram for load capacity prediction of a slender frame structure of a given configuration has been presented, some detailed work is required.

iii) An expert system could be expected to develop to include structural analysis, component analysis, and optimisation design.

iv) The influence of semi-rigid connections on the stiffness and the buckling behaviour of slender structures can be calculated systematically using the computer programs developed in this thesis and then tabulated for the reference of design.

REFERENCES

1. Godley, M.H.R., Private communication, 1990.

2. Yu, Wei-Wen and Senne, Joseph H. (ed.), Engineering Continuing Education --- The Eighth International Specialty Conference on Cold-formed Steel Structures: Recent research and development in cold-formed steel design and construction, University of Missouri-Rolla, Rolla, MO, USA, 1986, pp.715.

3. Jones, S.W., Kirby, P.A. and Nethercot, D.A., Modelling of semi-rigid connection behaviour and its influence on steel column behaviour, Joints in Structural Steelwork, Howlett, J.H., Jenkins, W.M. and Stainsby, R., (ed.), Pentech Press, 1981.

4. Ang, K.M. and Morris, G.A., Analysis of 3 dimensional frames with flexible beam-column connections. Canadian Journal of Civil Engineering, Vol.11, No.2, 1984.

5. Lui, E.M. and Chen, W.F., Joint flexibility in steel frames, Proc. of ASCE Convention on Connection Flexibility and Steel Frames, Chen, W.F., (ed.), 1985.

6. Jones, S.W., Kirby, P.A. and Nethercot, D.A., Columns with semi-rigid joints, J. Struct. Div., ASCE, Vol.108, 1982, pp.311-329.

7. Lewis, G.M., Cooper, R.A. and Freeman, M.D.T., Automated load testing of pallet rack connections, Strain, Vol.25, No.2, May 1989, pp.57-59.

8. Pekoz, T., Design of cold-formed steel storage racks. Thin-Walled Structures, Recent Technology Advance and Trends in Design, Research and Construction, Int. Conf., University of Strathclyde, Glasgow, Scotland, April 3-6 1979, Halsted Press, New York, NY, 1980, pp.145-159.

9. Wilson, W.M. and Moores, H.F., Tests to determine the rigidity of riveted joints of steel structures, Bull. Ill. Engrg. Exp. Sta. No.104, 1917.

10. Baker, J.F., The Steel Skeleton, Elastic Behaviour and Design, vol.1, Cambridge University Press, 1960.

11. Parsanejad, S. and Anderson, T., Experimental investigation of connection behaviour in light gauge racking systems, Int. Conference on Steel and Aluminium Structures, ICSAS 91, Singapore, 22-24 May 1991.

12. Aggarwal, A.K., Behaviour of moment-resistant beam-to-column connection, Int. Conference on Steel and Aluminium Structures, ICSAS 91, Singapore, 22-24 May 1991.

13. De Wolfe, J.T. and Sarisley, E.F., Column base plates with axial loads and moments, J. of Struct. Div., ASCE, Vol.106, 1980, pp.2167-2184.

14. Thambiratnam, D., Strain distribution in steel column base plates subjected to eccentric loads, Int. Conference on Steel and Aluminium

Structures, ICSAS 91, Singapore, 22-24 May 1991.

15. Timoshenko, S.P. and Gere, J.M., Theory of Elastic Stability, 2nd ed., McGraw-Hill, New York, 1961.

16. Rasmussen, K.J.R. and Hancock, G.J., The flexural behaviour of thin-walled singly symmetric columns, Int. Conference on Steel and Aluminium Structures, ICSAS 91, Singapore, 22-24 May 1991.

17. Jones, S.W., Kirby, P.A. and Nethercot, D.A., The analysis of frames with semi-rigid connections --- A state-of-the -art report. J. Construct. Steel Res. 1982, Vol.3, pp.2-13.

18. Romstad, K.M. and Subrumaniam, C.V., Analysis of frame with partial connection rigidity. J. Struct. Div., ASCE, Vol.96, 1970, pp.2283-2300.

19. Yu, C.H. and Shanmugam, N.E., Stability of frames with semi-rigid joints, Computers & Structures, Vol.23, 1986, pp.639-648.

20. Yu, C.H. and Shanmugam, N.E., Stability of semi-rigid frames, Int. Conference on Steel and Aluminium Structures, ICSAS 91, Singapore, 22-24 May 1991.

21. Monforton, G.R. and Wu, T.S., Matrix analysis of semi-rigidly connected frames, J. of Struct. Div., ASCE, Vol.89, No.ST6, Dec. 1963.

22. Ackroyd, M.H. and Gerstle, K.H., Strength of flexibly connected steel frames, J. of Engineering Structures, Vol.5, Part 1, Jan.1983.

23. Lui, E.M. and Chen, W.F., Analysis and behaviour of flexibly-jointed frames, J. of Engineering Structures, Vol.8, Part 2, Apr.1986.

24. Lui, E.M. and Chen, W.F., Steel frame analysis with flexible joints, Joint Flexibility in Steel Frames, Chen, W.F., (ed.), 1987.

25. Tan, S.H. and Rhodes, J., The behaviour of thin-walled frame systems, Int. Conference on Steel and Aluminium Structures, ICSAS 91, Singapore, 22-24 May 1991.

26. Davies, J.M., Down-aisle stability of rack structures, Eleventh Int. Speciality Conference on Cold-formed Steel Structures, St.Louis, Missouri, USA, October 20-21, 1992.

27. Davies, J.M., Stabilities of unbraced pallet racks, Fifth Int. Speciality Conference on Cold-formed Steel Structures, St.Louis, Missouri, USA, October 20-21, 1980.

28. Lewis, G.M., Stability of rack structures, Thin-Walled Structures, Vol.12, 1991, pp.163-174.

29. DIN 4422, Telescopic Steel Props: Safety Requirements, Testing. June 1987.

30. CEN/TC53-WG8-No36E Working Document, Scaffolds, Falsework and mobile access towers. Jan. 1992.

31. Howlett, J.H., Jenkins, W.M. and Stainsby, R., (ed.), Joints in Structural

Steelwork, Pentech Press, 1981.

32. Department of Civil Engineering, Aston University, Research Report, September 1989.

33. Feng, X., Godley, M.H.R. and Beale, R.G., Elastic buckling analysis of pallet rack structures, Proc Civil-Comp 93: 5th Int Conf Civil and Structural Engineering Computing, Civil-Comp Press, Edinburgh F(1993).

34. Maquoi, R., Semi-rigid joints: from research to design practice, Int. Conference on Steel and Aluminium Structures, ICSAS 91, Singapore, 22-24 May 1991.

35. Krishnamurthy, N. and Thambiratnam, D.P., Finite element analysis of column base plates, Computers and Structures, Vol.34, No.2, 1990, pp.215-223.

36. Paramasivam, P.; Thambiratnam, D. P., Strain distribution in steel base plates under eccentric load, Journal of Strain Analysis for Engineering Design, Vol.24, No.3, Jul. 1989, pp.173-183.

37. Stockwell, Frank W. Jr., Base Plate Design, Published by AISC, Chicago, IL, USA, 1987, pp.49.1-49.15.

38. DeWolf, John T., Column Anchorage Design, Published by AISC, Chicago, IL, USA, 1987, pp.15.1-15.22.

39. Thambiratnam, D. P.; Paramasivam, P., Base plates under axial loads

and moments, J. Structural Div., ASCE, 1986, Vol.112, No.5, pp.1166-1181.

40. Scholz, H., Approximate P-Delta method for sway frames with semi-rigid connections, Journal of Constructional Steel Research, Vol.15, No.3,1990, pp.215-231.

41. Bjorhovde, R., Brozzetti, J. and Colson, A., (ed.), Connections in steel structures, Elsevier Applied Science Publishers LTD, London and New York, 1988.

42. Driscoll, G. C., Elastic-plastic analysis of top- and seat-angle connections, Journal of Constructional Steel Research, Vol.8, 1987, pp.119-135.

43. Aggarwal, A. K. and Coates, R. C., Moment-Rotation characteristics of bolted beam-column connections, Journal of Constructional Steel Research, Vol.6, No.4, 1986, pp.303-318.

44. Timoshenko, S., Theory of Plates and Shells, McGraw-Hill, New York, 1959, pp.273.

45. Winterkorn, Hans F. and Fang, Hsai-Yang, (ed.), Foundation Engineering Handbook, 1975, pp.517.

46. Feng, X., Frame Analysis Program, Research Report, Institute of Building Structures, China Academy of Building Research, Oct. 1987.

47. British Standards Institution, Specification for the Use of Cold Formed Steel in Building, Addendum No 1(1975) to BS449, 1969.

48. Yu, Wei-Wen, Cold-formed Steel Structures, McGRAW-HILL BOOK COMPANY,1973.

49. Chen, W.F. and Lui, E.M., Stability Design of Steel Frames, CRC Press, Inc., 1991.

50. Structural Steelwork Handbook, Sections to BS4: Part 1 and certain others produced by the British Steel Corporation, Properties & Safe Load Tables, BCSA and SCI, 1989.

51. Gero, J.S. and Cowan, H.J., Design of Building Frames, Applied Science Publishers Ltd, London, 1976.

52. Morris, L.J., (ed.), Instability and Plastic Collapse of Steel Structures, Granada, 1983.

53. Eurocode 3: Design of Steel Structures - Part 1.1: General rules and rules for building, April 1992, Ref.No.ENV 1993-1-1:1992E.

54. Taylor, J.C., Baddoo, N.R., Morrow, A.W. and Gibbons, C., Steelwork Design Guide to Eurocode 3: Part 1.1 - Introducing Eurocode 3, The Steel Construction Institute 1993.

55. Feng, X., The computer programs for the analysis of slender structures considering semi-rigid connections, Research Report, No.276, Oxford

Brookes University, Oct. 1992.

56. Walker, A.C., (ed), Design and Analysis of Cold-Formed Sections, Intertext Books, 1975.

57. Armer, G.S.T. and Moore, D.B., (ed), Frame and Slab Structures, Butterworth & Co. Ltd, 1988.

58. Deepstor Data, Dexion Ltd., May 1991.

59. Feng, X., The analysis of telescopic props, Research Report, No.263, Oxford Brookes University, September 1990.

APPENDICES

A3.1: Analytical solutions to Fig 3.10

The loads in Fig 3.10 stem from the action of the axial force on the column. The column distributes the uniform load q in the web and two concentrated loads P in the flanges. They have the relationship with the original axial force P_c as:

$$P=\frac{P_c}{2(a+c)}.c$$

$$q=\frac{P_c}{2(a+c)} \qquad (3A.1)$$

where "a" is half length of the web and "c" is the length of the wing.

Because the structure in Fig 3.10 is symmetric, only half of the structure needs to be analyzed, see Fig 3A.1.

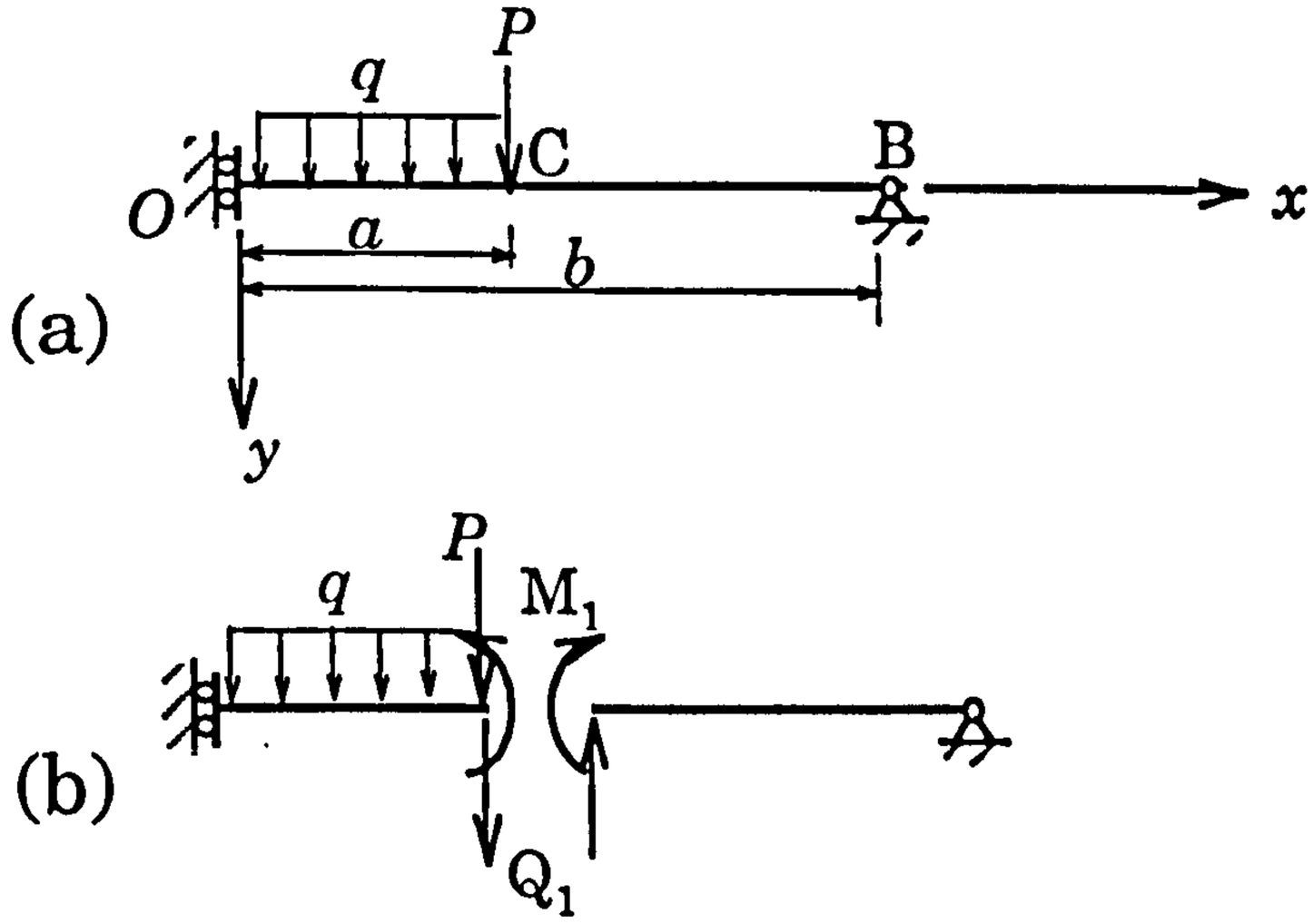

Fig 3A.1 Symmetrical model of Fig 3.10

The equilibrium equations for the model in Fig 3A.1 is written as

$$EIw_1^{(IV)}+kw_1=q \qquad (0\le x\le a) \qquad (3A.2)$$

$$EIw_2^{(IV)}+kw_2=0 \qquad (a\le x\le b) \qquad (3A.3)$$

where the superscripts denote the order of differentiating, EI is the flexural rigidity of the beam, w_1 and w_2 are the deflections in the loading region and unloading region of the beam, respectively.

The corresponding boundary conditions for w_1 are:

$$w_1^{(III)}|_{x=0}=0 \qquad (3A.4)$$

$$w_1^{(I)}|_{x=0}=0 \qquad (3A.5)$$

$$EIw_1^{(III)}|_{x=a}=-Q_1-P \qquad (3A.6)$$

$$EIw_1^{(II)}|_{x=a}=-M_1 \qquad (3A.7)$$

where M_1 and Q_1 are the internal bending moment and shear force at the cross-section "C" in Fig 3A.1.

Eq(3A.4) and Eq(3A.5) are the boundary conditions at the end of x=0, representing respectively that the shear force is zero, and the rotation is zero, whilst Eq(3A.6) and Eq(3A.7) represent the shear force equilibrium and bending equilibrium at x=a.

For the displacement in the region of a<x<b, w_2, the boundary conditions are:

$$EIw_2^{(III)}|_{x=a}=-Q_1 \qquad (3A.8)$$

$$EIw_2^{(II)}|_{x=a}=-M_1 \qquad (3A.9)$$

$$w_2^{(III)}|_{x=b}=0 \qquad (3A.10)$$

$$w_2^{(II)}|_{x=b}=0 \qquad (3A.11)$$

Similarly, the first two equations, Eq(3A.8) and Eq(3A.9), denote the

shear and bending equilibrium at the section of C, whilst the last two, Eq(3A.10) and (3A.10), denote that shear force and bending moment are zero at the end "B" in Fig 3.10.

The compatibility conditions between the deflection w_1 and w_2 are given as

$$w_1|_{x=a}=w_2|_{x=a} \qquad (3A.12)$$

$$w_1^{(I)}|_{x=a}=w_2^{(I)}|_{x=a} \qquad (3A.13)$$

The homogeneous equation corresponding to Eq(3A.2) is written as

$$EIw_1^{(IV)}+kw_1=0$$

which has the following solution

$$w_1^0=e^{\alpha x}(A_1\cos\alpha x+B_1\sin\alpha x)+e^{-\alpha x}(C_1\cos\alpha x+D_1\sin\alpha x)$$

where A_1, B_1, C_1 and D_1 are unknown constants, $4\alpha^4=k/EI$.

The particular solution for Eq(3A.2) is given by

$$w_1^*=\frac{q}{k}$$

So, the general solution for Eq(3A.2) is written as

$$w_1=w_1^0+w_1^* \qquad (3A.14a)$$

or

$$w_1 = e^{\alpha x}(A_1\cos\alpha x + B_1\sin\alpha x) + e^{-\alpha x}(C_1\cos\alpha x + D_1\sin\alpha x) + \frac{q}{k} \qquad (3A.14b)$$

Now, differentiating w_1 produces

$$\begin{aligned} w_1^{(I)} = {} & \alpha e^{\alpha x}[A_1(\cos\alpha x - \sin\alpha x) + B_1(\cos\alpha x + \sin\alpha x)] \\ & + \alpha e^{-\alpha x}[D_1(\cos\alpha x - \sin\alpha x) - C_1(\cos\alpha x + \sin\alpha x)] \end{aligned} \qquad (3A.15)$$

$$w_1^{(II)} = 2\alpha^2 e^{\alpha x}(-A_1\sin\alpha x + B_1\cos\alpha x) + 2\alpha^2 e^{-\alpha x}(C_1\sin\alpha x - D_1\cos\alpha x) \qquad (3A.16)$$

$$\begin{aligned} w_1^{(III)} = {} & 2\alpha^3 e^{\alpha x}[-A_1(\cos\alpha x + \sin\alpha x) + B_1(\cos\alpha x - \sin\alpha x)] \\ & + 2\alpha^3 e^{-\alpha x}[C_1(\cos\alpha x - \sin\alpha x) + D_1(\cos\alpha x + \sin\alpha x)] \end{aligned} \qquad (3A.17)$$

$$w_1^{(IV)} = -4\alpha^4 e^{\alpha x}(A_1\cos\alpha x + B_1\sin\alpha x) - 4\alpha^4 e^{-\alpha x}(C_1\cos\alpha x + D_1\sin\alpha x) \qquad (3A.18)$$

In the same way, the solution for Eq(3A.3) is given as

$$w_2 = e^{\alpha x}(A_2\cos\alpha x + B_2\sin\alpha x) + e^{-\alpha x}(C_2\cos\alpha x + D_2\sin\alpha x) \qquad (3A.19)$$

where A_2, B_2, C_2 and D_2 are unknown constants.

Differentiating w_2 gives

$$\begin{aligned} w_2^{(I)} = {} & \alpha e^{\alpha x}[A_2(\cos\alpha x - \sin\alpha x) + B_2(\cos\alpha x + \sin\alpha x)] \\ & + \alpha e^{-\alpha x}[D_2(\cos\alpha x - \sin\alpha x) - C_2(\cos\alpha x + \sin\alpha x)] \end{aligned} \qquad (3A.20)$$

$$w_2^{(II)} = 2\alpha^2 e^{\alpha x}(-A_2\sin\alpha x + B_2\cos\alpha x) + 2\alpha^2 e^{-\alpha x}(C_2\sin\alpha x - D_2\cos\alpha x) \qquad (3A.21)$$

$$w_2^{(III)}=2\alpha^3 e^{\alpha x}[-A_2(\cos\alpha x+\sin\alpha x)+B_2(\cos\alpha x-\sin\alpha x)] \\ +2\alpha^3 e^{-\alpha x}[C_2(\cos\alpha x-\sin\alpha x)+D_2(\cos\alpha x+\sin\alpha x)] \quad (3A.22)$$

$$w_2^{(IV)}=-4\alpha^4 e^{\alpha x}(A_2\cos\alpha x+B_2\sin\alpha x)-4\alpha^4 e^{-\alpha x}(C_2\cos\alpha x+D_2\sin\alpha x) \quad (3A.23)$$

Substituting Eq(3A.17) into Eq(3A.4) yields

$$-A_1+B_1+C_1+D_1=0 \quad (3A.24)$$

Similarly, substituting Eq(3A.15) into Eq(3A.5) gives

$$A_1+B_1-C_1+D_1=0 \quad (3A.25)$$

Substituting Eq(3A.22) into Eq(3A.10) gives

$$e^{\alpha b}[-A_2(\cos\alpha b+\sin\alpha b)+B_2(\cos\alpha b-\sin\alpha b)] \\ +e^{-\alpha b}[C_2(\cos\alpha b-\sin\alpha b)+D_2(\cos\alpha b+\sin\alpha b)]=0 \quad (3A.26)$$

Substituting Eq(3A.21) into Eq(3A.11) gives

$$e^{\alpha b}(-A_2\sin\alpha b+B_2\cos\alpha b)+e^{-\alpha b}(C_2\sin\alpha b-D_2\cos\alpha b)=0 \quad (3A.27)$$

Substituting Eq(3A.8) into Eq(3A.6) gives

$$EIw_1^{(III)}|_{x=a}+P=EIw_2^{(III)}|_{x=a} \quad (3A.28a)$$

or

$$w_1^{(III)}|_{x=a}=w_2^{(III)}|_{x=a}-\frac{P}{EI} \qquad (3A.28b)$$

It can be seen that Eq(3A.14b) and Eq(3A.19) contain 8 constants. They are A_1, B_1, C_1, D_1 and A_2, B_2, C_2, D_2. In addition, the shear force, Q_1, and the bending moment, M_1, at the cross-section "C" are to be determined. So, the ten parameters can be solved using 10 boundary conditions: (3A.4)~(3A.13)

Substituting Eq(3A.17) and Eq(3A.22) into Eq(3A.28) gives

$$\begin{aligned} &e^{\alpha a}[-A_1(\cos\alpha a+\sin\alpha a)+B_1(\cos\alpha a-\sin\alpha a)] \\ &+e^{-\alpha a}[C_1(\cos\alpha a-\sin\alpha a)+D_1(\cos\alpha a+\sin\alpha a)] \\ =&e^{\alpha a}[-A_2(\cos\alpha a+\sin\alpha a)+B_2(\cos\alpha a+\sin\alpha a)] \\ &+e^{-\alpha a}[C_2(\cos\alpha a-\sin\alpha a)+D_2(\cos\alpha a+\sin\alpha a)]-\frac{P}{2EI\alpha^3} \end{aligned} \qquad (3A.29)$$

Substituting Eq(3A.9) into Eq(3A.7) gives

$$EIw_1^{(II)}|_{x=a}=EIw_2^{(II)}|_{x=a} \qquad (3A.30a)$$

or

$$w_1^{(II)}|_{x=a}=w_2^{(II)}|_{x=a} \qquad (3A.30b)$$

Substituting Eq(3A.16) and Eq(3A.21) into Eq(3A.30b) gives:

$$e^{\alpha a}[-A_1\sin\alpha a+B_1\cos\alpha a)+e^{-\alpha a}(C_1\sin\alpha a-D_1\cos\alpha a)]$$
$$=e^{\alpha a}[-A_2\sin\alpha a+B_2\cos\alpha a)+e^{-\alpha a}(C_2\sin\alpha a-D_2\cos\alpha a)$$

or

$$e^{2\alpha a}[(A_2-A_1)tg\alpha a+(B_1-B_2)]+(C_1-C_2)tg\alpha a+(D_2-D_1)=0 \qquad (3A.31)$$

Substituting Eq(3A.14) and Eq(3A.19) into Eq(3A.12) gives

$$e^{\alpha a}[-A_1\sin\alpha a+B_1\cos\alpha a)+e^{-\alpha a}(C_1\sin\alpha a+D_1\cos\alpha a)]+\frac{q}{k} \qquad (3A.32)$$
$$=e^{\alpha a}[-A_2\sin\alpha a+B_2\cos\alpha a)+e^{-\alpha a}(C_2\sin\alpha a+D_2\cos\alpha a)$$

Substitute Eq(3A.15) and Eq(3A.20) into Eq(3A.13) gives

$$e^{\alpha a}[A_1(\cos\alpha a-\sin\alpha a)+B_1(\cos\alpha a+\sin\alpha a)]$$
$$+e^{-\alpha a}[D_1(\cos\alpha a-\sin\alpha a)-C_1(\cos\alpha a+\sin\alpha a)]$$
$$=e^{\alpha a}[A_2(\cos\alpha a-\sin\alpha a)+B_2(\cos\alpha a+\sin\alpha a)] \qquad (3A.33)$$
$$+e^{-\alpha a}[D_2(\cos\alpha a-\sin\alpha a)-C_2(\cos\alpha a+\sin\alpha a)]$$

$$A_1=R_{10}=\frac{R_8a_{12}-R_7a_{22}}{a_{12}a_{21}-a_{11}a_{22}}$$

$$B_1=R_9=\frac{R_8a_{11}-R_7a_{21}}{a_{12}a_{21}-a_{11}a_{22}}$$

Solving the above equations for the constants of A_1, B_1, C_1, D_1 and A_2, B_2, C_2, D_2 gives

$C_1=A_1$

$D_1=-B_1$

$A_2=A_1+u_2$

$B_2=B_1-u_1/G$

$C_2=C_1+u_3=A_1+u_3$

$D_2=D_1-u_4=-B_1-u_4$

$R_a=e^{\alpha b}(A_2.\cos\alpha b+B_2.\sin\alpha b)+e^{-\alpha b}(C_2.\cos\alpha b+D_2.\sin\alpha b)$

$R_8=-e^{2\alpha b}(R_3.u_2+u_1.R_4/G)-u_4$

$a_{21}=R_3.e^{2\alpha b}$

$a_{22}=1+R_4.e^{2\alpha b}$

$R_7=-u_3-R_5.R_6.u_2-2R_6.\cos\alpha b.u_1/G$

$a_{11}=1+R_5.R_6$

$a_{12}=2R_6.\cos\alpha b$

$R_6=-e^{2\alpha b}/(Y+X.tg\alpha b)$

$R_5=X.(1+tg\alpha b)$

$R_3=tg\alpha b.[1-R_5/(Y+X.tg\alpha b)]$

$R_4=1-(X+Y).tg\alpha b/(Y+X.tg\alpha b)$

$X=\cos\alpha b+\sin\alpha b$

$Y=\cos\alpha b-\sin\alpha b$

$u_4=e^{2\alpha a}.(u_2.tg\alpha a+u_1/G)-u_3.tg\alpha a$

$u_3=e^{2\alpha a}/(H-F.tg\alpha a)[u_2.F.(1-tg\alpha a)-u_1.(H+F)/G]$

$u_2=(u_1R_{14}/G+e^{-\alpha a}.q/k)/R_{12}$

$u_1=-P.e^{-\alpha a}/(2EI.\alpha^3)-R_{13}.e^{-\alpha a}.q/(R_{12}.k)$

$G=R_{14}.R_{13}/R_{12}+(H+F)[1+(F+H.tg\alpha a)/(H-F.tg\alpha a)]$

$R_{14}=2\sin\alpha a+(\cos\alpha a+\sin\alpha a.tg\alpha a)(H+F)/(H-F.tg\alpha a)$

$R_{12}=\cos\alpha a-\sin\alpha a.tg\alpha a$

$+(\cos\alpha a+\sin\alpha a.tg\alpha a)(1-tg\alpha a).F/(H-F.tg\alpha a)$

$R_{13}=(1+tg\alpha a).H-(F+H.tg\alpha a).F.(1-tg\alpha a)/(H-F.tg\alpha a)$

$H=\cos\alpha a+\sin\alpha a$

$F=\cos\alpha a-\sin\alpha a$

(3A.34)

The deflection at the end of B in Fig 3.10 is given by

$$\Delta_b^{(a)}=w_2^{(a)}|_{x=b}$$

$$=e^{\alpha b}(A_2\cos\alpha b+B_2\sin\alpha b)+e^{-\alpha b}(C_2\cos\alpha b+D_2\sin\alpha b)=R_a \quad (3A.35)$$

A3.2: Analytical solutions to Fig 3.11

The applied bending moment of the column in Fig 3.9 is equivalent to that of Fig 3.11. They have the relationship

$$M=2a.P_m$$

or

$$P_m=M/(2a) \quad (3A.36)$$

Due to the applied axial force, the bending moment model in Fig 3.11 will not cause the baseplate to uplift from the subgrade. This enables us to use the elastic foundation beam to analyze the baseplate.

The deformation in Fig 3.11 is antisymmetric. So only half of the baseplate needs to be considered, as shown in Fig 3A.2.

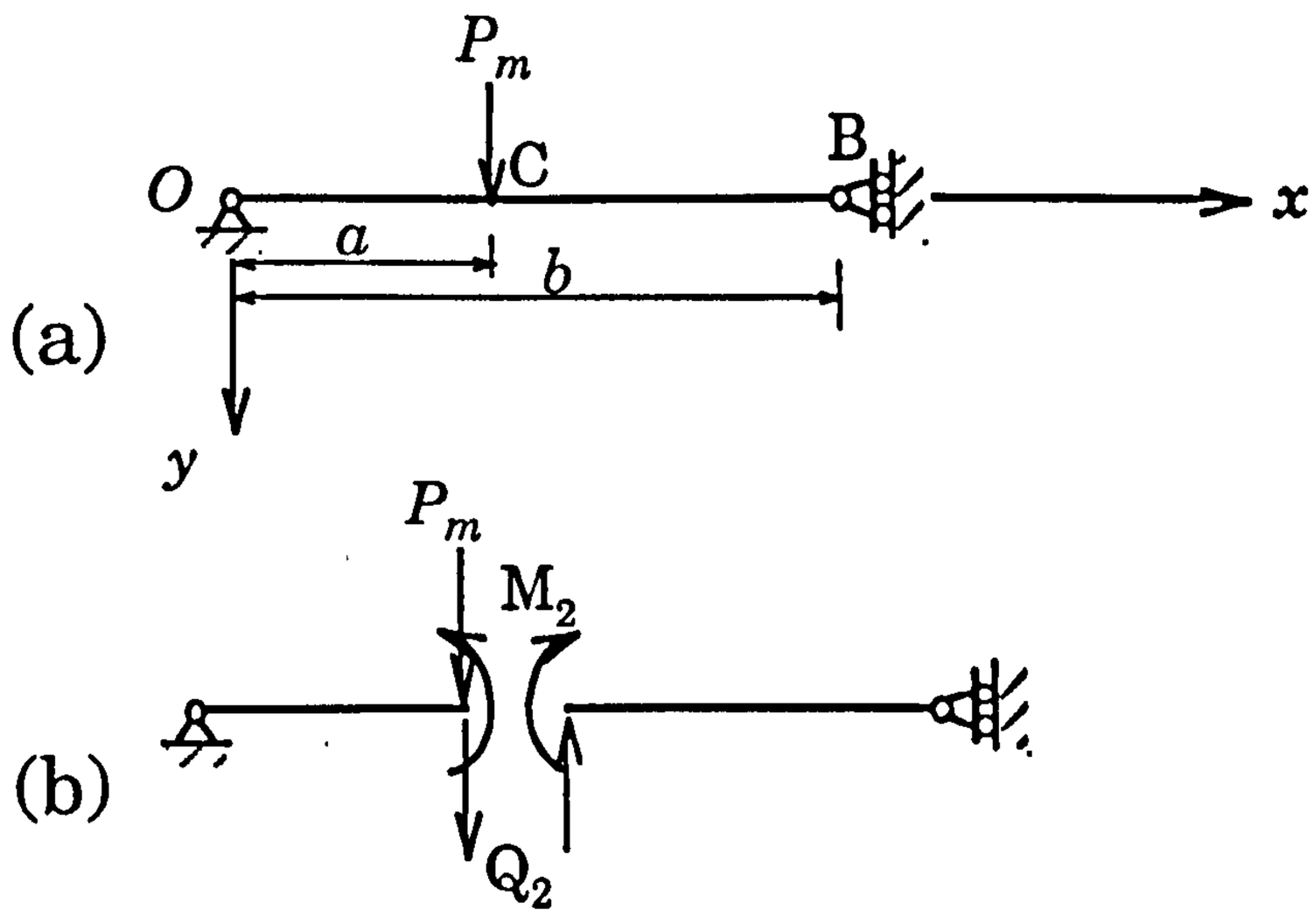

Fig 3A.2 Antisymmetrical model of Fig 3.11

The equilibrium equations of Fig 3A.2 are given by:

$$EIw_1^{(IV)}+kw_1=0 \qquad (0\le x\le a) \qquad (3A.37)$$

$$EIw_2^{(IV)}+kw_2=0 \qquad (a\le x\le b) \qquad (3A.38)$$

The boundary conditions for w_1 are:

$$w_1|_{x=0}=0 \qquad (3A.39)$$

$$w_1^{(II)}|_{x=0}=0 \qquad (3A.40)$$

$$EIw_1^{(III)}|_{x=a}=-Q_2-P_m \qquad (3A.41)$$

$$EIw_1^{(II)}|_{x=a} = -M_2 \qquad (3A.42)$$

where M_1 and Q_1 are the internal bending moment and shear force at the section C, respectively.

Eq(3A.39) is based on the antisymmetric condition that on the antisymmetric point x=0, the deflection is equal to zero, whilst Eq(3A.40) indicates that the bending moment is zero at x=0. Eq(3A.41) gives the shear force at x=a, and Eq(3A.42) gives the bending moment at x=a.

The boundary conditions for w_2 are:

$$EIw_2^{(III)}|_{x=a} = -Q_2 \qquad (3A.43)$$

$$EIw_2^{(II)}|_{x=a} = -M_2 \qquad (3A.44)$$

$$w_2^{(III)}|_{x=b} = 0 \qquad (3A.45)$$

$$w_2^{(II)}|_{x=b} = 0 \qquad (3A.46)$$

Eq(3A.43) gives the shear force and Eq(3A.44) gives the bending moment at x=a. Eq(3A.45) is based on the condition that the shear force at x=b is zero and Eq(3A.46) means that the bending moment is zero.

The compatibility conditions between the deflection w_1 and w_2 at the cross-section C, where x=a, are given as:

$$w_1|_{x=a}=w_2|_{x=a} \qquad (3A.47)$$

$$w_1^{(I)}|_{x=a}=w_2^{(I)}|_{x=a} \qquad (3A.48)$$

Solving Eq(3A.37) and Eq(3A.38), using the boundary conditions Eq(3A.39)-Eq(3A.48), gives:

$$w_1=e^{\alpha x}(A_1\cos\alpha x+B_1\sin\alpha x)+e^{-\alpha x}(C_1\cos\alpha x+D_1\sin\alpha x) \quad (0\le x\le a) \quad (3A.49)$$

$$w_2=e^{\alpha x}(A_2\cos\alpha x+B_2\sin\alpha x)+e^{-\alpha x}(C_2\cos\alpha x+D_2\sin\alpha x) \quad (a\le x\le b) \quad (3A.50)$$

where,

$4\alpha^4=k/(EI)$

$A_1=MR_{10}$

$B_1=MR_9$

$C_1=-A_1$

$D_1=B_1$

$A_2=M(R_{10}-R_1)$

$B_2=M(R_9+R_2)$

$C_2=M(S-R_{10})$

$D_2=M(R_9-T)$

$R_b=e^{\alpha b}[(R_{10}-R_1).\cos\alpha b+(R_9+R_2).\sin\alpha b]$

$+e^{-\alpha b}[(S-R_{10}).\cos\alpha b+(R_9-T).\sin\alpha b]$

$M=2aP_m$

$R_{11}=2(\mathrm{sh}\alpha a.\cos\alpha a.R_{10}+\mathrm{ch}\alpha a.\sin\alpha a.R_9)/a$

$R_{10}=(R_7-a_{12}.R_9)/a_{11}$

$R_9=(a_{11}.R_8-a_{21}.R_7)/(a_{11}.a_{22}-a_{21}.a_{12})$

$R_8=e^{2\alpha b}(R_1R_3+R_2R_4)+T$

$$a_{21}=e^{2\alpha b}R_3$$

$$a_{22}=1-e^{2\alpha b}R_4$$

$$a_{11}=1-R_5R_6$$

$$a_{12}=2R_6\cos\alpha b$$

$$R_7=S-R_5R_6R_1-2R_2R_6.\cos\alpha b$$

$$R_6=-e^{2\alpha b}/(Y+X.tg\alpha b)$$

$$R_5=(1+tg\alpha b).X$$

$$R_1=e^{-\alpha a}.[2tg\alpha a+(1+tg^2\alpha a)(H+F)/(H-F.tg\alpha a)]/(8a.G.EI.\alpha^3)$$

$$R_2=e^{-\alpha a}./(4a.G.EI.\alpha^3)$$

$$R_3=tg\alpha b.[1-R_5/(Y+X.tg\alpha b)]$$

$$R_4=1-tg\alpha b.(X+Y)/(Y+X.tg\alpha b)$$

$$X=\cos\alpha b+\sin\alpha b$$

$$Y=\cos\alpha b-\sin\alpha b$$

$$T=e^{2\alpha a}(-R_1.tg\alpha a-R_2)-S.tg\alpha a$$

$$S=e^{\alpha a}[H+F-F.(1-tg\alpha a).R_{14}/R_{12}]/[4G.EI.a.\alpha^3.(H-F.tg\alpha a)]$$

$$R_{14}=2\sin\alpha a+(\cos\alpha a+\sin\alpha a.tg\alpha a).(H+F)/(H-F.tg\alpha a)$$

$$R_{12}=\cos\alpha a-\sin\alpha a.tg\alpha a$$

$$+(\cos\alpha a+\sin\alpha a.tg\alpha a).F.(1-tg\alpha a)/(H-F.tg\alpha a)$$

$$R_{13}=(1+tg\alpha a).H-(F+H.tg\alpha a).F.(1-tg\alpha a)/(H-F.tg\alpha a)$$

$$H=\cos\alpha a+\sin\alpha a$$

$$F=\cos\alpha a-\sin\alpha a$$

(3A.51)

The deflection at x=a is given by

$$\Delta_a^{(b)}=w_1^{(b)}|_{x=a}=A_1(e^{\alpha a}-e^{-\alpha a})\cos\alpha a+B_1(e^{\alpha a}+e^{-\alpha a})\sin\alpha a$$

or

$$\Delta_a^{(b)}=2A_1 sh\alpha a.\cos\alpha a+2B_1 ch\alpha a.\sin\alpha a) \qquad (3A.52)$$

and the deflection at x=b given by

$$\Delta_b^{(b)}=w_2^{(b)}|_{x=b}$$

$$=e^{\alpha b}(A_2\cos\alpha b+B_2\sin\alpha b)+e^{-\alpha b}(C_2\cos\alpha b+D_2\sin\alpha b)=M.R_b \qquad (3A.53)$$

A6.1: Derivation of the stability functions for free sway structures

Eq(6.9) can be derived in either of the following methods so as to conform the derivation is correct.

Method 1:

Consider the column element in Fig 6.6. It is pinned at both ends and subjected to an axial load P and the bending moment M_{AB} and M_{BA}. The column has a length of L and flexural rigidity EI.

The bending moment at the position of x, M_x, is given by

$$M_x=M_{AB}+Py=-EI\frac{d^2y}{dx^2}$$

or

$$\frac{d^2y}{dx^2}+\frac{Py}{EI}=-\frac{M_{AB}}{EI} \qquad (6A.1)$$

where y is the deflection of the column element.

The solution to this second-order differential equation is

$$y=A\cos\alpha x+B\sin\alpha x-\frac{M_{AB}}{P} \qquad (6A.2)$$

where A and B are two arbitrary constants to be determined from boundary conditions, and

$$\alpha=\sqrt{\frac{P}{EI}}$$

The boundary conditions to Fig 6.6 are written below

$$(i) \qquad y|_{x=0}=0 \qquad (6A.3)$$

$$(ii) \qquad y'|_{x=0}=\theta_A \qquad (6A.4)$$

$$(iii) \qquad y'|_{x=l}=\theta_B \qquad (6A.5)$$

Substituting Eq(6A.2) into Eqs(6A.3), (6A.4) and (6A.5) and solving for the constants A and B produce

$$\therefore \qquad A=\frac{M_{AB}}{P} \qquad (6A.6)$$

and

$$\therefore \qquad B=\frac{\theta_A}{\alpha} \tag{6A.7}$$

Eq(6A.5) gives

$$-A\sin\alpha l\cdot\alpha+B\cos\alpha l\cdot\alpha=\theta_B \tag{6A.8}$$

Substituting Eqs(6A.6) and (6A.7) into (6A.8) yields

$$\therefore \qquad -\frac{M_{AB}}{P}\sin\alpha l\cdot\alpha+\frac{\theta_A}{\alpha}\cos\alpha l\cdot\alpha=\theta_B$$

that is:

$$M_{AB}=(\theta_A\cos\alpha l-\theta_B)\frac{P}{\sin\alpha l\cdot\alpha}$$

or:

$$M_{AB}=\frac{P}{\alpha}\frac{1}{tg\alpha l}\theta_A-\frac{P}{\alpha}\frac{1}{\sin\alpha l}\theta_B \tag{6A.9}$$

$$\because \qquad \alpha=\sqrt{\frac{P}{EI}}$$

$$\therefore \qquad \frac{P}{\alpha}=\frac{P}{\sqrt{\frac{P}{EI}}}=\frac{EI}{l}l\sqrt{\frac{P}{EI}}=iv \tag{6A.10}$$

where:

$$i=\frac{EI}{l} \quad ;$$

$$v=l\sqrt{\frac{P}{EI}} \quad ;$$

$$\therefore \qquad \alpha l=l\sqrt{\frac{P}{EI}}=v \qquad (6.11)$$

Substituting Eqs(6A.10) and (6A.11) into (6A.9) gives

$$\therefore \qquad M_{AB}=i\theta_A\frac{v}{tgv}-i\theta_B\frac{v}{sinv} \qquad (6A.12)$$

Considering the bending equilibrium with respect to the point B creates

$$M_{AB}+M_{BA}+P\Delta=0 \qquad (6A.13)$$

Consider another boundary condition,

$$y|_{x=l}=\Delta \qquad (6A.14)$$

that is:

$$\Delta=A\cos\alpha l+B\sin\alpha l-\frac{M_{AB}}{P} \qquad (6A.15)$$

Substituting Eqs(6A.15) into (6A.13) and solving for M_{BA} give

$$M_{BA}=-M_{AB}-P(A\cos\alpha l+B\sin\alpha l-\frac{M_{AB}}{P})$$
$$=-M_{AB}-PA\cos\alpha l-PB\sin\alpha l+M_{AB}$$
$$=-PA\cos\alpha l-PB\sin\alpha l \qquad (6A.16)$$

Further, substituting Eqs(6A.6) and (6A.7) into (6A.16) gives

$$M_{BA}=-P\frac{M_{AB}}{P}\cos\alpha l-P\frac{\theta_A}{\alpha}\sin\alpha l$$
$$=-M_{AB}\cos\alpha l-\frac{P}{\alpha}\theta_A\sin\alpha l \qquad (6A.17)$$

Substituting Eqs(6A.9) into (6A.17), we have

$$M_{BA}=-(\frac{P}{\alpha}\frac{1}{tg\alpha l}\theta_A-\frac{P}{\alpha}\frac{1}{\sin\alpha l}\theta_B)\cos\alpha l-\frac{P}{\alpha}\theta_A\sin\alpha l$$

$$=-\frac{P}{\alpha}\frac{\cos^2\alpha l}{\sin\alpha l}\theta_A+\frac{P}{\alpha}\frac{\cos\alpha l}{\sin\alpha l}\theta_B-\frac{P}{\alpha}\theta_A\sin\alpha l$$

$$=-\frac{P}{\alpha}\frac{\cos^2\alpha l+\sin^2\alpha l}{\sin\alpha l}\theta_A+\frac{P}{\alpha}\frac{1}{tg\alpha l}\theta_B$$

$$=-\frac{P}{\alpha}\frac{1}{\sin\alpha l}\theta_A+\frac{P}{\alpha}\frac{1}{tg\alpha l}\theta_B \qquad (6A.18)$$

Finally, substituting Eqs(6A.10),(6A.11) into (6A.18) produces

$$\therefore \qquad M_{BA}=-i\theta_A\frac{\nu}{sin\nu}+i\theta_B\frac{\nu}{tg\nu} \qquad (6A.19)$$

Equations (6A.12) and (6A.19) are the stability functions corresponding to the column element in Fig 6.6 when the shear force is zero, which are the same as Eq(6.9).

Method 2:

The slope-deflection relations have been given in Eq(6.7) based on the column element in Fig 6.5 as follows,

$$M_{AB}=4i\theta_A\varphi_2(\nu)+2i\theta_B\varphi_3(\nu)-6i\frac{\Delta}{l}\eta_3(\nu) \qquad (6A.20)$$

$$M_{BA}=2i\theta_A\varphi_3(\nu)+4i\theta_B\varphi_2(\nu)-6i\frac{\Delta}{l}\eta_3(\nu) \qquad (6A.21)$$

$$Q_{AB}=Q_{BA}=-\frac{6i}{l}\theta_A\eta_3(\nu)-\frac{6i}{l}\theta_B\eta_3(\nu)+12i\frac{\Delta}{l^2}\eta_2(\nu) \qquad (6A.22)$$

where

$$i=\frac{EI}{l}$$

$$\nu=l\sqrt{\frac{P}{EI}}$$

$$\varphi_2(v)=\frac{1-\frac{v}{tgv}}{tg\frac{v}{2}}$$

$$4(\frac{2}{v}-1)$$

$$\frac{v}{2}$$

$$\frac{v}{2}-1$$

$$\varphi_3(v)=\frac{sinv}{tg\frac{v}{2}}$$

$$2(\frac{2}{v}-1)$$

$$\frac{v}{2}$$

$$\eta_2(v)=\varphi_4(v)-\frac{v^2}{12}$$

$$\eta_3(v)=\varphi_4(v)$$

$$\varphi_4(v)=\varphi_1(\frac{v}{2})$$

$$\varphi_1(v)=\frac{v^2}{3(1-\frac{v}{tgv})}$$

Assuming that the shear force is zero, that is, $Q_{AB}=Q_{BA}=0$, Fig 6.5 reduces to Fig 6.6. Then, Eq(6A.22) becomes

$$\frac{6i}{l}\theta_A\eta_3(v)+\frac{6i}{l}\theta_B\eta_3(v)=12i\frac{\Delta}{l^2}\eta_2(v)$$

Substituting Eqs(6A.23) into (6A.20) yields

$$\therefore \qquad \frac{2\Delta}{l}\eta_3(\nu)=\frac{(\theta_A+\theta_B)\eta_3^{\,2}(\nu)}{\eta_2(\nu)} \qquad (6A.23)$$

$$M_{AB}=4i\theta_A\varphi_2(\nu)+2i\theta_B\varphi_3(\nu)-3i\frac{(\theta_A+\theta_B)\eta_3^{\,2}(\nu)}{\eta_2(\nu)}$$

$$\therefore \qquad M_{AB}=4i\theta_A\varphi_2(\nu)-3i\frac{\eta_3^{\,2}(\nu)}{\eta_2(V)}\theta_A+2i\theta_B\varphi_3(\nu)-3i\frac{\eta_3^{\,2}(\nu)}{\eta_2(\nu)}\theta_B$$

$$=i\theta_A(4\varphi_2(\nu)-3\frac{\eta_3^{\,2}(\nu)}{\eta_2(\nu)})+i\theta_B(2\varphi_3(\nu)-3\frac{\eta_3^{\,2}(\nu)}{\eta_2(\nu)})$$

$$\because \qquad 4\varphi_2(\nu)-3\frac{\eta_3^{\,2}(\nu)}{\eta_2(\nu)}$$

$$=4\frac{1-\frac{\nu}{tg\nu}}{4(\frac{2}{\nu}-1)}-3\frac{tg\frac{\nu}{2}}{9(1-\frac{\frac{\nu}{2}}{tg\frac{\nu}{2}})^2}\qquad\qquad\qquad

$$=\frac{(tgv-v)\frac{v}{2}}{(tg\frac{v}{2}-\frac{v}{2})tgv}-3\frac{\frac{(\frac{v}{2})^4tg^2\frac{v}{2}}{9(tg\frac{v}{2}-\frac{v}{2})^2}}{\frac{(\frac{v}{2})^2tg\frac{v}{2}}{3(tg\frac{v}{2}-\frac{v}{2})}-\frac{v^2}{12}}$$

$$=\frac{(tgv-v)\frac{v}{2}}{(tg\frac{v}{2}-\frac{v}{2})tgv}-\frac{(\frac{v}{2})^4tg^2\frac{v}{2}}{(\frac{v}{2})^3(tg\frac{v}{2}-\frac{v}{2})}$$

$$=\frac{(tgv-v)\frac{v}{2}-tgv\cdot tg^2\frac{v}{2}\cdot\frac{v}{2}}{(tg\frac{v}{2}-\frac{v}{2})tgv}$$

$$=\frac{\frac{v}{2}tgv-\frac{v^2}{2}-\frac{v}{2}\cdot tgv\cdot tg^2\frac{v}{2}}{(tg\frac{v}{2}-\frac{v}{2})tgv}$$

$$=\frac{\frac{v}{2}tgv(1-tg^2\frac{v}{2})-\frac{v^2}{2}}{(tg\frac{v}{2}-\frac{v}{2})tgv}$$

$$=\frac{\frac{v}{2}\cdot 2tg\frac{v}{2}-\frac{v^2}{2}}{(tg\frac{v}{2}-\frac{v}{2})tgv} \qquad (\because\ tgv=\frac{2tg\frac{v}{2}}{(1-tg^2\frac{v}{2})})$$

$$=\frac{v(tg\frac{v}{2}-\frac{v}{2})}{(tg\frac{v}{2}-\frac{v}{2})tgv}$$

$$=\frac{v}{tgv}$$

$$\because \quad 2\varphi_3(v)-3\frac{\eta_3{}^2(v)}{\eta_2(v)}$$

$$=2\frac{\frac{v}{\sin v}-1}{\frac{tg\frac{v}{2}}{2(\frac{2}{v}-1)}}-\frac{(\frac{v}{2})tg^2\frac{v}{2}}{(tg\frac{v}{2}-\frac{v}{2})}$$

$$=\frac{(\frac{v}{\sin v}-1)\frac{v}{2}}{(tg\frac{v}{2}-\frac{v}{2})}-\frac{(\frac{v}{2})tg^2\frac{v}{2}}{(tg\frac{v}{2}-\frac{v}{2})}$$

$$=\frac{\frac{v}{2}(\frac{v}{\sin v}-1-tg^2\frac{v}{2})}{(tg\frac{v}{2}-\frac{v}{2})}$$

$$=\frac{\frac{v}{2}(\frac{v-\sin v(1+tg^2\frac{v}{2})}{\sin v})}{(tg\frac{v}{2}-\frac{v}{2})} \qquad (\because \quad \sin v=\frac{2tg\frac{v}{2}}{1+tg^2\frac{v}{2}})$$

$$= \frac{\frac{\nu}{2}\left(\frac{\nu - 2tg\frac{\nu}{2}}{\sin\nu}\right)}{\left(tg\frac{\nu}{2} - \frac{\nu}{2}\right)}$$

$$= \frac{\nu\left(\frac{\frac{\nu}{2} - tg\frac{\nu}{2}}{\sin\nu}\right)}{\left(tg\frac{\nu}{2} - \frac{\nu}{2}\right)}$$

$$= -\frac{\nu}{\sin\nu}$$

$$\therefore \qquad M_{AB} = i\theta_A \frac{\nu}{tg\nu} - i\theta_B \frac{\nu}{\sin\nu} \qquad (6A.24)$$

In the same way , we can obtain another equation

$$M_{BA} = -i\theta_A \frac{\nu}{\sin\nu} + i\theta_B \frac{\nu}{tg\nu} \qquad (6A.25)$$

Eqs(6A.24) and (6A.25) are just the same as Eq(6.9).

A6.2: Calculation by the finite element analysis program LUSAS

Example 1:

Data files:

(1) PAA (Coarse mesh, 9 elements), P_{cr}=44314.7 N

(2) PBB (Fine mesh, 18 elements), P_{cr}=44306.2 N

(3) PCC (Finest mesh, 36 elements), P_{cr}=44305.7 N

Result from STAB3: P_{cr}=44305.64 N

Example 2:

Data file:

(1) PA1 (Fine mesh, 48 elements), P_{cr}=6886.94 N

Result from STAB3: P_{cr}=6887.0 N

A8.1: Summary of the major differences between the Euro-Norm and the German Standards

1.Initial eccentricity:

The eccentricities are referred to as the inclination of the applied vertical load from the central axis of the prop and are denoted by Δ_1 and Δ_2 in Fig 8.3.

According to the Euro-Norm[30], the following initial eccentricities shall be assumed:

Δ_1=10 mm, at the top of the prop,

and

$(\Delta_2)_0$=0.4D

$(\Delta_2)_{crit}$=0.5D+t_1, at the base of the prop,

where D is the outer diameter of the adjacent tube, t_1 is the wall thickness of a provided mantle tube piece (see pages 16,17 in [30])

According to the German Standards [29], the eccentricities are assumed as

Δ_1=5 mm at the prop head,

and

Δ_2=0.4D at the prop base.

See page 5 in [29].

2. Preflexure:

The preflexure of the prop is defined in [29] and [30] to be a single half sine wave as shown in Eq(8.4).

According to [30] (see page 18), the maximum offset is assumed as a_0=L/1000, where L is the extension length considered as shown in Fig 8.5.

According to [29] (see page 5), a_0=L/500.

3. The eccentricity-rotation relation (M_b/N-ψ_b curve):

At the base of the prop it is assumed by [30] (see page 19) as shown in Fig8.4, where ψ_b is the rotation of the baseplate and Δ_2=M_b/N indicates the corresponding eccentricity.

However, this relation is assumed by [29] (see page 5) to be a torsion trilinear spring as shown in Fig 8.7.

4. The calculation of cross-section properties:

Normally there are some pin holes on the top prop served as a coarse adjustment. This will no doubt reduce the moment of inertia of the cross-section, resulting in the reduction in the moment resistance of the cross-section. The net cross-section values need to be considered and are given [30] by (see Fig 8.8)

$$A_{gr}=\pi(R^2-r^2)$$

$$I_{gr}=\frac{\pi}{4}(R^4-r^4)$$

$$A_n=2(\psi_R\ R^2-\psi_r\ r^2)-d\ (\sqrt{(R^2-\frac{d^2}{4})}\ -\sqrt{(r^2-\frac{d^2}{4})}\ )$$

$$I_n=\frac{R^3}{2}[\psi_R\ R-\frac{d}{6}\sin\psi_R\ (3+2\sin^2\psi_R)]$$

$$-\frac{r^3}{2}[\psi_r\ r-\frac{d}{6}\sin\psi_r\ (3+2\sin^2\psi_r)]$$

$$I_i=I_{gr}\ \frac{1}{1+2\frac{d}{a}(\frac{I_{gr}}{I_n}-1)}$$

where A_{gr} and A_n are the areas of gross and net cross-sections, I_{gr} and I_n are

the corresponding inertia moments, I_i is the equivalent moment of inertia of the cross-section, and

$$\psi_R=\cos^{-1}(\frac{d}{2R}), \qquad \psi_r=\cos^{-1}(\frac{d}{2r})$$

However, A_{gr} and I_{gr} are calculated according to [29] as

$$A_{gr}=\pi(R^2-r^2)$$

$$I_{gr}=\frac{\pi}{4}(R^4-r^4)$$

A8.2: Use of the computer programs PROP800 and PROP500

PROP800 and PROP500 are developed based on the computational model in Fig 8.2(c). They are based on the formulations derived in Chapter 8 and in accordance with the New Euro-Norm [30] and the German Standards [29], respectively. They provide an analyst with various choices such as the eccentricities on the top and bottom of the prop, the gap on the baseplate, the rotational spring stiffness of the baseplate, and the initial preflexure of the prop.

Two ways of inputting data are adopted in PROP800 (or PROP500), depending upon the preference of analyst. One is interactive input, with which the initial data are input following computer's instructions showing on screen. The other is to use an input file, with which the initial data are edited in a file in advance.

Running PROP800 (or PROP500) requests information as to which type of input is required.

(i) If the answer is "SCREEN", then follow the instructions on screen and type in the required data:

L: Total length of the prop (Unit:mm).

L_1: Length of top prop (mm).

L_2: Length of bottom prop (mm).

D_1: Top end eccentricity (mm).
(Recommended 10 mm)

D_2: Eccentricity of baseplate (mm).

D: Radius difference between top prop and bottom prop (mm).

a_0: The factor of preflexure curve (mm).
(Recommended L/1000 mm)

P: The applied axial load (N).

E: Modulus of elasticity (N/mm^2).

S_{gy1}: Design tensile yield stress of top prop (N/mm^2).

S_{gy2}: Design tensile yield stress of bottom prop (N/mm^2).

gap: Baseplate gap (rad).

(Recommended 0.02 rad)

dx_1: Step length of the calculation point on top prop (mm).

(Suggested $L_1/30$ mm)

dx_2: Step length of the calculation point on bottom prop (mm).

(Suggested $L_1/30$ mm)

R_1: The outside diameter of top prop (mm).

t_1: The wall thickness of top prop (mm).

R_2: The outside diameter of bottom prop (mm).

t_2: The wall thickness of bottom prop (mm).

d: The diameter of the pin hole on top prop (mm).

a: The distance between the pin hole (mm).

The physical meanings of the above parameters have been indicated in Fig 8.3, with Δ_1 and Δ replaced by D_1 and D, and c by L_3.

(ii) If the answer is "FILE", then simply type in the name of the input file.

The order of data in the input file is assigned as: L, L_1, L_2, D_1, D_2, D, a_0, P, E, S_{gy1}, S_{gy2}, gap, dx_1, dx_2, R_1, t_1, R_2, t_2, d, a. They have the same physical meanings as those in Analyst-Computer Dialogue and all are read in free format.

The output results from PROP800 (or PROP500) include the files of OUTPUT and PLOT. They give the computed results and the corresponding plots, respectively.

Various computed results in OUTPUT include:

(1) Output of **initial data.**

(2) Connection forces, H_1,H_2,V_1, and reaction bending moment, M.

ON THE TOP-HALF PROP:

(3) The initial displacement, y_{10}.

(4) The added displacement, y_1.

(5) The bending moment, M_1.

(6) The shear force, Q_1.

ON THE BOTTOM-HALF PROP:

(7) The initial displacement, y_{20}.

(8) The added displacement, y_2.

(9) The bending moment, M_2.

(10) The shear force, Q_2.

THE OTHERS:

(11) The gap closed force.

(12) The position of plastic hinge.

(13) The final load, P_u, when the plastic bending limit is achieved.

(14) The section property I_1, A_1, and Z_1 of the top prop.

(15) The section property I_2, A_2, and Z_2 of the bottom prop.

(16) The plastic bending moment M_{1u} on the top prop.

(17) The plastic bending moment M_{2u} on the bottom prop.

The diagrams given by PLOT include:

(1) The initial displacement.

(2) The added displacement under loading.

(3) The bending moment along the prop.

(4) The shear force along the prop.

SOME PARTS EXCLUDED UNDER INSTRUCTION FROM THE UNIVERSITY